INVESTIGATION OF GASOLINE PARTIALLY PREMIXED COMBUSTION IN A SINGLE CYLINDER OPTICAL DIESEL ENGINE

A thesis submitted for the degree of Doctor of Philosophy

By

Pin Lu

College of Engineering, Design and Physical Sciences

Brunel University
London
United Kingdom

September 2014

Abstract

Gasoline Partially Premixed Combustion (PPC) was investigated in a single cylinder optical diesel engine. The PPC operation was achieved with a combination of high dilution and higher intake charge temperature at part-load conditions using Primary Reference Fuel (PRF). The relative air/fuel ratio (λ) was set to 2.3 and the EGR rate at 22%. Split injections of three fuel distribution strategies (50:50, 70:30 and 30:70) were studied. In addition, the effect of injection pressure (900 and 1200 bar) was investigated for each injection timing. The emission and performance of the gasoline PPC operations were then compared with those of the baseline diesel combustion operation.

Based on the thermodynamic analysis of the engine performance, detailed in-cylinder studies were carried out by means of optical techniques. The high speed imaging technique was employed to observe the fuel spray development and combustion processes. A simultaneous Mie-LIF technique was then developed and utilized for the visualization of fuel liquid and vapour formation.

The experimental results demonstrated that better output performance can be obtained when the combustion phasing (CA50) was properly controlled by injection timings. Simultaneous reduction of NOx and soot emissions was achieved under gasoline PPC operation. Further reduction in soot emissions was achieved at the higher injection pressure of 1200 bar. However, excessive uHC emissions were noted during the gasoline PPC operations. The Mie-LIF images illustrated the faster fuel evaporation process and less luminous combustion of gasoline PPC than the diesel operation. In addition, more luminous combustion was observed at 900 bar injection pressure than 1200 bar injection pressure.

Acknowledgements

I would like to express my greatest respect and gratitude to my supervisor Professor Hua Zhao, for his continuous encouragement, support and guidance during my PhD study.

I would like to thank Chief Technician, Christopher Allan, for his continual assistance on the procurement of parts and components during the course of this research. I would also like to extend my appreciation to Technicians, Andy Selway, Ken Anstiss and Clive Barrett for their patience and supports to my experimental work.

I would like to express my sincere gratitude to Dr. Mohammad Herfatmanesh for his unconditional help and guidance during my experimental work; Dr. Yan Zhang for his valuable support and suggestion on thesis writing; Dr. Mohammadreza Anbari Attar for sharing his knowledge on optical diagnostics; David Peirce, Ian May and Ewan Wilson for proof-reading the thesis.

Finally, I would like to sincerely thank my parents and all my family members for their endless and selfless love.

Abbreviations

ASOI	After the Start of Injection
ATDC	After Top Dead Centre
BMEP	Break Mean Effective Pressure
CA	Crank Angle
CFD	Computational Fluid Dynamic
CI	Compression Ignition
CN	Cetane Number
CO	Carbon Monoxide
CO2	Carbon Dioxide
CR	Compression Ratio
CV	Calorific Value
CVL	Copper Vapour Laser
DC	Direct Current
DCF	Dichroic Filter
DI	Direct Injection
DOC	Diesel Oxidation Catalyst
DPF	Diesel Particulate Filter
ECU	Electronic Control Unit
EGR	Exhaust Gas Recirculation
EPA	Environmental Protection Agency
Exciplex	Excited State Complex
FFT	Fast Fourier Transform
FID	Flame Ionisation Detector
FILE	Forward Illumination Light Extinction
fps	Frames per Second
FSN	Filter Smoke Number
H2	Hydrogen
HCCI	Homogeneous Charge Compression Ignition
HR	Heat Release
HSDI	High Speed Direct Injection
IC	Internal Combustion
ICCD	Intensified Charge Coupled Device

IMEP	Indicated Mean Effective Pressure
ISFC	Indicated Specific Fuel Consumption
IVC	Intake Valve Closure
LED	Light Emitting Diode
LIEF	Laser Induced Exciplex Fluorescence
LIF	Laser Induced Fluorescence
LII	Laser Induced Incandescence
LIS	Laser Induced Scattering
LLS	Laser Light Scattering
LRS	Laser Rayleigh scattering
LTC	Low Temperature Combustion
MK	Modulated Kinetics
N2	Nitrogen
NDIR	Non-Dispersive Infrared
NEDC	New European Driving Cycle
NI	National Instruments
NO	Nitrogen Monoxide
NO2	Nitrogen Dioxide
NOx	Nitrogen Oxides
O2	Oxygen
O3	Ozone
OH	Hydroxyl Radical
PCCI	Premixed Charge Compression Ignition
PIV	Particle Image Velocimetry
PM	Particulate Matter
PPC	Partially Premixed Combustion
ppm	Parts per Million
ppr	Pulse per Revolution
RCCI	Reactivity Controlled Compression Ignition
rpm	Revolutions per Minute
RS	Raman Scattering
SCR	Selective Catalytic Reduction
SI	Spark Ignition
SMD	Sauter Mean Diameter

SOC	Start of Combustion
SOI	Start of Injection
TDC	Top Dead Centre
TSCi	Transonic Combustion
uHC	Unburned Hydrocarbons
UV	Ultra Violet
VCO	Valve Covered Orifice

Contents

LIST OF FIGURES

LIST OF TABLES

CHAPTER 1

Introduction

1.1 Introduction

Internal Combustion (IC) engines have played a dominant role in the fields of power, propulsion and energy since it was firstly invented by Otto in 1876. Much of the world’s progress has been substantially promoted due to its application in industry and transportation. After over a century of development, IC engines have been considerably improved in terms of power performance, fuel economy and emission control. However, in recent decades, ever-tightening legislation has been employed around the world in order to restrict the pollution partially caused by emissions from vehicles, as illustrated by the European emission standard in Table 1.1. Therefore, many manufacturers have been forced to develop and produce more environmentally friendly IC engines.

Table 1.1 EU Emissions Standards for Passenger Cars

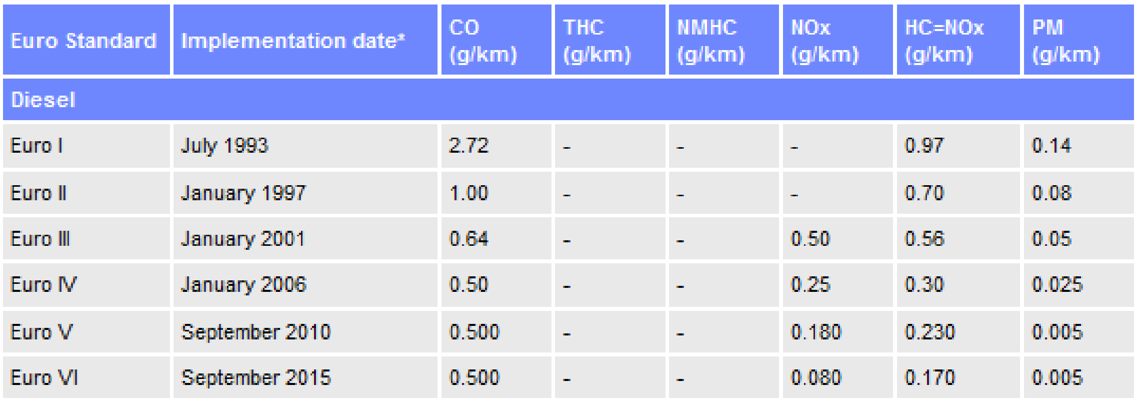

Euro Standard	Implementation date*	CO (g/km)	THC (g/km)	NMHC (g/km)	NOx (g/km)	HC=NOx (g/km)	PM (g/km)
Diesel							
Euro I	July 1993	2.72	-	-	-	0.97	0.14
Euro II	January 1997	1.00	-	-	-	0.70	0.08
Euro III	January 2001	0.64	-	-	0.50	0.56	0.05
Euro IV	January 2006	0.50	-	-	0.25	0.30	0.025
Euro V	September 2010	0.500	-	-	0.180	0.230	0.005
Euro VI	September 2015	0.500	-	-	0.080	0.170	0.005

Compression Ignition (CI) diesel engines have advantages of being robust and reliable, providing outstanding low speed torque and low fuel consumption, but they generate high levels of NOx and soot emissions. Over the last few decades, various after-treatments such as Diesel Particulate Filter (DPF), NOx trap/SCR catalysts, Diesel Oxidation Catalyst (DOC) have been widely utilized to minimize levels of NOx, soot, uHC and CO emissions. Nevertheless, deeper theoretical research regarding pollution formation and development of new technology will likely be required in order to meet further stringent emission legislation.

In the last decade, new combustion concepts, commonly known as Homogenous Charge Compression Ignition (HCCI), Controlled Auto Ignition (CAI), Low Temperature Combustion (LTC), Premixed Charge Compression Ignition (PCCI), have been researched to overcome excessive NOx and Particulate Matter (PM) emissions in CI diesel engines. Although these techniques have exhibited the potential for reduction of NOx and PM emissions, they suffer from a limited operation range, difficulty in controlling the combustion phasing (CA50) and high HC emissions.

Gasoline Partially Premixed Combustion (PPC) is a promising combustion concept which can achieve simultaneous reduction of NOx and soot emissions whilst retaining high engine efficiencies. Since gasoline PPC was firstly proposed by Kalghatgi in 2006, several attempts have been made to not only better understand the chemical reactions during this combustion process, but also build practical experimental investigations. Although quite a few indicative and promising results have been obtained by former researchers, very few studies have been performed combining thermodynamic analysis and in-cylinder visualization studies in the same engine and operating conditions. Thus, in this work, gasoline PPC operation is investigated using the combination of thermodynamic and optical diagnostic analysis in a single cylinder common rail fuel injection engine with optical access.

1.2 Objectives

The aim of this research is to investigate the effect of gasoline type fuel PPC operation on combustion and emissions characteristics by means of thermodynamic analysis combined with the application of optical diagnostic techniques. The objectives include

1. To determine the optimal fuel and mixture conditions for gasoline PPC operation at part-load.
2. The development and implementation of a high speed imaging technique for in-cylinder spray and combustion studies.
3. The development and implementation of a simultaneous Mie-LIF technique for fuel spray liquid and vapour phase visualization as the first time application during Gasoline PPC.

4. An investigation of the effect of injection timing, fuel quantity distribution and injection pressure on combustion and emissions characteristics under gasoline PPC operation.
5. A comparison between gasoline PPC and diesel baseline combustion in terms of mixing formation, combustion process and emission characteristics.

1.3 Outline of Thesis

Following a brief introduction of the thesis in Chapter 1, Chapter 2 reviews the relevant work carried out by other researchers. Firstly, the fundamentals of CI diesel engine combustion and emissions are introduced prior to the description of advanced combustion concepts and techniques. Secondly, the histories of Partially Premixed Combustion (PPC) and its development are presented in detail. Particularly, the effects of the control parameters on gasoline PPC operation are categorized and discussed. Lastly, the optical techniques for fuel spray and combustion visualization are reviewed.

Chapter 3 covers the experimental facilities and measurement equipment utilized in this study. The single cylinder optical research engine and its components, the intake and exhaust system, the fuel injection system and the data acquisition system are described. The data analysis process is explained prior to the description of fuel injector calibration procedure and determination of the relative air/fuel ratio.

Chapter 4 details the development of simultaneous Mie-LIF technique. After the introduction to the principle of Mie-LIF technique, the specification and setup of the laser, optical components, control system and data acquisition system are presented. Finally, the image analysis procedure is described.

Chapter 5 contains the engine experimental works and their thermodynamic analysis. The effects of injection control parameters on gasoline PPC's combustion and emissions characteristics are presented and discussed. In addition, the results of baseline diesel combustion are presented and compared with the gasoline PPC operations.

Chapter 6 focuses on the in-cylinder visualization studies on gasoline PPC. Simultaneous Mie-LIF images of fuel sprays are presented and used to identify the fuel liquid and vapour phases while a high speed imaging technique is utilized to analyse the fuel spray development and combustion process. Furthermore, the fuel vapour spray penetrations are discussed and compared.

Chapter 7 concludes all the experimental results and recommendations for future work are suggested.

CHAPTER 2

Literature Review

2.1 CI Diesel Engine Combustion

In a conventional diesel engine, there is a trade-off between NOx and soot emissions; reducing one leads to an increase in the other. Although exhaust gas emissions have been dramatically reduced by introducing aftertreatment and high fuel injection pressure equipment, the advanced combustion concepts are still urgently required to improve engine emissions, in order to meet increasingly stringent emissions legislation. Consequently, under the pressure of these regulations many manufactures have been forced to look into alternative combustion techniques. Over the last three decades, extensive research and effort have been aimed at reducing NOx and soot emissions simultaneously in CI diesel engines. In this section, Homogenous Charge Compression Ignition (HCCI), Low Temperature Combustion (LTC), Reactivity Controlled Compression Ignition (RCCI) and Transonic Combustion (TSCi) techniques are described in detail.

2.1.1 Conventional Compression Ignition Combustion

In the four stroke engine operating cycle, the liquid fuel is injected into the combustion chamber at high velocity during the compression stroke. Subsequently, the fuel vaporizes and mixes with the in-cylinder air until the temperature and pressure reach the fuel's auto-ignition point. The in-cylinder pressure increases further as combustion takes place. Figure 2.1 summarizes the overall compression ignition combustion process and different stages of combustion are defined.

Ignition delay: this is the period between the start of fuel injection and the start of combustion.

Premixed or rapid combustion phase: during this period, combustion takes place rapidly within a few crank angle degrees, since the fuel-air mixture is above flammability limits. In the meantime, the prepared fuel combusts, resulting in the high heat release rate characteristic.

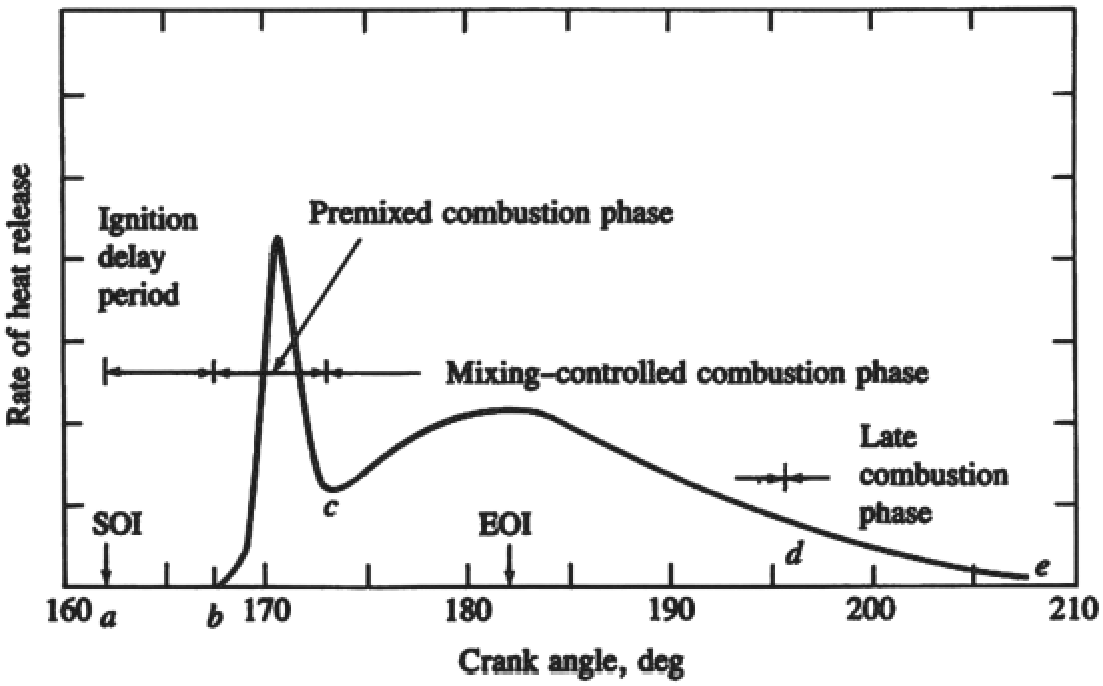

Figure 2.1 Typical DI Engine Heat Release Rate [1]

Mixing controlled combustion phase: after the fuel has been consumed by premixed combustion, the burning rate is slowed down, as the mixture available for burning is formed and consumed simultaneously.

Late combustion phase: this period normally occurs during expansion stroke. The small portion of fuel which hasn’t already been burned is consumed, along with the products of incomplete combustion and soot. The combustion process in this phase becomes slower due to falling in- cylinder temperature and pressure.

2.1.2 Homogenous Charge Compression Ignition (HCCI)

Over the past few decades, the Homogeneous Charge Compression Ignition combustion (HCCI) or Controlled Auto Ignition (CAI) combustion has been widely investigated by numerous researchers. Generally, HCCI combustion can be described as controlled auto ignition of a homogeneous fuel-air mixture without a continuous flame front. This combustion mode results in reduced levels of NOx emissions, due to lowered burned gas temperatures, and a near zero level of soot emissions, due to the elimination of the diffusion burning.

The HCCI combustion concept was initially proposed by Onishi [2] in 1979. In a two stroke engine, Onishi found that a significant reduction in emissions and improved fuel economy could be obtained by spontaneous ignition of the in-cylinder charge. He also concluded that a few critical requirements need to be met in order to achieve HCCI combustion: (1) High levels of dilution, (2) uniform mixing between residual and fresh charge and (3) repeatable cycle to cycle scavenging. The subsequent work by Najt and Foster [3] was to extend the HCCI operation to a four stroke engine. It was found that HCCI combustion is a chemical kinetic combustion process which is controlled by the combination of in-cylinder temperature, pressure and the composition of the charge. It is noted that this HCCI operation lacked control over ignition timings and limited to a certain operational range.

HCCI combustion is an attractive option for compression ignition diesel engines since it offers the potential for reducing NOx and soot emissions simultaneously while maintaining high efficiencies. However, it suffers from difficulties such as overly advanced ignition, requirements for elevated temperatures, and an excessive heat release rate at high load operation. In order to overcome these issues, numerous investigations and developments of diesel HCCI have been carried out based on three main categories. They are premixed HCCI [4, 5], early direct injection HCCI and late direct injection HCCI. Suzuki and Odaka [6, 7] used a gasoline type injector to introduce diesel fuel into the intake manifold. Knocking was suffered at high load operation and HC emissions were excessive, due to overmixed diesel fuel. In subsequent work, efforts were made to resolve the problem of overly advanced combustion phasing. It was achieved by using isooctane as the premixed fuel at some conditions [8, 9]. By injecting the fuel early during the compression stroke, the mixing process can be promoted due to higher in-cylinder temperature and pressure. Iwabuchi [10] studied early injection HCCI by investigating several key parameters in both experimental and CFD works. It was found that NOx emissions were suppressed to low levels, while soot and HC were very high. Higher fuel consumption was reported compared to conventional diesel combustion. In order to improve combustion, an impinging-spray-nozzle injector was introduced to generate wider dispersion angles and reduce penetration [11]. Consequently, fuel consumption was improved by 10%, soot and HC emissions were considerably reduced. The similar research in terms of early injection HCCI can be found in New ACE Institute [12-14], Hino Motors [15], and IFP [16]. Nissan Motor [17-19] has carried out numerous studies on late injection HCCI. They reported 4 to 5 times less NOx emissions and improved PM emissions and fuel consumption compared to conventional operation.

2.1.3 Low Temperature Combustion (LTC)

In low temperature combustion (LTC), the simultaneous reduction of NOx and soot emissions can be achieved by using an optimized injection strategy along with high levels of EGR, intake boosting and high injection pressures**.** Often, LTC employs a multiple injection strategy in order to reduce the injected fuel amount in the main injection which refers to a pilot-main injection strategy, main-post injection strategy and pilot-main-post injection strategy.

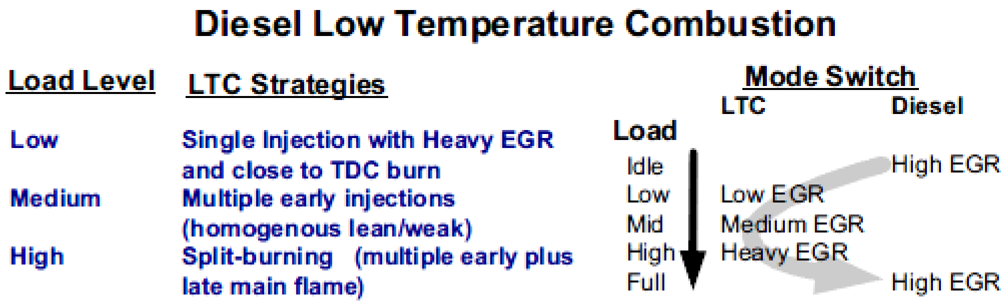

Figure 2.2 The Pathways for Enabling LTC

Asad and Zheng [20] summarized a route to run the engine under LTC mode. As shown in Figure 2.2, at low load operation, LTC might be achieved using a single injection strategy coupled with heavy EGR. As the load increased, a multiple injection strategy needed to be applied to create a more highly mixed charge before the start of combustion. The implementation of different EGR strategies was also useful to maintain low emission levels. In their experimental work, various injection strategies were investigated to improve emissions and efficiency in a high compression ratio diesel engine. They reported NOx emissions of 0.15 g/kWh and soot emissions of 0.01 g/kWh up to 7 bar IMEP using a multiple injection strategy. In contrast, the single injection strategy produced 5 to 8 times higher soot emissions under the same engine load. In their subsequent work [21], the effect of EGR and boost was investigated under single injection strategy LTC operation. It was reported that simultaneously low NOx and soot emissions were achieved under the single injection strategy with EGR. NOx emissions were more dependent on injection pressure than boost level at a low EGR rate. Higher injection pressure benefited soot emissions over all EGR levels while boosting improved soot emissions only when soot was excessive.

In a production V8 diesel engine, Ojeda and Zoldak [22] studied the effect of injection timing on combustion and emissions characteristics. The results showed that the utilization of high EGR and high injection pressure with late premixed injection strategy offered very low soot emissions due to better charge mixing before combustion. It was noted that the early premixed injection strategy was more challenging since it was difficult to accurately control the combustion phasing. Another work on early injection strategy LTC was carried out by Benajes [23]. They reported NOx emissions of 35 ppm and soot emissions of 0.05 FSN at an advanced injection timing of -24 degrees ATDC. In addition, the soot emissions were considerably varied by slight modifications to injection timing under the LTC operation regime.

The recent work by Benajes [24] investigated the effect of EGR and the Miller cycle in a heavy duty diesel engine. During the EGR experiment, large amounts of cooled EGR were introduced to decrease the intake oxygen concentration. In order to achieve Miller cycle operation, the intake valve closing was advanced to reduce the effective compression ratio, and intake pressure was increased to compensate for the air mass losses. The results indicated that both strategies presented the potential for reducing NOx and soot emissions. However, the net fuel consumption was penalized due to the massive EGR.

2.1.4 Reactivity Controlled Compression Ignition (RCCI)

Reactivity controlled compression ignition (RCCI) uses two types of fuel with different auto-ignition properties or reactivities, which are injected separately creating charge stratification. For instance, a lower reactivity fuel such as gasoline can be injected early into the intake manifold using a port fuel injector, while a more reactive fuel like diesel can be directly injected into the combustion chamber. This combustion concept offers high fuel economy with low emissions compared to conventional diesel combustion. However, it suffers from for the added expense of an additional fuel injection system, as well as poor consumer acceptance. The relevant research works can be found in several publications [25-27].

2.1.5 Transonic Combustion (TSCi^{TM})

Recently, a new combustion concept called transonic combustion (TSCi^{TM}) was proposed by De Boer [28, 29]. It is based on the principle of delaying injection of a supercritical fluid (fuel) to where predominantly heat release starts during the engine power stroke. Practically, the pressurized fuel (approximately 250 bar) needs to be heated up to approximately 370 ℃ using a TSCi^{TM} injector. In a 1.6 L CI engine, they reported high thermal efficiency of 42% with the use of EGR and supercritical fuel at 2 bar BMEP. Simultaneous low BSNOx (0.5 g/kWh) and soot emissions (0.17 FSN) were achieved. HC and CO emissions were also suppressed at low level.

2.2 CI Diesel Engine Emissions

In CI diesel engines, pollutant formation is strongly influenced by the fuel distribution and changes due to mixing. Nitric oxide (NO) forms throughout the high temperature burned gas regions as well as oxygen rich areas. Where the flame quenches on the wall, or excessive dilution with air occurs, hydrocarbons and aldehydes are generated; fuel vapour from the nozzle sac volume during the late stages of combustion could be another source of HC. In terms of soot formation, the rich unburned-fuel-containing core of the fuel sprays in the flame region promotes soot generation and the yellow luminous areas of the flame are representative of soot oxidization. In the following section, the formation of these three main pollutants in CI diesel engines is described in detail.

2.2.1 NOx

A common pollutant in CI diesel engine is oxides of nitrogen (NOx), which consist primarily of NO and NO_2. The oxidation of atmospheric nitrogen is the principal source of NO. The formation of NO from atmospheric nitrogen has been widely studied. Zeldovich [30] firstly suggested that the reactions of formation of NO from molecular nitrogen are:

$$O + N_2 = NO + N \qquad \text{Equation 2.1}$$

$$N + O_2 = NO + O \qquad \text{Equation 2.2}$$

Lavoie [31] et al. then added reaction to the mechanism showing as:

$$N + OH = NO + H \qquad \text{Equation 2.3}$$

NO forms in both the flame front and the postflame gases where higher temperatures and oxygen concentrations are present. Shundoh [32, 33] found that the local oxygen concentration played an important role in NO formation. He employed pilot injection and high injection pressure to reduce the NOx emissions, and the effect of nozzle hole diameter, swirl ratio and boosting on NOx emissions were investigated. In a constant volume chamber, Kitamura and Mohammadi [34] investigated NOx formation by sweeping ambient conditions and fuel injection parameters. The results showed that higher NOx formation rates and concentrations could be obtained as ambient pressure was increased, due to the promoted heat release process. Lowered oxygen concentrations substantially reduced NOx formation, with a slight effect on the combustion trend. In order to reduce NOx emissions, Oh and Lee [35] studied the effect of a two stage combustion strategy, coupled with CFD analysis, in a VGT diesel engine. They concluded that NOx emissions could be significantly reduced by decreasing the oxygen concentration during 2nd stage combustion. This could be achieved by injecting a large amount of fuel at the 1st stage to consume more oxygen.

Exhaust gas recirculation (EGR) has been widely accepted as a powerful tool for reducing NOx emissions. It considerably lowers in-cylinder temperature and reduces oxygen concentration which suppresses the NOx formation. Therefore, comprehensive studies [36-38] have been focusing on reducing NOx emission by means of EGR. In a turbocharged medium speed diesel engine, Six and Herzele [39] used cooled and high pressure loop EGR to reduce NOx emissions. It was found that NOx emissions were substantially reduced by the use of EGR. However, there were penalties in terms of CO emissions and fuel consumption. In order to overcome excessive CO and HC emissions when operating under a high level of EGR, Lee and Choi [40] applied a main-post injection strategy to improve combustion efficiency as well as soot emissions. Consequently, a noticeable improvement of CO, THC and soot emission could be obtained, without penalty in NOx emissions. In Li’s [41] work, the combination of a pilot injection strategy and cooled EGR was utilized to improve NOx emissions in a single cylinder diesel engine. The results showed that pilot injection could suppress NOx emissions as well as maximum pressure rise rate.

2.2.2 Soot

In diesel combustion, soot formation occurs at temperatures between about 1000 and 2800 K, at pressures of 50 to 100 atm, with sufficient air to fully burn the fuel. Figure 2.1 Indicates that exhaust particles mainly consist of highly agglomerated solid carbonaceous material and ash, and volatile organic and sulphur compounds.

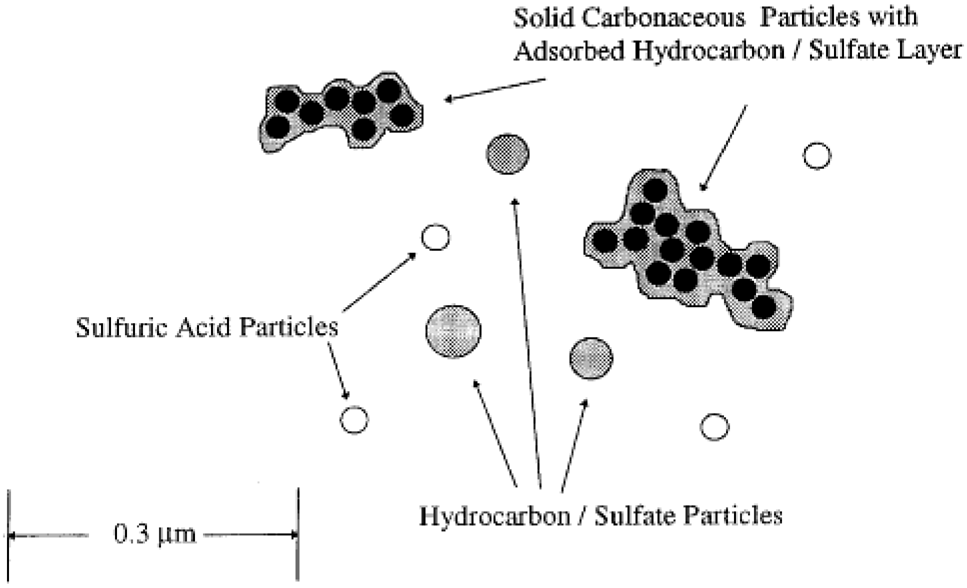

Figure 2.3 Typical Composition and Structure of Engine Exhaust Particles [42]

During the combustion process, although most of the carbonaceous matter is oxidized, it still pollutes engine emissions. Therefore, soot formation has been extensively studied by researchers [43-46]. In their works, engine combustion characteristics were discussed in relation to soot emissions. Furthermore, alternative fuels were employed in order to reduce engine soot emissions [47, 48]. Xu and Lee [49] studied soot formation of oxygenated diesel fuel using the forward illumination light extinction (FILE) technique. They reported different soot reduction performance at different stage of combustion for oxygenated fuels.

As optical techniques have been accepted as a useful means for soot detection and measurement, numerous studies can be found using luminosity measurements [47, 50], laser induced scattering and laser induced incandescence [51, 52]. Senda and Choi [53] utilized the combination of particle image velocimetry (PIV) and laser induced incandescence (LII) techniques to investigate soot formation process in a DI diesel combustion chamber. In addition, the spray properties, the vapour concentration and flow field characteristics on soot formation were discussed. Inagaki and Takasu [54] conducted quantitative measurements of soot concentration using laser induced incandescence (LII) in a diesel engine. The results quantitatively clarified the changes in soot formation caused by altered fuel chemical properties, injection pressure and the hole size of the injector.

Tao and Liu [55] investigated soot formation under low temperature combustion condition in a light duty diesel engine. The modelling studies of piston ring crevice model, KH/RT spray breakup model, a droplet wall impingement model, a wall heat transfer model and RNG k-Ɛ turbulence models were also involved in order to get better understanding of soot formation. In a high EGR environment, Idicheria and Pickett [56] carried out quantitative measurement of soot concentration in an optical constant volume chamber. The results indicated the importance of cooled EGR on reducing soot formation. Connor and Musculus [57] reported that post injection strategies presented an advantage for soot reduction in diesel engines.

2.2.3 Unburned Hydrocarbons

Under normal diesel operating conditions, uHC can be caused by two reasons: (1) over lean mixture formation during the ignition delay period, (2) undermixing of fuel injected at low velocity towards the end of the injection event. However, several techniques used to reduce NOx and soot emissions from a diesel engine can cause a dramatic deterioration of uHC emissions.

In order to understand the sources of HC emissions under the Premixed Compression Ignition (PCI) operation, Manbae [58] investigated exhaust HC speciation at three ERG rates and injection timings. They reported that an over-lean mixture causes an increase in fuel HC species like n-undecane and n-dodecane. Lower peak cylinder bulk temperature causes bulk quenching and higher emission of CO, small alkenes, acetylene and methane. By running a single cylinder light duty engine at Low Temperature Combustion (LTC) conditions, Richard [59] studied effects of fluid mechanics and chemical kinetics to the formation of CO and HC emissions. The variables such as rail pressure, swirl number and inlet temperature were swept using statistical experimental designs to correlate with the kinetic behaviour of HC and CO. It is found that the engine out HC/CO emissions was increased by reducing injection pressure; varying swirl dramatically changed the behaviour of the CO distribution due to changes in available

O_2 within the cylinder; intake temperature had only a small effect on the HC and CO emissions.

In a single cylinder optical engine under the homogeneous type diesel combustion operation, the formation mechanisms of unburned hydrocarbons was investigated by Kashdan [60]. The results showed that bulk quenching represents one of the most significant sources of unburned HC for the wall guided combustion chamber geometry. In addition, the other significant source of engine-out HC emissions was found at the end of combustion by means of liquid films. In the same engine, Mendez [61] studied the sources of unburned hydrocarbons in a low temperature combustion system. The results confirmed the effect of the wall-guided combustion chamber geometry on unburned HC emissions. The experimental data revealed that the level of UHC emissions correlated well with the heat release peak.

Comprehensive studies [62-65] have been carried out to determine the main source of UHC and CO emissions within PPCI regime. Planar Laser Induced Fluorescence (PLIF) technique was applied to measure in-cylinder distributions of UHC species. It was found that the UHC and CO emissions mainly generated from over-mixed, overly lean fuel-air mixtures located within the squish region. In addition, other sources of UHC and CO could be from piston fuel films and crevice flows.

Heywood [1] discussed the evidence that the piston and ring crevice regions are the main contributor to exhaust HC emissions. The changes of volume of crevice region substantially affect the HC emissions level. By changing the ring-orifice design, the reduction of between 47 and 74 percent from baseline HC level could be found. In a single-cylinder CFR engine, Haskell and Legate [66] measured the effect of the piston top-land clearance on exhaust HC emissions. They concluded that HC emissions increase as the clearance increases until the clearance equals approximately 0.18 mm. Although some unburned HC entered the crevice can be burned when it returned during the power stroke, massive HC emissions have been produced. It is noted that the HC emissions under the Partially Premixed Combustion (PPC) in this study could be major since the returning unburned HC may not burn up due to low temperature.

2.3 Diesel and Gasoline Partially Premixed Combustion (PPC)

Partially Premixed Combustion (PPC) is an advanced combustion mode which can simultaneously reduce the NOx and the soot emissions. In PPC operation, the combustion takes place when homogenous or low stratified conditions are achieved. It is noted that the distinction between PPC and HCCI is the degree of premixing. In HCCI combustion, the vaporized fuel is well mixed with the charge gas prior to the combustion, while more heterogeneous charge distribution including fuel-lean and fuel-rich mixture can be found in PPC mode. This directly results in that the HCCI combustion is more kinetically controlled and the effect of fuel injection timing is decoupled. Although chemical kinetics still play a crucial role in PPC combustion, the fuel injection timing needs to be properly selected in order to obtain the desired combustion timing. Additionally, certain amounts of EGR need to be employed to control the combustion temperature as well as the ignition dwell, which is the time from the end of injection to the start of combustion.

2.3.1 Diesel Partially Premixed Combustion (PPC)

In conventional diesel combustion, the fuel is injected slightly before TDC and combustion begins before the end of injection. However, the diesel PPC injection strategy can be categorized to two cases, placed either earlier or later than the conventional diesel combustion, according to the fuel injection and combustion timing.

There were several studies carried out focusing on the early [67-69] and late injection strategies [70-72]. Keeler and Shayler [73] investigated the effect of injection timing and EGR strategy on a turbocharged V6 DI diesel engine. By applying early pilot injection around -25 degrees ATDC with varied EGR rate, NOx and soot emissions can be reduced to levels not requiring aftertreatment. However, high noise [70] and fuel economy penalties were encountered. Kook and Bae [74] studied the effects of charge dilution on diesel combustion and emissions over a wide range of injection timings. The experiments were carried out on a small-bore single cylinder optical diesel engine; in-cylinder pressure and emissions were measured and combustion luminosity imaging was performed. The results showed that charge dilution decreased the adiabatic flame temperature at the fixed start of injection, while the earlier injection timing resulted in higher flame temperature than later injection. Subsequent research work by Horibe and

Takahashi [75] revealed that low CO, NOx and smoke emissions can be achieved by optimizing the combination of injection strategy and combustion chamber geometry under PPC operation. They reported that CO emissions were reduced by selecting injection timings which restricted the mixture distribution in the piston bowl and maximized peak heat release rate. In addition, the NOx-CO trade off can be improved when using a re-entrant combustion chamber with reduced spray angle. The other PPC work was carried out by Nevin and Sun [76] in a heavy duty diesel engine using early start of injection timings. At high speed, medium load operation, a 70% NOx reduction was achieved, while maintaining PM levels, by using late intake valve closing; at low load operation, 0.25 g/kW-hr NOx and 0.02 g/kW-hr PM could be obtained with late intake valve closing, reduced intake pressure and 40% EGR.

Compared to early injection PPC, the late injection occurs very near to TDC or in the early expansion stroke. In a single cylinder light duty diesel engine, Colban and Miles [77] investigated the effect of intake pressure on engine performance and emissions. The experiments used two strategies to achieve low temperature combustion: high EGR with early injection at -30 degrees ATDC, and moderate EGR with late injection near TDC. The intake pressure was varied from 1.0 to 2.0 bar at low load and medium load operation. The results indicated that for both strategies uHC and CO emissions were reduced by increasing intake pressure with corresponding improvements in ISFC and combustion efficiency. Soot concentrations were decreased with increased intake pressure with further reduced NOx emissions. In terms of the injection timings, late injection strategy improved engine noise and soot over the engine operation range, while the early injection strategy lowered uHC and CO emissions and gave better combustion efficiency and ISFC. In order to minimize the fuel consumption, NOx and soot emissions, Klingbeil and Juneja [78] performed premixed diesel combustion analysis in a heavy-duty diesel engine. They reported that low speed light load low emissions operation can be achieved with either very early injection timing (-21 degrees ATDC) or very late injection timing (4 degrees ATDC); for the high speed light load case, only the early injection strategy offered low emissions. It was also found that soot emissions can be effectively suppressed if 2-4 degrees CA ignition dwell (the delay between the end of injection and the start of combustion) was achieved.

A combustion concept called Modulated Kinetics (MK) was introduced by Kimura and Aoki [79, 18] in 1999. This concept provided simultaneous reduction of NOx and soot emissions, due to the low combustion temperatures and highly premixed combustion. The experiments were carried out in both single cylinder and multi cylinder engines. In this study, late injection timing was applied in order to reduce spray impingement on the cylinder walls. In addition, a large amount of EGR was employed to reduce the oxygen concentration. Moreover, it was necessary for the fuel injection event to end prior to ignition. Over 98% NOx reduction was reported and soot concentration could be reduced to less than 1 BSU, if the ignition delay was longer than injection duration. Figure 2.4 demonstrates the comparison between MK combustion and conventional DI diesel combustion.

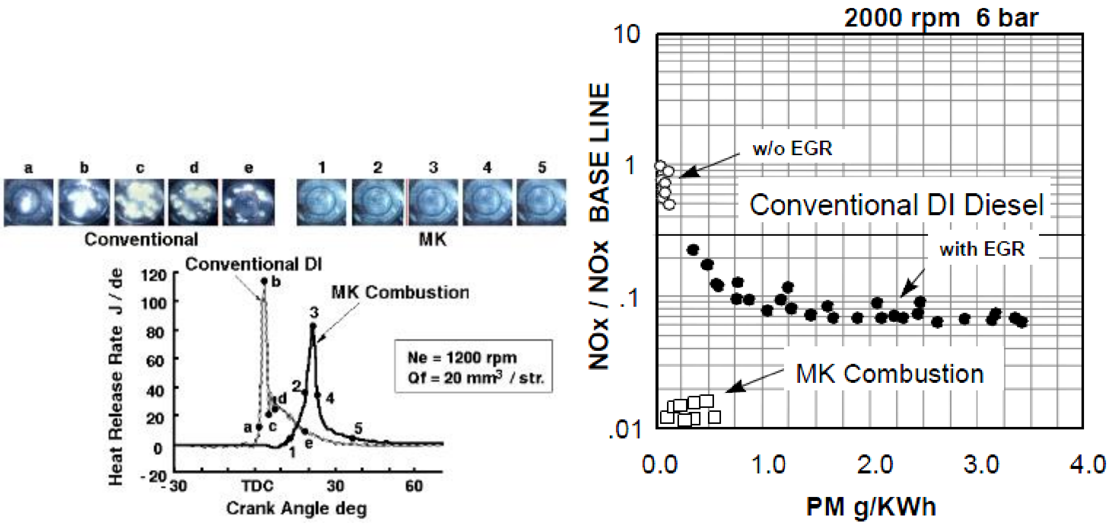

Figure 2.4 Comparison: MK Combustion vs Conventional DI Diesel Combustion

Although PPC combustion presents remarkable performance in terms of the reduction in NOx and soot emissions, excessive CO and uHC emissions are often encountered [80-82]. Also, alleviation of the combustion noise corresponding to the rapid rise of in-cylinder pressure requires more dilution condition and appropriate injection timing control which could lead to more CO and uHC emission production. Accordingly, the fuel consumption can be higher than conventional diesel combustion [81]. In order to overcome this issue, Kanda and Hakozaki [83] in Honda investigated a late injection strategy in a direct injection diesel engine with PPC combustion mode. It was found that IMEP decreased along with increased soot, uHC and CO emissions when injecting fuel early. On the other hand, significant improvements in IMEP and emissions were achieved with the injection timing close to TDC. They also reported that the modified re-entrant type configuration provided better performance on both PPC and diffusive combustion operation in terms of fuel economy, combustion stability and emissions.

Karra and Kong [84] studied the effect of high injection pressure with converging nozzles injector on diesel emission characteristics in a medium duty engine. During the experiments, single early injection and early pilot + late main injection strategies were used with varied injection pressure and EGR rate. They concluded that the high injection pressure considerably reduced soot emissions, with an increase in NOx emissions under conventional injection timing ranges. By using a late injection strategy, no noticeable soot reduction can be observed at high injection pressure. The use of an injector with converging nozzles allowed high injection pressure due to better flow coefficients. However, this type of injector didn't present an advantage in terms of overall emission reduction.

2.3.2 Gasoline Partially Premixed Combustion (PPC)

Although diesel PPC has presented a remarkable advantage in NOx and soot emissions control, a large amount of EGR is required in order to control the ignition delay (SOI-SOC). This is further deteriorating uHC and CO emissions as well as the fuel consumption and combustion stability. Gasoline fuel has inherent auto-ignition resistance which substantially retards the start of combustion. Therefore, it is possible to use the gasoline fuel operating PPC mode in a compression ignition engine.

In 2006, Kalghatgi [85] first proposed the injection of a fuel with high resistance to auto-ignition into a compression ignition engine. The work was carried out in a single cylinder engine based on a heavy duty SCANIA D12 6-cylinder diesel engine and four fuels including Swedish MK1, lower CN diesel and commercial gasoline were used for the purpose of comparison. At an engine speed of 1200 rpm, gasoline PPC was successfully run by using a single injection near TDC. However, the early injection strategy was not applicable, due to either failure of auto-ignition or excessive heat release. By running gasoline PPC, an IMEP of 14.86 bar could be reached with ISFC of 178 g/kWh, ISNOx of 1.21 g/kWh and smoke of 0.36 FSN, with ISHC and ISCO less than 4 g/kWh. This was because the significantly higher ignition delay of gasoline offered much lower NOx and smoke emissions for a given load compared to diesel fuels. In addition, for a given intake pressure and EGR level, much higher IMEP could be achieved while maintaining low NOx and smoke for gasoline PPC than diesel fuel. It is noted that the performance of gasoline PPC was not comparable to diesel fuel with low smoke level at the same operating conditions. This can be improved by optimizing injection strategies and engine design. In his subsequent work with the same engine, Kalghatgi [86] investigated the effect of pilot injection on reducing the maximum pressure rise rate, the cyclic variation as well as the emissions. The engine was running at 1200 rpm with an intake pressure of 2 bar, intake temperature of 40 ℃ and 25% EGR, at different fuelling rates and with different injection strategies. In the diesel single injection case, the smoke decreased when the fuelling rate was reduced for a given injection timing, and the same soot reduction can be found as injection timing was retarded for a given fuelling rate. By using a pilot injection early during the compression stroke, the specific fuel consumption increased while the smoke level reduced compared to a single injection strategy. In terms of gasoline PPC, the pilot injection considerably reduced the maximum heat release rate for a given IMEP and allowed heat release to take place later, with low cyclic variation compared to a single injection strategy. Consequently, higher mean IMEP and lower smoke were achieved due to the stable combustion process and longer ignition delay, respectively. At the best operating point, a mean IMEP of 15.95 bar was reached with smoke of 0.07 FSN, ISNOx of 0.58 g/kWh, ISFC of 179 g/kWh, ISHC of 2.9 g/kWh, ISCO of 6.8 g/kWh and peak pressure of 120 bar. At the same operating conditions, diesel fuel had to have an IMEP of 6.5 bar to achieve a similarly low level of smoke emissions.

2.3.2.1 Fuel Property Effects in PPC

In PPC operation, fuel properties directly affect the ignition delay, which exerts influence over NOx and smoke emissions. Therefore, numerous studies have been carried out to investigate the effect of fuel-type on PPC combustion.

Following the initial attempts with gasoline PPC operation, Kalghatgi [87] studied different auto-ignition quality fuels in a half litre single cylinder diesel engine. The fuels tested were: commercial diesel fuel with a cetane number of 56; commercial gasoline fuel with a RON of 95 and MON of 85 (estimated CN of 16); blended gasoline fuel with an estimated CN of 21. During the experiments, the engine was running at low speed light load and high speed high load with intake boosting. In the meantime, the injection timings and EGR rate were adjusted in order to control the combustion phasing. The results showed that the engine could be successfully run in PPC mode with all different fuels. At low speed and light load, the gasoline fuels produced less NOx emissions and maximum pressure-rise rate compared to the diesel fuel; lower octane ranking fuel was more easily controlled in PPC operation than high octane ranking gasoline. At the engine speed of 2000 rpm with 2 bar intake pressure and a fixed EGR rate, the 95 RON gasoline could get ISNOx below 0.4 g/kWh with little smoke production in an IMEP range of 10-12 bars, whereas it was not possible to operate on the diesel fuel with such low NOx emissions. At the engine speed of 3000 rpm, the 84 RON fuel could achieve simultaneous low NOx and smoke emissions, but the diesel fuel could not. However, the gasoline fuels suffered from high HC and CO emissions due to the lean combustion process. Fuel consumption for all of the fuels was comparable, at around 203 g/kWh ISFC at 2000 rpm with 11 bar IMEP. It is noted that at high load the high maximum pressure rise caused by more premixed combustion can be suppressed by optimizing the injection timing.

Based on the same engine, Hildingsson [88] further investigated the effect of different fuel research octane numbers (RON) on the PPC's emissions. RON of 91, 84, 78 and 72 were tested and compared at low speed light load by sweeping start of injection; an EGR sweep was also performed at higher speed and load. It was found that all of the fuels could be run in PPC mode with ISNOx below 0.3 g/kWh and very low smoke emissions. Although CO and HC emissions were higher for gasoline fuels, they can be reduced by using lower injection pressure at low load, without incurring a penalty in terms of smoke emissions. In addition, the fuel in the range of 75 to 85 RON was reported to be best for such engine compression ratio (16:1) and operating conditions. The subsequent work carried out by Petersen [89] used 15 different fuels to study uHC and CO emissions in a light duty diesel engine operating at two PPC conditions. The early single injection strategy was applied at low speed light load (1500rmp, 3.0 bar IMEP) and higher speed medium load (2000rmp, 6.0 bar IMEP). It is found that for the low speed light load case uHC and CO emissions were highly affected by chemical kinetics control which can be determined by the factors of the injection timing, the ignition delay and the premixed combustion phasing. Furthermore, the combustion phasing (CA50) was constant at more advanced injection timings with the same uHC and CO emissions. However, different fuels showed different combustion phasing (CA50), resulting in significant differences in uHC and CO emissions. The biofuels presented lower uHC and CO emissions compared to gasoline type fuel due to higher ignition quality of the biofuels used. At a higher speed medium load condition, uHC and CO emissions were less sensitive to the fuel type compared to its counterpart condition. It is also noted that uHC and CO emissions were not strongly dependent on the combustion temperature, which revealed that it was more controlled by the injection timing.

Comprehensive research work on different types of gasoline fuel PPC was carried out by Manente [90, 91] in Lund University. In a heavy duty single cylinder CI engine, the engine performance and emissions were investigated using different types of gasoline-like fuels in the RON range of 69 to 99. The engine load was swept from 1 to 12 bar IMEP at 1000 and 1300 rpm, with high EGR and boosting. Gross indicated efficiencies of more than 50% were reported with a peak of 57% at 8 bar IMEP. This was attributed to high combustion efficiency (more than 98%), very low exhaust loss (approximately 20%) and heat transfer (approximately 30%), Figure 2.5. In all test conditions, NOx emissions were consistently below 0.5 g/kWh. However, soot emissions were independent of RON ranking. 0.5 FSN was obtained for RON higher than 95 while for lower RON fuels 3 FSN was reached at 13 bar IMEP. Additionally, the maximum pressure rise rate of 19 bar/CAD appeared with high RON fuel (higher than 95) owing to over rapid heat release. For the fuels with RON below 90, the pressure rise rate could be suppressed to below 14 bar/CAD.

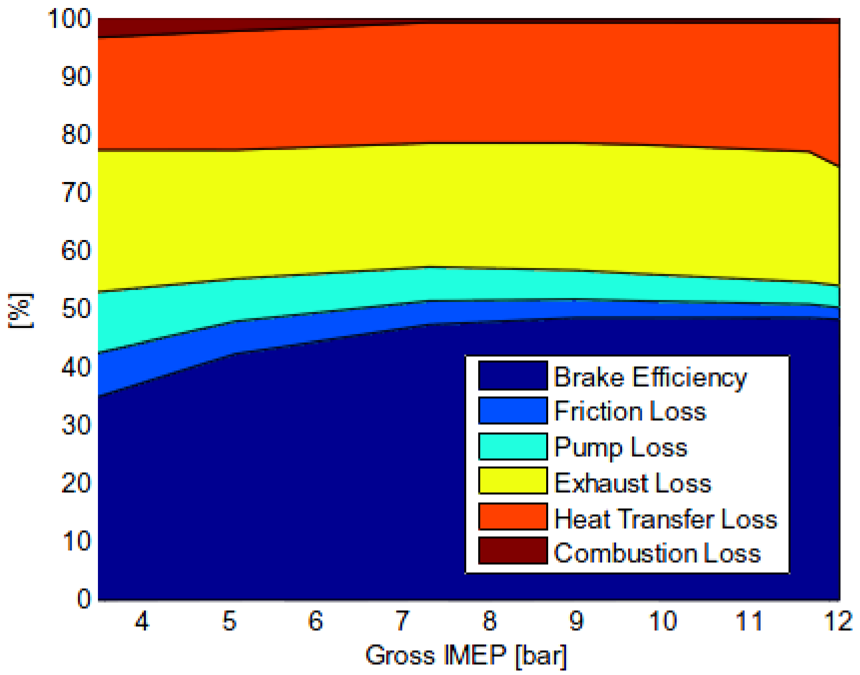

Figure 2.5 Brake Efficiency and Energy losses as a Function of IMEP at 1300 rpm (Fuel FR47333CVX)

Following the above mentioned work, Ethanol fuel was applied in PPC operation in order to improve the soot emissions at high engine load. It is noted that the compression ratio was reduced from 18:1 to 14.3:1 to allow high load operation as well as sufficient mixing. The results showed that by using 50% of EGR, the NOx could be controlled, with emissions below 0.3 g/kWh at high load. Gasoline fuel produced soot emissions in the range of 1-2 FSN while 0.06 FSN was achieved when fuelling on Ethanol. Improved gross indicated efficiency of 54-56% was reported with rapid combustion control using high boosting. It was suggested that the combustion temperature was in the range of 1500 to 2000K, due to the low values of both CO and NOx emissions. According to the engine performance and emissions, a suitable fuel for PPC operation with a similar compression ratio should have a RON below 90.

In Liu and Wang's [92] work, experiments assessing the performance and emissions of wide distillation fuel (WDF) blends with RON of 90, 97, 100 and diesel fuel were conducted in a direct injection diesel engine. The results indicated that WDF90 produced higher combustion efficiency at medium load compared to other WDF fuels but with slightly increased NOx emissions. The soot emissions were considerably reduced at both medium and high load for all three WDF fuels compared to diesel fuel. It was also found that thermal efficiency can be increased by using WDF fuel PPC compared to SI operation.

Recent research carried out by Leermakers [93] was focused on the fuels which have a fixed RON of 70 but with different boiling ranges, aromatic- and bio-content. The experiments were performed in a 2 Litre single cylinder CI engine with reduced compression ratio of 15.7:1. It was reported that the gasoline boiling range fuel gave average performance over the whole load range, but with slightly higher NOx emissions at low load and reduced efficiency at low speed. The fuels with boiling points in the diesel range demonstrated better indicated efficiency at low engine speed with a penalty in terms of combustion stability. The diesel fuel with low aromatics gave poor smoke and NOx emissions, as well as poor stability and combustion efficiency at low speed. The fuel with added bio-content had the best NOx emissions at light load and decent combustion efficiency at low speed. However, this fuel suffered from excessive smoke emissions and was sensitive to injection pressure.

In order to define the fuel property on PPC operation, Kalghatgi [94] developed a description to evaluate the auto-ignition quality of the fuel. An Octane Index, $OI = (1-K) \cdot RON + K \cdot MON$ was introduced. Where MON and RON are the research and motor octane numbers, K is an empirical constant. This equation represented the propensity of a fuel to be ignited - high OI has more resistance to auto-ignition. Four model fuels made of isooctane, n-heptane, toluene and four unleaded gasolines with RON of 72, 78, 84, 91 were tested in a light duty single cylinder CI engine. The results showed that although the ignition delay was not increasing linearly with OI, it changed little over the auto-ignition range of practical diesel fuels. It was suggested that a good surrogate for gasoline in partially premixed CI engines is a mixture of toluene, iso-octane and n-heptane with the same RON and MON.

2.3.2.2 Fuel Injection Strategies in PPC

In Partially Premixed Combustion operation, the injection strategy played crucial role in charge premixing and combustion phasing control. In addition, the ignition delay, which is partially determined by injection strategy, directly affects the engine-out emissions. Therefore, the optimization of fuel injection parameters such as injection timing, injection quantity and injection pressure are required in order to obtain stable and clean PPC operation.

Rezaei and Zhang [95] investigated two-stage split-injection strategies for PPC mode in a light duty 2.2 L four cylinder CI engine. The fuel used was a mixture of 50% ULG95 gasoline and 50% EN590 diesel fuel. Apart from injection strategy, other parameters affecting the combustion process were fixed by the Taguchi-DOE in order to identify the individual effects of parameters. Generally, split injection strategy produced approximately 50% and 90% less BSNOx and smoke emissions, respectively. However, the brake-thermal efficiency was reduced, due to increased THC emissions caused by the two-stage injection strategy. At low load (1.37 bar BMEP) operation, the smoke emissions were determined by the 1st and 2nd injection timings while the 1st injection quantity and 2nd injection timing had more influence on smoke emissions at 2.97 bar BMEP. For both loads, brake-thermal efficiency, CO and THC emissions were influenced by the 1st injection timing, whereas CA50 was affected by the 2nd injection timing. The effects on NOx emissions were varied as the injection parameters changed at different load condition.

Another work reported by Turkcan and Ozsezen [96] studied the effect of 2nd injection timing on the combustion and emissions characteristics in a single cylinder CI engine. The experiments were carried out at low and high load with alcohol-gasoline fuel blends.

It was concluded that 2nd injection timing directly control the combustion and emissions characteristics. By retarding the 2nd injection timing, the maximum cylinder pressure and heat release rate decreased considerably. At low equivalence ratios, NOx, uHC, CO emissions and IMEP, indicated efficiency can be improved by optimizing the 2nd injection timing. It was noted that the 2nd injection timing had less effect on uHC and CO emissions than it did on NOx and smoke emissions. In addition, when the percentage ethanol content was increased in the fuel blends, the maximum in-cylinder pressure, heat release rate and NOx emissions decreased. In contrast, with increased methanol content these parameters increased and the start of combustion and combustion phasing were advanced.

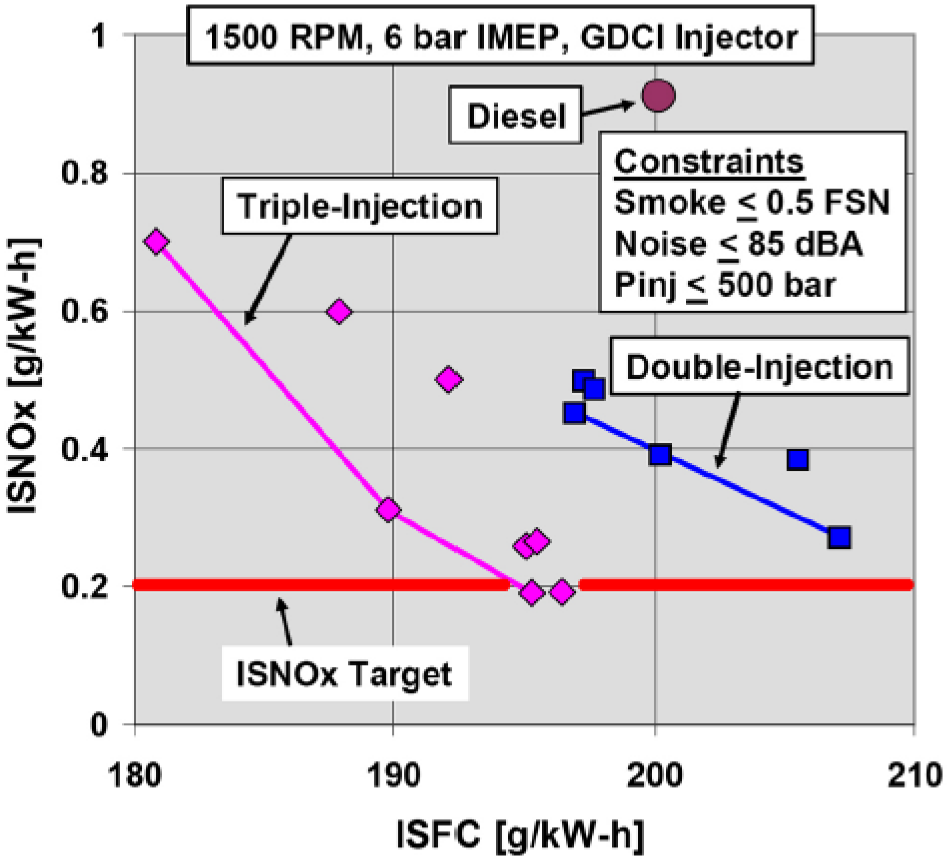

Figure 2.6 Combustion Performance Using Double and Triple Injection Strategy

Sellnau and Sinnamon [97] applied the multiple injection strategy combined with intake boost and moderate EGR to achieve reduced NOx and PM emissions, Figure 2.6. The engine was running at 1500 rpm and 6 bar IMEP using RON91 gasoline fuel throughout the experiments. By using Design of Experiments methods and Response Surface Modeling methods, an optimized triple injection strategy was shown to offer the best fuel economy. Additionally, this strategy allowed a lower injection pressure to be used compared to conventional diesel combustion. It was reported that a minimum ISFC of 181 g/kWh was achieved, which was 8% more efficient than diesel combustion. At this fuel consumption condition, ISNOx of 0.7 g/kWh and FSN of 0.3 could be obtained. The threshold of 0.2 g/kWh for NOx emissions can be reached if a 7.7% fuel consumption penalty is accepted, due to the trade-off between ISFC and ISNOx. $ISCO_2$ emissions (542 g/kWh) were approximately 14% less than the diesel baseline, and UHC emissions of 0.75 g/kWh were observed.

In order to achieve an efficient and clean combustion, Shi and Reitz [98] developed a CFD simulation which could be used to optimize the injection variables. In a heavy duty CI engine at medium and high load conditions, diesel, gasoline and E10 were used to optimize the injection parameters of pilot injection timing, main injection timing, pressure and quantities. The results indicate that the gasoline-like fuel had the potential to achieve clean combustion. At medium engine load, the 2nd injection timing considerably affected engine performance with a gasoline type fuel. At the high load condition, the ignitability of fuel was not major factor, but injection pressure, swirl and nozzle design became more influential. Moreover, the results showed lower octane number gasoline type fuel helped to improve combustion stability as well as to reduce engine noise.

2.3.2.3 Boosting Effects in PPC

Intake boosting is commonly used in PPC operation since the oxygen concentration needs to be compensated when a large amount of EGR is employed. In order to get a better understanding of the effect of different intake conditions, Weall and Collings [99] investigated combustion and emissions characteristics under different intake pressures and temperatures in a 2 L light duty 4 cylinder CI engine. It was reported that appropriate intake pressure, temperature and fuel stratification were required to achieve PPC operation. At low speed light load, NOx emissions could be reduced by increasing the intake pressure and temperature. In the meantime, the use of raised intake pressure can reduce the requirement for high intake temperature. Soot emissions could be kept at zero at such an operating condition. In addition, decreasing fuel RON ranking could allow the usage of relatively lower intake pressure and temperature. In Yang's [100] research work, intake boosting was employed to improve the CI engine high load performance. The low-octane distillate fuel Hydrobate and gasoline was used with constant intake temperature of 60 ℃ at 1200 rpm engine speed. It was concluded that the combustion efficiency and gross thermal efficiency could be improved by increasing the intake pressure.

2.3.2.4 Dual Fuel PPC

Kokjohn and Hanson [101] investigated dual fuel premixed combustion in a heavy duty 2.44 L single cylinder CI engine. The experiments were performed with port fuel injection of gasoline and direct injection of diesel. It was reported that the engine operating regime could be extended by optimizing the fuel blends. At the high load of 11 bar IMEP, NOx and soot emissions were suppressed to 0.01 g/kWh and 0.008 g/kWh, respectively. In the meantime, 50% thermal efficiency (170 g/kWh net ISFC) could be achieved under US 2010 heavy duty emission regulations without aftertreatment. In addition, simulation work was involved to explain the fuels reactivity. It was demonstrated that the ignition occurred where the concentration of diesel was high, and the gasoline didn’t start burning until the diesel fuel thermal ignition commenced. In subsequent work, Hanson [102] studied the effects of different fuel quantity percentages in dual fuel PPC operation, Figure 2.7. At the engine load of 9 bar net IMEP, when 89% of total amount fuel was port injected (gasoline), 62% of the diesel fuel was injected as 1st injection while the rest was injected during the 2nd injection, a net indicated efficiency of 53% could be achieved with low NOx and soot emissions below US 10 regulations.

Lee [103] carried out a study involving simulation work to investigate the effect of premixed fuel ratio on combustion and emissions characteristics in a single cylinder CI engine. In the same manner, the gasoline fuel was supplied by a port injector to create premixed charge, while a typical diesel injector was used for triggering the combustion event. The premixed ratio from 0 to 0.85 between dual fuels was used during the experiments. It was found that a reduction of combustion pressure and temperature could be seen when the premixed ratio was increased. Consequently, both NOx and soot emissions were improved compared to a conventional diesel engine. In addition, the NOx emissions could be further suppressed when EGR was applied. uHC emissions were reduced as the premixed ratio increased, and were also related to the EGR rate. The simulation work presented good agreement with the experimental results, which can be used to predict the trend of emissions under the dual fuel PPC operation.

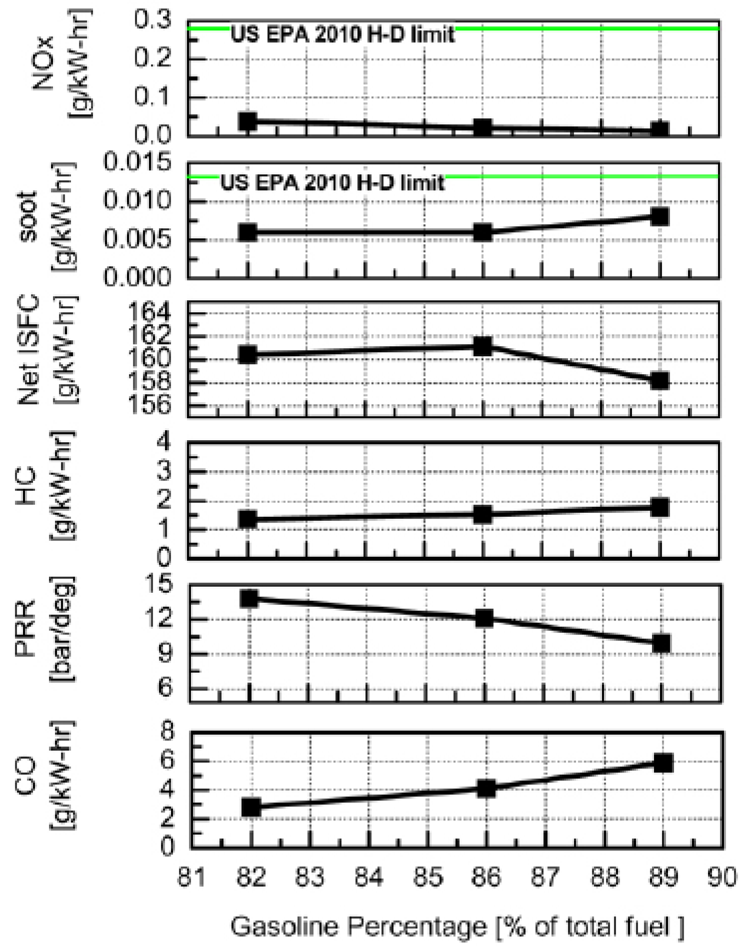

Figure 2.7 Engine Emissions as a Function of the Gasoline Percentage

A recent research work carried out by Ma and Zheng [104] reported high efficiency and low emissions on a single cylinder diesel engine in a dual fuel PPC operation. They investigated the effects of diesel injection strategies on combustion, emissions and the operation range by using gasoline and diesel dual fuel. At 1500 rpm high load condition, the single injection strategy offered ultra-low NOx and soot emissions. However, as NOx emissions were sensitive to EGR rate, this injection strategy was appropriate when sufficient EGR was available. In terms of double injection strategy, early 2nd injection timing strategy provided lowest ISFC of 173 g/kWh, NOx emission of 0.2 g/kWh and soot emission of 0.003 g/kWh, but with a penalty in terms of maximum pressure rise rate. The results also showed that the combustion phasing could be retarded by using a higher gasoline fuel percentage so that a lower combustion temperature was achieved, resulting in reduced NOx, soot emissions and maximum pressure rise rate. In contrast, late 2nd injection timing strategy demonstrated the ability to reduce maximum pressure rise rate due to prolonged combustion duration. Therefore, this injection strategy could be used for extending the high load operation regime. However, high levels of soot emissions could be problematic due to high load operation. This issue might be solved by increasing the diesel injection pressure. The high HC and CO emissions in this dual fuel PPC operation could be suppressed to within EURO VI limits if an appropriately specified oxidation catalyst was utilized.

2.3.2.5 Spark Assistance PPC

Since commercial gasoline fuel has a high octane ranking which is difficult to be ignited under the PPC operation, this issue can be solved by introducing a spark plug to assist the ignition. In spark assistance PPC operation, it allows usage of high octane ranking fuel which makes ultra-low emissions possible.

Benajes and Garaia [105, 106] investigated the light load spark assistance PPC in a single cylinder optical engine. By promoting the auto-ignition with a spark plug, temporal and spatial control over the combustion process could be achieved. In addition, the cycle to cycle repeatability of PPC under low load operation was considerably improved thanks to the spark assistance. The image results demonstrated that the combustion stability was improved with the increase in combustion intensity and duration. In his subsequent work, the effects of different injection strategies on combustion characteristics were studied under the spark assistance PPC operation. Additionally, optical measurement of OH* and natural luminosity images were utilized to describe the combustion process. For single injection strategy, the combustion process was initiated by means of a first kernel due to the spark plug discharge. The kernel gradually grew and generated a partially premixed flame propagation leading to the next stage of combustion. For a double injection strategy, the leaner equivalence ratios at the start of combustion triggered a fainter kernel, and the combustion developed with a slower flame propagation rate compared to the single injection strategy. As shown in Figure 2.8 and 2.9, the mean natural luminosity and OH radical represented in-chamber luminosity and temperature, respectively. It was noted that the double injection strategy produced higher IMEP with lower fuel injected mass, and a reduction of the coefficient of variation was also obtained.

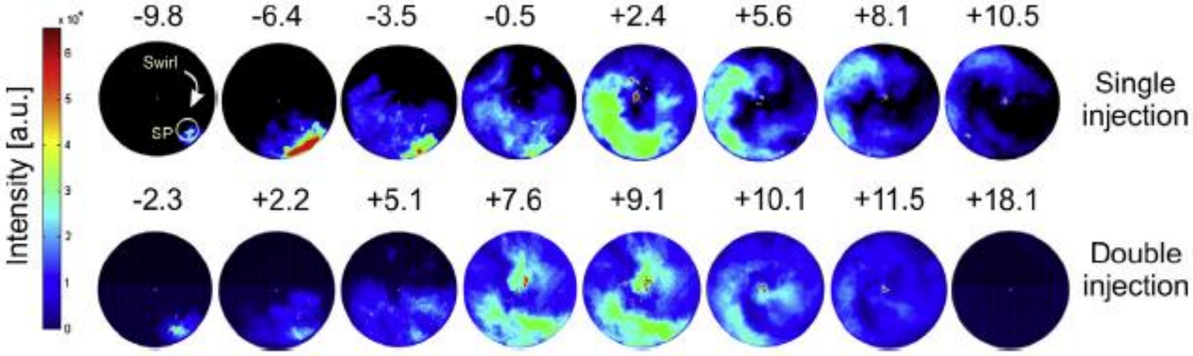

Figure 2.8 Temporal Evolution of the Natural Luminosity for Two Injection Strategies

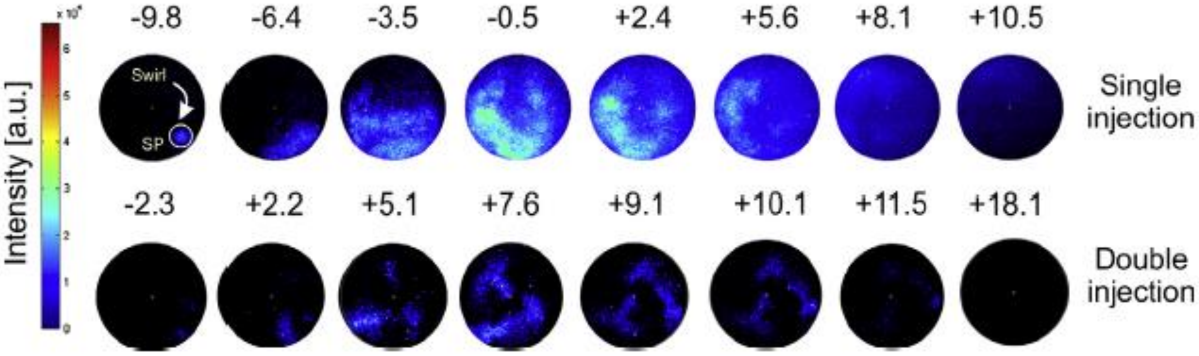

Figure 2.9 Temporal Evolution of the OH Radical Luminosity for Two Injection Strategies

2.3.2.6 Lambda and EGR Effects in PPC

In PPC operation, low NOx and soot emissions can be achieved simultaneously due to reduced combustion temperatures and well premixed charge. However, control is difficult since this combustion mode is sensitive to the lambda and EGR values. Therefore, it is necessary to understand the effects of lambda and EGR rate on PPC operation.

Hanson and Splitter [107] investigated the effects of injection strategies, intake pressures and EGR levels on combustion and emissions characteristics under PPC operation. In a heavy duty 2.44 L single cylinder CI engine at medium speed (1300 rpm) and load (11.5 bar net IMEP), the EGR rate was swept from 0 to 45%, while different intake pressures were tested in the range of 185 to 230 kPa. During the experiments, other parameters were kept constant in order to identify the effect of each single factor. In Figure 2.10, the results showed that NOx and soot emissions were decreased as EGR rate increased at fixed CA 50. There was a simultaneous slight improvement in ISFC due to reduced wall heat losses. In terms of the effect of the intake pressure (Figure 2.11), increased NOx and soot emissions were obtained when the intake pressure increased. This was attributed to the shortened ignition delay, which had a negative effect on the fuel-air mixing process. At the higher intake pressure point, increased CO emissions were found since low temperatures occurred during late cycle combustion. In addition, the single injection strategy resulted in improved ISFC with similar NOx and soot emissions compared to the double injection strategy. Lewander and Ekholm [70] reported similar results in their work. By operating PPC mode on a 12 L, six cylinder diesel engine, they found that the best trade-off between emissions and efficiency was using an early injection strategy with 40% EGR.

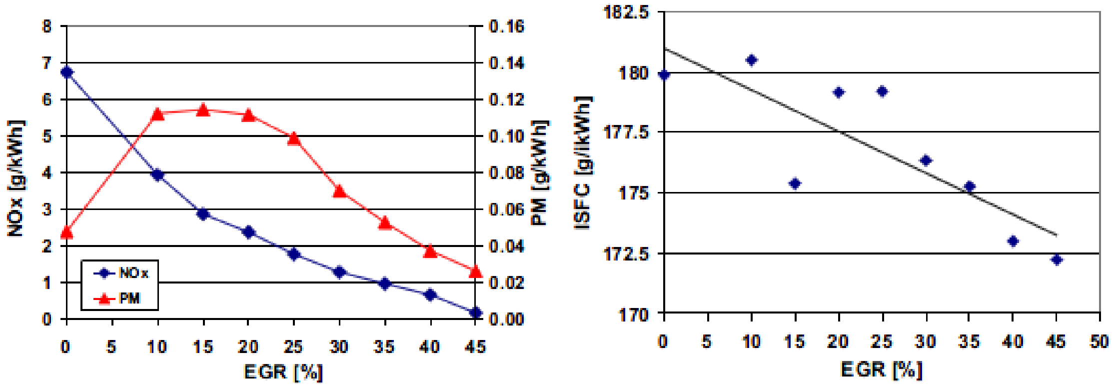

Figure 2.10 Engine Emissions and ISFC as a Function of EGR Rate

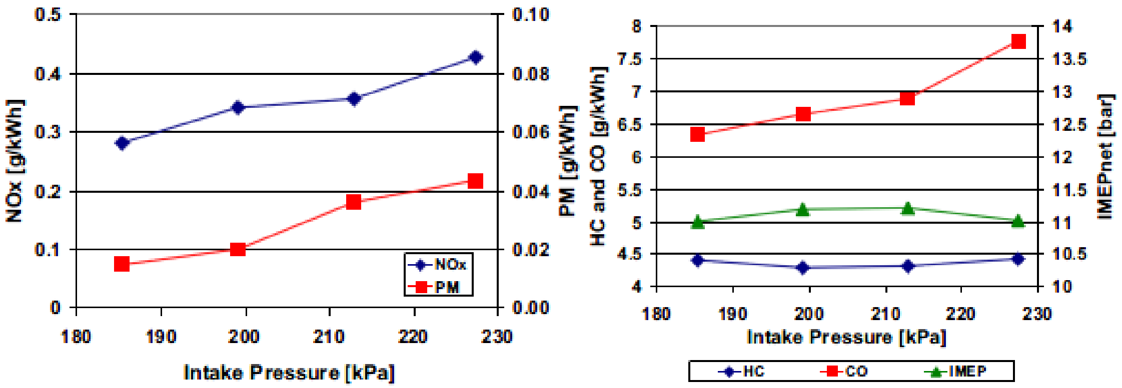

Figure 2.11 Engine Emissions and IMEP as a Function of Intake Pressure

Solaka [108] studied the combustion performance and emissions characteristics at low load PPC operation in a light load diesel engine. The experiments were carried out using four gasoline boiling range fuels between 2 and 8 bar gross IMEP at 1500 rpm with 50% EGR. It was found that the light load operating regime could be extended down to 2 bar gross IMEP by increasing lambda with constant EGR ratio for all the fuels. Compared to diesel fuel, much lower soot emissions could be achieved for gasoline fuels. However, CO and HC emissions were excessively high when operating on high octane number fuel. In a 2.7 L V6 diesel engine, Kalghatgi [109] reported very low emissions and high efficiency gasoline PPC operation without any major changes to the engine system. During the experiments, a diesel fuel with 54 cetane number and 84 RON gasoline were used with different injection strategies and operating parameters. For the gasoline fuel, a lower EGR rate was necessary in order to achieve comparable NOx emissions level as the diesel fuel case. In the meantime, extremely low smoke emissions and lower brake specific fuel consumption were obtained at reduced injection pressure. However, CO and HC emissions were penalized. At high load operation, the operating regime was limited to below 12 bar IMEP. In addition, a large amount of EGR needed to be introduced to suppress the NOx emissions. The CO levels were excessive and a high performance turbocharger was required to deliver adequate intake mass. Moreover, the cold start might be problematic for gasoline fuel and a spark plug might be needed to solve this issue.

Comprehensive gasoline type fuel PPC studies have been carried out by Manente [110-112]. Using a 2L single cylinder diesel engine, the EGR rate and injection timing were swept from light to high load under ethanol fuel PPC operation. It was concluded that a combustion efficiency of 97% could always be obtained even at the high EGR rate condition; high thermal efficiency (47%) was achieved due to the usage of an oxygenated fuel (ethanol) resulting in low specific fuel consumption. At both the high and light load, simultaneous low NOx, soot, CO and HC emissions could be achieved when the EGR rate was in the range of 40%-47%, and the lambda value was between 1.15 to 1.25. HC emissions were decreased when the EGR rate increased, due to the lower combustion temperature. It was noted that an excessive pressure rise rate appeared when the single injection strategy was used. The injection strategy optimized results showed that when the pilot injection was at -60 degrees ATDC with pilot-main ratio of 50:50, NOx and soot emissions were suppressed below EURO VI regulations without using an exhaust aftertreatment, and HC and CO were within EURO VI with a 95% efficiency exhaust catalyst.

In his subsequent work [113], the effects of intake pressure, EGR, and injection strategies on combustion and emissions characteristics at high load PPC operation were investigated. At 16-18 bar gross IMEP, gasoline fuels with RON of 99, 89 and 69 were tested. The results showed that by using an EGR rate of 46-52%, and lambda values between 1.54 and 1.58 for all three fuels, high gross indicated efficiency of 54% could be achieved with maximum pressure rise rate below 15 bar/deg. NOx and soot emissions were below 0.25 g/kWh and 1.50 FSN, respectively. In order to achieve the whole load range gasoline PPC operation [112], 11 fuels were tested in the load range of 5 to 26 bar gross IMEP at 1250 and 600 rpm. During the experiments, the intake boosting level and EGR rate were selected to match the different engine loads. The results demonstrated that the whole load range operation could be achieved using a gasoline fuel with an octane number below 70. By optimizing the EGR and lambda combination, 52%-55% gross indicated efficiency were obtained with low NOx emissions (0.1-0.5 g/kWh). The worst result in terms of soot emissions for a gasoline type fuel was 0.5 FSN, while the diesel fuel gave 2.8 FSN.

2.3.2.7 Combustion Efficiency in PPC

In Partially Premixed Combustion, massive uHC and CO emissions could possibly be created mainly due to relatively low combustion temperature caused by amount of EGR. On the other hand, the combustion phasing (CA50) mainly determined by injection strategy seriously affects uHC and CO emissions. All these factors make the combustion efficiency fairly sensitive during the PPC operation.

Manente [91,112] has been making lots of effort to gain a high efficient combustion under the gasoline PPC operation. Because of the appropriate selection of EGR and Lambda, high combustion efficiency (up to 99%) was achieved in a heavy duty Scania D13 from 5 to 25 bar gross IMEP. Even with 60% of EGR, the combustion efficiency above 99% can be obtained which demonstrated low uHC and CO emissions [111]. However, relatively poor combustion efficiency was measured with certain high octane number fuels due to excessive uHC and CO emissions caused by longer ignition delay.

A similar study has been carried out by Kokjohn and Hanson [101]. They investigated the potential of controlling premixed charge combustion strategies by varying fuel reactivity. The results demonstrated that the combustion efficiency were particularly sensitive to initial conditions at high EGR-high PRF (primary reference fuel) conditions, where combustion efficiency began to deteriorate due to low combustion temperatures and reduced hydrocarbon oxidation in the near-wall and crevice region. In Leermakers' work [93], the influence of physical and chemical properties of fuels' load range capacity in Partially Premixed Combustion was studied. The results showed that the combustion efficiency was reduced with the fuels which elongated the ignition delay.

Shi and Reitz [59] optimized the injection strategies for heavy-duty engine fuelled with diesel and gasoline-like fuel operating under mid and high load conditions. They found that the premixed combustion mode resulted in high UHC and CO emissions due to the fact that the early injection leaded to wall-wetting while the late injection had poor air-fuel mixing and combustion efficiency.

2.4 In-Cylinder Visualization of Spray and Combustion

In-cylinder diagnostics have been widely used to investigate fluid mechanics, spray evolution, mixing and combustion in modern internal combustion engines. The information of temporal and spatial evolution related to fuel injection characteristics and engine combustion processes can be provided by numerous optical techniques.

2.4.1 Mie-Scattering

Mie scattering is normally used for observing fuel liquid droplets. Its working principle is based on the scattering of light from a particle of diameter much larger than the wavelength or size parameter, $a = {}^{\pi d}/_{\lambda} \gg 1$. Although this technique is limited to qualitative visualization of the liquid fuel distribution, since the scattering signal intensity is determined by the droplet size and concentration, numerous studies have been carried out in order to evaluate the liquid fuel spray formation, mixing and penetration [114-116].

2.4.2 Rayleigh-Scattering

Rayleigh scattering is a useful optical technique for fuel vapour visualization. It is based on the principle of the elastic collisions between gas molecules and incident laser light. With the same wavelength as the incident light, this scattering light is proportional to laser intensity, gas intensity and their associated Rayleigh scattering cross-sections. Moreover, Rayleigh scattering is orders of magnitude weaker than the Mie scattering signal and is independent of ambient conditions. However, it is difficult to differentiate between Rayleigh and Mie scattering signals as both processes are elastic [116, 117].

2.4.3 Laser Induced Fluorescence

Laser induced fluorescence (LIF) is frequently used to detect the charge concentration and temperature. By applying a single laser pulse within a few nanoseconds, volume elements in the sub-millimetre range can be observed. The LIF technique is based on the principle of excitation, leading to the emission light from an atom or molecule. A detailed description of the LIF technique can be found in Chapter 4.

In IC engine applications, the tracers added to the fuel absorb the laser light leading to strong fluorescence. These fluorescence signals are proportional to the molecular density (tracers), thus it is possible to use LIF for species concentration measurement. Williams and Ewart [118] performed quantitative measurements of fuel distributions in a direct injection gasoline engine. In their study, the early injection DI homogeneity and cyclic variation of injector plumes were investigated using the PLIF technique. The results showed that the inhomogeneity is 10% on a scale above 350μs at ignition for an early injection strategy. For a late injection strategy, stratified combustion was significantly affected by the CoV of the injector plumes, since the spark plug was close to the boundary of a plume. In a high pressure and temperature constant volume chamber, Schulz and Gronki [119] studied fuel vapour distribution using Rayleigh scattering and tracer LIF techniques. Compared to Rayleigh scattering, 5-nonanone tracer LIF presented the advantage of non-resonant detection and the elastic scattering signal could be minimised by using appropriate filters. The results indicated that the fuel distribution images obtained by LIF were similar to those measured by Rayleigh scattering. Further quantitative measurement for fuel number densities could be obtained from Rayleigh scattering experiments.

In LIF measurement, the fuel tracer selection is important since it should behave like the tested fuel in terms of spray formation, evaporation and reactivity. However, this requirement is difficult to meet, and only the tracers which are similar to the fuels can be selected during the experiments. Therefore, many researchers have investigated the effects of different fuel tracers in particular applications [120-122]. Baritaud [123] proposed to use biacetyl as a fuel tracer in isooctane fuel. Several requirements were considered such as: absorption of the available laser wavelength, satisfactory quantum yield, low quenching by oxygen, sufficient red shift, good solubility and similar boiling point to the fuel. Similarly, Bruneaux [124] investigated gaseous fuel jet formation using biacetyl as a fuel tracer. The experiments were conducted in a high pressure chamber with a diesel-like injection strategy and quantitative fuel concentration measurements were performed. Wermuth and Sick [125] compared absorption and fluorescence data of acetone, 3-pentanone, biacetyl and toluene under different engine temperature and pressure conditions. At a given condition, the temperature, pressure and composition dependence of tested tracers were examined in a small-bore optical engine. The results could be used for extending the data base for predicting the strength of fluorescence signals. By seeding the fuel tracers with the air in the intake manifold, the air/fuel ratio could be determined by observing the intensity of the fluorescence signal [126]. This was based on the principle of the proportional relationship between local concentration and fluorescence intensity.

Sarner and Richter [127] used LIF imaging of formaldehyde and a fuel tracer (Toluene) to investigate the fuel distribution in a direct injection HCCI engine. Two pulsed Nd:YAG lasers of 266 nm and 355 nm were employed to excite the fuel tracer and formaldehyde, respectively. As formaldehyde is generated during the low temperature reactions before combustion takes place, it is possible to use formaldehyde to represent fuel distribution until it is consumed. By testing early and late injection strategies, it was found that formaldehyde could replace traditional fuel tracers for detecting low temperature fuel reaction characteristics. In subsequent work [128], the same optical setup was utilized to investigate fuel tracer and formaldehyde transport under the cool chemistry in the piston bowl. At low load operation, different EGR levels didn’t shift the location of the low temperature reactions. The formaldehyde signal was present where the fuel signal appeared before the heat release process commenced.

In the fuel spray visualization by LIF, both liquid and vapour signals are included in the detected fluorescence emissions; while the fuel liquid phases can be captured using Mie-scattering techniques. Therefore, it is possible to differentiate fuel liquid and vapour phases by applying Mie-scattering and LIF techniques simultaneously [129-132]. In a simulated test cell, Stojkovic and Sick [133] investigated the evolution and impingement of a hollow-cone-type spray using simultaneous Mie-LIF techniques. The isooctane fuel doped with 3-pentanone was excited by a KrF excimer-laser beam for the purposes of LIF measurement, while a versatile optical setup was developed allowing simultaneous measurements of Mie-scattering. It was found that the sauter mean diameter (SMD) could be determined by the ratio of LIF to Mie signals. Uhi [134] studied fuel spray characterisation in an optical diesel engine using combined Mie/PLIF techniques. The temporal evolution of the liquid and the gaseous fuel were qualitatively presented. The effect of injection pressure and fuel spray penetration was analysed using these image results. In a 4 cylinder optical diesel engine, Maunoury [135] revealed the influence of the injection timing on the spray penetration and dynamics, through simultaneous Mie-LIF experiments. In a recent research work, Zeng and Xu [136] conducted simultaneous Mie and LIF measurements to investigate the spray characteristics of gasoline, methanol and ethanol fuels at engine cold-start conditions. It was concluded that the engine performance could be improved by increasing the temperature of injected fuels. By using a similar combination Mie-LIF setup, Andersson and Jonas [137] compared evaporation characteristics among different types of fuel-tracer mixtures. A selective and sequential evaporation of fuel components with different volatility was reported.

As natural thermal stratification is a significant factor for high load HCCI operation, a planar temperature imaging technique was developed based on a tracer single-line PLIF by Dec and Hwang [138]. Temperature map images were obtained from PLIF images, since a high temperature sensitivity tracer (toluene) was added to the fuel. In addition, a PDF analysis was employed to provide a more quantitative evaluation of PLIF results. The results demonstrated that the wall heat transfer and turbulent in-cylinder flow dominated the creation of natural thermal stratification, which was crucial for high load HCCI operation. In order to understand depth of field effects in laser sheet imaging, Lee and Nishida [139] developed a microscopic imaging technique to obtain high spatial resolution LIF tomograms of the pre-swirl spray. During the measurement, the laser sheet-straddling large-sized droplets were filtered by using the mean intensity ratio, while small-sized droplets over the laser sheet edge were eliminated through line profile inspection. Consequently, the depth of field effects in droplet sizing were reasonably well accounted for. However, unavoidable energy fluctuations of the laser sheet and non-uniform fluorescence distributions were still problematic.

2.4.4 Laser Induced Exciplex Fluorescence

In normal LIF measurement, it is impossible to separate the fluorescence signal from the liquid and vapour phases. This is attributed to the fact that the absorption and fluorescence spectra of the fuel itself and fuel tracers are identical to the spectra of molecules in the vapour phase. In order to overcome this issue, Melton [140] developed the laser induced exciplex fluorescence (LIEF). In this technique, the newly formed species called excited state complex or exciplex (M-G)* behave as the dominant emitter in the liquid phase, while the monomer M* is the dominant emitter in the vapour phase. Thus, simultaneous measurement of the liquid and the vapour phases can be achieved when appropriate organic dopants are chosen. Unfortunately, in practical experiments the powder form tracer like TMPD usually causes the failure of fuel injection equipment.

2.4.5 High Speed Imaging

In IC engines, the implementation of high speed imaging allows the visualization of temporal and spatial resolution of fuel spray, as well as engine combustion. The experimental setup simply requires a light source and an image capture device. Practically, for high speed visualization, the light source is selected by considering its brightness, spectral distribution and repetition rate, due to the requirement of a large amount of light over a short time duration. Similarly, high speed cine film cameras are commonly used due to their high repetition rate. By using a Copper Vapour laser and a NAC Memrecam FX6000 high speed camera, Reza and Lu [141] visualized the fuel injection formation and combustion process in a high speed optical diesel engine. This technique was also widely employed in many studies [142-145].

2.5 Summary

In this chapter, the fundamentals of an IC diesel engine’s combustion and emissions were explained. The new combustion concepts for simultaneously reducing NOx and soot emissions were described. Particularly, diesel and gasoline PPC combustion were discussed in detail. In gasoline PPC combustion, the effects of different engine control parameters and fuel types were comprehensively reviewed. Finally, optical techniques for in-cylinder fuel spray and combustion visualization were described.

CHAPTER 3

Experimental Facilities and Data Analysis

3.1 Introduction

This chapter includes the experimental setup and test facilities in this study. A description of the test bed, the single cylinder optical research engine as well as its fuel injection system, intake and exhaust system, and data acquisition system are presented. The facilities and operation for high speed imaging technique are introduced. The fuel injector calibration, air and EGR flow measurements are discussed prior to determination of the lambda calculation. In addition, the method for the lambda calculation based on the exhaust species is presented. Finally, the thermodynamic data analysis is explained in detail.

3.2 Single Cylinder Common Rail DI Diesel Engine with Optical Access

3.2.1 General Description

In this study, all experimental testing was performed on a single cylinder Ricardo Hydra optical engine. The engine is equipped with an extended cylinder block with a standard production cylinder head and common rail fuel injection system. The engine specification is given in Table 3.1. As shown in Figure 3.1, the engine is mounted on a Cussons Technology single cylinder test bed comprising of a seismic mass engine mounting with a 30 kW DC dynamometer and engine coolant and oil circuits.

Table 3.1 Ricardo Hydra Engine Specifications

Ricardo Hydra Single Cylinder optical Engine	
Bore	86 mm
Stroke	86 mm
Swept volume	499 cm3
Compression Ratio	16:1
Piston Bowl Diameter/Depth	43.4/11.6 mm, re-entrant bowl with flat bottom
Swirl Ratio	1.4
Engine Speed for Testing	1500 rpm

In order to accommodate the extended piston, an extended cylinder block is utilized which has an upper and lower portion connecting to the cylinder head platform and engine crankcase respectively. The engine cylinder block features three cut-outs where glass windows can be installed for the purpose of optical access.

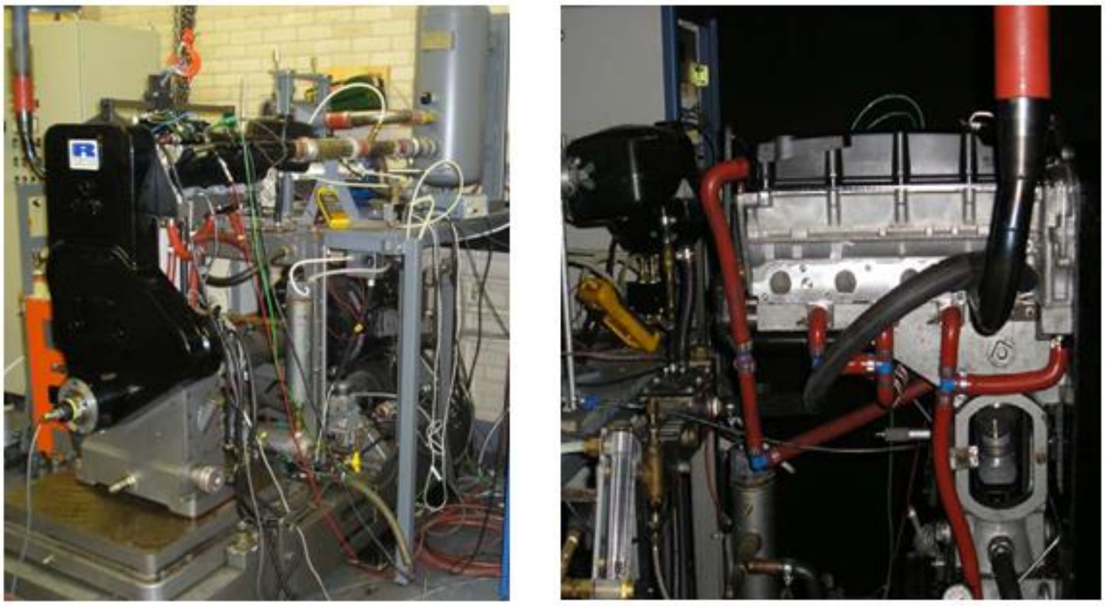

Front view

Side view

Figure 3.1 Front and Side View of the Ricardo Hydra Engine

Optical engines have inherent limited operating time due to the considerable mechanical and thermal stresses on the optical components during the firing cycles. Therefore, both the lubricating oil and coolant are pre-heated to the desired engine temperature before starting the engine. The lubrication system consists of a wet sump, test bed mounted, gravity-fed pressure pump driven by an electric motor and two immersion heaters in the sump. Oil is drawn from the sump and pumped through an oil filter before being fed to the main oil gallery in the crankcase. This provides lubrication to the crankshaft and big end bearing in the crankcase in addition to the camshaft in the cylinder head. The lower piston and piston rings are lubricated by splashed oil while the upper piston and cylinder block are lubricated by two carbon rings made of Le Carbone Lorraine grade 5890 carbon and lubricant paste smeared onto the top compression piston ring. The coolant system consists of a test bed mounted electric water pump and a thermostat controlled immersion heater. Before operation, the engine coolant and lubricating oil are heated up to 90 ℃ and 80 ℃, respectively.

3.2.2 Cylinder Head

A production cylinder head from a Ford 2.0 litre ZSD 420 Duratorq turbocharged DI diesel engine is mounted on the single cylinder engine. The aluminium cylinder head features double overhead camshafts, four valves, a central located injector and a glow plug. The unused cylinders are disabled by removing the rocker arms. Additionally, the corresponding oil feed holes on the rocker shafts are blocked off in order to avoid unnecessary oil squirting. Since the glow plug is not required in this study, a Kistler 6125 piezoelectric pressure transducer is mounted into its place for cylinder pressure measurement.

3.2.3 Optical Configuration

3.2.3.1 Extended Piston and Cylinder Block

Optical access through the extended piston design allows the combustion chamber to be visualised through the axis of the cylinder via a fused silica window mounted in the crown of the piston. The extended hollow piston and cylinder block are required in order to position a 45 degree mirror between upper and lower sections for the purpose of viewing the combustion chamber. As shown in Figure 3.2, the lower piston is modified to allow the upper piston to be bolted on. Due to the splash lubrication for lower cylinder wall, thus conventional oil scraper rings are used to prevent excess oil.

As the upper cylinder block and extended piston cannot be lubricated by engine oil in order to avoid rapid contamination of the optical surfaces, hence two carbon graphite rings are utilized as previously mentioned for the purpose of lubrication. In addition, two conventional steel compression rings are fitted on top of the carbon rings for sealing. Moreover, high performance Rocol lubricant paste is employed to the upper cylinder block for further lubrication between the piston and the cylinder block.

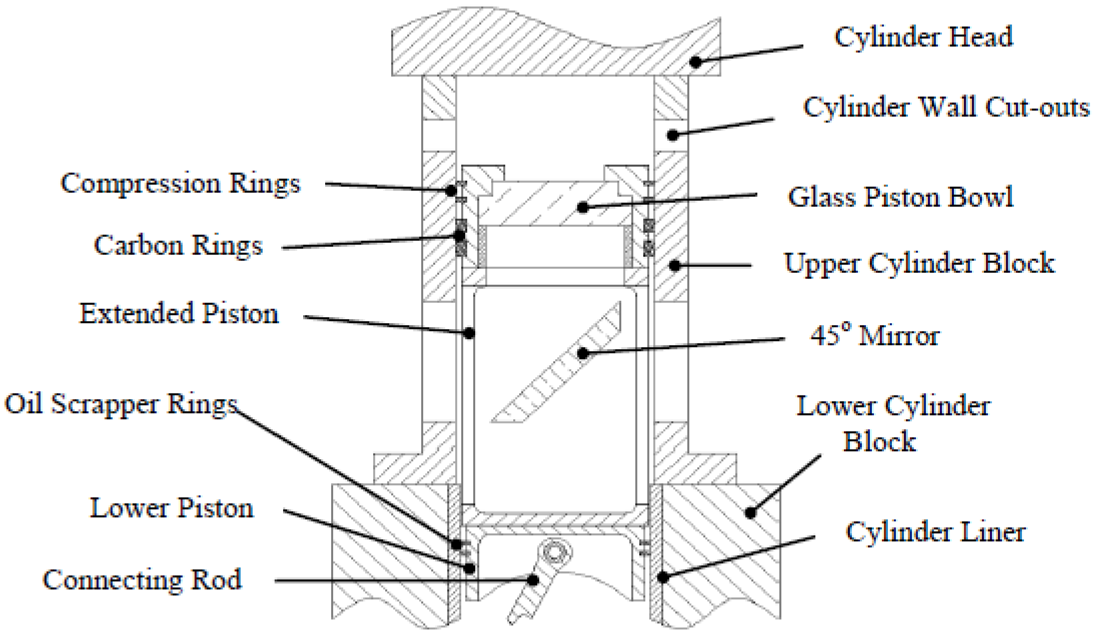

Figure 3.2 Sectional Schematic View of the Optical Layout

3.2.3.2 Optical Windows

As shown in Figure 3.3, three rectangular cut-outs are machined for fitting with the fused silica windows as the side optical access. Two of these windows are in the plane which can be used for laser sheet imaging while the third window is placed at 90 degrees for the purpose of detecting. In this work, the side windows were blocked by metal blanks but it provided the access for the glass piston cleaning during the experiments.

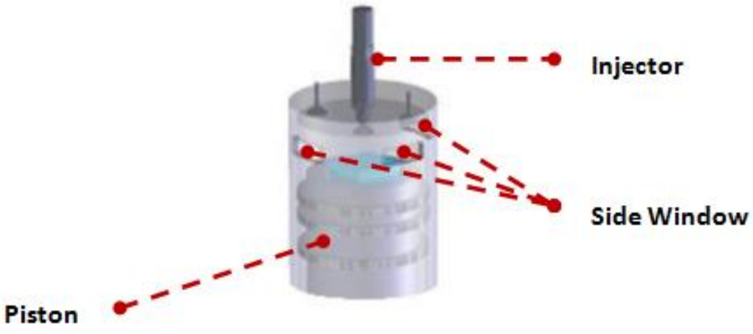

Figure 3.3 Schematic View of Side Windows

In this study, a fused silica widow in the piston crown is used to provide an optical access of 43.4mm in diameter. Figure 3.4 demonstrates the sealing arrangement of the upper part of the piston.

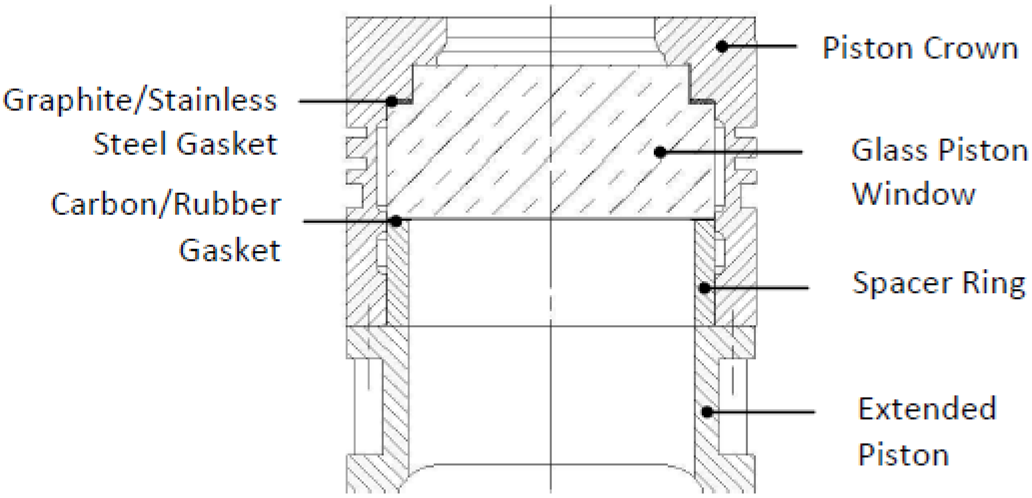

Figure 3.4 Schematic View of the Piston Assembly

It can be seen that a steel spacer ring is positioned between the lower and the upper parts of the extended piston to provide a proper fit of the glass and gaskets. The tight clamping of the spacer ring is not suggested due to the brittle nature of the glass window and the stress concentrations during the engine operation. In order to overcome this issue, three raised edges were machined on the surface of the spacer ring to contact with the carbon gasket so that high pressure points were created to enhance sealing. Moreover, the increased in-cylinder pressure during the compression stroke forces the window down against a Klingersil gasket made of carbon and rubber which further improved the sealing between the glass and the metal. Consequently, the leakage at the glass-metal contact is considerably reduced. However, it is noted that the piston window needs to be replaced with a metal blank during the emission test in order to achieve longer period of fired engine operation without risking damaging the optical window.

3.2.4 Crank Shaft Position System

A shaft encoder is installed on the crankshaft in order to determine the angular position of the piston. This shaft encoder produces two signals which are one pulse per revolution (ppr) at TDC and a clock of 1800 ppr. The Electronic Control Unit (ECU) uses these signals to control the fuel injection and data acquisition system. As shown in Figure 3.5, a Light Emitting Diode (LED) triggered by the TDC pulse is fitted at the side of 45 degree mirror to provide a TDC reference on the high speed movie frames.

In order to identify the compression TDC during the 4-stroke operation, a hall-effect sensor is mounted next to a metal disc driven at half of the crank shaft speed.

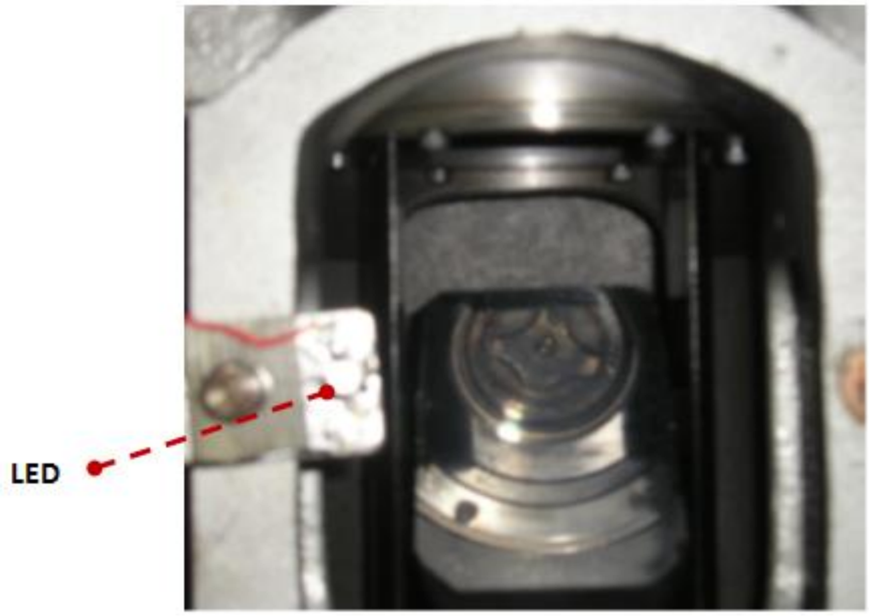

Figure 3.5 LED Position

3.2.5 Fuel Supply and Injection Systems

A Delphi HP common rail fuel system is applied in this study. This fuel system is capable of providing maximum injection pressure of 1350 bar independent of the engine speed. As shown in Figure 3.6, the fuel supply system consists of a fuel filter, a low pressure pump and a fuel tank. As the fuels with different properties are tested in this study, a Powerstar 4 pneumatic high pressure pump is employed in order to maintain the fuel injection characteristics. This pneumatic pump converts pressurized inlet air to a hydraulic output pressure of up to 1200 bar, providing flexible control in terms of injection rate and timing as well as the use of special fuels in small quantities.

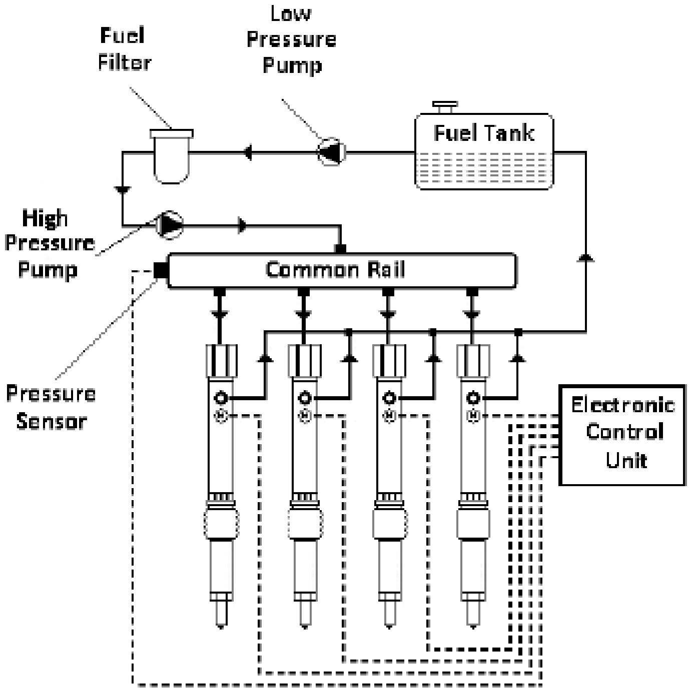

Figure 3.6 Schematic Diagram of Common Rail Fuel Injection System [146]

The common rail utilized in this study consists of four outlets and one of them is connected to the fuel injector through the high pressure pipe while others are blanked off. A Delphi rail pressure sensor fitted at the end of the fuel rail sends the signal to the ECU for injection pressure management. As shown in Table 3.2, a Delphi multi-hole Valve Covered Orifice (VCO) injector is applied in this study and it is capable of producing a maximum of 1600 bar injection pressure.

Table 3.2 Fuel Injector Specification

Delphi Standard Injector	
Number of Holes	6
Hole Size	0.154 mm
Cone Angle	154 degree
Flow Rate	0.697 l/min
Type	VCO

An EC-GEN 500 ECU supplied by EmtroniX is employed to control the injection system while computer based software called EC-Lab provides remote communication. The ECU receives the input signals from the shaft encoder, hall-effect sensor and fuel rail pressure. In the meantime, it is possible to set the injection pressure, number of injections, timing and quantity in EC-Lab for the fuel injection control. As a part of EmTroniX system, the injection driver converts the pulses to corresponding current and voltage signals required by the injector to drive the fuel injection event.

3.2.6 Intake System

The single cylinder engine is designed to be operated at either naturally aspirated or supercharged modes. A changeover valve is used to switch engine operation between these two modes. In addition, the EGR can be simulated by introducing nitrogen or CO_2 into the intake system. Figure 3.7 shows the intake system of the engine.

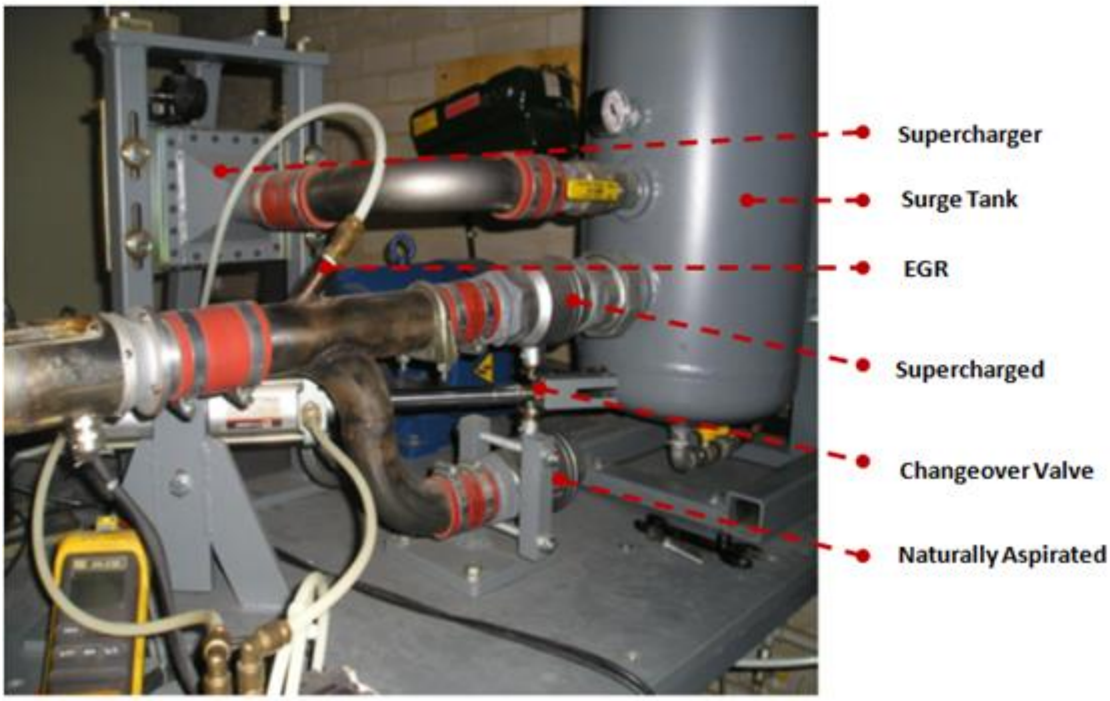

Figure 3.7 Ricardo Hydra Engine Intake System

3.2.6.1 Forced Induction

A forced induction system fitted to the intake system allows the engine to run under boosted conditions. An Eaton M45 supercharger, a positive displacement roots type blower with three lobes and helical rotors driven with an AC motor rotating at 2600 rpm is applied to provide the compressed air into the intake system. This supercharger is capable of providing a maximum of 0.5 bar boost pressure and the boost pressure can be manually controlled by adjusting a bypass valve. A Kistler 4045A5 piezo-resistive pressure transducer is fitted in the intake manifold coupling with an amplifier and digital oscilloscope to detect the intake manifold pressure. The boost pressure of 0.335 bar is used in this study. Figure 3.8 shows the supercharger and the bypass valve.

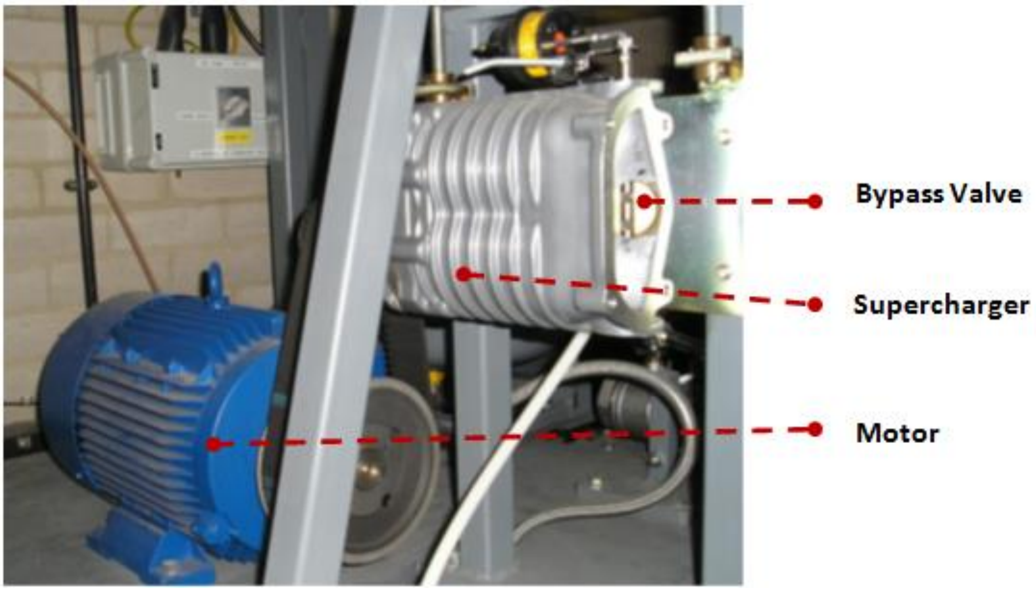

Figure 3.8 Supercharging System

3.2.6.2 Intake Heating

A 3kW heater is installed prior to the intake manifold in order to replicate a typical HSDI diesel engine operating condition. A thermocouple combined with a heater control box allows for closed-loop temperature control. In this study, the intake temperature of 100℃ and 150℃ was used for diesel and gasoline operation, respectively. Figure 3.9 shows the intake heating setup.

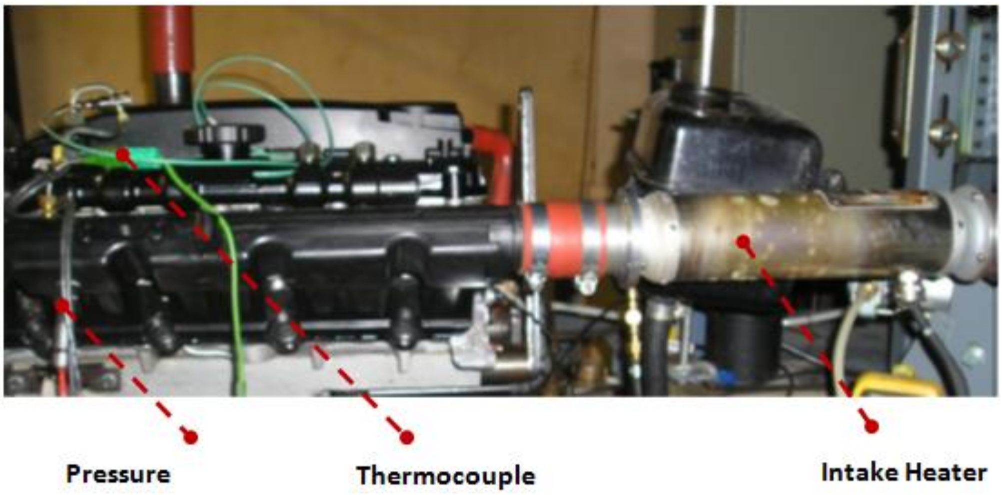

Figure 3.9 Intake Heating System

3.2.6.3 EGR System

In this study, EGR is simulated by using nitrogen gas. This was mainly attributed to that the limited running time of optical engine doesn't allow the real exhaust gas to be circulated through the system within very short period. The nitrogen gas flow delivered from a pressurised bottle is measured by a flow meter. The EGR rate used during the experiments was 22%. The detailed description for the EGR system is presented in the section of air and EGR flow rate measurement.

3.3 In-Cylinder Pressure Data Acquisition System

The in-cylinder pressure measurement is primarily used to perform the heat release analysis. Moreover, in the optical engine operation, it is also used to check the presence of piston window leakage.

3.3.1 In-Cylinder Pressure Measurement

As mentioned previously, a Kistler 6125A piezoelectric pressure transducer coupled with a Kistler 5011 charge amplifier is used to measure the in-cylinder pressure. The transducer is un-cooled with a range of 0-250 bar and a sensitivity of -15 pC/bar. The signal measured by the transducer is converted to the output voltage through the charge amplifier and is subsequently fed to the data acquisition system.

Before the experiments commence, the pressure transducer can be calibrated by using a deadweight tester. The amplifier is calibrated over a range of 0-200 bar and is set to give the maximum output voltage of 10V at 200 bar. It is worth noting that the overloading of the charge amplifier should be avoided in order to preserve the device.

3.3.2 Data Acquisition System

A Labview programme is used for the data recording. The programme is running on a PC connecting to a National Instruments data acquisition card. The signals from the shaft encoder and the in-cylinder pressure transducer amplifier are sent to the NI BNC-2110 board which is then connected to the NI OCI-MIO-16E data acquisition board. The two signals sent from the shaft encoder, the 1800 ppr are used as the clock while 1 ppr signals are the reference for the start of recording cycles. Thus the data is recorded at 0.2 °CA intervals. The in-cylinder pressure as a function of crank angle is recorded in real-time by the software. Although IMEP, p-V diagram, heat release rates and mass fraction burned can be calculated and display on-line, the data acquisition system is mainly used only for recording the pressure data. The post data analyses such as the evaluation of IMEP and heat release rate are carried out in Microsoft Excel.

3.4 Optical Setup

The optical techniques employed in this study include high speed imaging and simultaneous Mie-LIF. The simultaneous Mie-LIF technique is to visualize the liquid and vapour phases of fuel spray through excitation of the fuel tracer. The principle and experimental setup for simultaneous Mie-LIF are explained in Chapter 4. The high speed imaging technique provides the temporal evolution of fuel spray and combustion process. The experimental setup and procedure for high speed imaging are detailed in the following section.

3.4.1 High Speed Imaging

High speed imaging is utilized to capture the video images of the fuel spray as well as the subsequent combustion event. A CU15 Oxford Laser is employed in order to provide the illumination for the combustion chamber. Table 3.3 shows the specification for the Copper Vapour laser.

Table 3.3 Copper Vapour Laser Specifications

Type	Copper Vapour Laser (CU15 Oxford)
Wavelength	511 nm
Average Power	8.5 W
Pulses Width	10-40 ns
Pulse Repetition Rate	10 kHz

As shown in Figure 3.10, the laser beam illuminates the combustion chamber via an optical fibre through a 45 degree mirror positioned underneath of glass piston window. As previously mentioned, an LED triggered by reference signal from shaft encoder indicates the TDC position presenting on the captured videos. Therefore, it is possible to recognize the crank position of all the other frames by referring the TDC positioned frame. Figure 3.10 shows the arrangement of high speed imaging system.

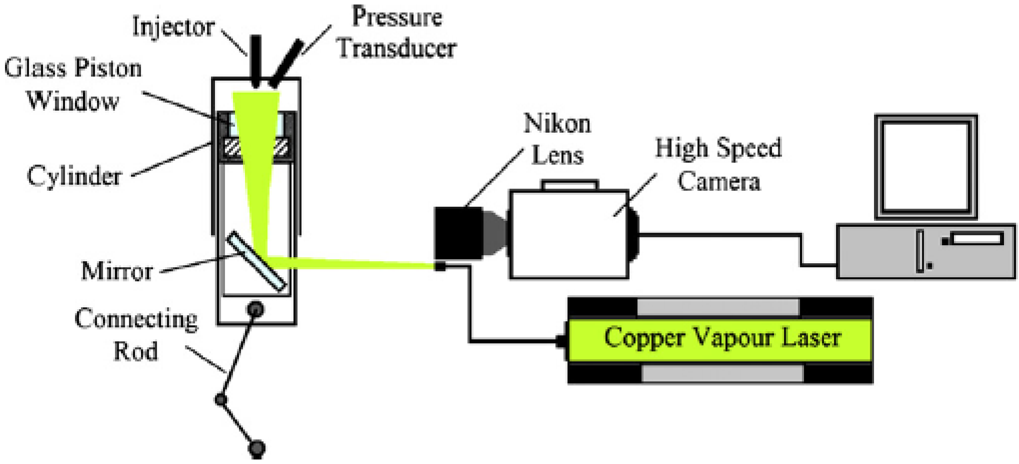

Figure 3.10 High Speed Video Imaging Optical Arrangement [141]

A NAC Memrecam FX6000 high speed video camera equipped with a high speed colour CMOS sensor is used. The high speed camera was set to capture videos at 10,000 frames per second (fps), corresponding to one frame per 0.9 degree crank angle at the engine speed of 1500 rpm. The image resolution is determined by the frame rate, thus the image resolution of 512 x 248 pixels can be obtained at 10,000 fps.

3.5 Exhaust Emission Measurement

In this study, the gaseous pollutant emissions of CO, CO_2, O_2, uHC and NOx were measured by a Horiba MEXA-7170DEGR analyser while the soot concentrations were measured though the use of an AVL 415 smoke meter.

3.5.1 Horiba MEXA-7170DEGR Emissions Analyser

The Horiba MEXA-7170DEGR was utilized to measure the aforementioned exhaust emissions. The device consists of four analyser modules controlled by a PC performing as the main control unit. The measurement principle for each module is described in detail in the following sections. The touch screen interface displays real-time emissions values in both graphical and numerical formats.

3.5.1.1 Horiba MPA-720: O_2 Measurement

The Horiba MPA-720 magneto-pneumatic analyser was applied to measure the oxygen concentration. This analyser module operates based on the principle of paramagnetism, which is magnetic phenomenon that acts on certain materials when an external magnetic field is applied upon them. For all common exhaust gas components, only oxygen and oxides of nitrogen namely NO and NO2 are affected by the presence of an external magnetic field however the influence for oxides of nitrogen is unnoticeable in comparison. Figure 3.11 shows a schematic diagram of a magneto-pneumatic oxygen analyzer.

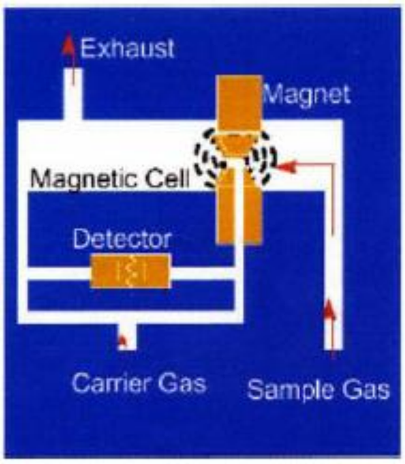

Figure 3.11 Schematic Diagram of a Magneto-Pneumatic Analyser (Horiba Instruments Ltd)

The sample gas flows through the magnetic cell where an electromagnetic field is created around the poles via the electromagnet driven by AC current. A rise in pressure around the poles which is proportional to the oxygen concentration can be detected when the altering magnetic field attracts the oxygen molecules. A condenser microphone in the analyser generates an output electrical signal once a change in pressure occurs.

3.5.1.2 Horiba FIA-720: Unburned Hydrocarbon Measurement

The Horiba FIA-720 Flame Ionisation Detector (FID) was used for measuring the uHC concentration. The analyser module operates based on the principle that ions are generated when a gas containing hydrocarbons is burned, and the rate of ion production is proportional to the hydrocarbon concentration. As shown in Figure 3.12, hydrogen is burned using high purity air in the detector. At this stage, the hydrogen is used as the fuel gas since minimal ionisation occurs during the combustion process. Subsequently, the sample gas is compared with the newly coming hydrogen results in ions production due to presence of thermal disassociation by hydrocarbons. A high DC voltage is applied between the burner jet and a collector around the flame in order to migrate ions into one and the electrons to the other , so that an electrical current proportional to the level of ionisation can be created corresponding to the number of carbon atoms. Consequently, this method presents the total hydrocarbons without recognizing specific information available on specific hydrocarbon components.

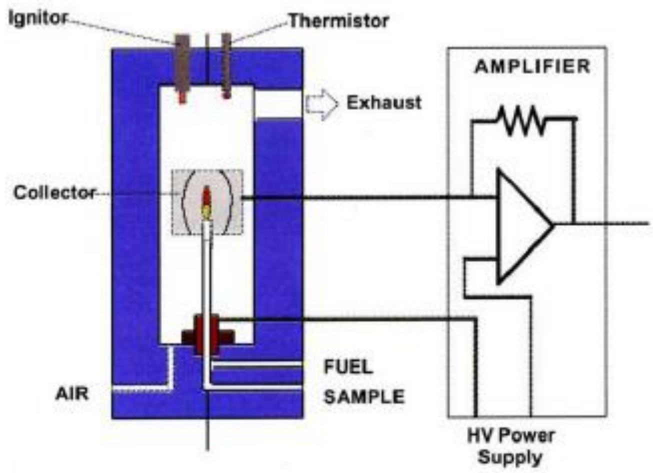

Figure 3.12 Schematic Diagram of a FID Analyser (Horiba Instruments Ltd)

3.5.1.3 Horiba CLA-720A: NOx Measurement

The Horiba CLA-720A chemiluminescence analyser was used for the measurement of NO and NO_2 concentrations. The principle of this analyser module is based on the reaction between NO and ozone (O_3) resulting in the oxidation of NO to NO_2. The reaction of NO with ozone (O_3) as shown below:

$$NO + O_3 \rightarrow NO_2^* + O_2$$

$$NO_2^* \rightarrow NO_2 + hv$$

The excited molecules decay to the ground state through the emission of a photon and this light intensity is proportional to the concentration of NO molecules. The sample gas enters the reaction chamber and reacts with the ozone. After passing a bandpass filter, the light emitted through the chemiluminescence process is detected by a light detector and outputs a voltage signal. Figure 3.13 shows the schematic diagram of a chemiluminescence detector.

During the measurement, the particular interference might occur such as presence of CO2 and H_2O molecules through collision with other molecules. In order to reduce this interference, the sample gas needs to be diluted with nitrogen before entering the detector.

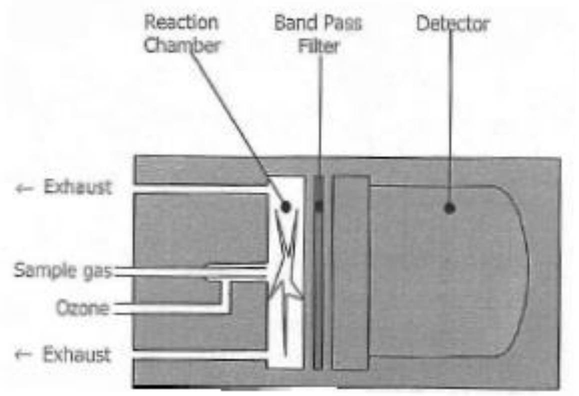

Figure 3.13 Schematic Diagram of a Chemiluminescence Detector (Horiba Instruments Ltd)

3.5.1.4 Horiba AIA-72X: CO and CO_2 Measurement

A Horiba AIA-72X analyser module operating based on Non-Dispersive Infrared (NDIR) method was used for the measurement of CO and CO2 concentrations. The principle of this measurement is based on that different molecules absorb infrared radiation at different wavelengths so that the concentration of each molecule is proportional to the level of absorption. Figure 3.14 indicates the schematic diagram of a NDIR analyser.

The analyser consists of a sample cell and a comparison cell. The sample gas is pumped through the sample cell while the comparison cell is filled with nitrogen gas. An infrared light source passes through both cells. The comparison cell containing nitrogen does not absorb radiation in the infrared region thus the beam passes through without attenuation. In contrast, the gas in the sample cell absorbs radiation at specific wavelengths depending on the species presented and the concentration. Afterwards, the infrared lights are passed through the detector cells which contain two sealed cells filled with the sample gas separated by a membrane. The changes in the sample gas temperature caused by the different radiation results in a differential expansion.

Consequently, an electrical signal proportional to the gas concentration is generated by the movement of the membrane.

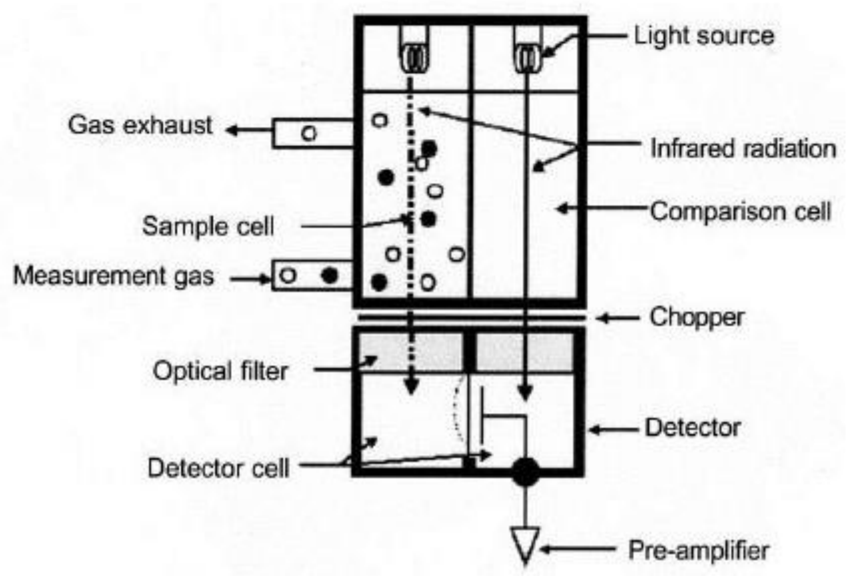

Figure 3.14 Schematic Diagram of NDIR Analyser (Horiba Instruments Ltd)

A light chopper is applied allowing intermittent transmission of infrared light to enable the detection of the changes in the species concentration in the sample cell. In addition, an optical filter between the sample sell and the detector cell is used to block the transmission of wavelengths absorbed by other species.

3.5.2 AVL 415: Soot measurement

The AVL 415 smoke meter was used to measure the soot concentration. A diaphragm type pump fitted on the analyser sucks the exhaust gas via a sampling line to a paper filter and a flow meter. The working principle of AVL 415 is to measure and compare the reflectance between the clean and blackened filter papers. Figure 3.15 shows the schematic diagram of AVL 415 smoke meter.

The level of paper blackening is graded as: a clean white filter paper has the value of zero and a completely blackened paper has the value of 10 corresponding to soot concentration of 0 and 32000mg/m^3, respectively. The related equation is given by,

$$P_B = 10 \times \left(1 - \frac{R_B}{R_W}\right) \qquad \text{Equation 3.1}$$

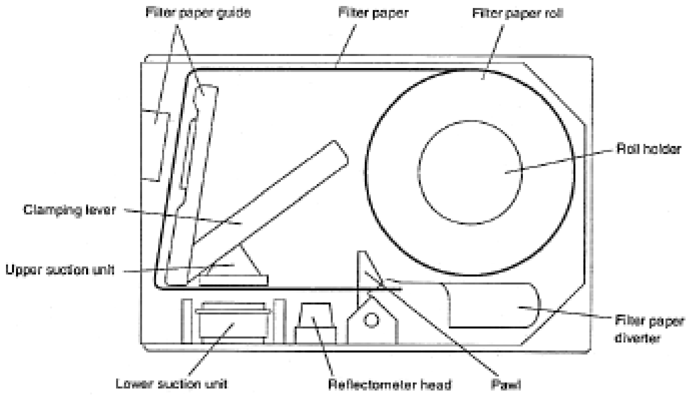

Figure 3.15 Schematic Diagram of AVL 415 Smoke Meter (AVL LIST GmbH)

Where P_B Paper blackening

R_B Reflection power of blackened filter paper

R_W Reflection power of white filter paper

During the experiments, the soot concentration is measured in Filter Smoke Number (FSN). FSN is defined as FSN=P_B when L_{eff}=405 mm, based on ISO10054 standards, and L_{eff} is given by:

$$L_{eff} = \frac{V_{eff}}{A} \qquad \text{Equation 3.2}$$

Where L_{eff} Effective length of the gas column drawn through the filter

V_{eff} Effective volume of the gas drawn through the filter

A Area of the blackened filter paper

Further, V_{eff} is defined by the following expression:

$$V_{eff} = V_S - V_D - V_L \qquad \text{Equation 3.3}$$

Where V_S Sample volume

V_D Dead volume of clean air between the filter paper and the end of the sampling line sucked through before the sample gas

V_L Leak volume, the volume of clean air and sample gas lost due to minor leaks

During the measurement process, the FSN number is displayed on a digital screen when the start button is pressed. The average for three consecutive sample measurements is shown for each test point.

3.6 Air and EGR Flow Rate Measurement

In this study, the air flow measurement is accomplished by using a Romet Rotary Gas Meter connected to the exhaust port through a surge tank with motored engine operation. The surge tank was used to stabilize the flow in order to obtain an accurate reading. During the measurement, the engine was motored with EGR and intake heating to simulate actual engine running condition. The air flow rate data was collected after at least 1 minute of engine operation to ensure the accuracy. The results showed the error was less than 3%.

A separate rota meter flow meter is used to measure the flow rate of simulated EGR gas of nitrogen gas.

3.7 Data Analysis

The in-cylinder pressure data is used to calculate the mean effective pressure and the heat release rate. By further processing the data, the combustion characteristics such as combustion duration, combustion phasing and ignition delay can be obtained. In addition, the engine efficiencies can be calculated by considering the energy exchange process.

3.7.1 Cylinder Volume Calculation

The cylinder volume is calculated through the engine geometry at any crank position using the following equation:

$$V = V_c + \frac{\pi B^2}{4}(l + a - s) \quad \text{Equation 3.4}$$

Where V   Cylinder volume

V_c Clearance volume

B   Cylinder bore

l Connecting rod length

a Crank radius

s Distance between crankshaft and piston pin axes

s is given by:

$$s = a\cos\theta + \sqrt{(l^2 - a^2 sin^2\theta)} \qquad \text{Equation 3.5}$$

Compression ratio is defined as:

$$r_c = \frac{V_d + V_c}{V_c} \qquad \text{Equation 3.6}$$

Where $\mathrm{r_c}$ Compression ratio

$\mathrm{V_d}$ Displacement volume

Further, the ration of connecting rod length to crank radius is given by:

$$R = \frac{l}{a} \qquad \text{Equation 3.7}$$

Where R Ratio of connecting rod length to crank radius

Equation 3.4 can be rearranged to:

$$V = V_c\left\{1 + \frac{1}{2}(r_c - 1)\left[R + 1 - cos\theta - \sqrt{(R^2 - sin^2\theta)}\right]\right\} \qquad \text{Equation 3.8}$$

3.7.2 Engine Combustion and Heat Release Analysis

The engine output and combustion characteristics are calculated based on the in-cylinder pressure data.

3.7.2.1 Indicated Mean Effective Pressure

Indicated Mean Effective Pressure (IMEP) is a theoretical measure of the effectiveness of the engine in producing work as a function of the displacement volume. In the pressure-volume diagram, gross IMEP is equal to the enclosed areas between the compression and expansion stroke, while net IMEP is the result of subtracting the negative work from the gross IMEP. Figure 3.16 shows the p-V diagram of a four-stroke diesel engine.

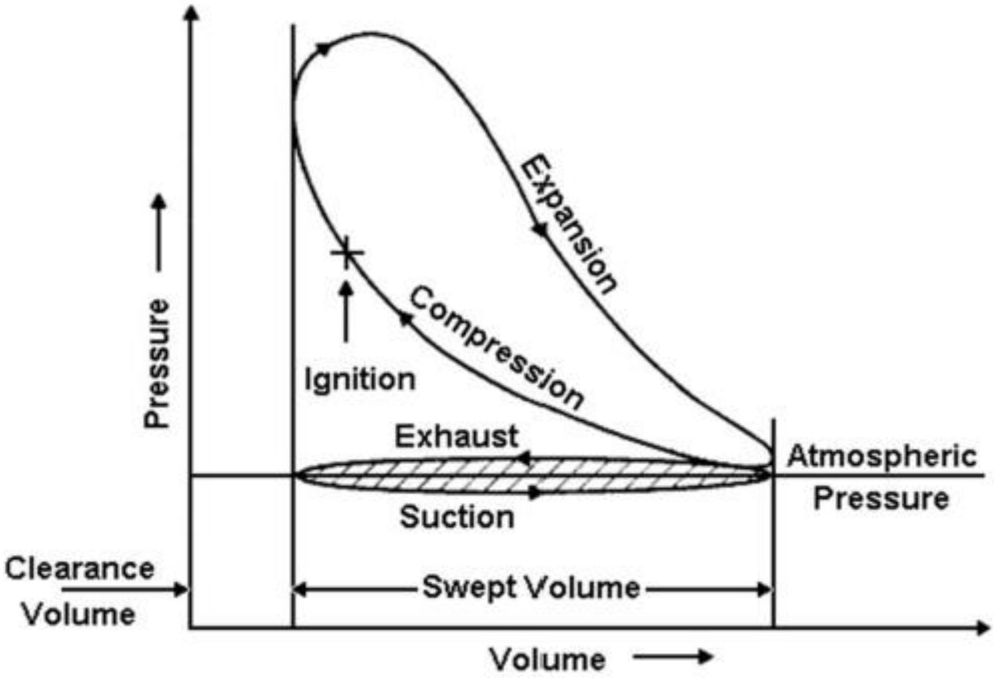

Figure 3.16 Four-Stroke Engine p-V Diagram [147]

IMEP is calculated by numerical integration of the p-V diagram:

$$IMEP = \frac{1}{V_d}\int_{y}^{x} p \cdot dV \qquad \text{Equation 3.9}$$

Where p In-Cylinder pressure

3.7.2.2 Heat Release Rate

The heat release rate is calculated based on the in-cylinder pressure and volume. It indicates the amount of heat added, or subtracted, to the cylinder contents for achieving the same in-cylinder pressure. In order to calculate the heat release rate, one-zone is applied considering the cylinder as an open system and the first law of thermodynamics uses as:

$$\frac{dQ}{dt} - p\frac{dV}{dt} + \sum_i \dot{m}_i\, h_i = \frac{dU}{dt} \qquad \text{Equation 3.10}$$

Where $\frac{\mathrm{dQ}}{\mathrm{dt}}$ Rate of heat transfer into system across boundary

$p\frac{dV}{dt}$ Rate of work transfer by system

$\dot{m}_i$ Mass flow rate into system at location i

h_i Enthalpy of flux i

U Internal energy of cylinder contents

The mass flows through the boundary are the injected fuel and the crevice flow when the both intake and exhaust valves are closed. By neglecting the crevice flow, Equation 3.10 becomes:

$$\frac{dQ}{dt} - p\frac{dV}{dt} + \dot{m}_f h_i = \frac{dU}{dt}$$ Equation 3.11

U is taken as the sensible internal energy of the in-cylinder charge, U_s, and h_f as the sensible enthalpy of the injected fuel. Hence $\frac{dQ}{dt}$ becomes the net heat release rate $\frac{dQ_n}{dt}$ which is the difference between the heat release rate and heat transfer from the system. Since $h_{s,f} \approx 0$, Equation 3.11 can be written as:

$$\frac{dQ_n}{dt} = P\frac{dV}{dt} + \frac{dU_s}{dt}$$ Equation 3.12

Considering the charge as an ideal gas, Equation 3.12 is written as:

$$\frac{dQ_n}{dt} = P\frac{dV}{dt} + mc_v\frac{dT}{dt}$$ Equation 3.13

Where c_v Specific heat at constant volume

T Absolute temperature

Considering the ideal gas law, $PV = mRT$, with R assumed constant:

$$V\frac{dp}{dt} + P\frac{dV}{dt} = mR\frac{dT}{dt}$$ Equation 3.14

Where R Ideal gas constant

The gas temperature T can be eliminated by combining Equation 3.13 and Equation 3.14 as:

$$\frac{dQ_n}{dt} = \left(1 + \frac{C_v}{R}\right)P\frac{dV}{dt} + \frac{C_v}{R}V\frac{dp}{dt}$$ Equation 3.15

Considering $\gamma = \frac{C_p}{C_v}$, ratio of specific heat, Equation 3.15 can be written as:

$$\frac{dQ_n}{dt} = \frac{\gamma}{\gamma-1} P \frac{dV}{dt} + \frac{\gamma}{\gamma-1} V \frac{dp}{dt}$$ Equation 3.16

The value of γ is not constant during the different stages of the engine cycle, however a single value of 1.3 is used for γ since it is commonly applied for diesel heat release rate analysis. Equation 3.16 is a simplified formula for calculating the heat release rate data in this study.

3.7.3 Engine Efficiencies Calculation

The analysis of engine's efficiencies is employed to evaluate the source of losses during engine work cycles, as shown in Figure 3.17.

The efficiencies in Figure 3.17 are determined as follows

$$FuelMEP = \frac{m_f \cdot LHV_f}{V_d}$$ Equation 3.17

$$Q_h MEP = \eta_c FuelMEP$$ Equation 3.18

$$IMEP_{gross} = \frac{W_g}{V_d} = \frac{1}{V_d} \int_{compression}^{expansion} P \cdot dV$$ Equation 3.19

$$IMEP_{net} = \frac{W_n}{V_d} = \frac{1}{V_d} \oint p \cdot dV$$ Equation 3.20

$$BMEP = \frac{4 \cdot \pi \cdot T}{V_d}$$ Equation 3.21

$$\eta_t = \frac{IMEP_{gross}}{Q_h MEP}$$ Equation 3.22

$$\eta_t = 1 - \frac{\sum_i x_i \cdot LHV_i \cdot (m_f + m_a)}{m_f \cdot LHV_f}$$ Equation 3.23

$$\eta_g = \frac{IMEP_{gross}}{FuelMEP};\ \eta_n = \frac{IMEP_{net}}{FuelMEP};\ \eta_b = \frac{BMEP}{FuelMEP};$$

$$\eta_{ge} = \frac{IMEP_{net}}{IMEP_{gross}};\ \eta_m = \frac{BMEP}{IMEP_{net}}$$ Equation 3.24

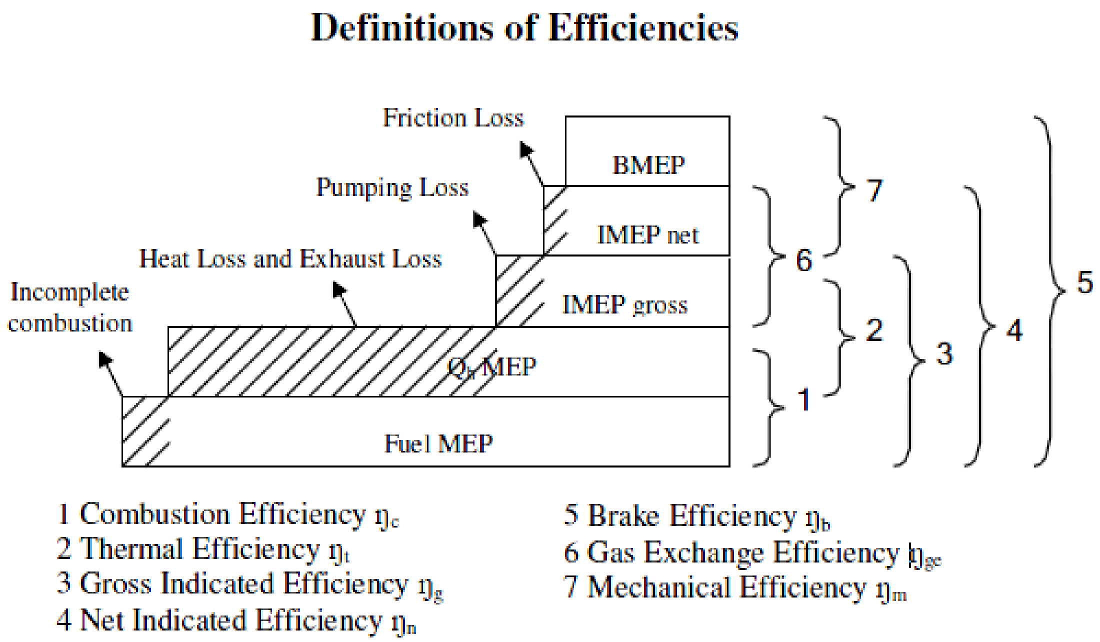

Figure 3.17 Definitions of Efficiencies [148]

Where m_f	Mass of fuel in one cycle
m_a	Mass of intake air in one cycle
W_g	Gross work in one cycle
W_n	Net work in one cycle
T	Break torque
x_i	The mass friction of CO and HC respectively (H2 is ignored)
LHV_i	Low heating values for CO (10.1 MJ/kg) and HC (44 MJ/kg) respectively

3.7.4 Fuel Mass Fraction Burned Analysis

As the Mass Fraction Burn (MFB) curve is used to identify the start of combustion (CA of 10% MFB), combustion phasing (CA of 50% MFB) and combustion duration (CA 10%-90% MFB), it is necessary to estimate the MFB profile from the cylinder pressure and volume data. According to analysis developed by Rassweiler and Withrow [149], the cylinder pressure rise during any crank angle interval, $\Delta\theta$, is considered to be caused by the pressure rise due to volume change, Δp_v, and the pressure increase due to combustion, Δp_c:

$$\Delta p = \Delta p_v + \Delta p_c \qquad \text{Equation 3.25}$$

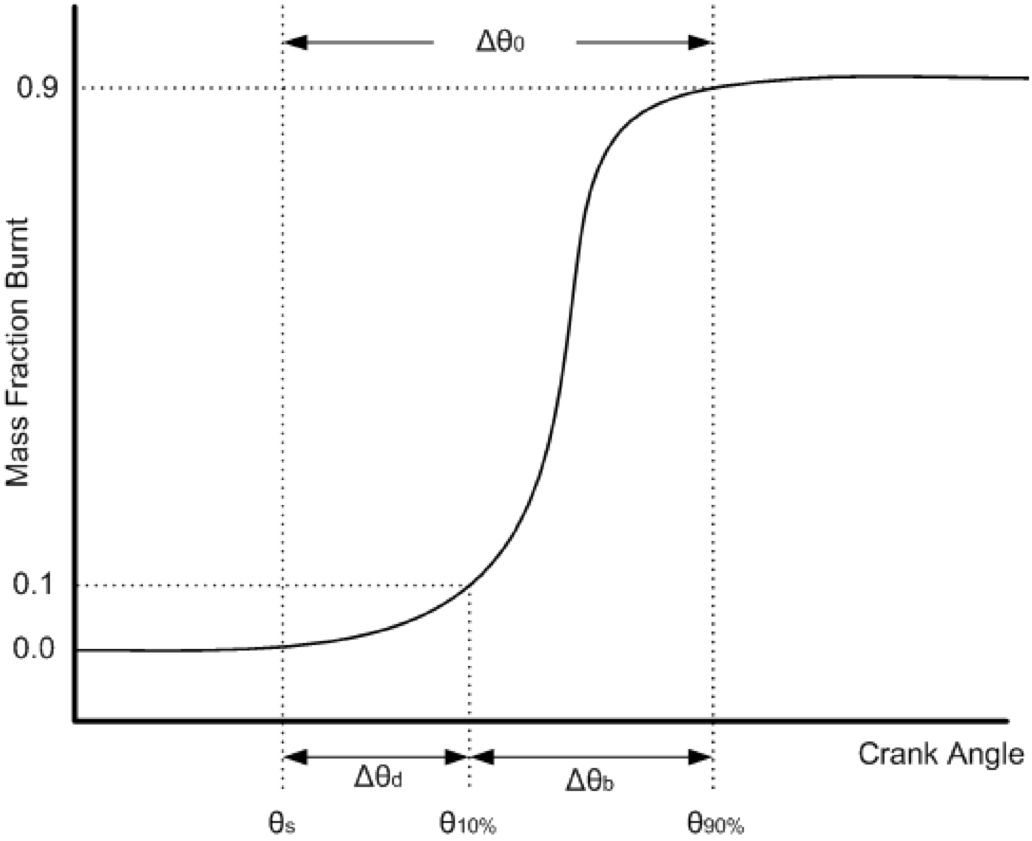

Figure 3.18 Definitions of Flame-development Angle, $\Delta\theta_d$, and Rapid-burning Angle, $\Delta\theta_b$, on A Mass Fraction Burned Curve [150]

As the crank angle (θ_i) increments to its next value (θ_{i+1}), the volume changes from V_i to V_{i+1}, and the pressure changes from p_i to p_{i+1}. The pressure change due to the piston movement is related to the volume change by the polytropic relationship

$$\Delta p = p_i\left[\left(\frac{V_i}{V_{i+1}}\right)^n - 1\right] \qquad \text{Equation 3.26}$$

Combining Equation 3.25 and 3.26, Δp_c can be evaluated:

$$\Delta p_c = p_{i+1} - p_i\left({}^{V_i}\!/_{V_{i+1}}\right)^n \qquad \text{Equation 3.27}$$

Where V_i is the cylinder volume given by Equation 3.8.

Since the combustion process is not occurring at the constant volume, the pressure rise due to combustion is not directly proportional to the mass of fuel burned. Therefore, the clearance volume at top dead centre, V_c, is taken into account of the volume effect:

$$\Delta p_c{}^* = \Delta p_c \left({}^{V_i}/_{V_c} \right)$$ Equation 3.28

Assuming that the referenced pressure rise due to combustion is proportional to the mass fraction burned (χ), the mass fraction burned at the end of the interval ($\Delta\theta$) is given by

$$\chi = \frac{m_{b,i}}{m_{b,total}} = \frac{\sum_1^i \Delta p_c{}^*}{\sum_1^N \Delta p_c{}^*}$$ Equation 3.29

3.8 Fuel Injection Calibration

In this study, Zeuch's method is applied to measure the fuel injection rate prior to the engine experiments, from which the relative air fuel ratio (lambda) can be determined for a known air flow rate.

3.8.1 Principle of Fuel Injection Rate Measurement

In Zeuch's method [151-154], fuel is injected into a constant volume chamber filled with the fuel. Consequently, the pressure inside the constant volume chamber increases with fuel injection and this augmentation is proportional to the quantity of fuel injected. Thus, the fuel quantity is measured by detecting the change in the pressure. When the a volume of fuel ΔV is injected into a constant volume chamber of volume V, the pressure rise ΔP can be determined by equation,

$$\Delta P = k\frac{\Delta V}{V}$$ Equation 3.30

Where k is the Bulk modulus of fuel.

The fuel injection rate can be calculated by differentiating Equation 3.30 with respect to time as shown below,

$$\frac{dV}{dt} = \frac{V}{k} \times \frac{dP}{dt}$$ Equation 3.31

Where t Time taken for injection

3.8.2 Bulk Modulus Determination

The bulk modulus of a liquid represents the compressibility upon the application of pressure. In this application, the bulk modulus of the liquid fuel is proportional to the pressure rise due to the injected fuel into the constant volume chamber. Thus, the evaluation of bulk modulus for the test fuel, in this study PRF and diesel, is required in order to achieve an accurate measurement of fuel injection rate [155-162].

The bulk modulus of diesel fuel has been measured by a former student [146] and the result was used for the diesel injection rate measurement. However, the bulk modulus for PRF still needs to be determined.

The bulk modulus of the liquid can be defined as:

$$k = a^2 \times \rho \qquad \text{Equation 3.32}$$

Where a The speed of sound

ρ The density of the fluid

A relationship is obtained linking the density to the speed of sound:

$$\rho(p,T) = \rho(p_0,T) + \int_{p_0}^{p} \frac{dp}{a^2} + T\int_{p_0}^{p} \left(\frac{\alpha^2}{C_p}\right) dp \qquad \text{Equation 3.33}$$

Where α The isobaric coefficient of thermal expansion

C_p The isobaric heat capacity

In the right side of Equation 3.33, the first term can be obtained by directly measuring the density at atmospheric pressure. The second term can be evaluated directly by means of the speed of sound along the isotherms considered. The last term is normally ignored as it is very small for the fuels of interest.

If the speed of sound a could be determined as a function of p, at a constant temperature, and ρ is measured at an initial point (p_0=p_{atm}), the density values can be obtained. Consequently, the bulk modulus k can be obtained applying Equation 3.32 by knowing a and ρ values. Figure 3.19 shows the measured bulk modulus for diesel fuel and calculated bulk modulus for PRF in reference document.

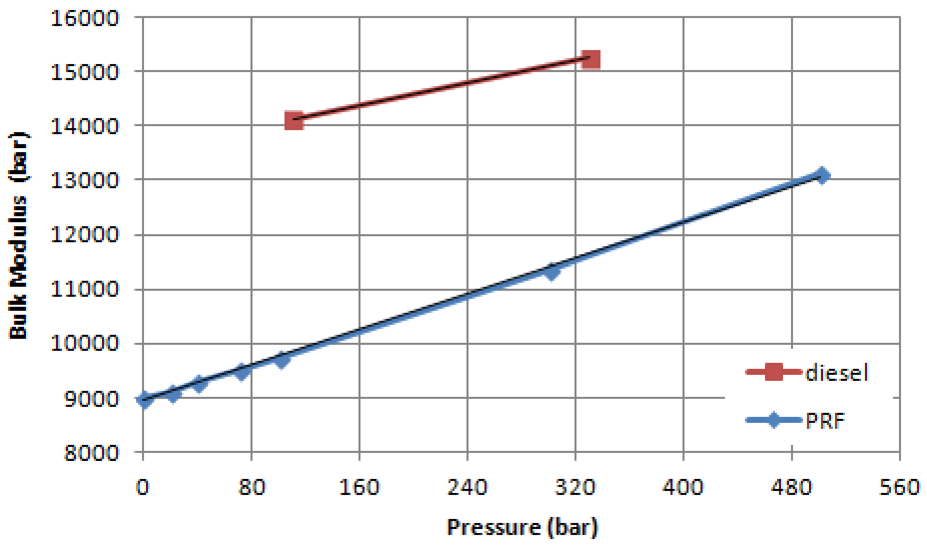

Figure 3.19 Bulk Modulus of Diesel Fuel and Primary Reference Fuel (PRF)

In order to ensure the accuracy of fuel injection quantity calculation by Zeuch's method, fuel mass measurements were carried out to validate the results. This was done by injecting fuel into a gas tight glass beaker on an electronic weight. The measurements were repeated 5 times at the same injection duration and pressure, and the average value was utilized to compare with the results from Zeuch's method. The comparison results showed that the errors through different means were less than 3%. In addition, the accuracy of fuel injection measurement was checked with AFR value on the exhaust analysis.

3.8.3 Experimental Setup

This setup arranges that a VCO solenoid injector is fitted onto a constant volume chamber of approximately 50 cm^3. Three pressure transducers are installed to measure the instantaneous pressure and pressure change. A Kistler 4043A50 piezo-resistive absolute pressure transducer measures the chamber pressure before the start of fuel injection, namely back pressure. The other two Kistler 701A piezoelectric pressure transducers with different sensitivity (high and low) are employed to measure the small and large amount of fuel quantities, respectively. Table 3.4 presents the specifications of Kistler transducers. A piezo-resistive charge amplifier Kistler 4618A2 is connected to the back pressure transducer Kistler 4043A50, while other pressure transducers are connected to a digital charge amplifier Kistler 5001.

Table 3.4 Characteristic Features of Kistler Pressure Transducers

Type	Measuring Range (bar)	Overload (bar)	Sensitivity		Natural Frequency (kHz)	Operating Temperature Range (℃)
			pC/bar	mV/bar		
4043A10	0~50	125	N/A	10	>180	-20~50
710A	0~250	400	82.9	N/A	≈70	-150~200
710A	0~250	400	82.4	N/A	≈70	-150~200

As shown in Figure 3.20, a high pressure direct acting coaxial solenoid valve is mounted on top of constant volume chamber prior to a pressure relief valve. The combination of the valves allows the compressed fuel flow back to fuel tank after the measurement as well as regulation of the back pressure. In order to validate the fuel quantity results taken by Zeuch's method, an ONO SOKKI FP-200 fuel flow meter is used to measure the fuel flow rate. During the test, the injection signal is sent to solenoid value to trigger the closed mode to start the measurement. All the measurement data are sent and recorded by a digital oscilloscope and the data processing is carried out in Microsoft Excel.

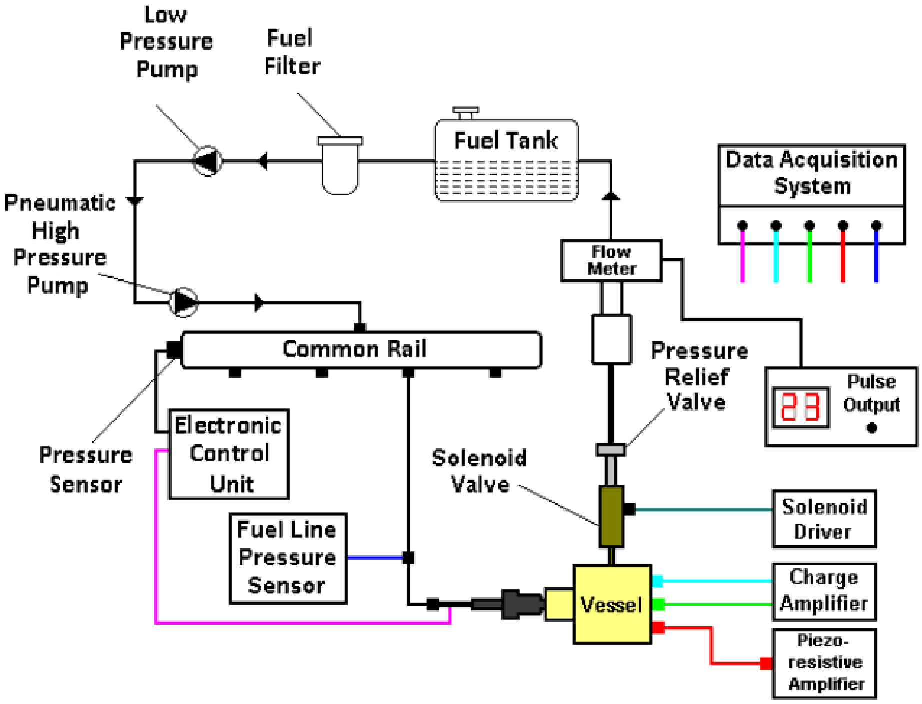

Figure 3.20 Schematic Diagram of the Experimental Setup Based on Zeuch's Method [146]

3.8.4 Data Analysis and Results

As the pressure data collected by the data acquisition system fluctuates due to the signal interference, a smoothing processing is needed before further data analysis can be done. Therefore, the Fast Fourier Transform (FFT) function in software called Origin is applied to filter the pressure signals. By using the filtered pressure value, the fuel injection quantity can be determined by calculating the injection rate applying Equation 3.31.

Since the injection quantity is determined directly by the injection duration set in ECU, the correct injection duration is required corresponding to the measured injection rate. Therefore, for each injection strategy, the injection duration is purposely selected until the desired injection rate, namely injection quantity, is achieved. Table 3.5 shows the injection strategies for fuel quantity calibration experiments.

Table 3.5 Fuel Injection Quantities for All Strategies

Strategy	**Fuel**	**Dwell Angle (degCA)**	**Quantity (mm^3)**	
Two injection (50:50)	PRF	Variable from 35 to 100	10.88	10.88
Two injection (70:30)	PRF	Variable from 35 to 100	15.24	6.53
Two injection (30:70)	PRF	Variable from 35 to 100	6.53	15.24
Two injection (10:90)	Diesel	Variable from 10 to 20	1.88	16.94

In Figure 3.21, the injection rates for different injection quantity distribution strategies at 50 ° CA dwell angle are depicted. By adjusting the injection duration, desired injection rates are obtained for each single injection so that the accurate control for total fuel injection quantity can be achieved.

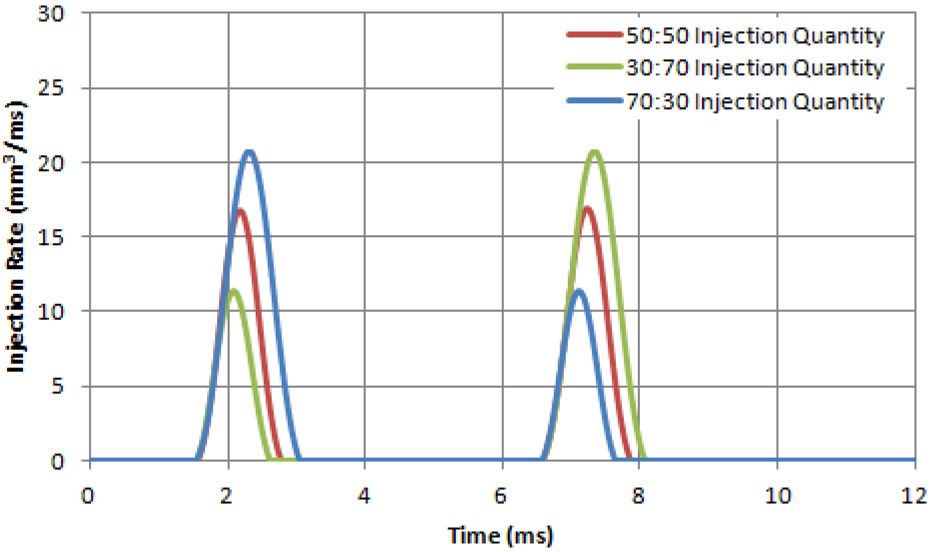

Figure 3.21 Injection Rate Profile for Dwell 50 °CA Strategies, 21.77 mm^3

It is worth noting that the interference existed between two injections causes the variation on the 2nd injection quantity due to the high pressure waves in the fuel line. In addition, it is found that the crank angle lag between two injections called dwell angle affects the 2nd injection quantity as well. Therefore, it is necessary to adjust the 2nd injection duration in order to obtain the desired injection quantity. Figure 3.22 shows the injection duration for the primary reference fuel under the different dwell angle at 1200 bar injection pressure. It can be seen that for different dwell angle, the injection duration for the 2nd injection duration needs to be adjusted to obtain the wanted injection quantity while the 1st injection duration keeps constant. Moreover, the variation of the 2nd injection duration becomes small when the dwell angle increases. This is mainly attributed to the interference between two injections is reduced at large dwell angles. In Figure 3.23, the fluctuation of 2nd injection duration still appears at 900 bar injection pressure and the longer injection duration is experienced compared to 1200 bar injection pressure strategies. The injection duration against dwell angle for diesel case is presented in Figure 3.24.

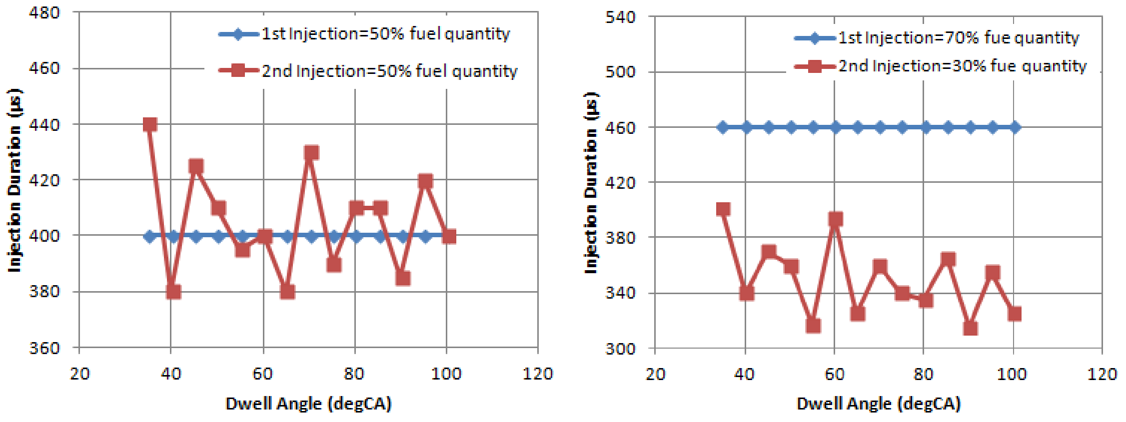

Figure 3.22 Injection Duration against Dwell Angle at 1200 bar Injection Pressure (PRF)

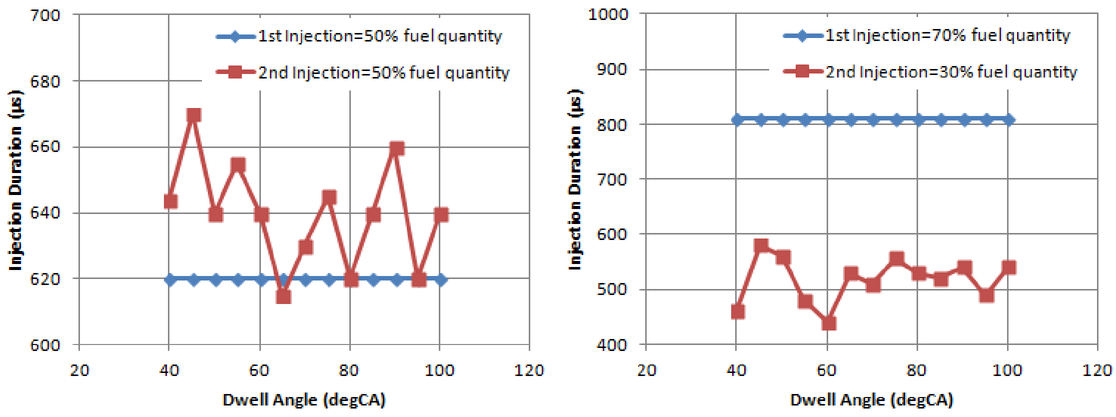

Figure 3.23 Injection Duration against Dwell Angle at 900 bar Injection Pressure (PRF)

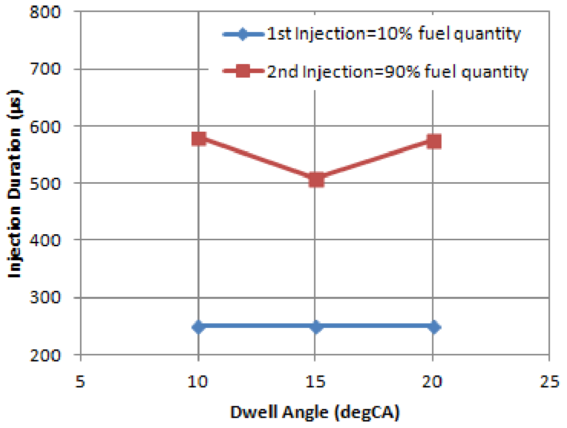

Figure 3.24 Injection Duration against Dwell Angle at 1200 bar Injection Pressure (diesel)

3.9 Lambda Determination Based on Exhaust Components Measurement

Exhaust gas composition is determined by the relative proportions of fuel and air introduced to the engine, fuel composition and completeness of combustion. The fuel/air ratio of the engine can be calculated by knowing these relationships and the exhaust gas composition.

Numerous studies have been taken to evaluate the air fuel ratio from engine exhaust gas. The earliest cited paper in the literature was written by D'Alleva [163]. In his publication, the A/F ratio was determined in the charts based on exhaust concentrations according to the fuel h/c ratio. The improvement to D'Alleva's charts was made by Eltinge [164]. The incomplete combustion cases were included and the charts can be used without the O2 measurement. Spindt [165] created a formula to calculate the fuel/air ratio without the assumption of complete combustion. In 1979, an evolutionary improvement based on Spindt's equation was reported by Brett/Schneider [166]. Both water in the ambient air and absorbed in a measured NOx were taken into account. Additionally, oxygenated fuel was introduced into the equation. Simons [167] from German TUEV proposed the calculation of the equilibrium constant K using the O_2 measurement. It was indicated that K could vary and was normally lower than 3.5. However, Fukui, Tamura, Omori, Satioh in Mitsubishi [168] found that the equilibrium constant changed by the action of the catalyst and that the water-gas equilibrium was affected by the existed water in the ambient air. The determination of A/F ratio using direct engine out gasses was recommended. Generally, Brett/Schneider's method presents a complete analysis and covers all the important factors and is widely used. Simons equation gives more reliable and accurate calculation that can be applied without considering the catalyst effects on the equilibrium constant.

The Brett/Schneider's method is used in the present study. The general formula for the composition of fuel can be represented as $C_nH_mO_r$. Since the conventional petroleum-based fuels are used in this study, oxygen is absent. Thus, considering the exhaust production of CO_2, H_2O, CO, H_2, O_2, NOx, N_2, uHC and soot particles (to be omitted when it is sufficiently small), the overall combustion reaction can be written explicitly as:

$$C_nH_mO_r + \frac{n_{O_2}}{\phi}(O_2 + 3.773N_2) = n_P\big(\tilde{x}_{C_aH_b} + \tilde{x}_{CO}CO + \tilde{x}_{CO_2}CO_2 + \tilde{x}_{O_2}O_2 + \tilde{x}_{N_2}N_2 + \tilde{x}_{NO}NO + \tilde{x}_{NO_2}NO_2 + \tilde{x}_{H_2O}H_2O + \tilde{x}_{H_2}H_2\big) \qquad \text{Equation 3.34}$$

Where $C_nH_mO_r$ The fuel

$(O_2 + 3.773N_2)$ The oxidizer

ϕ The measured equivalence ratio

$\tilde{x}_i$ The mole fraction of ith component

n_P The total number of moles of exhaust products

The number of moles of O_2 required for complete combustion of one mole of fuel $C_nH_mO_r$ is given by

$$n_{O_2} = n + \frac{m}{4} - \frac{r}{2} \qquad \text{Equation 3.35}$$

The relationship between moles of exhaust products, (HC), (CO), (CO_2) mole fractions, hydrocarbons assumed the same composition as fuel, is as follows

$$n_P = \frac{n}{\big(n(HC)+(CO)+(CO_2)\big)} \qquad \text{Equation 3.36}$$

Mole fraction (H_2) is given by,

$$(H_2) = \frac{(CO)\cdot(H_2O)}{K\cdot(CO_2)} \qquad \text{Equation 3.37}$$

Mole fraction (H_2O) is determined using Equation 3.37 and H balance

$$(H_2O) = \frac{m\left(\frac{1}{n_P} - (HC)\right)}{2\left(1 + \frac{(CO)}{K(CO_2)}\right)} \qquad \text{Equation 3.38}$$

Mole fraction (O_2), is derived from Σmol fraction=1, using N balance and O balance, where NO is assumed negligible

$$(O_2) = \frac{\left(1 - (HC) - \left(1 + \frac{\varphi}{2}\right)\big((CO) + (H_2O)\big) - (H_2) - (1+\varphi)(CO_2) + \frac{r\varphi}{2n_P}\right)}{(1+\varphi)} \qquad \text{Equation 3.39}$$

The ratio of oxygen species in exhaust to oxygen required for stoichiometric combustion is

$$\lambda = \frac{n_P\left((CO)+2(CO_2)+2(O_2)+(H_2O)\right)-r}{2n_{O_2}} \qquad \text{Equation 3.40}$$

3.10 Summary

This chapter summarises the experimental facilities applied in this work. The single cylinder optical engine and its components, the intake and exhaust system, the fuel injection system, and the data acquisition system are described. The devices for the in-cylinder pressure, intake and EGR flow, exhaust emissions and optical measurement are introduced. The detailed data analysis process is explained. Finally, the experimental procedure for fuel injection calibration and the fundamentals for Lambda determination are explained.

CHAPTER 4

Development of Simultaneous Mie-Scattering and Laser Induced Fluorescence Technique

4.1 Introduction

In order to investigate the fuel injection and mixture preparation process in detail, it is necessary to visualize both liquid and vapour phases of the fuel spray. The simultaneous Mie-Scattering and LIF techniques are developed for in-cylinder fuel spray visualization. The principle of this technique is explained prior to presenting the experimental setup. The imaging devices and optics selection are described. Synchronization of the fuel injection, the laser and imaging system is discussed in detail. The means for improving image quality is introduced. Finally, the procedure of image data processing is presented.

4.2 Principle of Mie-Scattering Technique

Mie-scattering is elastic scattered light of particles that have a diameter similar to or larger than the wavelength of the incident light. That is to say when the diameter of a particle is much larger than the wavelength or size parameter, $a = {}^{\pi d}/_{\lambda} \gg 1$, the light-scattering process is defined as Mie-scattering. For visible wavelengths, Mie-scattering appears from particles larger than 0.5 μm. The scattering intensity from the particles of diameter d is given by

$$I_{sca}(n, \theta, d) = I_0 C_n f(n, \theta) d^2 \qquad \text{Equation 4.1}$$

Where

n is the real part of the refractive index of the particle,

θ is the scattering angle

C_n is the number density of particles

$\mathrm{f(n, \theta)}$ is a complicated function of the refractive index, particle shape, and the scattering angle.

The Mie-scattering technique is limited to qualitative measurement since the scattering light intensity is proportional to both droplet concentration and size distribution. In addition, there is a strong angular dependency of the scattered intensity, especially for smaller particles, which has to be considered for successful Mie imaging experiments. In this study, Mie-scattering is used for the visualisation of liquid fuel spray and droplet distribution in the cylinder.

4.3 Principle of Laser-Induced Fluorescence Technique

LIF has proven to be a strong tool for flow visualization, as well as for quantitative measurements of concentration and temperature in liquid and gaseous flows. The visualization of the presence of a species can be made by means of LIF by adding a fluorescent tracer to the non-fluorescent fluid or gas.

In the LIF measurement, the emission of light (LIF signal) is formed from an atom or molecule following the excitation by a laser beam. The molecule is excited from a lower electronic state to an upper electronic energy level by photons during the laser radiation. It is noted that the wavelength of the laser light is carefully selected to coincide with the absorption wavelength of the species to be detected.

Figure 4.1 indicates five significant processes when a molecule is excited by a laser source.

1. The molecule can be returned to its original quantum state by laser-induced stimulated emission, denoted as $B_{21}I_v$.
2. Absorption of an additional photon can excite the molecule to higher states, even to ionized levels, shown as Q_{ion}.
3. The internal energy of the system can be altered in inelastic collisions with other molecules, producing rotational energy transfers, represented by $Q_{rot,vib}$. It is worth noting that in some cases the inelastic collisions with other molecules also result in electronic energy transfer Q_{elec}, which is often referred to as quenching.
4. Interactions between the individual atoms of the molecule produce internal energy transfer and dissociation of the molecule. The dissociation in this case is called predissociation because it is produced by a change from a stable to a repulsive electronic state, which is not stable.

5. The originally populated state and nearby states indirectly populated through collisions return to lower states through the emission of light, producing the LIF.

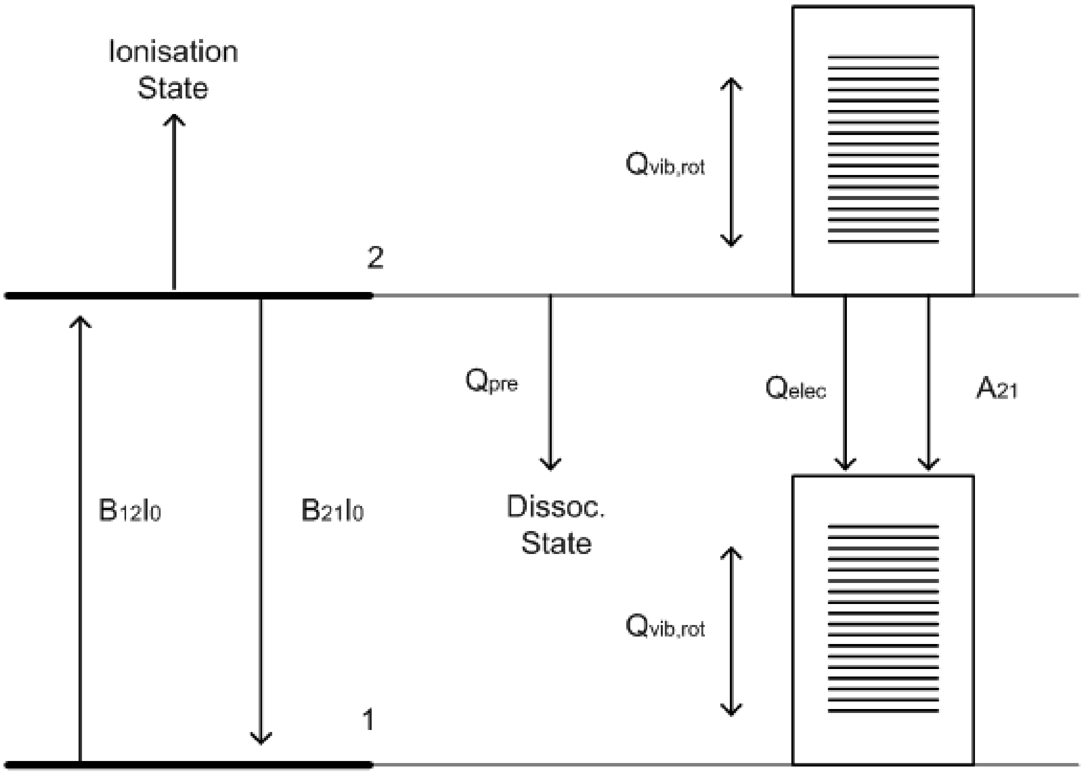

Figure 4.1 Main Energy Transfer Process in LIF [144]

Where

A_{21}=spontaneous emission from the upper to lower electronic states

$B_{21}I_0$=stimulated emission

$B_{12}I_0$=stimulated absorption

Q_{ion}=photo-ionization

Q_{pre}=predissociation

Q_{elec}=electronic collisional quenching

$Q_{vib,rot}$=vibrational and rotational collisional quenching

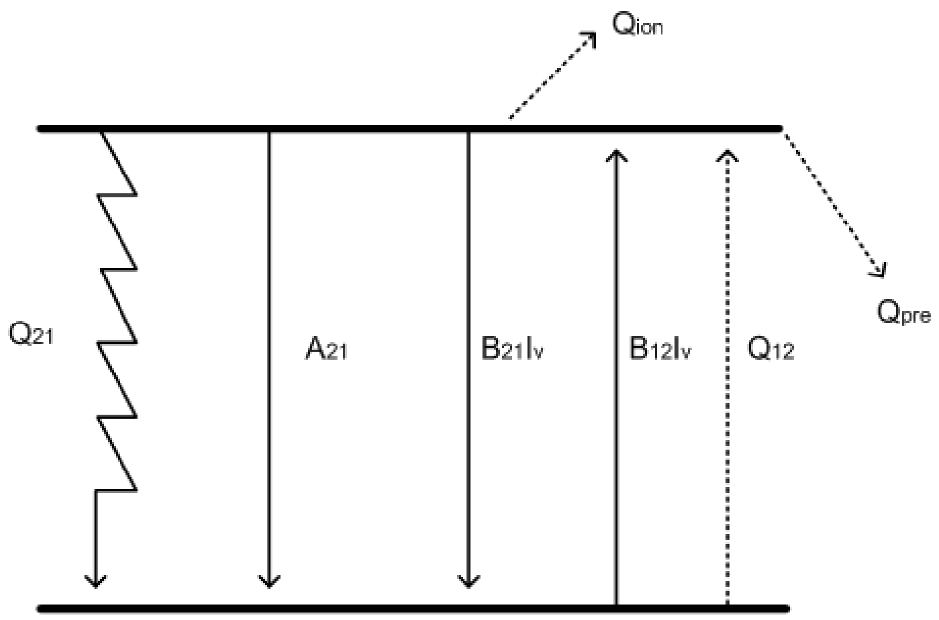

Figure 4.2 Simple Two-energy-level Diagram for LIF Modelling

A two-energy-level model is often used as a first approximation in actual data analysis. Such a model is appropriate to LIF detection of some molecular systems with fully equilibrated or fully frozen rotational level manifolds. It is also capable of illustrating the crucial properties of LIF. As shown in Figure 4.2, a typical two-energy-level model is depicted. The rate equations for the lower and upper energy level are:

$$ {dN_1}/{dt} = -N_1(Q_{12} + B_{12}I_v) + N_2(Q_{21} + A_{21} + B_{21}I_v) \qquad \text{Equation 4.2} $$

$$ {dN_2}/{dt} = N_1(Q_{12} + B_{12}I_v) - N_2\left(Q_{21} + B_{21}I_v + A_{21} + Q_{ion} + Q_{pre}\right) \qquad \text{Equation 4.3} $$

Where B_{12}, B_{21} are the Einstein coefficients for stimulated absorption and emission, A_{21} is the Einstein coefficient for spontaneous emission, and I_v ($Wcm^{-2}Hz^{-1}$) is the laser spectral intensity. The two energy levels are normally separated by a few electron-volts, thus collisional excitation Q_{12} can be omitted in most combustion measurements. Most excited states are not predissociative (Q_{pre}), unless specifically chosen, and photo-ionization (Q_{ion}) can often be ignored. Equation 4.2 and 4.3 become:

$$ {dN_1}/{dt} = -N_1B_{12}I_v + N_2(Q_{21} + A_{21} + B_{21}I_v) \qquad \text{Equation 4.4} $$

$$ {}^{dN_2}\!/_{dt} = N_1 B_{12} I_v - N_2 (Q_{21} + A_{21} + B_{21} I_v) $$ Equation 4.5

Since there is negligible population of the upper level prior to the laser excitation, the initial condition $N_2|_{t=0}=0$ is applied in Equation 4.5. Moreover, the population of molecules should be conserved without chemical reactions occurring during the measurement.

$$ N_1 = N_1 + N_2 = constant = N_1^0 $$ Equation 4.6

Where N_1^0 is the total population prior to laser excitation. The solution to the two-level system is given by:

$$ N_2 = N_1^0 B_{12} I_v \tau \left(1 - e^{-t/\tau}\right) $$ Equation 4.7

Where the time constant τ is $(Q_{21} + A_{21} + B_{21} I_v + B_{12} I_v)^{-1}$. For laser pulses that are long compared to τ, the system reached the steady-state value of:

$$ N_2 = N_1^0 B_{12} I_v \tau $$ Equation 4.8

Or more conveniently written as:

$$ N_2 = B_{12} I_v \frac{A_{21}}{A_{21}+Q_{21}} \frac{1}{1+{}^{I_v}\!/_{{I_v}^{sat}}} $$ Equation 4.9

Where the saturation intensity ${I_v}^{sat}$ is defined as:

$$ {I_v}^{sat} = \frac{A_{21}+Q_{21}}{B_{21}+B_{12}} $$ Equation 4.10

Assuming the fluorescence is emitted equally into 4π steradiants, the total number of photons N_p striking on to a photodetector from a collection volume V_c is given by:

$$ N_p = \eta \frac{\Omega}{4\pi} N_1^0 V_c B_{12} E_v \frac{A_{21}}{A_{21}+Q_{21}} \frac{1}{1+{}^{I_v}\!/_{{I_v}^{sat}}} $$ Equation 4.11

Where:

Ɛ=transmission efficiency of the collection optics

Ω=the collection solid angle (sr)

E_v=the spectral fluence of the laser (J cm^{-2}Hz^{-1})

$\mathrm{V_c}$=the sampling volume, defined by the cross-sectional area of the laser beam A and the axial extent along the beam L from which the fluorescence is detected

For a particular experimental setup, the fluorescence signal can be expressed as

$$P_{flu} = \eta_c \Omega V_c f_1(T) x_m N I_v \frac{A_{21}}{A_{21}+Q_{21}} \frac{B_{12}}{1+{I_v}/{I_v}^{sat}} \qquad \text{Equation 4.12}$$

Where:

$f_1(T)$=the fractional population of the lower electronic state

x_m=the mole fraction of the absorbing species

N=the total gas number density (cm^{-3})

I_v=the spectral power of incident laser light (Wcm^{-2}Hz^{-1})

$f_1(T)$ represents the fraction of molecules of the absorbing species which are in the specific electronic-vibrational-rotational energy level excited by the laser, and is given by the Boltzmann distribution. Therefore, the grouping $[f_1(T)x_mN]$ represents the number density of the absorbing species at ground state, N_1^0. Equation 4.12 can be further simplified for two limiting cases which correspond to either low or high laser intensity. In the lower laser intensity case, namely $I_v \ll {I_v}^{sat}$, it becomes:

$$P_{flu} = \eta_c \Omega V_c f_1(T) x_m N I_v B_{12} \frac{A_{21}}{A_{21}+Q_{21}} \qquad \text{Equation 4.13}$$

This is called the linear fluorescence equation since the fluorescence is linearly proportional to laser intensity. If the laser intensity is increased until $I_v \gg {I_v}^{sat}$, Equation 4.12 simplifies to:

$$P_{flu} = \eta_c V_c f_1(T) x_m N B_{12} \frac{A_{21}}{B_{12}+B_{21}} \qquad \text{Equation 4.14}$$

In this case the fluorescence is said to be in the saturation limit. In this saturation regime, the fluorescence signal is independent of both the laser irradiance and the quenching, obviating the need to measure or evaluate either one.

4.4 Experimental Setup

The laser diagnostic experimental setup for this study is outlined in the following section. The detailed descriptions of the light source, imaging system, optics setup and synchronisation are explained.

4.4.1 Excitation Source

A Q-Switched Nd:YAG laser (Figure 4.3) operating at a wavelength of 355nm was used for Mie-LIF measurement. In this study, the laser produced energy of 50mJ at 10 Hz pulse repetition rate and was externally triggered by the engine cranking signal. The specifications of the laser device are shown in Table 4.1.

Table 4.1 Nd:YAG laser Specifications

Model	Continuum Surelite II
Max Output Power	1.25 w
Wavelength	355 nm
Maximum Pulse Energy	125 mJ
Pulse Length	4-6 ns
Pulse Repetition Rate	10 Hz
Nd:YAG Rod Diameter	7 mm
Beam Divergence	0.6 mrads

Figure 4.3 Continuum Surelite II Q-Switched Nd:YAG laser

4.4.2 Imaging System

An Oriel InstaSpec V intensified CCD camera system was used to record ultra-low light images. A Charge Coupled Device, or CCD, is a silicon-based semiconductor chip bearing a two-dimensional matrix of photo-sensors, or pixels. In this study, a 578x385 CCD chip was utilized in order to match the layout of an image doubler.

As shown in Figure 4.4, the camera was connected to a camera control unit, which provides the internal and external triggering, and was connected to a data acquisition card installed in a PC to transfer the recorded image. As the CCD in the detector is a scientific slow scan device, the image acquisition rate is therefore dramatically reduced to 0.2 Hz (1 frame per 5 seconds).

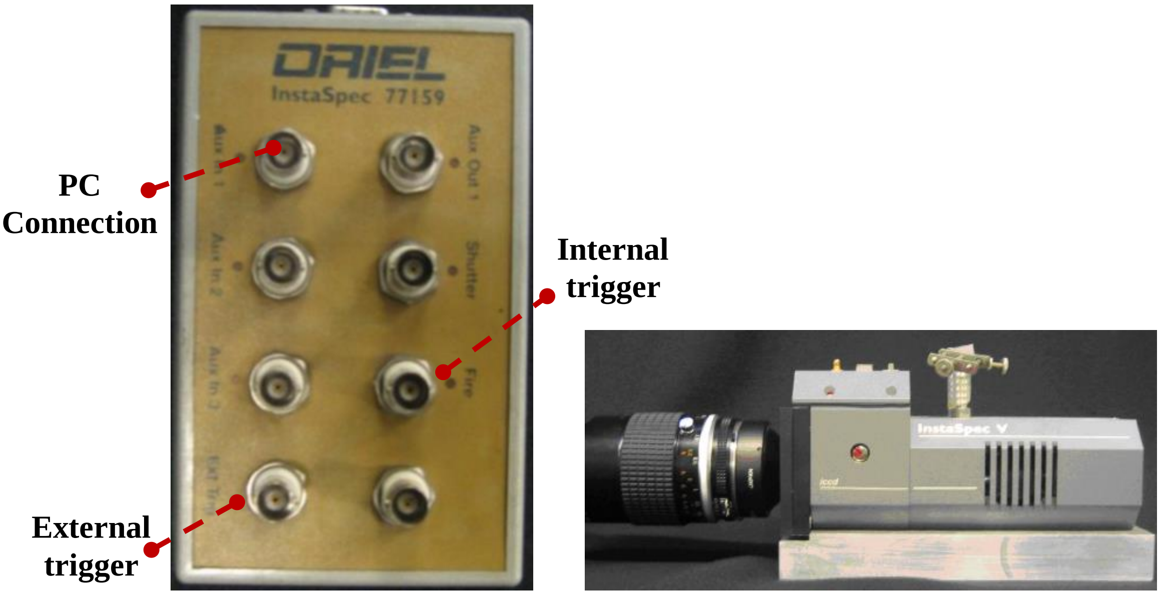

Figure 4.4 Control Unit (Left) and ICCD Camera (Right)

A Nikon UV-105 high performance lens (Figure 4.5) was utilized in the experiments. The lens is developed for specialized multispectral applications in the ultraviolet (UV), visible, and infrared portions of the spectrum. The UV-Nikkor lens coupled with the ICCD camera is capable of transmitting on a broad spectral range, from 220 to 900 nm, with a high transmission (up to 70%), which is well suited for simultaneous Mie (355nm) and LIF (450-470nm) measurements.

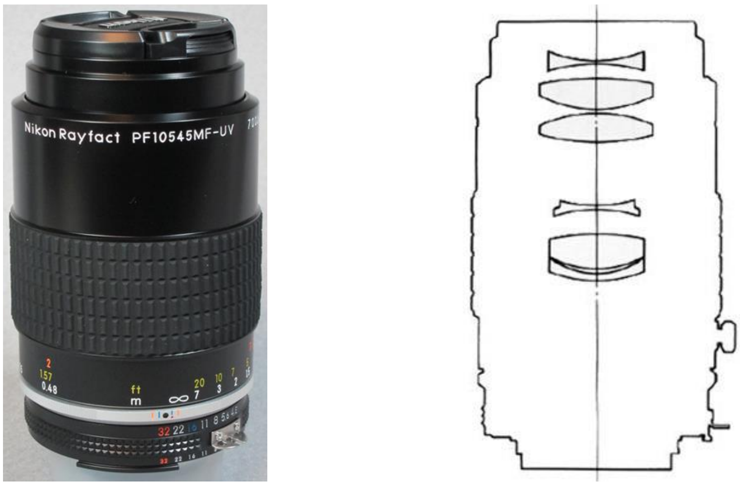

Figure 4.5 UV-Nikkor 105mm f/4.5 Lens

The software called Andor MCD was used for controlling the ICCD camera, as well as image data acquisition. The ICCD and image data acquisition can be triggered internally for focusing purposes, but an external trigger was used for the actual fuel spray measurements.

4.4.3 Synchronisation

In order to perform the simultaneous Mie-LIF measurement, the laser light, fuel injection and ICCD camera need to be synchronised. A schematic drawing of devices with connections for synchronisation is shown in Figure 4.6. In this experiment, the laser was triggered externally by the TTL signal from the engine shaft encoder. As the laser has 10 Hz repetition rate, it is necessary to run the engine at 1200 rpm, equating to 20 revolutions per second. Additionally, a signal skip unit was used after the shaft encoder to skip one TTL signal in every two signals, so that a 10 Hz TTL signal could be generated and sent to the laser. It is worth noting that a signal delay generator was added prior to the laser in order to synchronise the laser light with the fuel injection event. In addition, the laser energy could be adjusted by changing the Q-Switched delay (120μs in this case) through the delay generator.

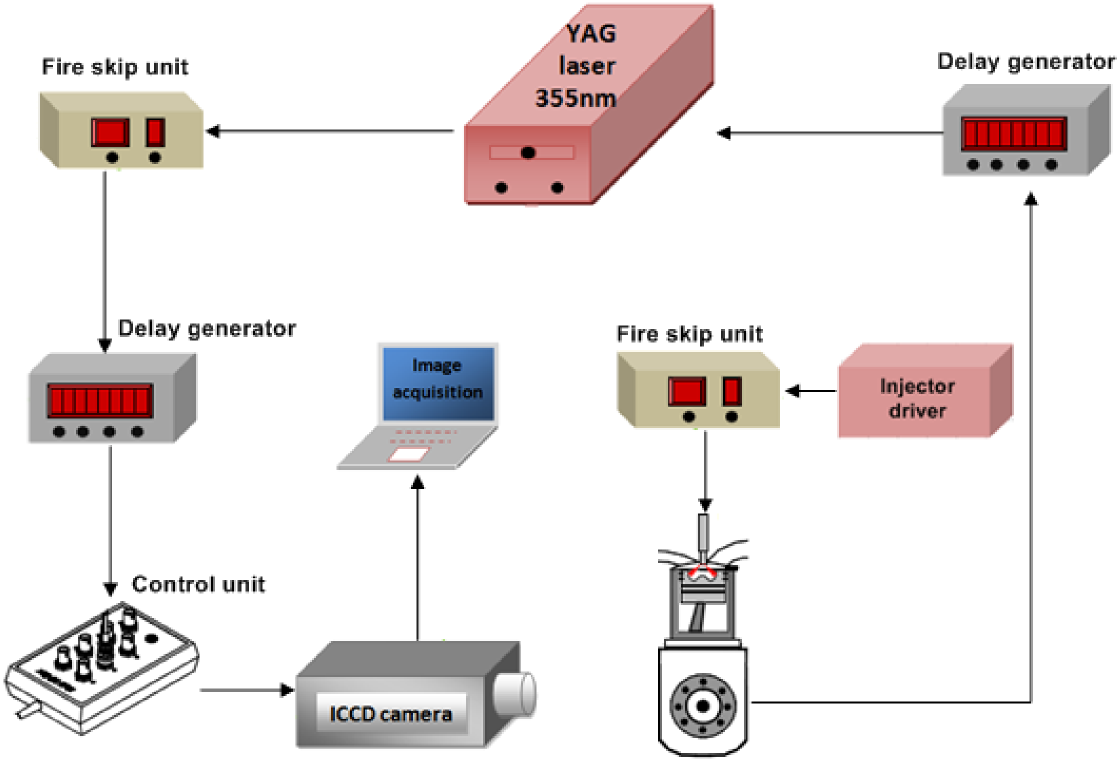

Figure 4.6 A Schematic Drawing of the Synchronisation

A 10 Hz laser output signal was sent out after inherent 180µs delay from laser device for triggering the ICCD camera. As mentioned above, the minimum time for camera to save the image data was 5 seconds. Therefore, a fire skip box was utilized to skip 55 laser operating cycles, equating to approximately 5.5 seconds. Moreover, a SRS DG535 delay generator was connected prior to the ICCD camera in order to freely adjust the position of the ICCD gate, as well as the gate width. In this application, the ICCD gate was set at 550 ns to minimize the background light.

The injection control unit designed by EmTroniX has an 'Enable' input function to allow injections to be enabled or disabled by sending the injection enable signal externally. In this case, the same TTL signal generated by the engine shaft encoder for triggering the laser device was also used for enabling the injections. It is noted that the other fire skip box was applied before the injection control unit for preventing unnecessary window fouling. 400µs delay was measured between raising edge of injection signal to the actual start of injection. By detecting laser light with a photodiode device, the synchronisation between injection and laser could be checked and adjusted. Considering the inherent 250 ns delay of the ICCD camera, the ICCD gate was slightly advanced of where the laser light was.

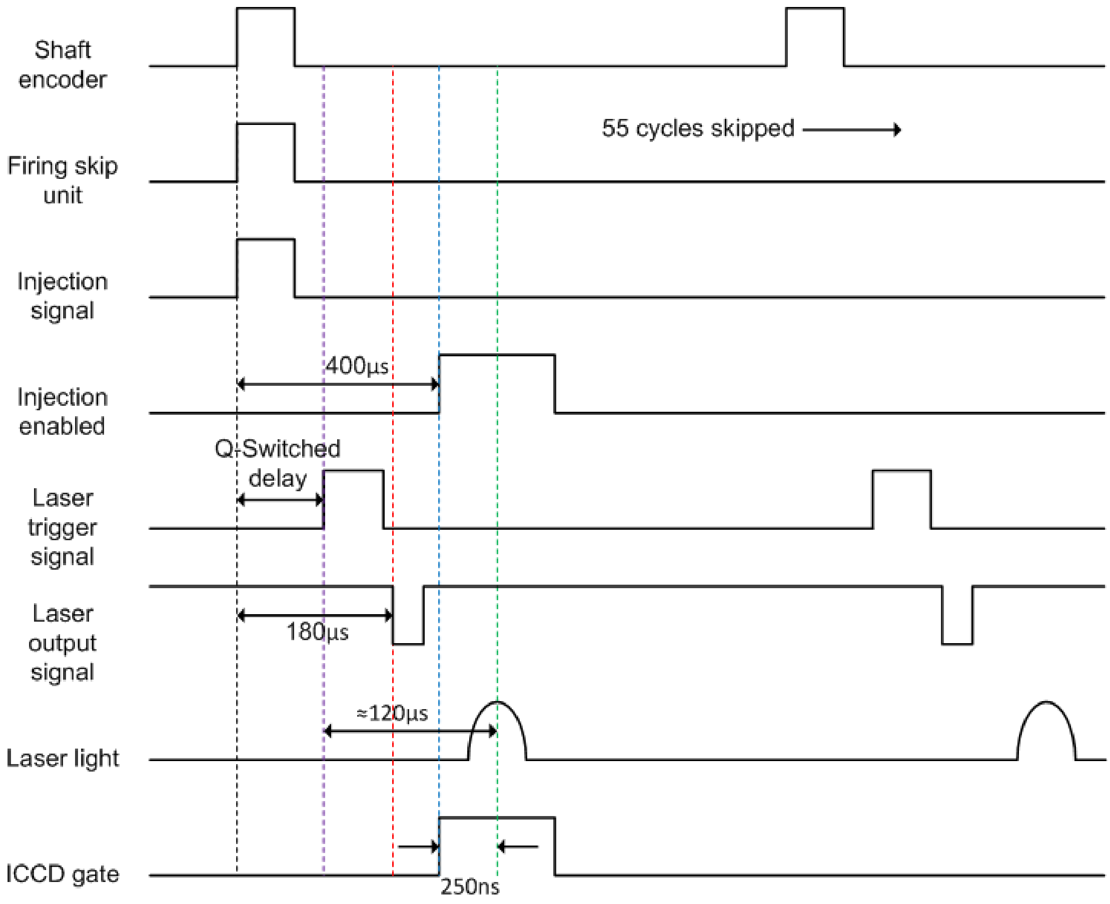

Figure 4.7 Mie-LIF Control System Timing Diagram

4.4.4 Optical Setup

In order to achieve simultaneous Mie and LIF measurement, it is essential to separate elastic scattering and fluorescence signals by selecting appropriate optical filters based on the fluorescence spectra of the tracer. Figure 4.8 shows the fluorescence spectra of two signals in a mixture of 90% PRF (70% isooctane and 30% heptane by volume) and 10% biacetyl. The LIF signal is produced by biacetyl after laser excitation and the elastic scattered light of liquid particles dominates the Mie signal. Although the Mie and LIF signal emissions peak at 355 and 465 nm, respectively, an overlap in spectrum between these two signals appears within the range from 380 to 420nm. This cross-talk can be eliminated by employing a long-pass filter to cut off at 420nm for LIF signal and a 355nm band-pass filter for Mie signal. It is worth noting that a qualitative measurement was carried out in this study, hence the small interference between the two signals can be ignored.

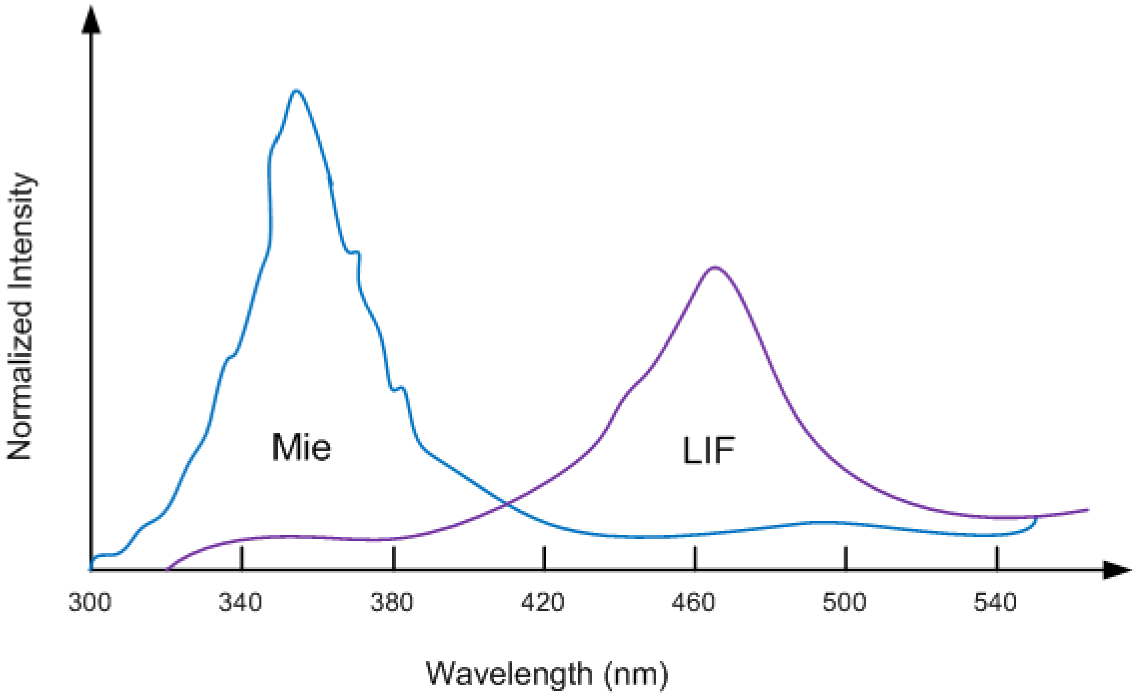

Figure 4.8 Mie-Scattering and LIF Fluorescence Spectra

Figure 4.9 shows the entire setup for simultaneous Mie-LIF measurements in the single cylinder optical engine. This setup was arranged so that the 355nm wavelength Nd:YAG laser was reflected onto the 45 degree laser mirrors (①), and then the laser beam was expanded to the desired dimensions through the use of the beam expander (②). Afterwards, the expanded beam hit a dichroic filter (③), where 50% of the laser beam was passed through and 50% reflected into the combustion chamber by the 45 degree mirror (④) positioned below the piston assembly. Once the fuel was illuminated by the expanded laser beam, the fluorescence signal generated followed the direction of the purple line shown on the diagram, while the elastic scattering signal was reflected at the same wavelength as that of the laser light. Because it was designed to transmit above 360nm, the dichroic filter (③) transmitted the fluorescence signal at the longer wavelength and halved the elastic scattering signal. It is noted that an image doubler (⑥) supplied by La vision was placed in front of the ICCD camera, so that both Mie and LIF images could be taken simultaneously. In addition, by using a 355nm band pass filter (⑨) on one channel of the image doubler, the Mie scattering signal could be separated from the LIF signal. In the same manner, the LIF signal was obtained by applying a 420nm long pass filter (⑩) in front of the other channel. Figure 4.10 shows the spectral response curves of the optical filters used. Consequently, Mie scattering and LIF signal were collected simultaneously.

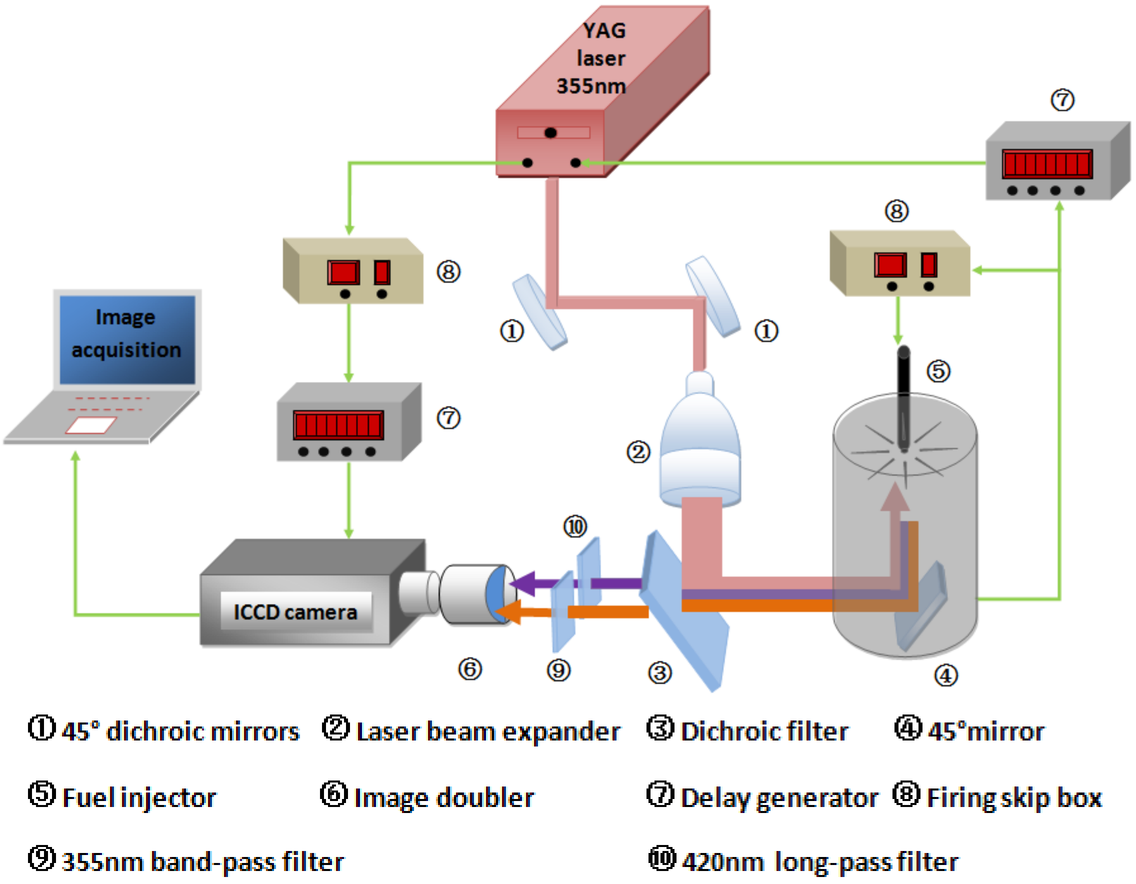

Figure 4.9 Schematic Diagram of Mie-LIF Setup

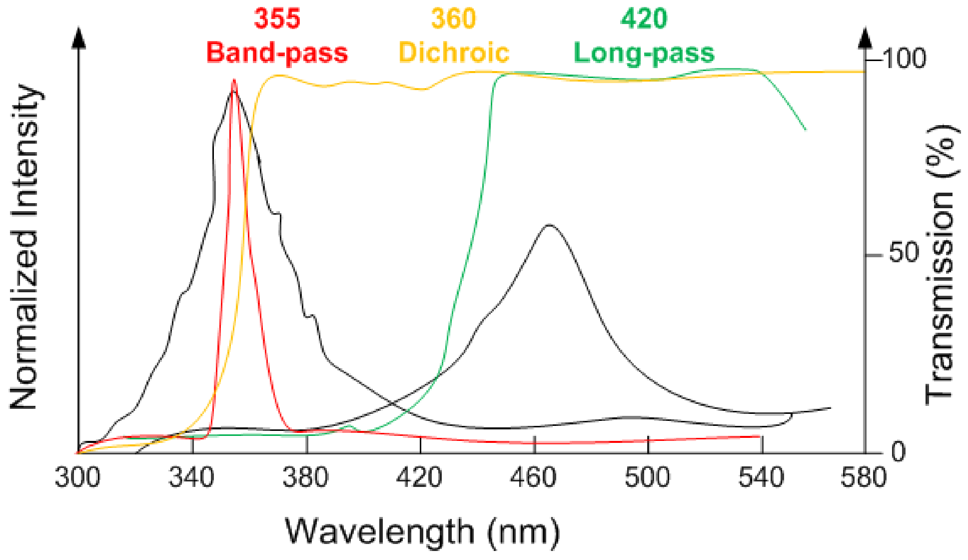

Figure 4.10 Spectral Transmission Responses of Optical Filters (manufacture book)

4.5 Complications

During the implementation of the simultaneous Mie and LIF measurements, several difficulties were experienced. In the following section, these issues are explained and the solutions for these difficulties are discussed.

4.5.1 Suppression of Reflection by Laser Light Scattering

As shown in Figure 4.11, the expanded laser beam was directed into the combustion chamber via a 45 degree mirror. The elastic scattering signal and fluorescence signal of the fuel spray were generated simultaneously by the 355nm laser light. However, further consideration should be given for the reflected scattering light from solid surfaces (the cylinder head in this case). In the LIF imaging channel, this reflected scattering light can be eliminated by utilization of the 420nm long-pass filter, while in the Mie-scattering channel, the reflected laser light could not be removed by optical filters since both of Mie signal and reflected light were at the same wavelength of 355nm. In order to minimize the reflected light in the Mie signal, the cylinder head surface needed to be blackened.

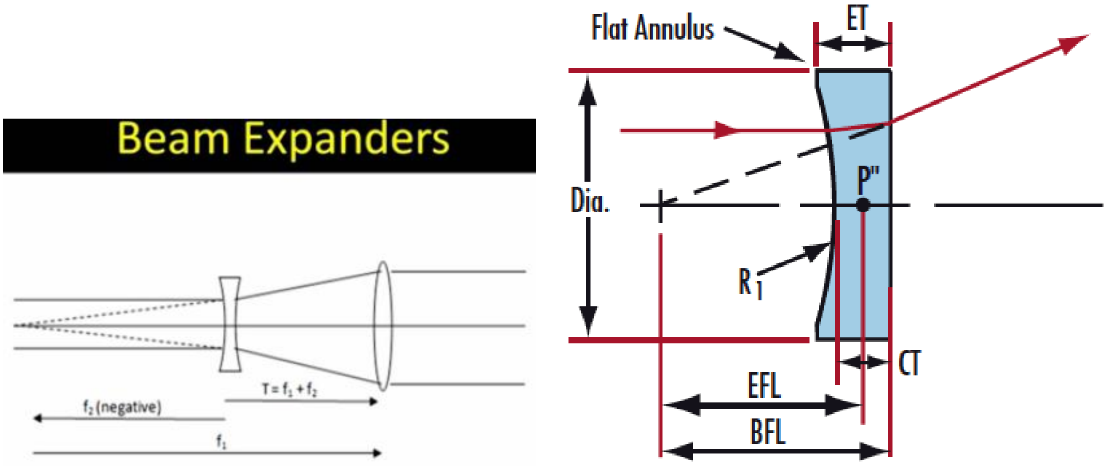

Figure 4.11 Working Principle of Beam Expander (Left) and Plano-Concave Lens (Right)

As it is unrealistic to anodize the cylinder surface anodization due to the high cost, the candle soot and high temperature paint were tried and tested. It was noted that the candle soot was more effective in suppressing the laser reflection from the cylinder surface, but the soot deposit tended to fall off from the surface and was blown away by the in-cylinder charge flow motion. After some trials and errors, it was found that the spray of high temperature black paint prior to candle soot coverage improved soot adhesion to the metal surface and prolonged the running time of candle soot coverage.

The second measure to minimise the reflected light in the recorded images involved the adjustment of laser light direction. As shown in Figure 4.11, the laser beam was originally expanded and collimated to the desired dimension of laser beam through a beam expander (diameter≈65mm). This expanded parallel laser beam directly hit the flat cylinder head was reflected black along the same optical path as the signals to the ICCD camera (Figure 4.9). By replacing the Beam Expander or placing in front of it a plano-concave lens, the expanded laser beam would be divergent so that its reflections from cylinder head were mostly out of the field of view of the imaging system.

Furthermore, the ICCD gate width was adjusted to minimise the impact of unwanted light noise in the recorded images. Since the life-time of a fluorescence signal is within a few hundreds of nanoseconds, the ICCD gate-width was set to 500 ns which resulted in the reduction of scattering light reflection.

Figure 4.12 shows the images taken before and after the measures taken to minimise the presence of reflection in the Mie scattering images.

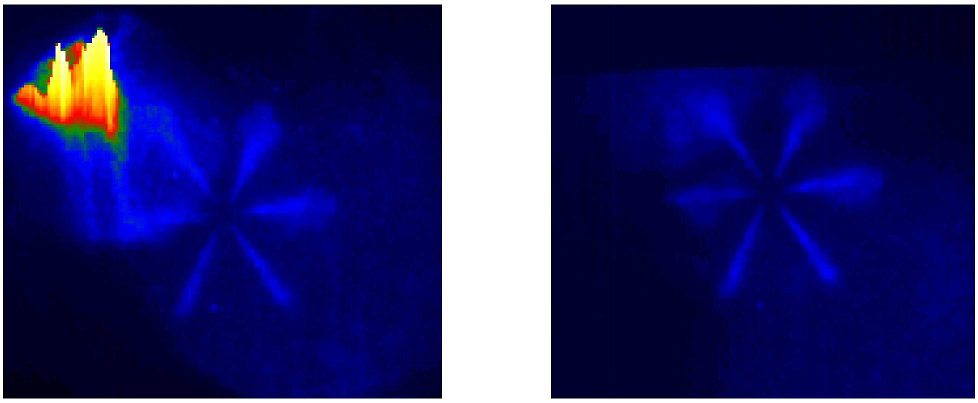

Figure 4.12 Original Mie Image (Left) and Improved Image (Right)

4.5.2 Failure of Fuel Injection Equipment

A mixture of PRF and fuel tracer biacetyl was used during the entire experiment. The considerably lower lubricity of this mixed fuel may cause mechanical failure of the diesel injection system. Additionally, the fuel tracer biacetyl deposits on the inner surface of fuel rail. In order to overcome these issues, a fuel additive named OLI9900 was added into the PRF to lubricate the diesel injector. However, no solution can be found to avoid the biacetyl deposition. Daily fuel line flushing was needed to minimize fuel line components fouling.

4.6 Data Analysis

An image processing programme based on LabView was developed to analyse the Mie and LIF images. In order to remove unwanted background noise, a background remove programme was used to obtain the pure fuel spray image. As shown in Figure 4.13, the fuel spray image is clearly displayed by subtracting the background image from the original image. After the noise was removed, it was necessary to extract the vapour signals from Mie and LIF images. In a similar manner, a Mie-LIF subtraction programme was developed by the author.

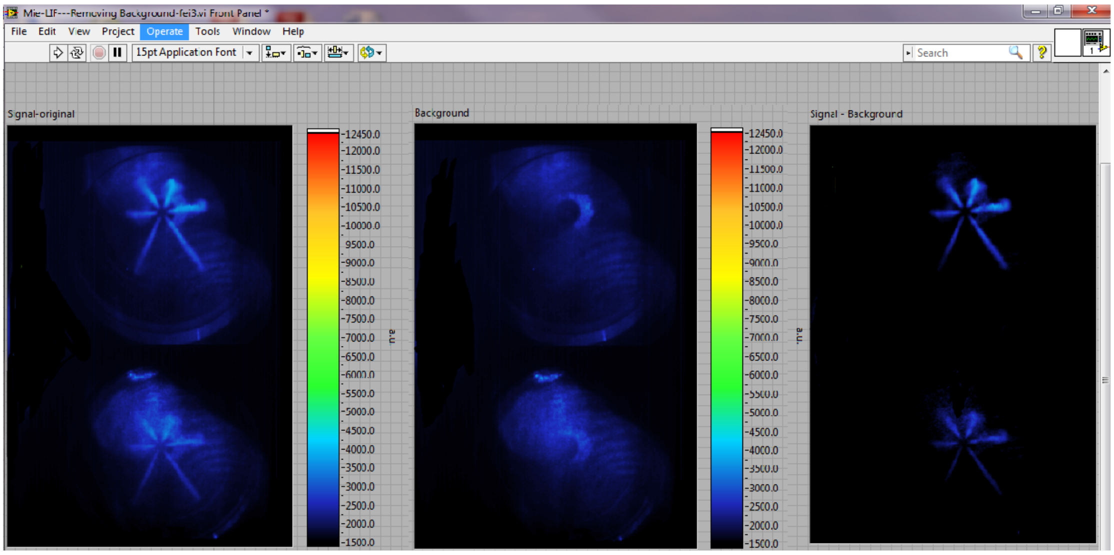

Figure 4.13 Background Removal Programme

4.7 Summary

In this chapter, the fundamentals and implementation of simultaneous Mie-LIF techniques were described in detail. The explanations of the laser device, imaging system and optical setup were given. Synchronization with fuel injection, laser light and image data acquisition were discussed. Most importantly, the optical set up for simultaneous Mie-LIF was presented. In addition, the quality of image data was improved by introducing different techniques. Furthermore, the procedure for post image data processing was described.

CHAPTER 5

Thermodynamic Analysis of Gasoline PPC (Partially Premixed Combustion)

5.1 Introduction

In order to get better understanding of gasoline PPC combustion, systematic engine experiments were carried out on the single cylinder common rail DI diesel engine with optical access. A detailed description is given to each test condition, injection strategies and the test plan prior to the discussion of results. For all the engine tests, in-cylinder pressure data were recorded from which heat release rates were calculated. In addition, both gaseous pollutant emissions and soot concentrations were measured and presented.

5.2 Experiments

All the experiments were performed on the single cylinder common rail direct injection (DI) diesel engine. The details of the engine are presented in Chapter 3. During these experiments, the piston window was replaced with a metal blank in order to achieve more extended period of fired engine operation.

5.2.1 Test Conditions

Substantial preliminary engine tests had been carried out to determine the relative air/fuel ratio (Lambda), EGR and the primary reference fuel (PRF), which would be required to achieve stable partially premixed combustion (PPC). The preliminary results had shown that PPC was sensitive to lambda and EGR for a given PRF. For the engine speed and load conditions to be tested, it was found that PRF70 exhibited most stable combustion at λ=2.3 and EGR=22%. Based on the preliminary investigation, the test condition of the experimental work was then determined, as shown in Table 5.1, and the details are as follows.

Engine Speed: Engine speed was maintained at 1500rpm throughout the experiments. This speed was chosen as a typical of low/medium speed HSDI diesel engine operation. In addition, this engine speed could be readily achieved when the engine was operated with optical windows. When the high speed camera is working at a frequency of 10,000 frames per second, the video images will have a temporal resolution of 0.9 °CA per frame.

Table 5.1 Test Conditions

	A	B	C	D	E	F
Injection strategy (%)	50:50	70:30	30:70	50:50	70:30	10:90
Fuel (vol %)	70% isooctane + 30% heptane					Diesel
Injection pressure (bar)	1200			900		1200
Injection quantity (mm^3)	21.77					18.82
Intake Temperature (°C)	150					100
Engine Speed (rpm)	1500					
Intake Pressure (bar)	1.335					
EGR (%)	22 (N_2)					
λ	2.3					
Load	68% of full load of NA operation					

Intake Condition: Intake air was boosted by 0.335bar using the supercharger in order to achieve the desired air/fuel ratio. Intake temperature was set and maintained at approximately 150 °C for PRF cases while 100 °C for diesel cases by means of the intake air heater. The higher intake temperature was needed for gasoline PPC in order to reach auto-ignition temperature. In addition, it is to compensate for relatively lower engine temperature when the engine was running with optical windows.

Fuel: All the experiments in this chapter were performed by reference fuel with an octane number of 70. The fuel was made of Isooctane (octane ranking 100) and Heptane (octane ranking 0) by volume. The fuel quantity of 21.77mm^3 was selected for PPC studies while 18.82mm^3 was used for diesel baseline studies so that identical fuel energy was provided for PPC and diesel operations. Since a diesel fuel injector was utilized by different types of fuels throughout all experiments, a fuel additive called OLI9900 was added into PRF to lubricate the diesel injector. In accordance with the advice by the supplier, the concentration of additive was fixed within the range of 100-200mg/Litre.

Injection Pressure: The fuel injection system in this study is capable of providing up to 1600bar injection pressure. However, 1200 bar injection pressure was adopted in the experiments as a typical injection pressures in product engines. 900 bar injection pressure was used for PPC cases in order to identify the effect of injection pressure on mixing process of the more volatile PRF.

Lambda: The lambda value was kept constant at 2.3 throughout experiments. The lambda calculation was based on fuel quantity calibration and air flow measurement. In order to check and correct for any measurement error, the composition of exhaust gases was analysed to inversely calculate lambda. The detailed arithmetic process was explained in Chapter 4.

EGR: 22% EGR rate was used for all of the experiments and pure Nitrogen gas was applied.

Load: Compression ignition engine load is determined by the injected fuel quantity. The fuelling rate of full load engine operation at lambda of 1.7 is approximately 27.69mm^3/cycle at 100 ℃ of intake temperature and 1500rpm of engine speed. In this study, the fuel rate was set at 21.77mm^3/cycle which corresponds to approximately 68% of full load naturally aspirated operation. It is worth noting that 21.77mm^3/cycle was the fuelling rate with PRF70 (primary reference fuel with octane number of 70) fuel and it equates to 18.82mm^3/cycle of diesel fuel of the same total heating value.

Piston Bowl: A flat glass piston bowl was used for in-cylinder pressure measurements and all the optical techniques applied in this research work. The exhaust emission measurement was carried out by a metal piston blank in order to preserve the glass window.

5.2.2 Injection strategies

The injection strategies were divided into two categories, 900bar and 1200bar. The purpose for setting up 1200bar injection pressure was to have identical injection parameters as the diesel baseline experiments so that their combustion characteristics and emission results could be compared. The 900bar injection pressure was chosen for reducing surface wetting caused by fuel injection impingement as well as to detect the changes on fuel evaporation process when different injection pressure was employed. All the strategies were carried out by adjusting the injection pulse width to the desired total fuel demand of 21.77mm^3 (PRF) and 18.82 mm^3 (diesel), respectively.

Based on the preliminary experiments, the injection strategies for gasoline type fuel PPC experiments were formulated as follows:

- Two injections were applied to all the experiments. The first injection took place during the compression stroke to produce a premixed air-fuel mixture, while the second injection occurred around TDC to trigger the start of combustion. Injections of both equal quantity and varied quantities of each injection were examined.
- In the case of equal fuel injection quantity for the first and second injections, theoretically identical injection quantity would be expected for the first and second injections when the fuel injection pulse width was set to the same duration. However, measurements performed on a fuel injection rig showed that slight adjustment for second injection duration was needed to have exactly 50% of total fuel injection quantity, due to pressure wave influence in the fuel rail.
- In the cases of variable fuel injection quantity distribution for the first and second injection, 70:30 and 30:70 injection quantity strategies were used on 1200bar injection pressure case. While only 70:30 was tested for 900bar injection pressure case. 70:30 strategy means that 70% of total amount fuel was injected in the first injection and rest of fuel was injected for the second injection. In the latter case, 30% and 70% of injection quantity were set for the first and second injection, respectively.
- The effect of fuel injection timing was investigated by firstly adjusting the second fuel injection timing whilst the first injection timing was kept constant. Then variable first injection timings were tested for a given second injection timings that produced the best bsfc and least emissions.

It is noted that experiment points and results might not be most optimized in this research work due to the limited operational time of the optical engine. But the chosen tests and strategies will provide the better understanding of the gasoline type fuel PPC operations and the effects of fuel injection parameters, which would enable further improvement and detailed development works to be effectively carried out.

In Figure 5.1, the tested points for all gasoline PPC strategies have been plotted as a function of the first and second injection timings. It is noted that the A (AA, AAA), B (BB, BBB) and C (CC, CCC) represent the fuel quantity split strategy of 50:50, 70:30

and 30:70, respectively; while D (DD, DDD) series used 50:50 fuel quantity split, and E (EE, EEE) series applied 70:30 strategy.

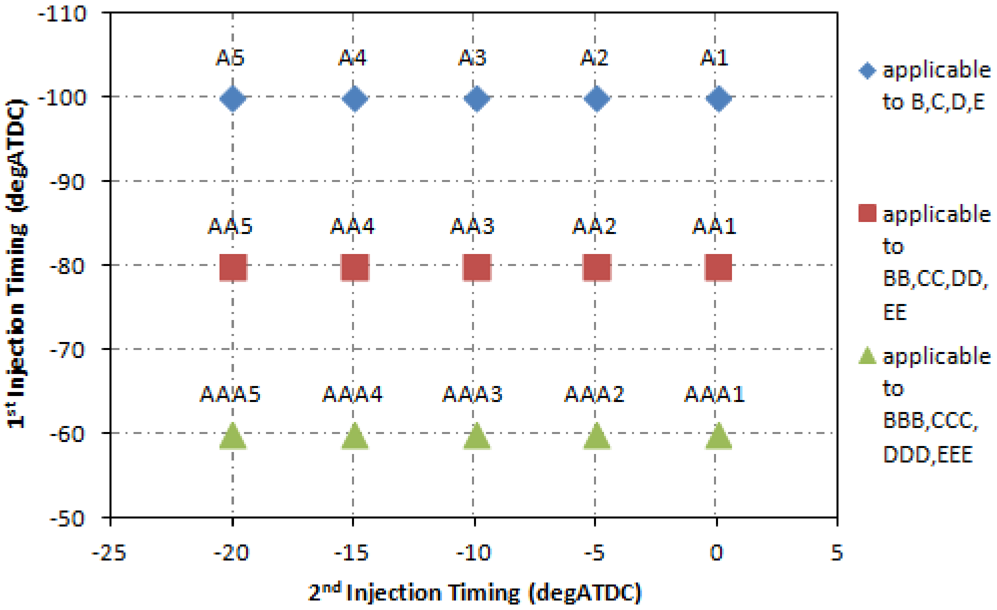

Figure 5.1 Gasoline PPC Injection Strategy

5.2.3 Test Plan

All the strategies were run at two different injection pressures of 900 bar and 1200 bar, respectively. In-cylinder pressure data were taken and IMEP, heat release rate as well as combustion characteristics were subsequently calculated by the methods described in data analysis section 3.7. In addition, exhaust gas and soot emission were measured with the metal piston blank for all strategies. Analysis of the in-cylinder pressure, heat release rate and IMEP led to the selection of better performance strategies for the subsequent high speed combustion image analyses and simultaneous liquid and fuel vapour measurement by the Mie and LIF techniques. Table 5.2 summarises the tests performed for each strategy.

Table 5.2 Test Plan

Test number			In-cylinder pressure	Emissions & soot	High speed imaging	Mie & LIF imaging
A1	AA1	AAA1	√	√		
A2	AA2	AAA2	√	√	√	√
A3	AA3	AAA3	√	√		
A4	AA4	AAA4	√	√		
A5	AA5	AAA5	√	√		
B1	BB1	BBB1	√	√		
B2	BB2	BBB2	√	√	√	√
B3	BB3	BBB3	√	√		
B4	BB4	BBB4	√	√		
B5	BB5	BBB5	√	√		
C1	CC1	CCC1	√	√		
C2	CC2	CCC2	√	√		
C3	CC3	CCC3	√	√		
C4	CC4	CCC4	√	√		
C5	CC5	CCC5	√	√		
D1	DD1	DDD1	√	√		
D2	DD2	DDD2	√	√	√	√
D3	DD3	DDD3	√	√		
D4	DD4	DDD4	√	√		
D5	DD5	DDD5	√	√		
E1	EE1	EEE1	√	√		
E2	EE2	EEE2	√	√	√	√
E3	EE3	EEE3	√	√		
E4	EE4	EEE4	√	√		
E5	EE5	EEE5	√	√		
F1	FF1	FFF1	√	√		
F2	FF2	FFF2	√	√	√	√
F3	FF3	FFF3	√	√		
F4	FF4	FFF4	√	√		
F5	FF5	FFF5	√	√		

5.2.4 Data Processing and Analysis

In the experimental results, the IMEP values were calculated from in-cylinder pressure data. The start of combustion (CA10) and combustion phasing (CA50) were determined from the 10% and 50% mass fraction of fuel burned, respectively. The combustion duration was defined as the number of crank angles between 10% and 90% of mass fraction of fuel burned. The ignition delay was determined by the crank angle between the start of 2nd injection (SOI) and onset of combustion (CA10).

The exhaust gas and soot emissions were measured for all the strategies. The NOx and uHC emissions were measured in Parts per Million (ppm), while soot emission was measured in Filtered Smoke Number (FSN) by an AVL smoke meter.

5.3 Gasoline Partially Premixed Combustion at Injection Pressure of 1200bar

The effect of injection timings on partially premixed combustion of gasoline type fuel their and exhaust emissions were investigated at an injection pressure of 1200bar. The split of two injections was varied as 50:50, 70:30 and 30:70, respectively. The In-cylinder pressure, IMEP, combustion characteristics and exhaust gas emission results will be discussed and compared to the baseline diesel combustion operations.

5.3.1 In-Cylinder Pressure and Heat Release Rate Analysis for Strategy AA (50:50 fuel distribution with fixed 1st injection timing at -80 °CA ATDC)

In order to illustrate the effect of 2nd injection timing, only results from AA test cases will be analysed in detail as they show similar trends with the other cases with earlier (A series) and retarded (AAA series) first injections and they also produce the least emissions.

The in-cylinder pressure results for strategy AA averaged over 20 consecutive cycles are presented in Figure 5.2. The in-cylinder pressure trace for strategy AA1 increased gradually to its peak value at TDC, and decreased smoothly afterwards until 12.6 °CA ATDC. From this point, the decrease rate of in-cylinder pressure slowed down due to heat release from combustion. After lasting for approximately 10 °CA, the in-cylinder pressure trace then decreased steadily after 21 ° CA ATDC during the rest of expansion stroke. Strategy AA1 had an IMEP value of 2.76 bar.

The in-cylinder pressure trace for strategy AA2 followed the pressure curve of strategy AA1 until TDC, and increased at a higher rate to its peak value of 56.4 bar at 11.4 ° CA ATDC. A much higher in-cylinder pressure can be observed for strategy AA2 compared to strategy AA1. This was mainly attributed to the advanced 2nd injection timing, which shifted the combustion event closer to TDC where combustion was taking place in a smaller volume. After this peak point, the in-cylinder pressure line decreased smoothly during the rest of the expansion stroke. Strategy AA2 produced an IMEP value of 2.87 bar.

In-cylinder pressure in Strategy AA3 followed the same curve as the AA1 and AA2 until TDC. The pressure subsequently increased sharply to the maximum value of 57.5 bar at 10.8 ° CA ATDC, which was 1.1 bar higher and 0.6 ° CA earlier than strategy AA2. The higher combustion pressure and earlier combustion phasing (CA50) were caused by further advanced 2nd injection timing. This case produced an IMEP value of 2.82 bar.

The in-cylinder pressure traces for strategies AA4 and AA5 followed the pressure line of previous strategies until -5.2 ° CA ATDC and then increased rapidly to the same peak pressure of 68.2 bar at 4.4 ° CA ATDC and 4 ° CA ATDC, respectively. These peak pressures took place approximately 6 ° CA before strategy AA3 due to advanced 2nd injection timing. Moreover, they were 10.7 bar higher than strategy AA3 as the earlier combustion event commenced closer to TDC. After those peaks, the in-cylinder pressure curves for strategy AA4 and AA5 decreased with identical trends during the rest of expansion stroke. Strategy AA4 and AA5 produced IMEP values of 2.42 and 2.28 bar, respectively.

The heat release rate for strategies AA1 to AA5 are depicted in Figure 5.3.The heat release rate for strategy AA1 increased gradually until 0.2 °CA ATDC and then suffered a noticeable reduction due to the charge cooing effects caused by 2nd fuel injection event. It lasted for approximately 6 ° CA and subsequently increased again to its peak value of 20.4 J/deg at 16.6 ° CA ATDC. The first small increment in the heat release rate was derived from the partial combustion by the pre-injected fuel while the last rise of the heat release rate was a result of combustion of all charges trigger by the second injection. Finally, the heat release rate decreased smoothly during the rest of the expansion stroke. It was noted that tiny diffusion combustion sign could be detected at the end of premixed combustion even though it was difficult to distinguish these two combustion phases from the heat release data.

The heat release rate for strategy AA2 had a minor decrease at -4 °CA ATDC due to the charge cooling effect caused by the start of the 2nd injection and heat transfer effect within compression stroke which lasted until -0.2 ° CA ATDC. The heat release rate subsequently increased rapidly to its top value of 38.5 J/deg at 8.8 °CA ATDC because of premixed combustion. The maximum heat release rate for this strategy took place approximately 7.8 ° CA before strategy AA1 as the 2nd injection timing was brought forward. After this peak point, the heat release rate line decreased sharply until 17 °CA ATDC and then a minor raise can be seen immediately as the evidence of diffusion combustion. Finally, the rate of heat release line decreased smoothly during the rest of expansion stroke.

The heat release rate for strategy AA3 experienced a relatively slow rising period which lasted for approximately 4 °CA. This was again attributed to the charge cooling effect by the 2nd injection as well as heat transfer effect. It subsequently increased rapidly to the peak value of 42.9 J/deg at 7.2 °CA ATDC which was 1.6 °CA before strategy AA2 because of the further advanced 2nd injection timing. After this point, the heat release rate curve decreased dramatically until 14.8 ° CA ATDC and a small bump appeared afterwards lasted for approximately 5 °CA. That was recognized as a small amount of diffusion combustion following the premixed combustion. Eventually, the rate of heat release line gradually decreased during the rest of the expansion stroke.

The heat release rate for strategies AA4 and AA5 were showing similar trend with a drop at -8.4 ° CA ATDC due to the charge cooling and heat transfer effects. Subsequently, those two heat release rate lines increased sharply to their peak values of 45.2 and 44.2 J/deg, at 0.6 and -1 °CA ATDC, respectively. The maximum heat release rate values were achieved in strategies AA4 and AA5 as combustion event commenced at the end of the compression stroke when the cylinder volume was at its minimum. Accordingly, the shortest combustion duration and ignition delay were obtained in strategies AA4 and AA5 compared to previous strategies. Afterwards, the heat release rate lines decreased rapidly until zero without apparent sign of diffusion combustion during the rest of expansion stroke.

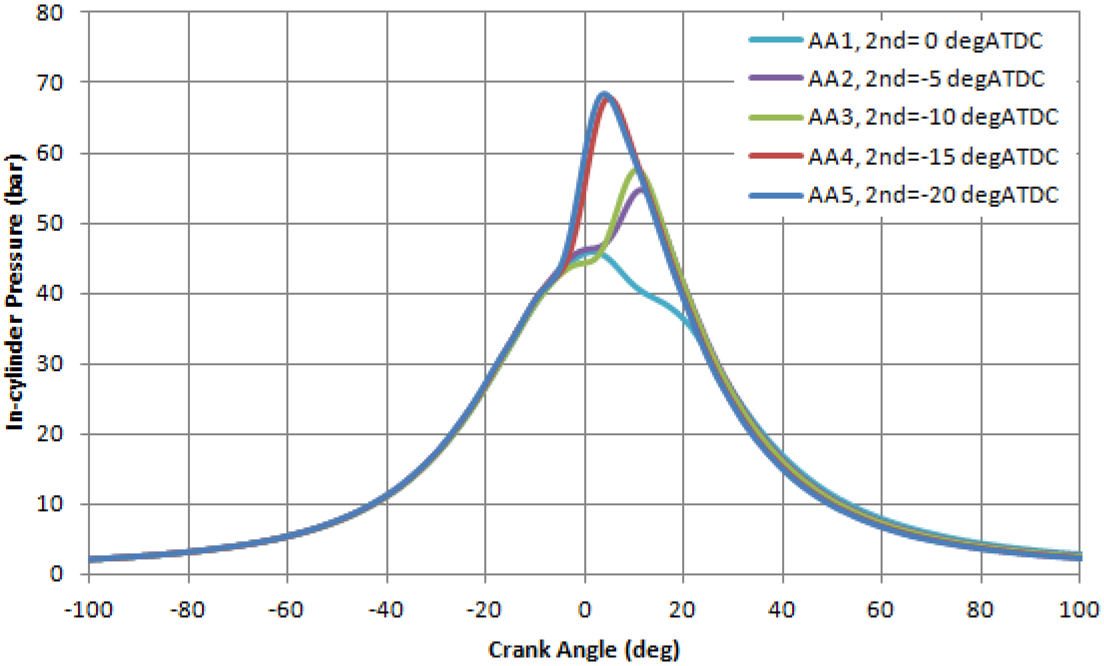

Figure 5.2 In-Cylinder Pressure Traces for Strategy AA (1st injection timing=-80 degATDC)

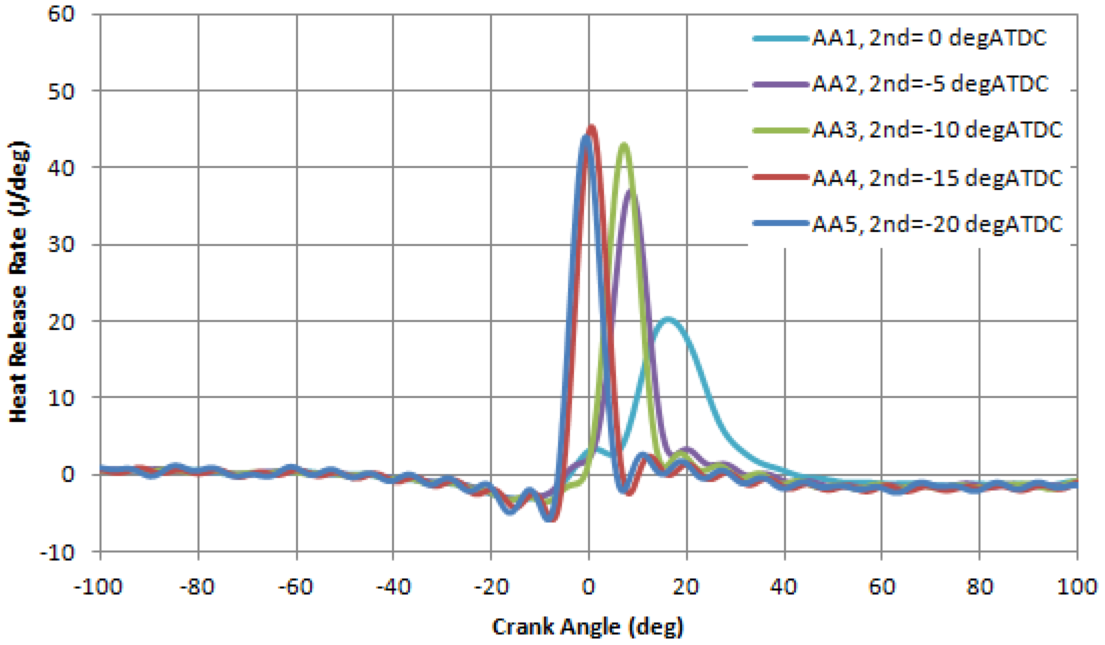

Figure 5.3 Heat Release Rate Traces for Strategy AA (1st injection timing=-80 degATDC)

5.3.2 Analysis of the Effect of Injection Timings on Performance and Combustion of 50:50 Double Injection at 1200 bar Injection Pressure

The effect of injection timings (strategies A, AA and AAA) on IMEP is shown in Figure 5.4. The IMEP reached a peak value of 2.8 bar in the top right region when the start of 1st injection timing occurred within the range of -100 to -80°CA ATDC and 2nd injection timing between -10 to 0°CA ATDC. At early 1st injection timings of -80 and -100°CA ATDC, the IMEP value increased slightly from 2.4 bar to 2.8 bar as 2nd injection was retarded towards TDC. When 1st injection was retarded to -60°CA ATDC, the IMEP became lower. In addition, the effect of 2nd injection timing became more pronounced at this retarded 1st injection. As shown in the lower right region, the IMEP value reached its peak and started to decrease once 2nd injection timing was getting closer to TDC for the retarded 1st injection timing. Since the start of combustion (SOI) and combustion phasing (CA50) would be determined by the temporal history and spatial distribution of the fuel/air mixture and temperature, the results suggest that the more homogeneous mixture formed by the earlier 1st injection was desirable for increased fuel conversion efficiency. In order to better explain such results, further analyses of combustion characteristics, emissions and in-cylinder mixture diagnostics would be required.

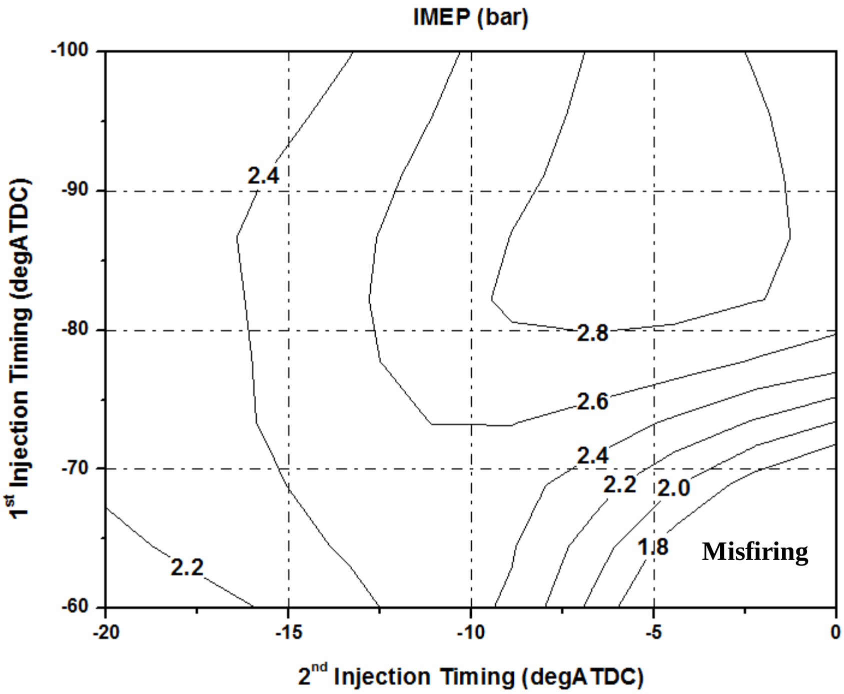

Figure 5.4 IMEP of 50:50 Fuel Distribution at 1200 bar Injection Pressure

The combustion phasing (CA50) and combustion duration (CA10-CA90) for the 50:50 double injection strategies A, AA and AAA are plotted in Figure 5.5. The combustion phasing (CA50) was retarded from 2°CA ATDC to 14°CA ATDC when 2nd injection timing was retarded close to TDC at 1st injection timings of -100 to -80°CA ATDC. In contrast, for the late 1st injection timing, CA50 exhibited more retarded timings as 2nd injection timing was retarded to -5 °CA ATDC. The combustion duration (CA10-CA90) shown in Figure 5.6 had a similar trend as CA50. At early 1st injection timings, combustion duration gradually increased to 17°CA ATDC when 2nd injection timing was closed to TDC. While for late 1st injection timing cases the combustion duration reached its longest duration at 5°CA ATDC 2nd injection timing. The retarded 1st injection timing prolonged the combustion duration because insufficient mixing process occurred when fuel was injected late. Ignition delay defined by the crank angles between start of 2nd injection (SOI) to 10% mass fraction burned (CA10) for strategy A, AA, and AAA are shown in Figure 5.7. Generally, the ignition delay was shortened when 2nd injection timing was closer to TDC when the charge temperature was higher. 1st injection timing did not have obvious effects on the ignition delay at most of cases apart from a few late injection timing strategies.

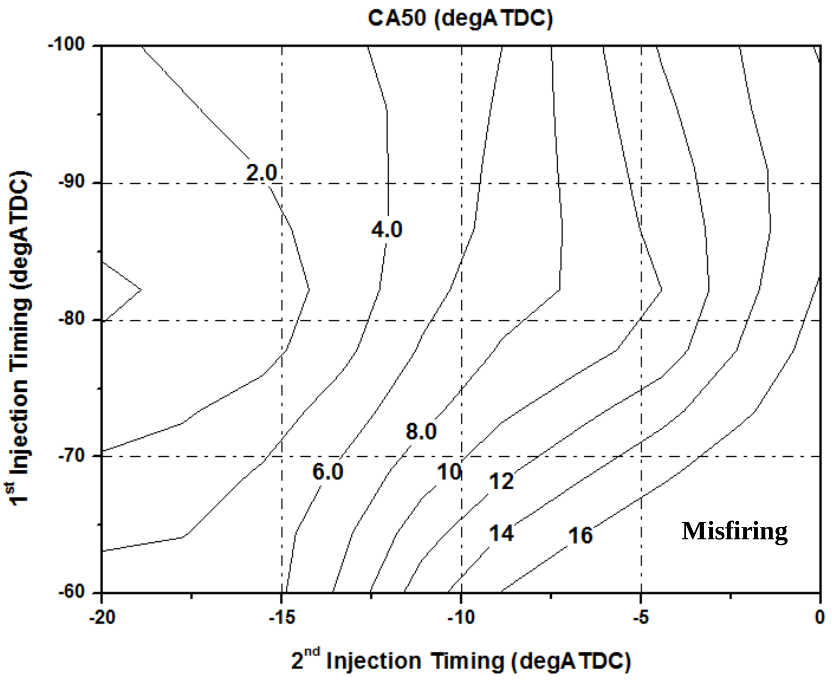

Figure 5.5 Combustion Phasing (CA50) of 50:50 Fuel Distribution at 1200 bar Injection Pressure

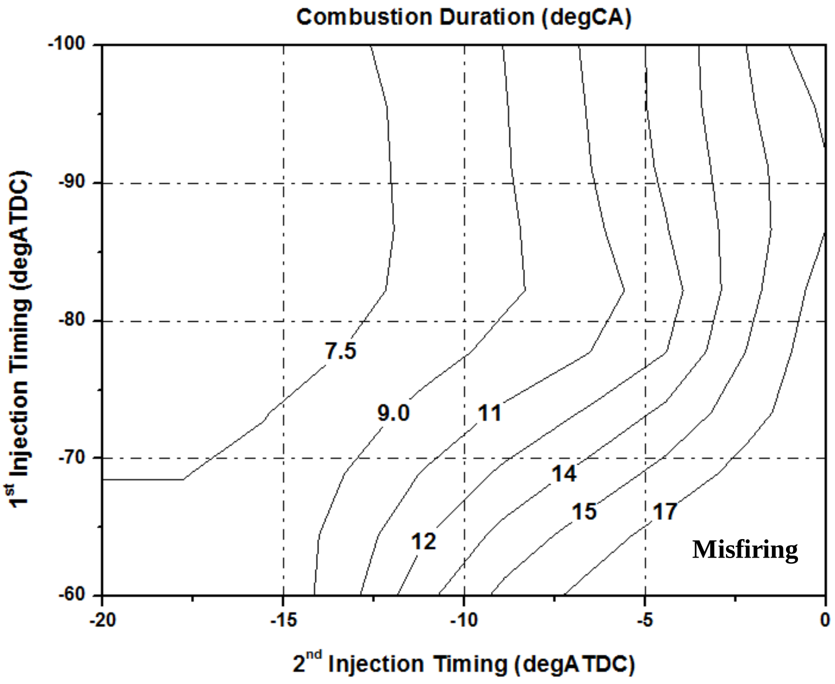

Figure 5.6 Combustion Duration (CA10-CA90) of 50:50 Fuel Distribution at 1200 bar Injection Pressure

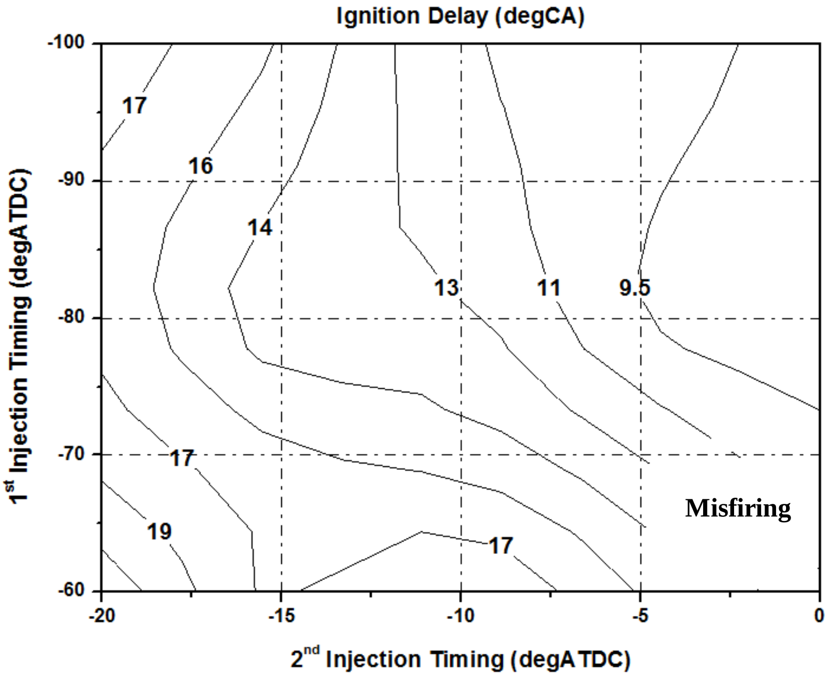

Figure 5.7 Ignition Delay (SOI_{2nd}-CA10) of 50:50 Fuel Distribution at 1200 bar Injection Pressure

The efficiencies as a function of injection timings are discussed in following section. As shown in Figure 5.8, the combustion efficiency was improved by advancing 2nd injection timing due to reduced uHC and CO emissions. Adequate combustion process was achieved thanks to higher combustion pressure and temperature attributed to early 2nd injection timing resulted in lower uHC and CO emissions. The combustion efficiency slightly decreased as 1st injection timing was retarded at fixed 2nd injection timing owing to increased uHC and CO emissions caused by reduced combustion temperature. Thermal efficiency in Figure 5.9 indicated improved results when 1st injection timing was set at the early stage of the compression stroke with 2nd injection timing closed to TDC. Apart from this optimized area, the thermal efficiency deteriorated by retarded 2nd injection timing when 1st injection timing was constant. For early 2nd injection strategies, thermal efficiency was not much affected by injection timings. The indicated efficiency was demonstrated in Figure 5.10 which produced similar profile as thermal efficiency but with lower values since combustion efficiency was taken into account.

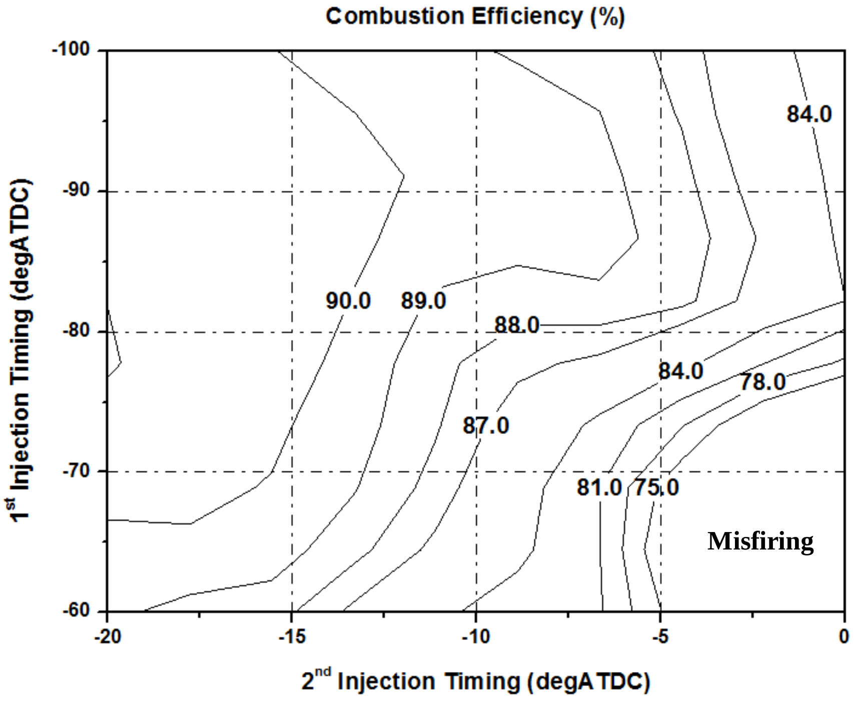

Figure 5.8 Combustion Efficiency of 50:50 Fuel Distribution at 1200 bar Injection Pressure

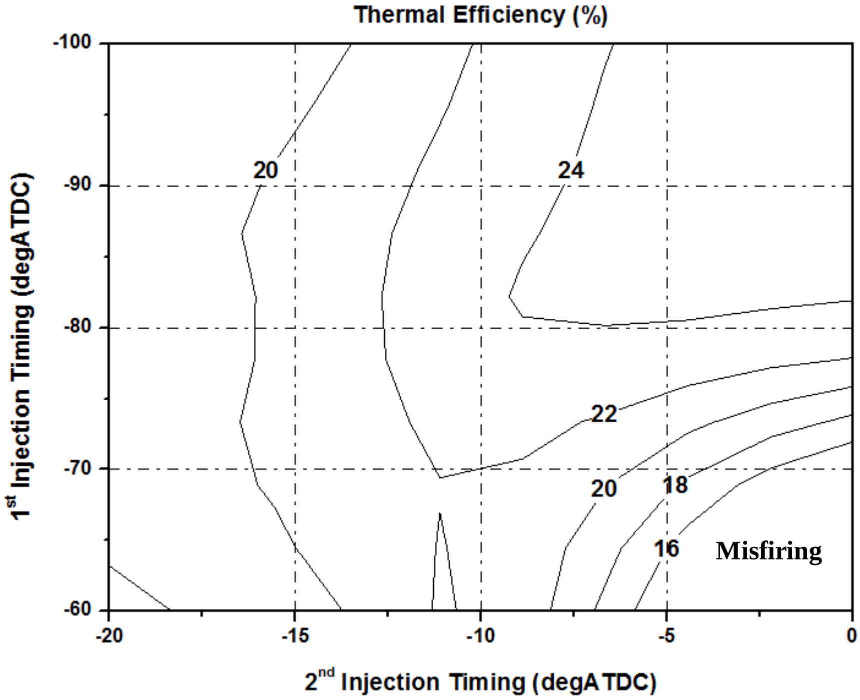

Figure 5.9 Thermal Efficiency of 50:50 Fuel Distribution at 1200 bar Injection Pressure

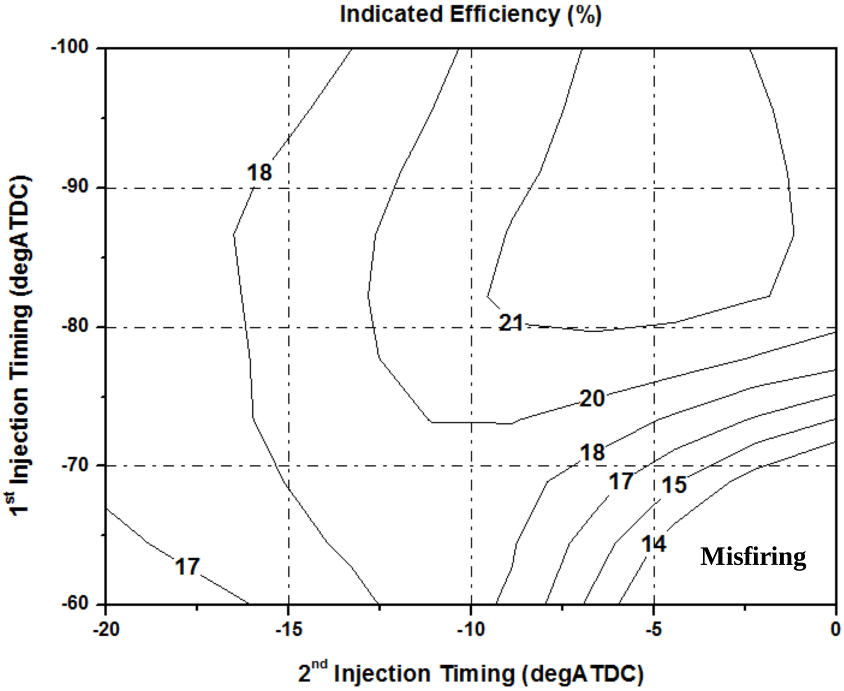

Figure 5.10 Indicated Efficiency of 50:50 Fuel Distribution at 1200 bar Injection Pressure

5.3.3 Analysis of the Effect of Injection Timings on Emissions of 50:50 Double Injection at 1200 bar Injection Pressure

The exhaust emissions and soot concentrations as a function of injection timings were measured for the 50:50 double injections and are discussed in this section. As shown in Figure 5.11, uHC emissions stayed at fairly high level owing to incomplete combustion of gasoline PPC combustion. The higher uHC emissions could be caused by the slowed oxidation rate due to lower combustion temperature in the presence of EGR. In addition, early 1st injection increased the propensity of wetting wall (the wall-wetting effect), which would be studied by the in-cylinder LIF and Mie scattering measurements. Furthermore, some of the premixed mixture from 1st injection could be too lean to be burned (the over-mixing effect). The uHC emissions increased considerably when 2nd injection timing was closed to TDC, because of the presence of fuel rich regions (the under-mixing effect) after the start of combustion when the ignition delay became shorter. The uHC emissions exhibited slight deterioration when 1st injection timing was retarded with fixed 2nd injection timing, probably due to less homogeneous mixture formation from 1st injection.

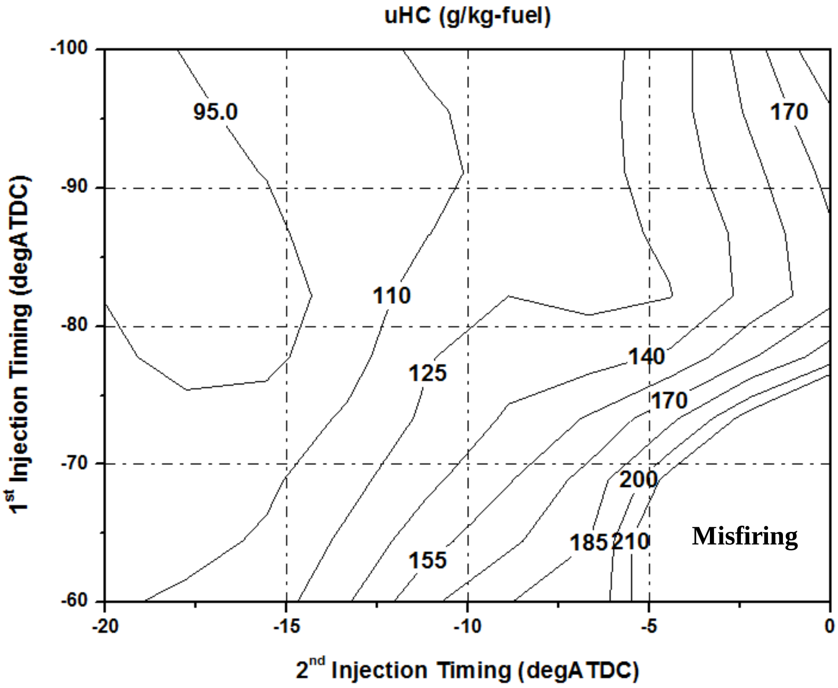

Figure 5.11 uHC Emissions of 50:50 Fuel Distribution at 1200 bar Injection Pressure

NOx emission level is mainly determined by surrounding temperature and availability of excessive oxygen when combustion takes place. As shown in Figure 5.12, NOx emissions were maintained at very low levels since low combustion temperature and lean oxygen condition were achieved due to effect of recirculated exhaust gas. The NOx emissions gradually increased to a maximum value of 3.3 g/kg-fuel when 2nd injection timing was advanced. This was mainly attributed to earlier injection timing led combustion to take place closer to TDC at higher in-cylinder pressure and temperature. In contrast, 1st injection timing has little effect on NOx emissions in most regions except the earliest 2nd injection regions where the mid 1st injection produced slightly higher NOx emission, when the NO formation would be more sensitive to the local AFR at higher combustion temperature due to advanced combustion timing (Figure 5.5) and faster combustion (Figure 5.6).

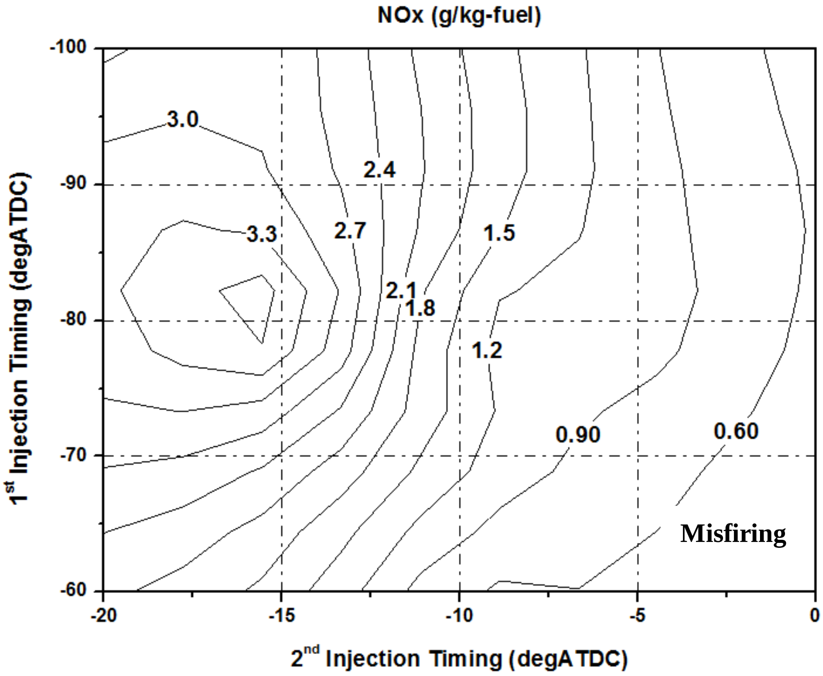

Figure 5.12 NOx Emissions of 50:50 Fuel Distribution at 1200 bar Injection Pressure

As shown in Figure 5.13, near zero soot emissions were obtained for all strategies thanks to gasoline PPC combustion. First of all, the excellent fuel evaporation characteristics of gasoline type fuel were expected (to be verified by the in-cylinder studies) to substantially promote the formation of homogeneous mixture as fuel rich regions due to poor atomization and evaporation were minimized. Secondly, the auto-ignition resistance of the higher octane fuel resulted in a longer ignition delay so that sufficient fuel-air mixing preparation period could be obtained before combustion took place. Figure 5.13 shows that retarded 1st injection timings reduced soot emissions, probably caused by the faster evaporation at higher in-cylinder temperature and less liquid impingement due to higher charge density in the later compression stroke. 2nd injection timings had no obvious effect on the soot emissions.

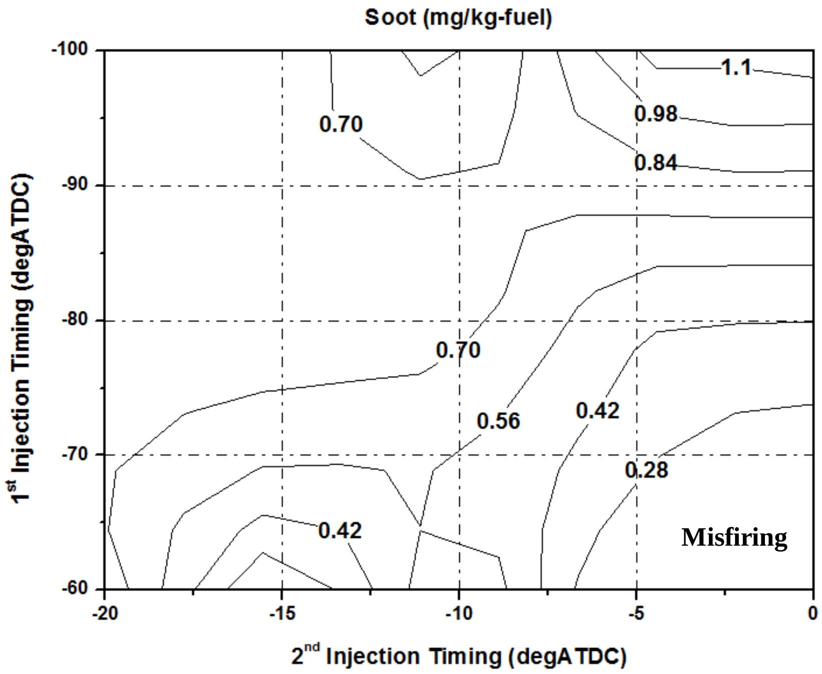

Figure 5.13 Soot Emissions of 50:50 Fuel Distribution at 1200 bar Injection Pressure

5.3.4 In-Cylinder Pressure and Heat Release Rate Analysis for Strategy BB (70:30 fuel distribution with fixed 1st injection timing at -80 °CA ATDC)

The in-cylinder pressure results for strategy BB averaged over 20 consecutive cycles are presented in Figure 5.14. In strategy BB, 70% of total fuel was injected early during 1st injection while the rest of fuel was injected around TDC as 2nd injection. As shown in Figure 5.14, the in-cylinder pressure of strategy BB1 increased steadily until 0.8 °CA ATDC when the rate of pressure rise decreased suddenly. At approximately 12 ° CA ATDC, the pressure picked up rapidly to its peak value of 53.2 bar at 13.2 °CA ATDC due to premixed combustion. The temporal change in the in-cylinder pressure can be explained by the two stages of heat release process. The first part of the pressure rise between 0.8 ° CA ATDC and 12 ° CA ATDC was associated with the slower autoignition reactions of premixed lean mixtures from 1st fuel injection event. The auto-ignition of 2nd injection fuel caused the more rapid pressure rise just before the peak cylinder pressure. The pressure curve afterwards decreased smoothly during the rest of expansion stroke. Strategy BB1 had an IMEP value of 2.99 bar.

The in-cylinder pressure trace for strategy BB2 followed the pressure trend of strategy BB1 until TDC point and accelerated to reach its peak value of 59 bar at 9.2 ° CA ATDC due to premixed combustion. The peak pressure in strategy BB2 took place approximately 4 ° CA before strategy BB1 as well as about 10% higher. This was mainly because advanced 2nd injection timing pushed combustion process towards TDC resulting in higher combustion pressure. The in-cylinder pressure trace steadily declined following the same trend as strategy BB1 during the rest of the expansion stroke. This case produced 2.64 bar IMEP.

Similarly, the in-cylinder pressure traces for strategy BB3 and BB4 followed pressure lines of previous strategies before TDC and rapidly reached their peak pressures at 6.4 and 6.1 ° CA ATDC, respectively. Both strategies had a maximum in-cylinder pressure of 63.3 bar. These two strategies produced nearly identical in-cylinder pressure profiles and combustion events despite the different 2nd injection timings. These two strategies had IMEP values of 2.62 and 2.24 bar.

The in-cylinder pressure for strategy BB5 produced highest and most advanced pressure profile. It again followed the pressure lines of previous strategies until -5.2 ° CA ATDC and climbed up sharply to the maximum pressure of 64.4 bar at 5.4 ° CA ATDC. The earliest 2nd injection timing contributed to this higher in-cylinder pressure profile as onset of combustion process was placed at TDC. The in-cylinder pressure decreased gradually after peak point during the rest of expansion stroke and produced an IMEP value of 2.28 bar.

The heat release rate traces for strategy BB1 to BB5 are depicted in Figure 5.15. The heat release rate for strategy BB1 increased steadily to its first peak at -2.6 ° CA ATDC due to fuel energy release by 1st injection event. After a few crank angles, the heat release rate rose again reaching a peak value of 24.7 J/deg at 9.4 ° CA ATDC due to the premixed combustion caused by 2nd fuel injection. The heat release rate curve fell gradually until 17.6 ° CA ATDC when the slower diffusion combustion became more apparent.

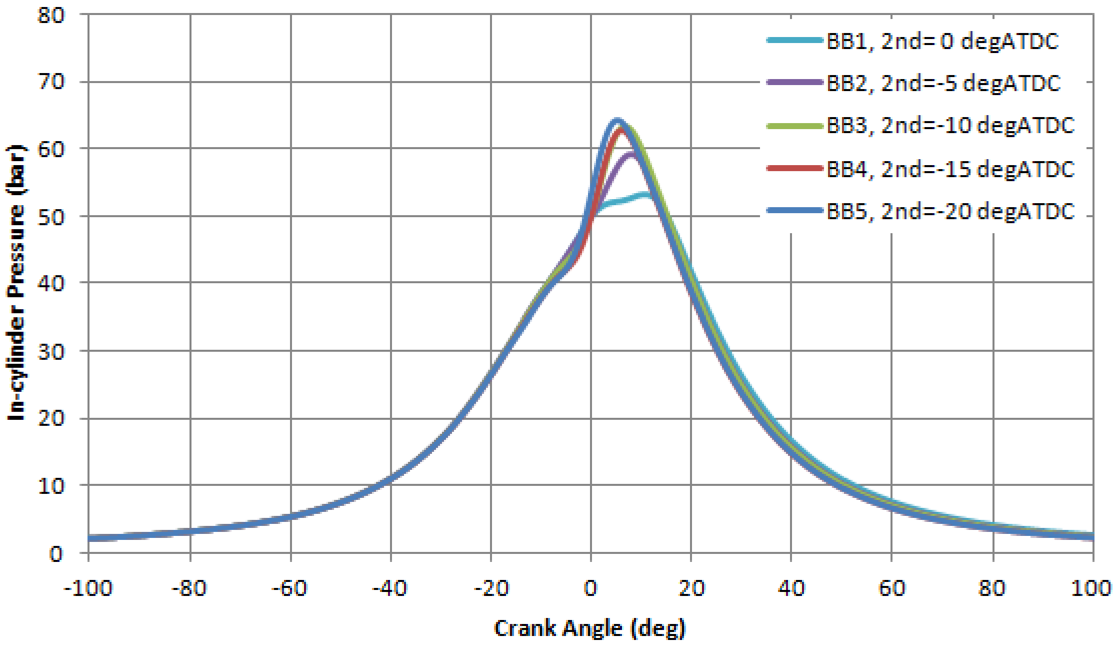

Figure 5.14 In-Cylinder Pressure Traces for Strategy BB (1st injection timing=-80 degATDC)

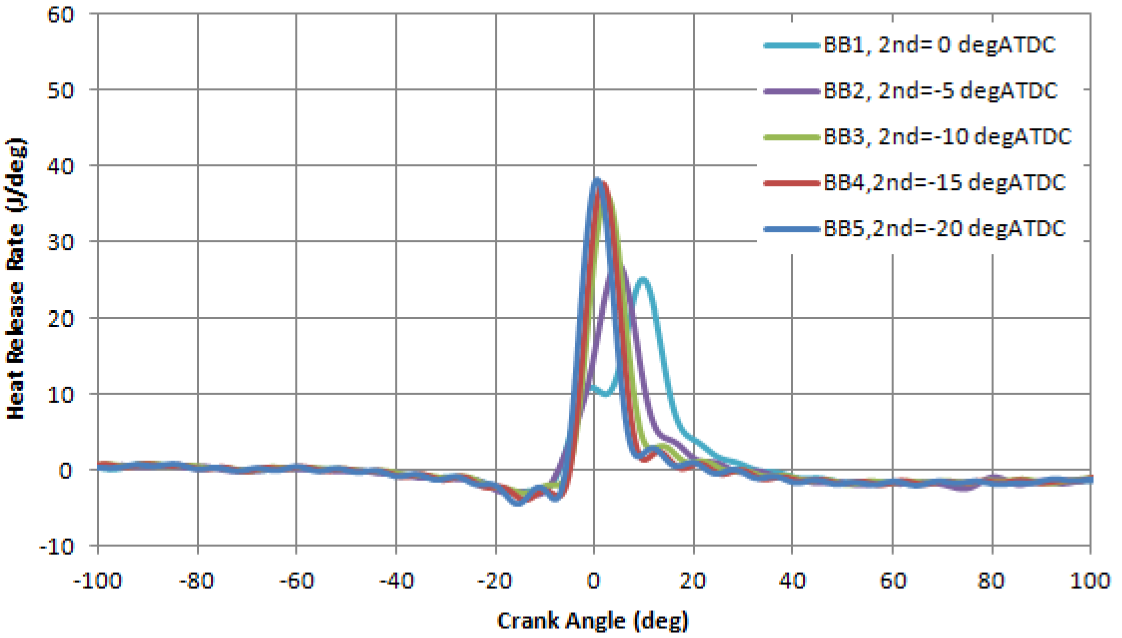

Figure 5.15 Heat Release Rate Traces for Strategy BB (1st injection timing=-80 degATDC)

The heat release rate for strategy BB2 rose progressively to its maximum value of 28 J/deg at 3.2 ° CA ATDC due to premixed combustion process. Compared to strategy BB1, no double peaks could be observed from the heat release rate curve. This was mainly attributed to the fact that the 2nd injection event was closer to the timing when the first combustion event commenced so that no obvious separated heat release progresses could be distinguished. After the peak point, the heat release rate decreased steadily until 13.8 ° CA ATDC when the diffusion combustion started to dominate combustion process as evidenced by the slower rate of heat release rate afterwards during the rest of expansion stroke.

The heat release rate for strategy BB3 encountered a minor decline at -9.4 °CA ATDC owing to the charge cooling effect caused by 2nd fuel injection event. It subsequently climbed up rapidly to its maximum value of 36 J/deg at 1.8 °CA ATDC due to premixed combustion. The peak heat release rate was higher than strategy BB2 since more rapid combustion process was achieved under higher temperature and pressure circumstance in strategy BB3 thanks to advanced 2nd injection timing. The heat release rate fell considerably after the peak point during the rest of expansion stroke with an apparent sign of diffusion combustion at the tail of heat release rate trace.

The heat release rate profiles for strategy BB4 and BB5 showed most advanced and highest heat release rate peaks. The heat release rate curves suffered noticeable falls at -12.8 °CA ATDC due to the charge cooling by 2nd injection. They rapidly climbed up to the maximum values of 38 J/deg at 0.8 and 0.4 °CA ATDC, respectively. The maximum heat release rate values were higher because the onset of combustion process was moved to TDC. The heat release rate for strategy BB4 and BB5 decreased sharply during the rest of expansion stroke with sign of diffusion combustion of the slower heat release at the end.

5.3.5 Analysis of the Effect of Injection Timings on Performance and Combustion of 70:30 Double Injection at 1200 bar Injection Pressure

Figure 5.16 shows the IMEP value for strategies B, BB and BBB. The highest IMEP value of 2.8 bar was achieved in the top right corner with earlier 1st injection timing and retarded 2nd injection timing late, whilst the lowest IMEP values were found in the lower right corner when both injections were retarded. For the case of early 1st injection timings (-100 to -80 °CA ATDC), the IMEP value increased when 2nd injection timing was retarded. When 2nd injection was placed around -10 °CA ATDC ,the IMEP reached a maximum value of 2.6 bar as 1st injection timings were retarded from -80 to -60 °CA ATDC. When early 2nd injection timings (-20 to -10 ° CA ATDC) were used, the 1st injection timing had little influence on IMEP values. However, when late 2nd injection timings (-10 to 0 °CA ATDC) were used, the IMEP dropped down to below 1.9 bar as 1st injection timing was retarded.

The combustion phasing (CA50) and combustion duration (CA10-90) for 70:30 fuel distribution (Strategies B, BB and BBB) are plotted in Figures 5.17 and 5.18, respectively. The CA50 was delayed as either of 1st or 2nd injection timing was retarded. It can be seen that 2nd injection timing had more effect on CA50 than 1st injection timing as shown by steeper slope of contour lines. In terms of the combustion duration, 1st injection timing showed little effect in early 2nd injection timing area (-20 to -10 °CA ATDC) but it slightly shortened the combustion duration within late 2nd injection timing (-10 to 0 °CA ATDC) region. The retarded 2nd injection timing considerably prolonged the combustion duration since lowered combustion temperature slowed down the combustion speed.

The ignition delay (SOI-CA10) for strategies B, BB and BBB are shown in Figure 5.19. The results indicated that 1st injection timing had little effect on ignition delay, which means the onset of combustion was strongly determined by 2nd injection timing.

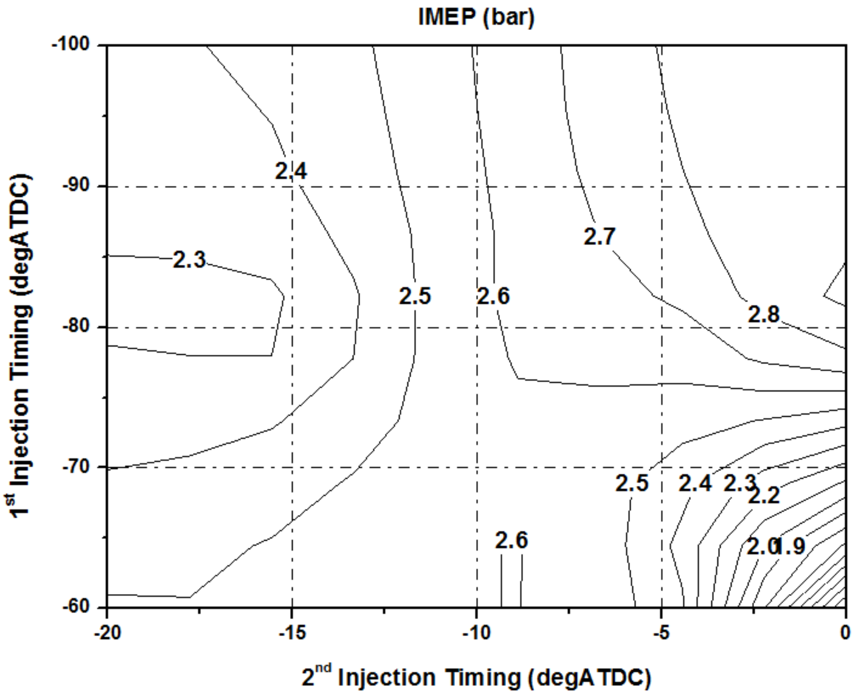

Figure 5.16 IMEP of 70:30 Fuel Distribution at 1200 bar Injection Pressure

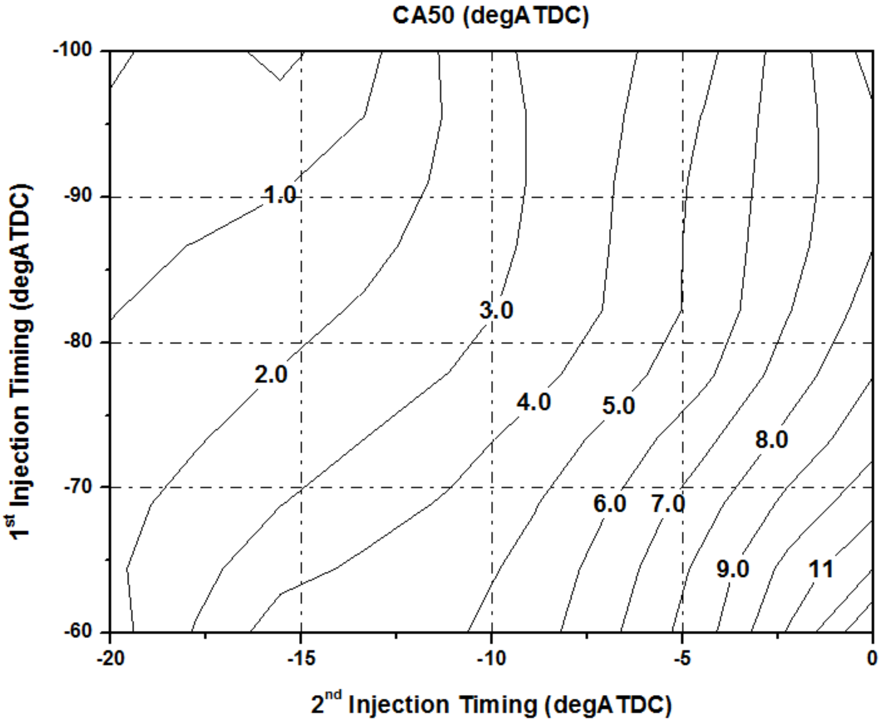

Figure 5.17 Combustion Phasing (CA50) of 70:30 Fuel Distribution at 1200 bar Injection Pressure

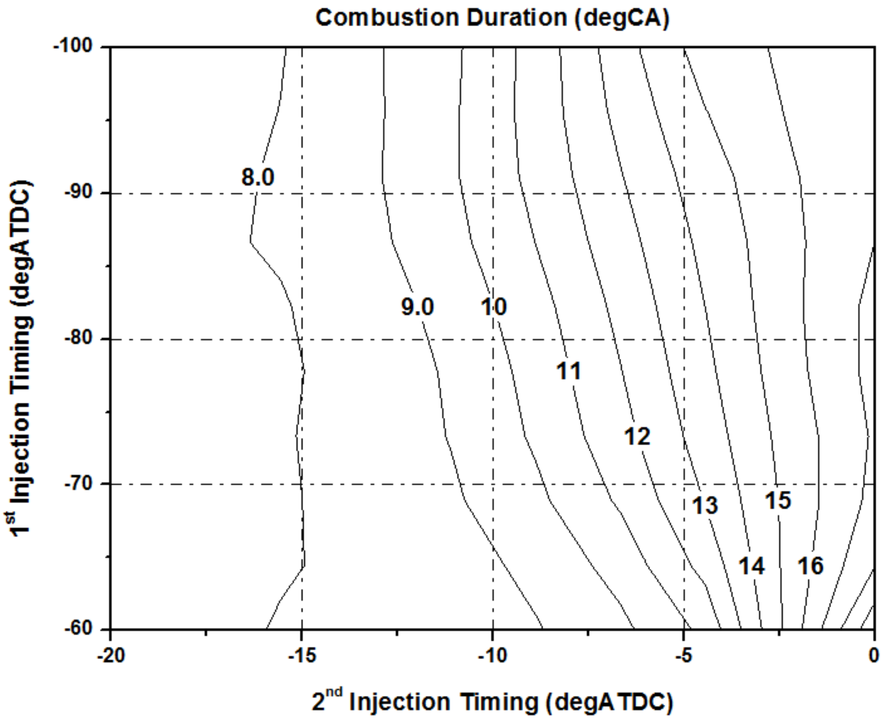

Figure 5.18 Combustion Duration (CA10-90) of 70:30 Fuel Distribution at 1200 bar Injection Pressure

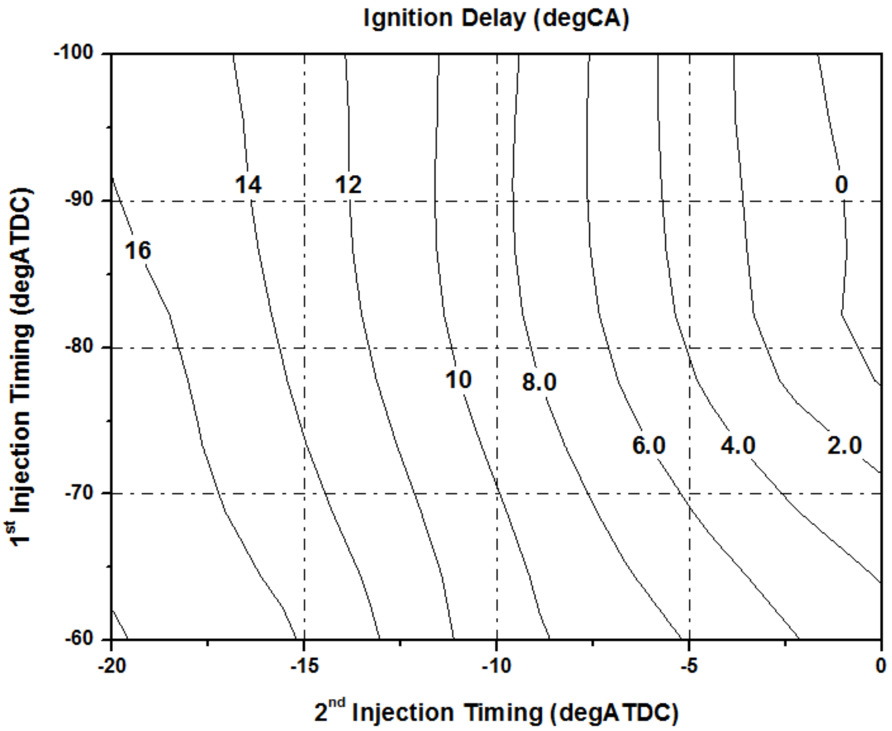

Figure 5.19 Ignition Delay (SOI_{2nd}-CA10) of 70:30 Fuel Distribution at 1200 bar Injection Pressure

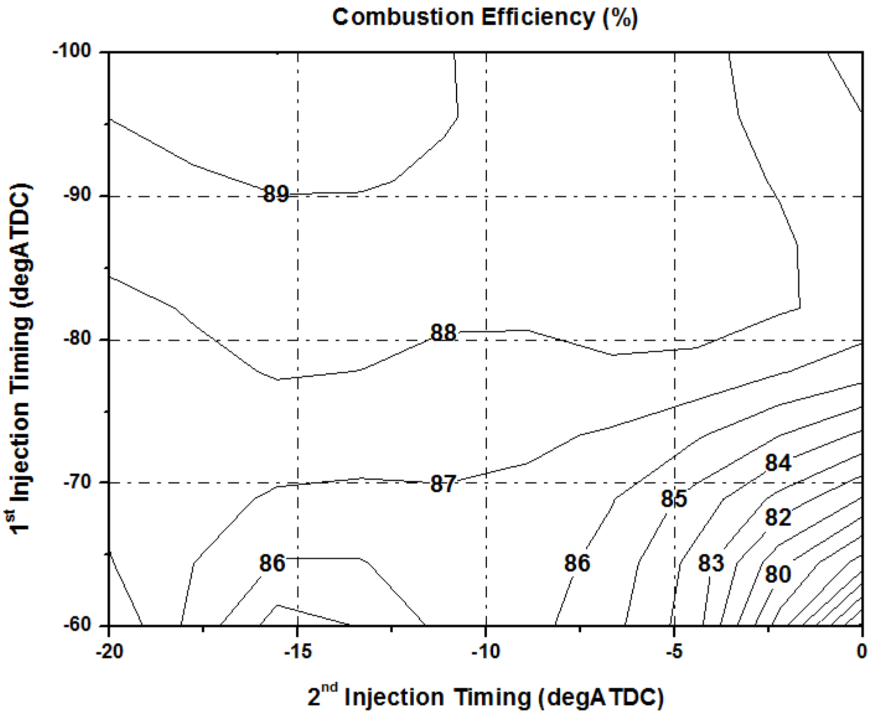

Figure 5.20 Combustion Efficiency of 70:30 Fuel Distribution at 1200 bar Injection Pressure

The combustion efficiencies in Figure 5.20 showed a maximum value of 89% for early injection timings strategies. Enhanced combustion temperature due to early injection timings contributed to more completed combustion process resulted in improved combustion efficiency. At the region of early 1st injection timings (-100 to -80 ° CA ATDC), the combustion efficiency stayed at high level for most of different 2nd injection timings. While in the area of early 2nd injection timings (-20 to -10 ° CA ATDC), slight reduction in combustion efficiencies was encountered due to lowered combustion temperature caused by retarded combustion phasing. For the late injection (-80 to -60 ° CA ATDC for 1st injection timing, -10 to 0 ° CA ATDC for 2nd injection timings) strategies, the combustion efficiency gradually decreased to 80%.

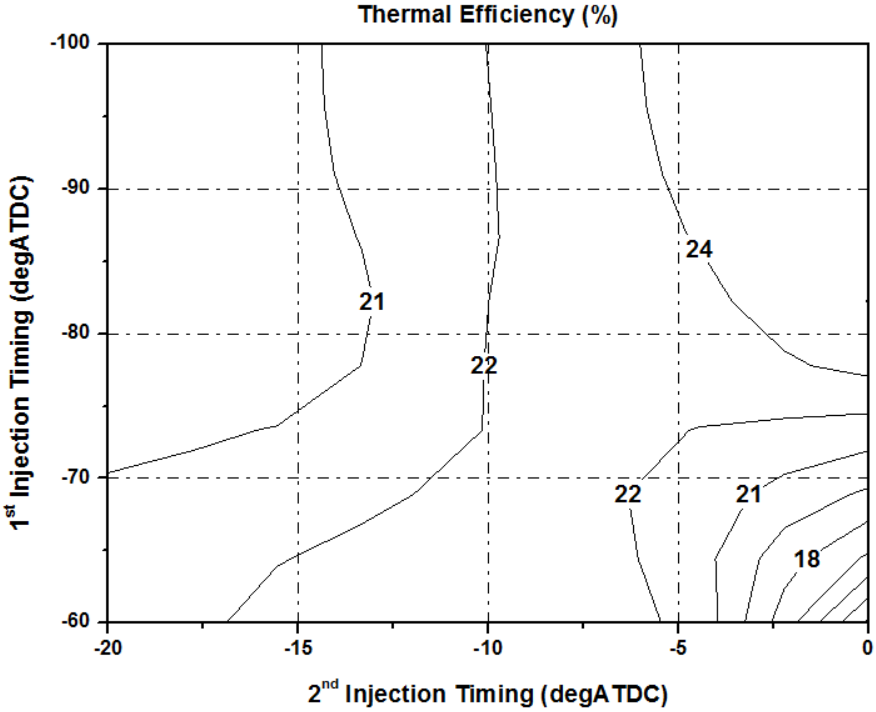

Figure 5.21 Thermal Efficiency of 70:30 Fuel Distribution at 1200 bar Injection Pressure

The thermal efficiency is presented in Figure 5.21. Generally, 1st injection timings had much less influence on the thermal efficiency than 2nd injection timing apart from the most retarded 1st injection timing (-60 ° CA ATDC). For the fixed 1st injection timing, the thermal efficiency progressively increased when 2nd injection timing was retarded as the combustion phasing was optimised. The thermal efficiency was reduced by 21% at early injection timing (-100 to -80 ° CA ATDC for 1st injection timing, -20 to -15 ° CA ATDC for 2nd injection timings) cases and 18% at late injection timings (-70 to -60 ° CA

ATDC for 1st injection timing, -5 to 0 degrees ° CA ATDC for 2nd injection timings), respectively. The reduction in the former cases was mainly attributed to excessive heat losses caused by higher combustion temperature whilst in the latter cases they were due to late combustion phasing by retarded injection timing. The indicated efficiency shown in Figure 5.22 presented the similar trend to the thermal efficiency. By taking combustion efficiency into account, the indicated efficiency showed an averaged 2% reduction from the thermal efficiency.

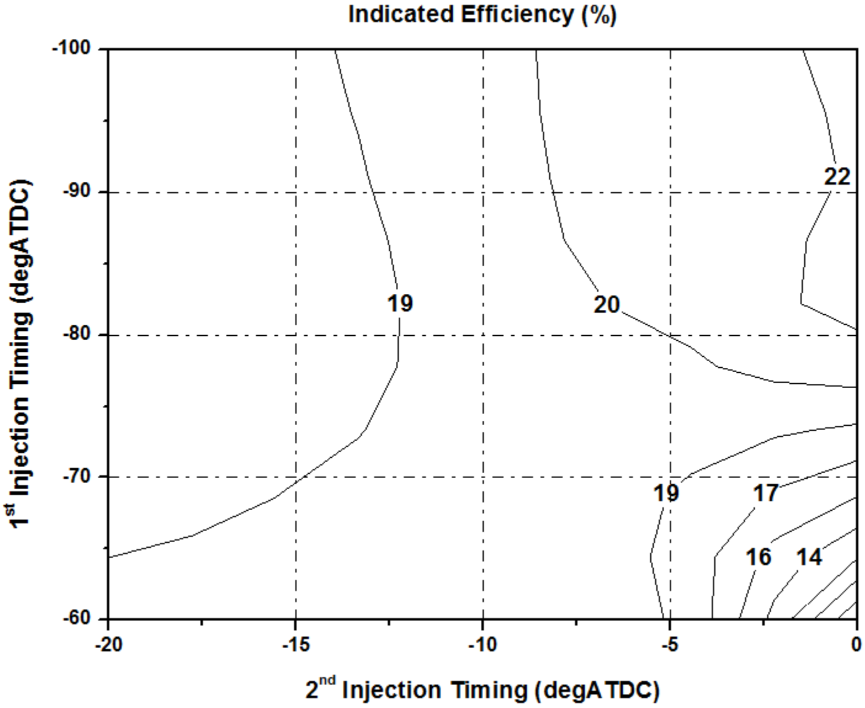

Figure 5.22 Indicated Efficiency of 70:30 Fuel Distribution at 1200 bar Injection Pressure

5.3.6 Analysis of the Effect of Injection Timings on Emissions of 70:30 Double Injection at 1200 bar Injection Pressure

As shown in Figure 5.23, the uHC emissions remained at fairly high levels for the same reasons discussed in 5.3.4, including over-mixing and possible liquid fuel impingement of the first injection, under-mixing of 2nd injection and lower combustion temperature with EGR. The uHC emissions progressively increased from 100 to 200 g/kg-fuel when both injection timings were retarded. This was mainly attributed to increased inhomogeneity and reduced combustion temperature due to delayed combustion phasing.

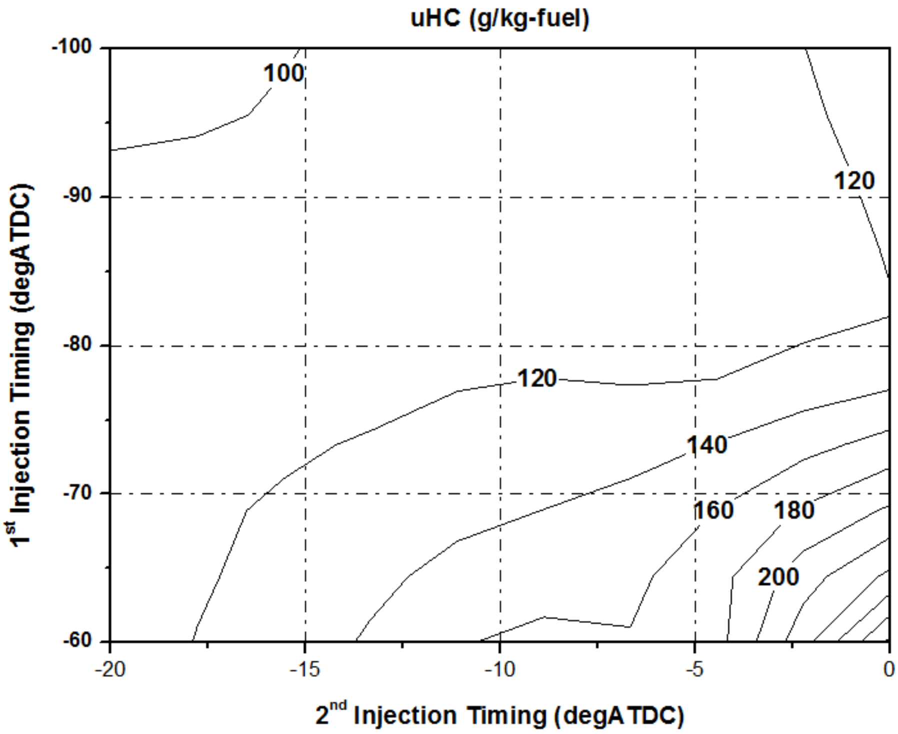

Figure 5.23 uHC Emissions of 70:30 Fuel Distribution Strategy at 1200 bar Injection Pressure

Figure 5.24 shows that the NOx emissions were kept below 2.2 g/kg-fuel due to exhaust gas recirculation and lean premixed mixture. The higher specific heat capacity of pure nitrogen gas (simulated EGR gas) helped lowering combustion temperature so that NOx emissions were minimized. In addition, the portions of oxygen were replaced by nitrogen gas thereby slowed down the formation of NOx emissions. The NOx emissions went up when both injection timings were advanced. This was mainly attributed to the higher combustion temperature when the combustion phasing was closer to TDC.

The soot concentrations in Figure 5.25 were much higher than those of the 50:50 fuel injection operations in Figure 5.13. In the top left corner with the earliest 1st injection and 2nd injection, soot emissions were almost 100 times higher. This could be mainly caused by the increased fuel impingent during extended 1st injection duration. The minimum soot emission was obtained with the retarded 1st injection and intermediate 2nd injection. In general, 2nd injection timing had much less influence on soot emissions.

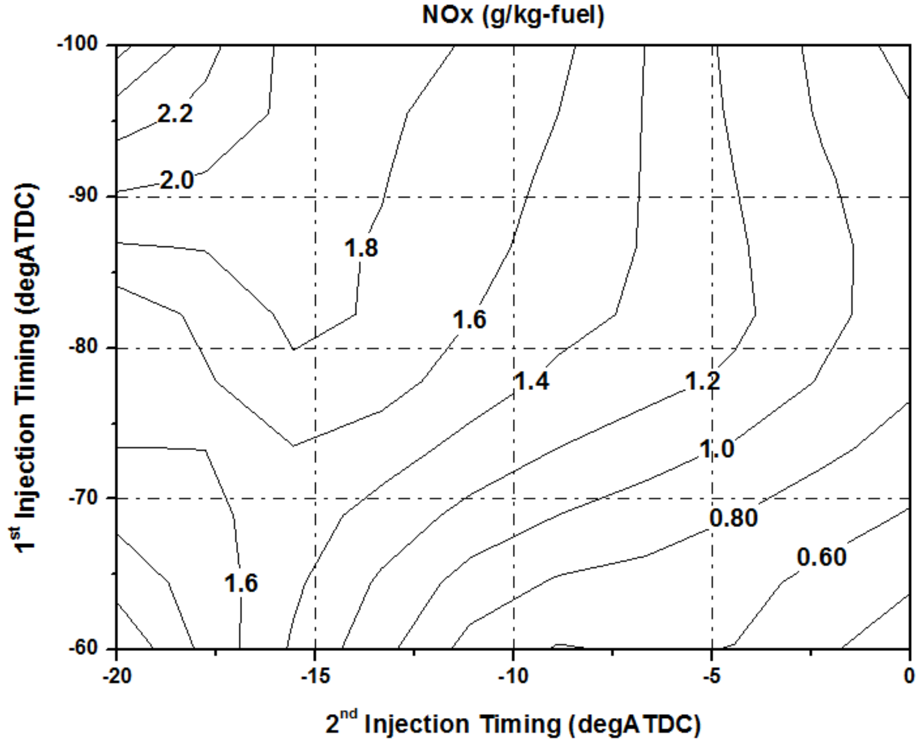

Figure 5.24 NOx Emissions of 70:30 Fuel Distribution at 1200 bar Injection Pressure

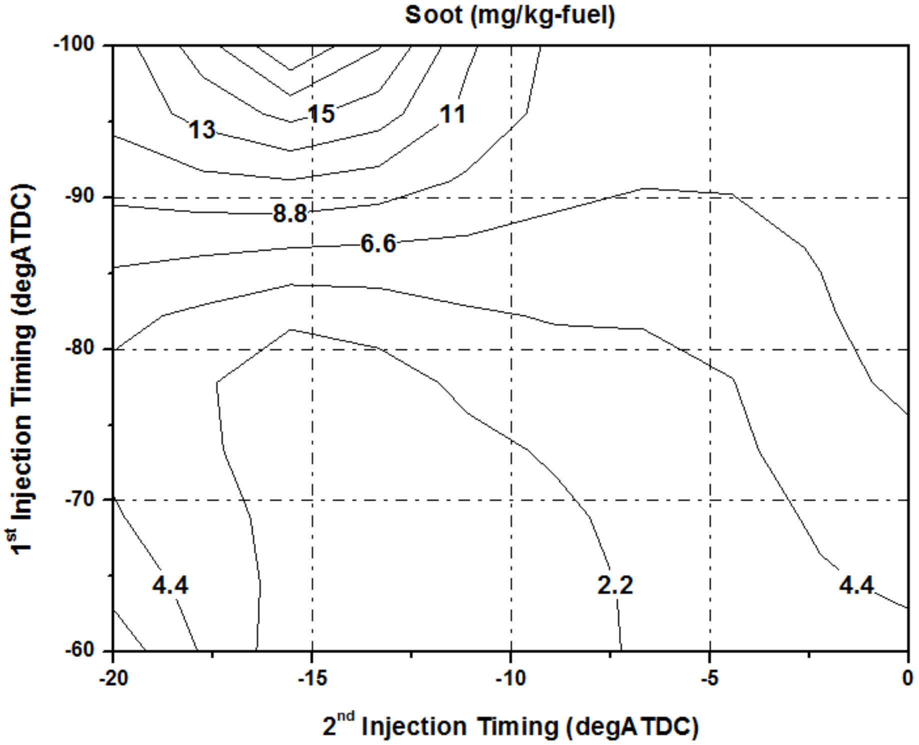

Figure 5.25 Soot Emissions of 70:30 Fuel Distribution at 1200 bar Injection Pressure

5.3.7 In-Cylinder Pressure and Heat Release Rate Analysis for Strategy CC (30:70 fuel distribution with fixed 1st injection timing at -80 °CA ATDC)

In the case of 30:70 fuel distribution operations, only in-cylinder pressure, heat release rate and exhaust emissions for strategy CC will be discussed because the operating range was limited by excessive misfiring operations.

The in-cylinder pressure data for strategy CC averaged over 20 consecutive cycles are presented in Figure 5.26. Strategy CC1 and CC2 were not included in the analysis since there were no combustion could be detected in these two cases. The failure for the fuel to achieve auto-ignition with injection around TDC could be attributed to the greater charge cooling effect of more fuel from 2nd injection and the decreasing pressure and temperature after TDC. The in-cylinder pressure trace of strategy CC3 followed the motoring pressure curve until TDC and suffered a minor decrease lasting for a few crank angles until 3.2 ° CA ATDC when combustion started. Subsequently, the in-cylinder pressure went up smoothly to its peak point of 55.5 bar at 12 °CA ATDC due to premixed combustion. After the peak point, the pressure declined gradually during the rest of expansion stroke. Strategy CC3 produced an IMEP value of 2.63 bar.

The in-cylinder pressure curve for strategy CC4 followed that of strategy CC3 to -5 ° CA ATDC and stayed constant until -1 °CA ATDC. From TDC it increased rapidly to the maximum pressure of 63.3 bar at 7 °CA ATDC, which was approximately 5 °CA before strategy CC3 and about 12% higher. This was mainly attributed to advanced 2nd injection timing for strategy CC4 placed combustion process closer to TDC. The in-cylinder pressure decreased gradually during the rest of expansion stroke with relatively lower pressure compared to strategy CC3. By setting the 2nd injection timing at -15 °CA ATDC, the strategy CC4 produced 2.28 bar IMEP. The in-cylinder pressure line for strategy CC5 followed the strategy CC4 until -7 ° CA ATDC and progressively ascended to its maximum pressure of 67.3 bar at 3.6 ° CA ATDC due to premixed combustion. Strategy CC5 produced the highest peak pressure but the lowest IMEP of 2.1 bar because of too advanced combustion phasing.

The heat release rate results for strategy CC3, CC4 and CC5 are shown in Figure 5.27. The heat release rate for strategy CC3 suffered a minor decline at -3 °CA ATDC owing to charge cooling effect caused by onset of 2nd fuel injection. The heat release rate increased progressively to the maximum value of 45.1 J/deg at 8.8 °CA ATDC due to premixed combustion. The heat release rate line afterwards descended quickly until 16.4 ° CA ATDC and a small bump can be observed shortly due to diffusion combustion at the end of the heat release process. The heat release rate trace for strategy CC4 experienced an apparent fall at -7.2 ° CA ATDC due to the charge cooling effect from 2nd injection. After reaching its peak at 3.2 ° CA ATDC., the heat release rate dropped down to zero level during the expansion stroke without any sign of diffusion combustion.

By having the most advanced 2nd injection timing at -20 ° CA ATDC, strategy CC5 presented earliest heat release rate profile during compression stroke. The heat release rate for strategy CC5 encountered an obvious fall at -12.2 ° CA ATDC due to charge cooling. It rapidly reached its peak of 45.1 J/deg, the same as previous strategies, at -1 ° CA ATDC. The negative work done by the heat released before TDC contributed to the lower IMEP value in strategy CC5. The heat release rate sharply fell down during the rest of expansion stroke without obvious evidence of diffusion combustion.

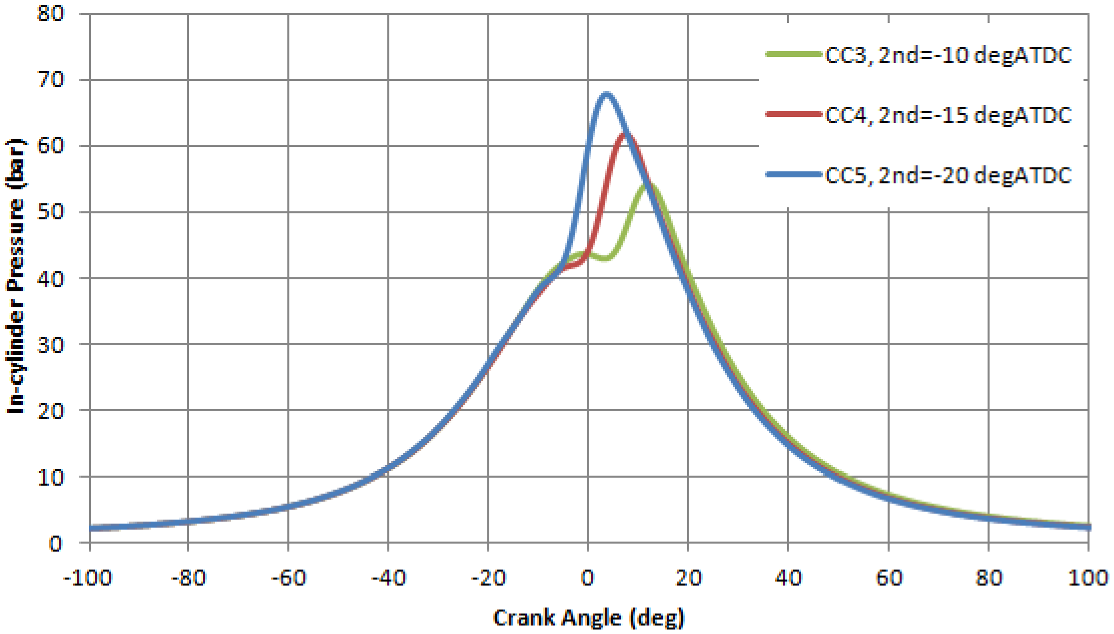

Figure 5.26 In-Cylinder Pressure Traces for Strategy CC (1st injection timing=-80 degATDC)

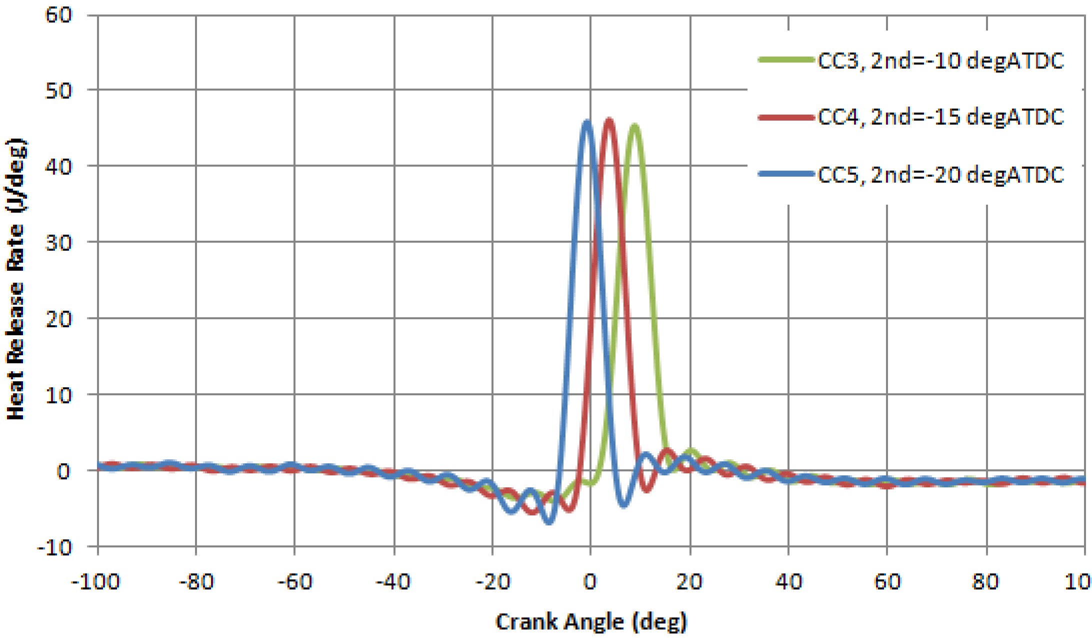

Figure 5.27 Heat Release Rate Traces for Strategy CC (1st injection timing=-80 degATDC)

5.3.8 Emission Analysis for Strategy CC (30:70 fuel distribution with fixed 1st injection timing at -80 °CA ATDC)

The exhaust emissions and soot concentration for strategy CC are plotted in Figure 5.28 and Figure 5.29, respectively.

The NOx emissions for strategy CC were higher than the 50:50 fuel distribution and 70:30 fuel distribution operations as more fuel was injected in 2nd injection, which led to higher combustion temperature due to more near stoichiometric combustion sites. On the other hand, uHCs were lower than the 50:50 and 70:30 cases as fuel impingement and over-mixing effects were reduced as a smaller quantity of fuel was injected in 1st injection. In addition the higher combustion temperature would increase the oxidation rate of uHCs. For the same reason the uHCs decreased and NOx emission increased at higher combustion temperature of more advanced 2nd injections.

The soot concentrations were lower than the 70:30 operations, probably due to the reduction in the fuel impingement of 1st injections. The ultra-low soot emissions can be explained by the high octane and high volatility of the fuel used. The resulting faster atomization and extended ignition delay period helped to minimize the formation of fuel rich regions and hence the formation of soot. Furthermore, higher combustion temperature enhanced the soot oxidation process and reduced the soot concentration in the exhaust.

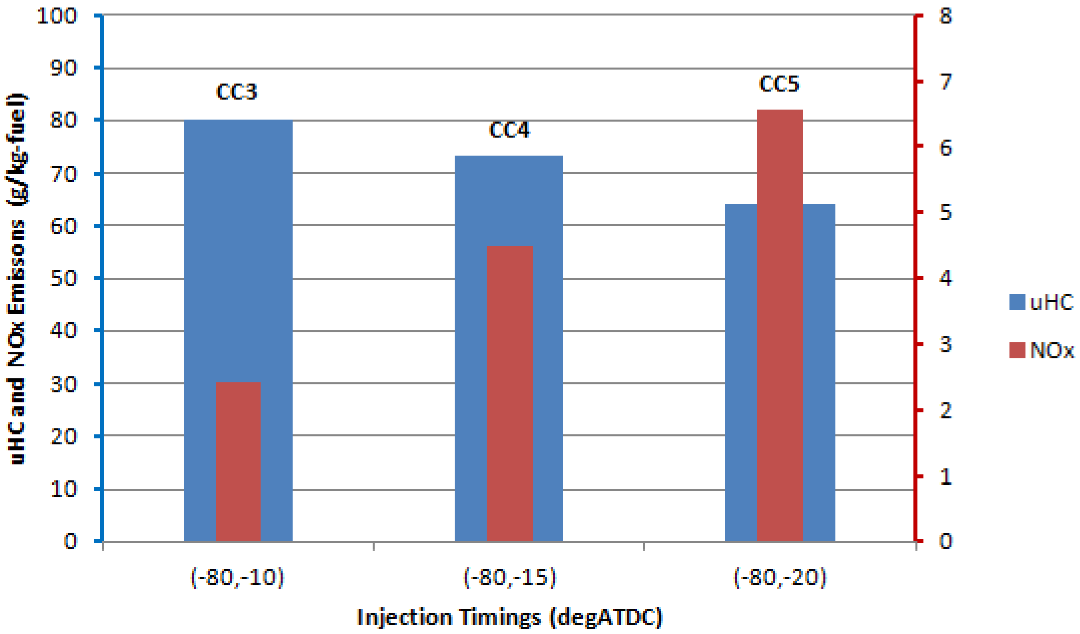

Figure 5.28 uHC and NOx Concentration for Strategy CC

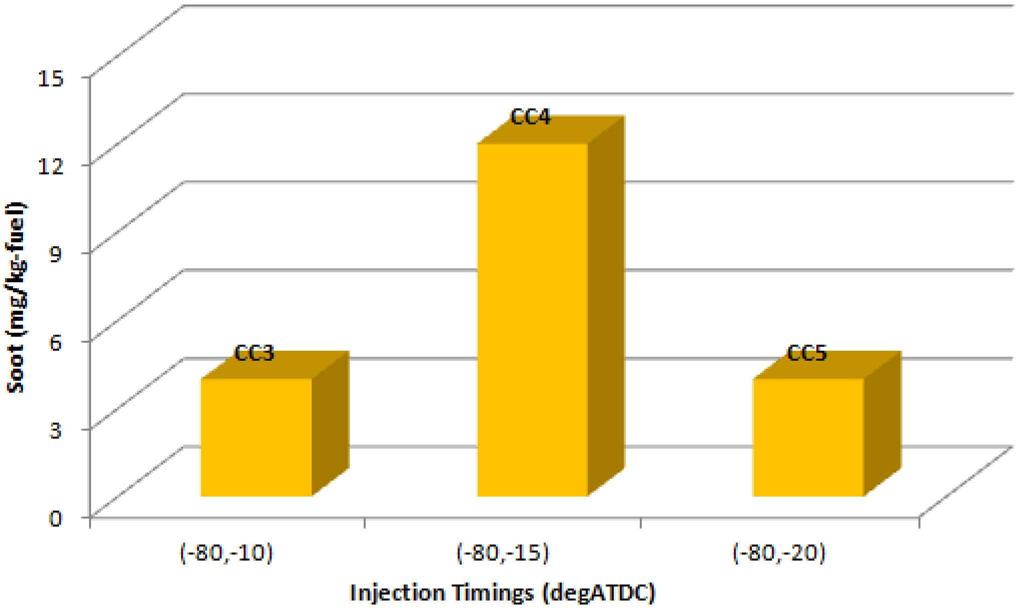

Figure 5.29 Soot Concentrations for Strategy CC

5.4 Gasoline Partially Premixed Combustion at Injection Pressure of 900bar

As discussed in the previous sections, fuel impingement on cylinder walls was considered a major cause for the higher soot emissions detected with early 1st injection. Therefore, combustion characteristics and emissions were investigated at injection pressure of 900bar. The quantity of 1st injection was varied from 50% to 70%. As the 30:70 strategy at 1200bar had a much narrower operating range and lower IMEP values, it was not selected for further studies at 900bar injection pressure.

5.4.1 In-Cylinder Pressure and Heat Release Rate Analysis for Strategy DD (50:50 fuel distribution with fixed 1st injection timing at -80 °CA ATDC)

The in-cylinder pressure results for strategy DD averaged over 20 cycles are presented in Figure 5.30. The strategy DD1 was not included in data analysis since there was no combustion could be detected. The in-cylinder pressure trace for strategy DD2 increased smoothly and reached its first peak at TDC. After this peak point, it decreased slightly until 9.5 °CA ATDC and rose again to the second peak pressure of 44.7 bar at 14.2 °CA ATDC due to premixed combustion. Late combustion can be recognized by distinguishing two in-cylinder pressure peaks caused by retarded 2nd injection timing. The in-cylinder pressure decreased steadily afterwards during the expansion stroke. Strategy DD2 produced an IMEP value of 2.97 bar.

The in-cylinder pressure trace for strategy DD3 rose gradually until -2.6 ° CA ATDC and then remained constant for a few crank angles until 3.6 °CA ATDC. Subsequently the pressure reached to its peak point of 54.7 bar at 11.6 °CA ATDC. After this peak point, the pressure for strategy DD3 descended steadily during the expansion stroke and remained slightly lower than strategy DD2 and hence a lower IMEP of 2.55 bar.

By further advancing 2nd injection timing to -15 ° CA ATDC, the in-cylinder pressure trace for strategy DD4 exhibited an enlarged pressure profile. The maximum pressure of 62.5 bar was reached at 5.6 °CA ATDC, 6 °CA before strategy DD3 and 8 bar higher. The advanced 2nd injection timing contributed to rapid combustion process. 2.35 bar IMEP was produced in strategy DD4. The strategy DD5 exhibited a highest maximum pressure of 68 bar at 2.6 °CA ATDC but produced a lower IMEP value of 2.26 bar due to too advanced combustion.

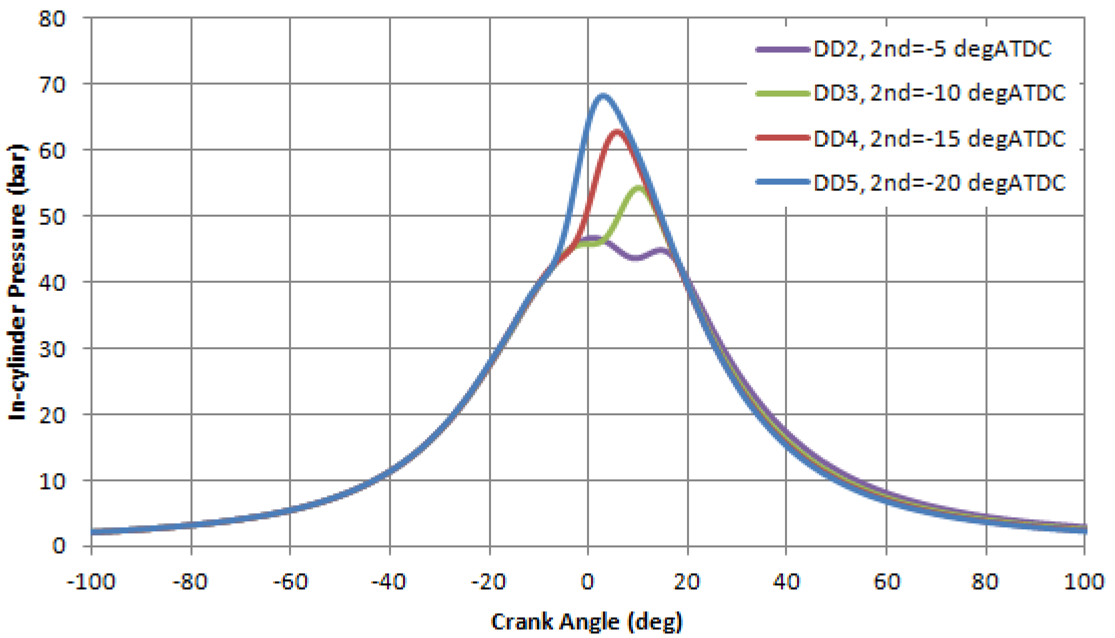

Figure 5.30 In-Cylinder Pressure Traces for Strategy DD (1st injection timing=-80 degATDC)

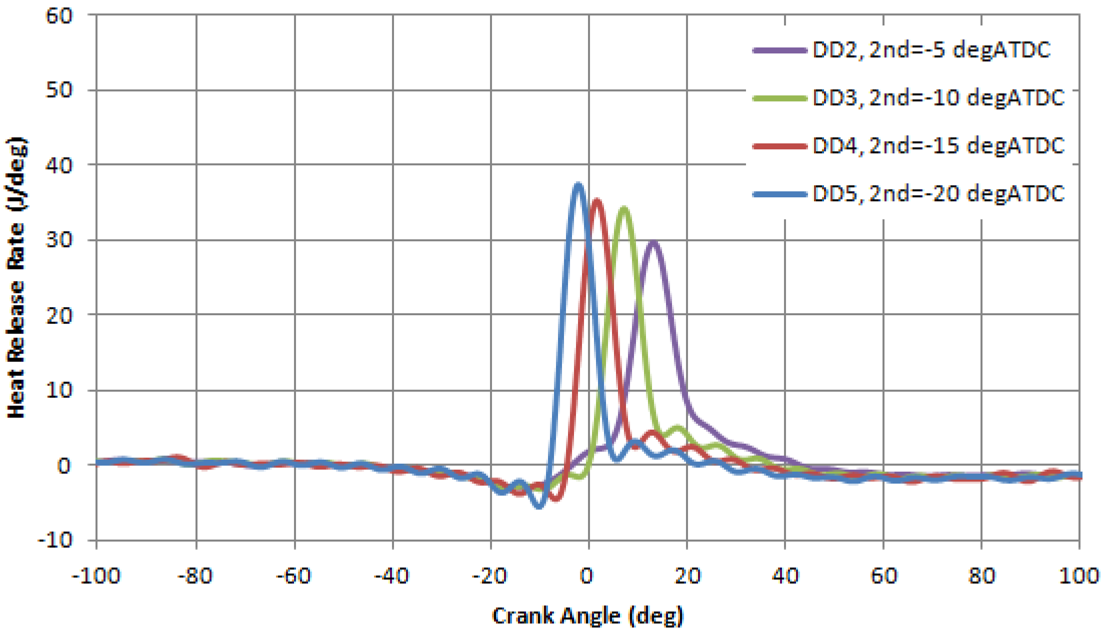

Figure 5.31 Heat Release Rate Traces for Strategy DD (1st injection timing=-80 degATDC)

As shown in Figure 5.31. The heat release rate for strategy DD2 increased smoothly until TDC due to released energy from first injected fuel. After encountering a slower period, the heat release rate climbed up progressively to the peak of 30 J/deg at 12 °CA ATDC because of premixed combustion after 2nd injection. After this peak point, the rate of heat release line decreased steadily until 20 °CA ATDC from where the diffusion combustion started dominating combustion process. Strategy DD3 showed a similar two-stage ignition process. The peak heat release rate for strategy DD3 was higher and approximately 5 °CA earlier than strategy DD2.

In comparison, as 2nd injection was advanced to -15 °CA ATDC (strategy DD4) and -20 °CA ATDC (strategy DD5), the first ignition and heat release process was absent as the charge cooling effect of 2nd injection suppressed the auto-ignition of premixed mixture from 1st injection. The presence of diffusion combustion was also more pronounced as evidenced by the tail of the heat release rate.

5.4.2 Analysis of the Effect of Injection Timings on Performance and Combustion of 50:50 Double Injection at 900 bar Injection Pressure

As shown in Figure 5.32, for a given 1st injection timing, the highest IMEP value was obtained in the middle of the graph when 2nd injection timing was around -10 ° CA ATDC. A maximum value of 3.1 bar was found with the early 1st injection timing of -100 ° CA ATDC and 2nd injection timing of around -10 ° CA ATDC, which is higher than those of 1200 bar injection pressure. However, 1st injection timing has little effects on IMEP.

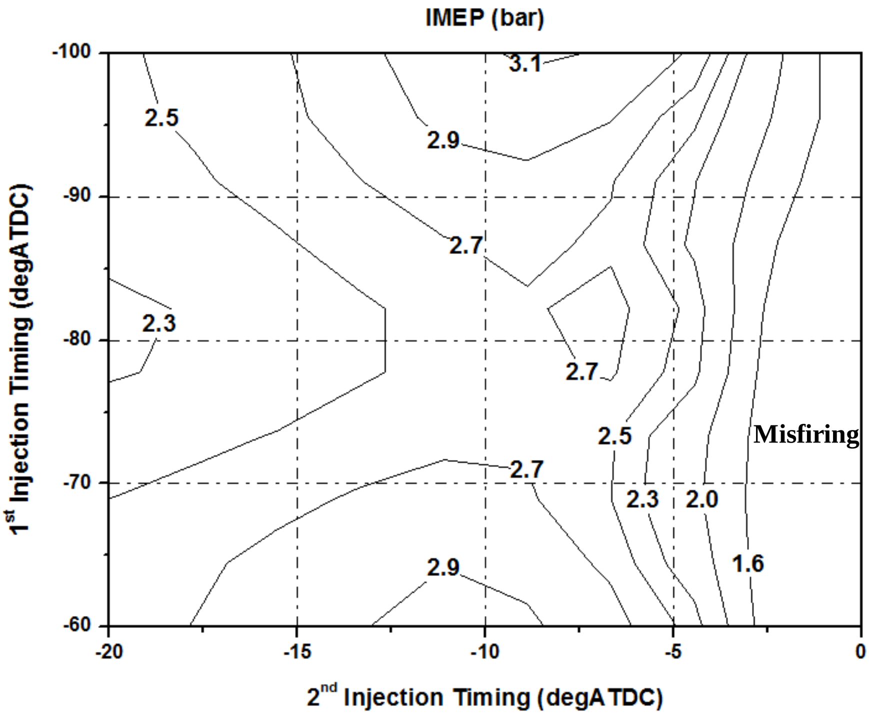

Figure 5.32 IMEP of 50:50 Fuel Distribution at 900 bar Injection Pressure

The contours of combustion phasing (CA50) and combustion duration (CA10-90) are plotted in Figure 5.33 and Figure 5.34, respectively. When 2nd injection timing was advanced from -5 ° CA ATDC to -20 ° CA ATDC, the CA50 was shifted by 10 ° CA independently to 1st injection timing, which indicates that auto-ignition combustion from 2nd injection was responsible for the start of combustion. When 2nd injection timings were retarded to TDC, CA50 was progressively delayed to 18 °CA ATDC when 1st injection timing was advanced to -100 ° CA ATDC. In this case, the combustion event seemed to be slowed down by the presence of a more homogenous mixture from 1st injection, as further evidenced by the extended combustion duration shown in the top right corner of Figure 5.34. Otherwise, the combustion duration (CA10-90) remained fairly constant in most of the region.

As shown in Figure 5.35, the ignition delay was gradually shortened when 2nd injection timing was retarded over operating range. This reduction was almost independent to 1st injection timing but was speeded up in the area near to TDC which indicated that onset of combustion became more rapid when 2nd injection timing was closer to TDC due to higher surrounding temperature.

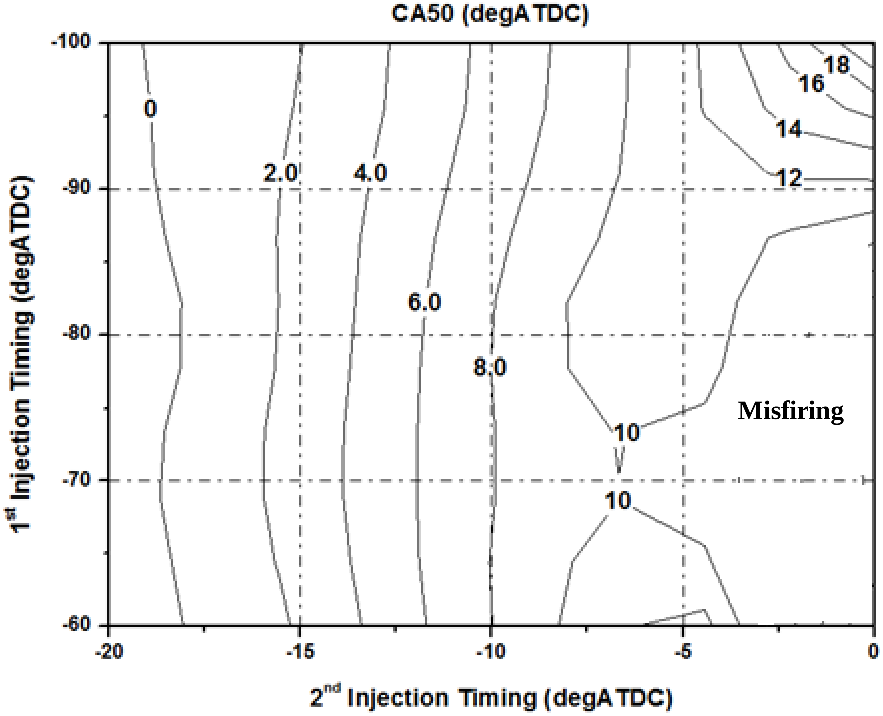

Figure 5.33 Combustion Phasing (CA50) of 50:50 Fuel Distribution at 900 bar Injection Pressure

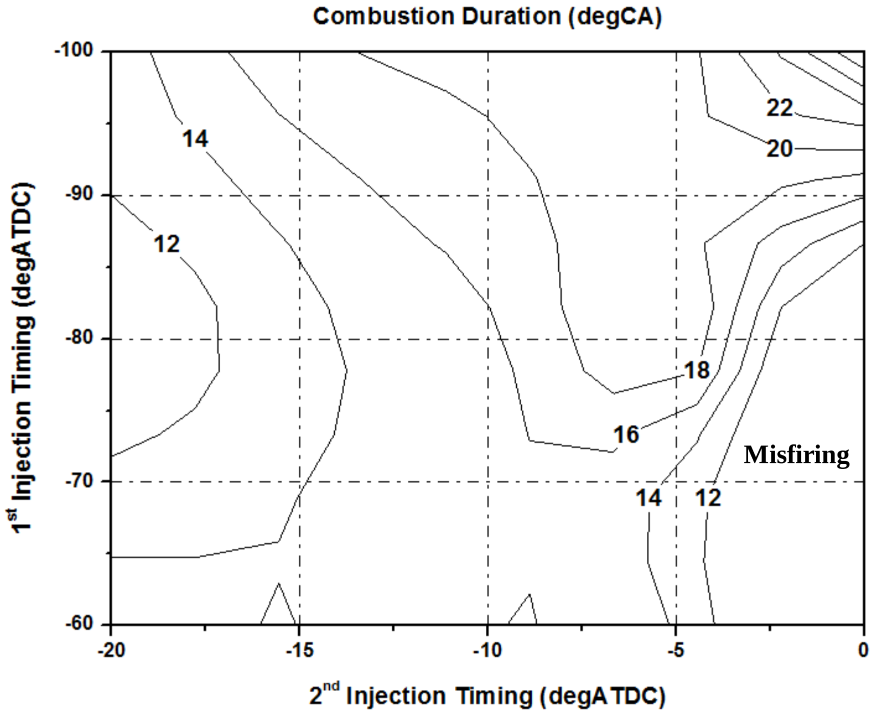

Figure 5.34 Combustion Duration (CA10-90) of 50:50 Fuel Distribution at 900 bar Injection Pressure

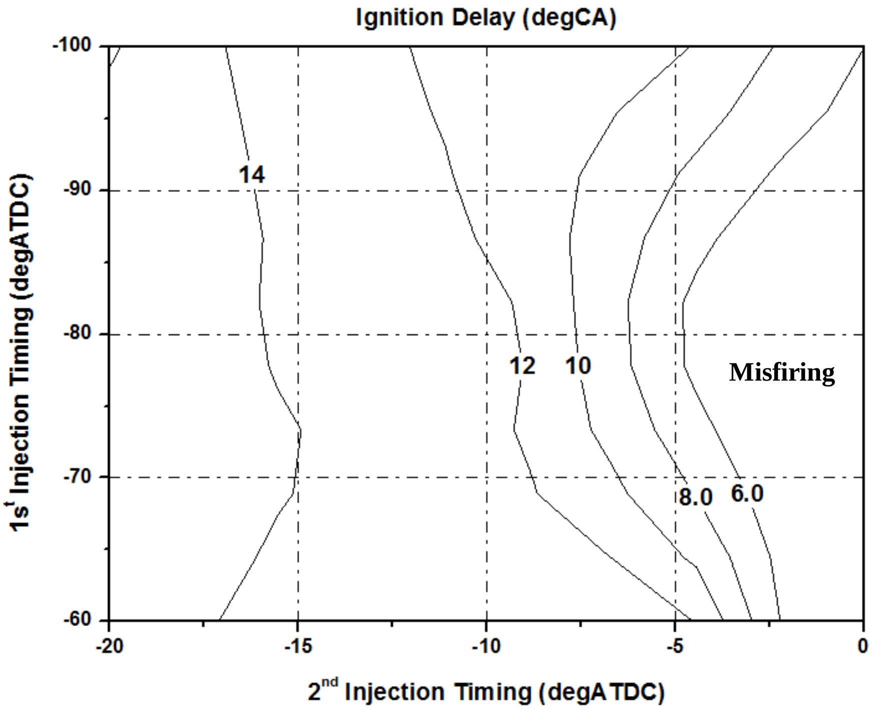

Figure 5.35 Ignition Delay (SOI_{2nd}-CA10) of 50:50 Fuel Distribution at 900 bar Injection Pressure

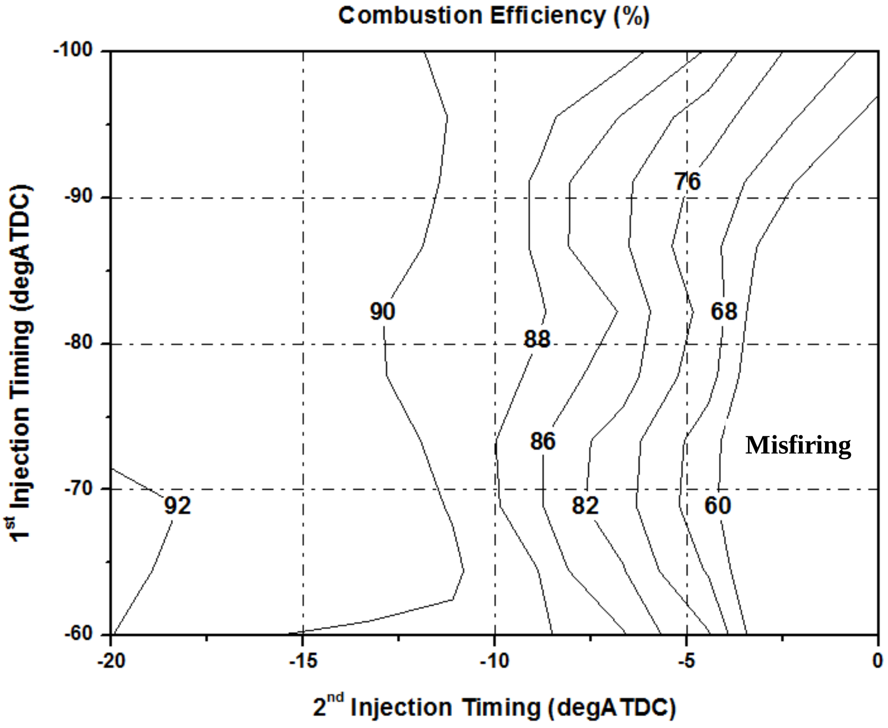

Figure 5.36 Combustion Efficiency of 50:50 Fuel Distribution at 900 bar Injection Pressure

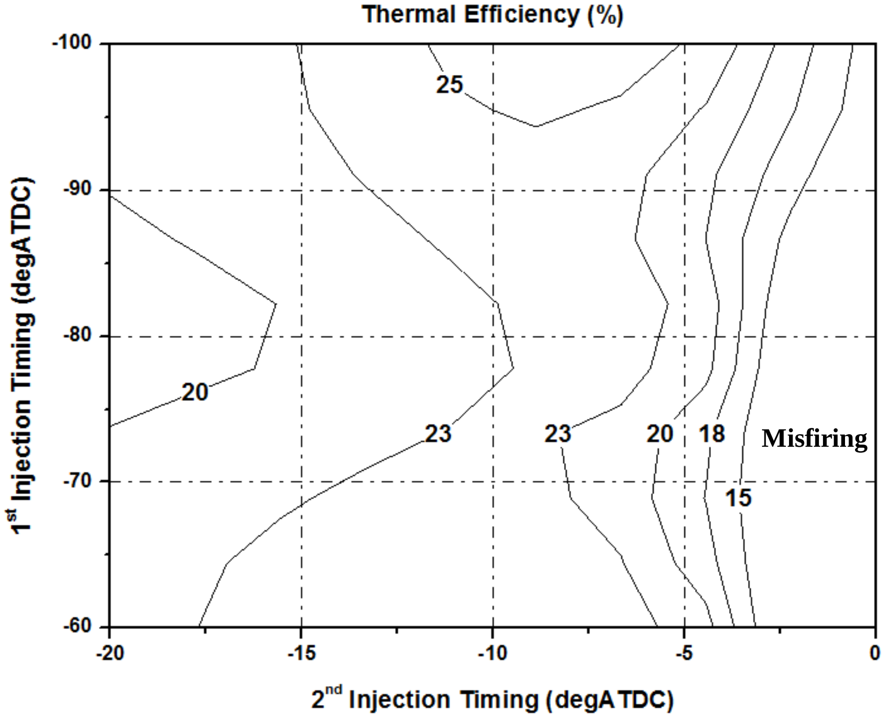

Figure 5.37 Thermal Efficiency of 50:50 Fuel Distribution at 900 bar Injection Pressure

The combustion efficiency shown in Figure 5.36 demonstrated that the most completed combustion took place at advanced 2nd injection timings and late 1st injection timings, because of the higher combustion temperature, less wall wetting and over-mixing. Figure 5.37 shows that the maximum value of 25% was reached when 2nd injection timing was placed around -10 ° CA ATDC. The thermal efficiency subsequently dropped down below 20% when 2nd injection timing was retarded or advanced from due to non-optimised combustion phasing. The thermal efficiency was nearly independent to 1st injection timing during operating range. As shown in Figure 5.38, the indicated efficiency presented identical trend as thermal efficiency but with lower value due to consideration of combustion efficiency.

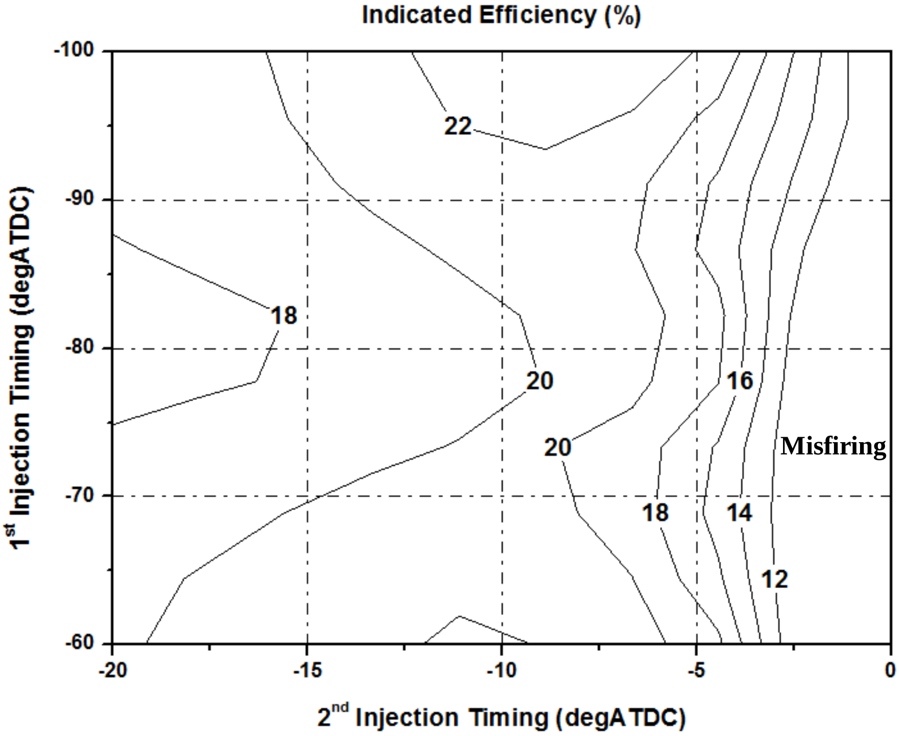

Figure 5.38 Indicated Efficiency of 50:50 Fuel Distribution at 900 bar Injection Pressure

5.4.3 Analysis of the Effect of Injection Timings on Emissions of 50:50 Double Injection at 900 bar Injection Pressure

As shown in Figure 5.39, the uHC emissions for strategies D, DD and DDD were relatively high. As discussed in the previous sections, their formation was a combination of wall wetting and over-mixing from 1st injection and under-mixing from 2nd injection as well as incomplete oxidation at reduced combustion temperatures.

Similarly, Figure 5.40 shows that the NOx emission was kept low by low temperature combustion with EGR.

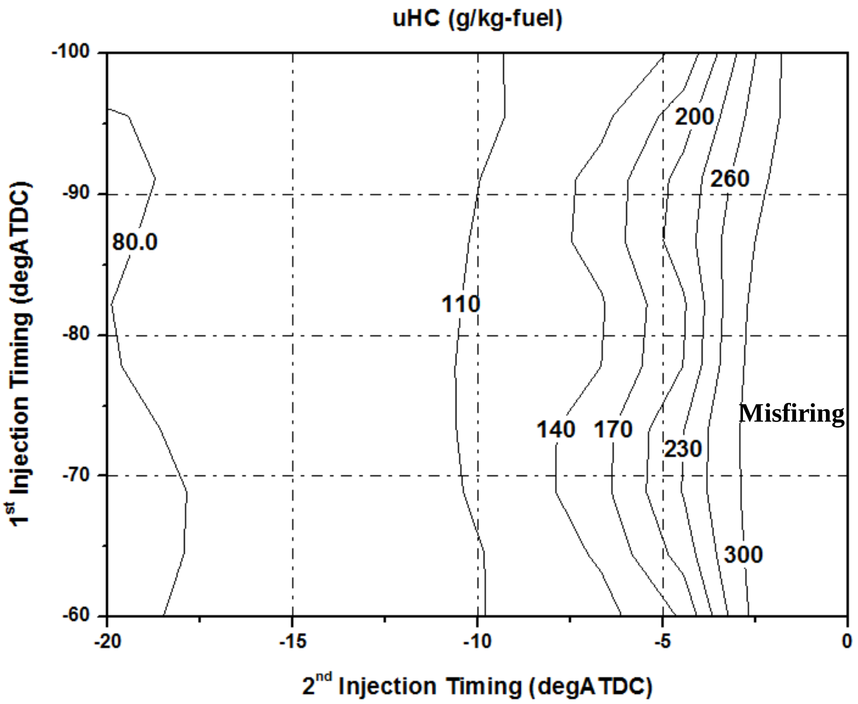

Figure 5.39 uHC Emissions of 50:50 Fuel Distribution at 900 bar Injection Pressure

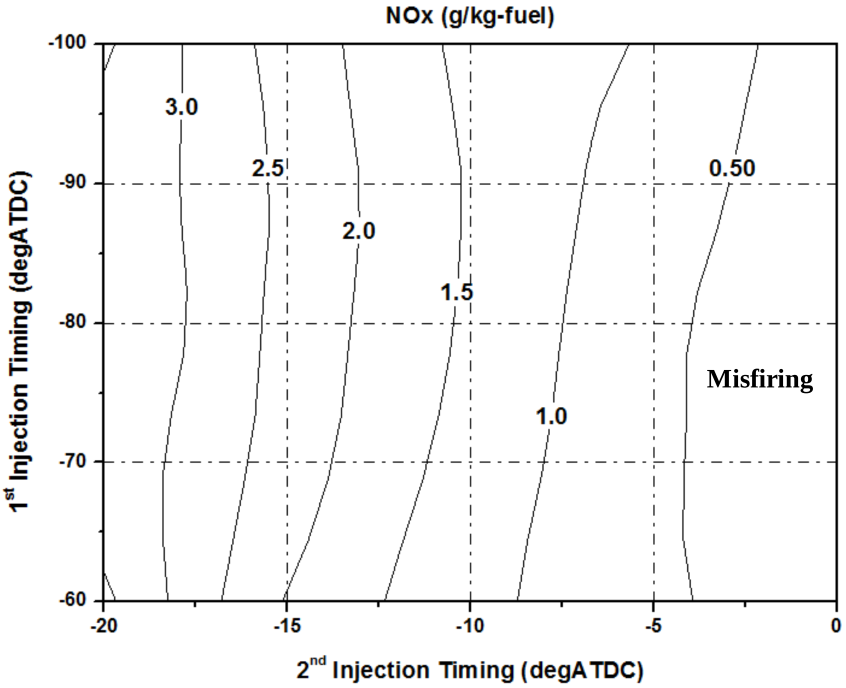

Figure 5.40 NOx Emissions of 50:50 Fuel Distribution at 900 bar Injection Pressure

As shown in Figure 5.41, soot emissions were still low but orders of magnitude higher than those of 1200bar injection pressure, due to poorer atomization at reduced injection pressure. The soot emissions steadily decreased when 2nd injection timing was advanced for a given 1st injection probably due to the faster soot oxidation process at elevated combustion temperature. Highest soot emissions were found with the earliest 1st injection because of poor atomization and wall impingement when the in-cylinder temperature and pressure were lower at the start of the compression stroke. On the other hand, the most retarded 1st injection could lead to more soot emission by the less complete mixing process.

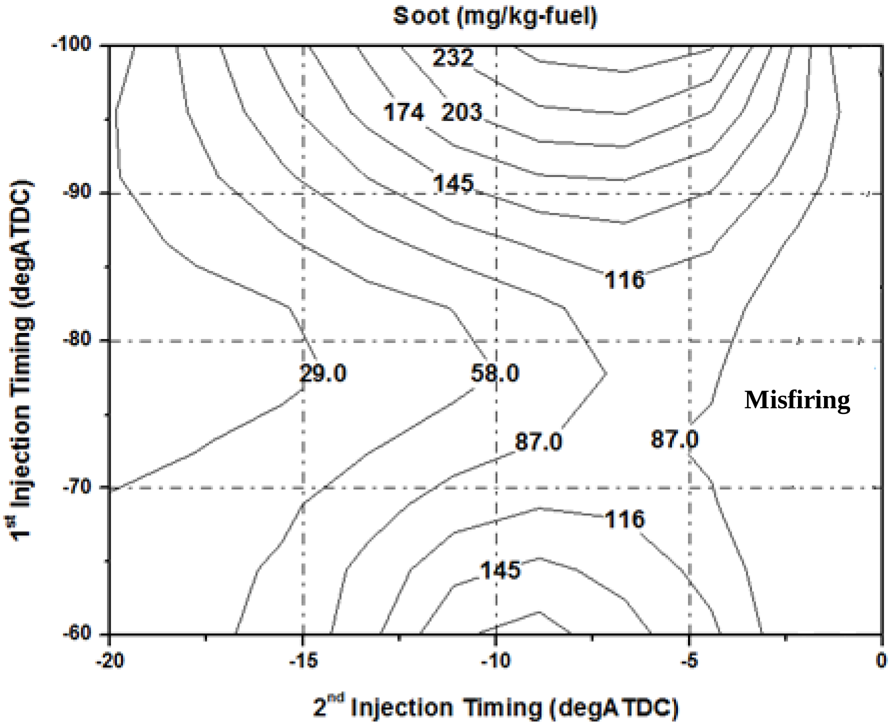

Figure 5.41 Soot Emissions of 50:50 Fuel Distribution at 900 bar Injection Pressure

5.4.4 In-Cylinder Pressure and Heat Release Rate Analysis for Strategy EE at 90 bar injection pressure (70:30 fuel distribution with fixed 1st injection timing at -80 ° CA ATDC)

The in-cylinder pressure traces and corresponding heat release rates for strategy EE averaged over 20 continuous cycles are plotted in Figure 5.42 and Figure 5.43, respectively. Similar to all the previous cases, the heat release process was characterized with two peaks; first one from the auto-ignition of the lean/diluted premixed mixture of 1st injection and a second peak following the auto-ignition of the mixture from 2nd injection. As 2nd injection was advanced, the second peak advanced and then merged with the first peak forming a single and great peak in the heat release rate.

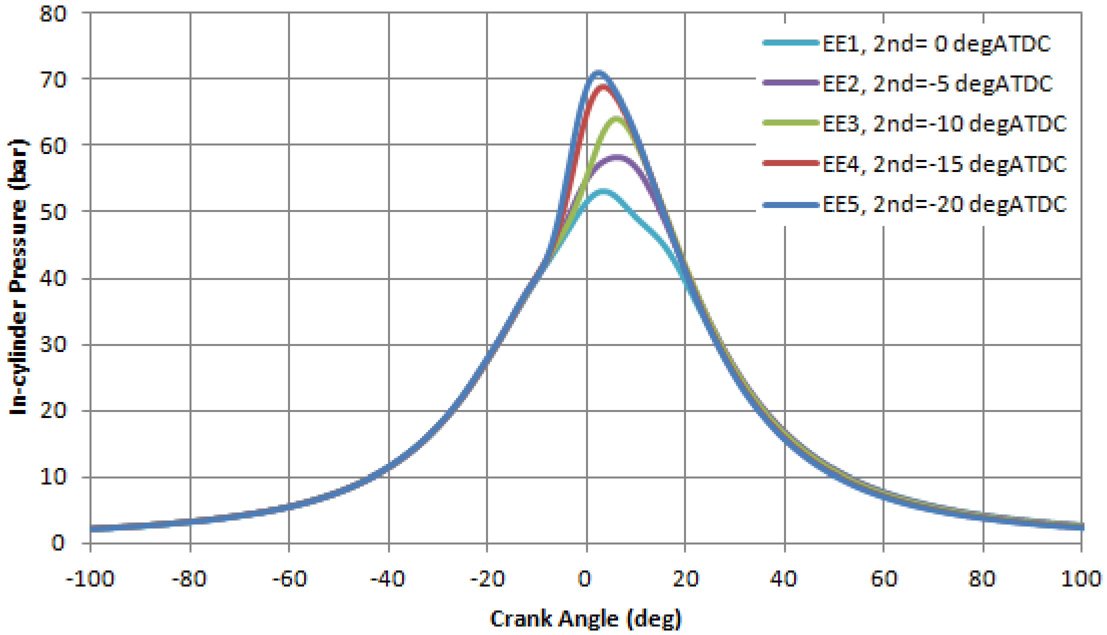

Figure 5.42 In-Cylinder Pressure Traces for Strategy EE (1st injection timing=-80 degATDC)

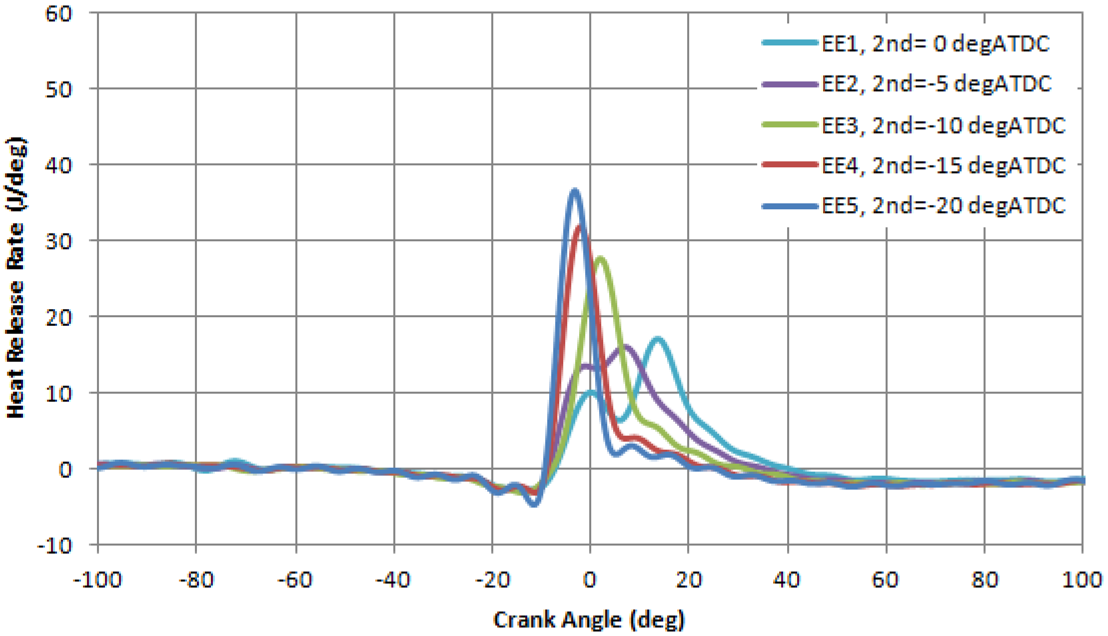

Figure 5.43 Heat Release Rate Traces for Strategy EE (1st injection timing=-80 degATDC)

5.4.5 Analysis of the Effect of Injection Timings on Performance and Combustion of 70:30 Double Injection at 900 bar Injection Pressure

Compared with Figure 5.16 (70:30 fuel injection at 1200bar), 1st injection timing had little effect on the IMEP values other a small region at the top right corner, where the maximum IMEP of 2.9 bar was obtained with earlier 1st injection and retarded 2nd injection. In addition, Figures 5.45 to 5.47 show that the combustion phasing, combustion duration and ignition delay were only affected by 2nd injection timing. As 2nd injection was advanced, the ignition delay became longer due to lower charge temperature, the CA50 occurred earlier as the heat release rate increased and combustion duration became shorter due to more premixed combustion from the 1st injection as well as the 2nd injection after a longer ignition delay.

As shown in Figure 5.48, combustion efficiencies at 900 bar, were slightly higher than those at 1200bar (Figure 5.20). The maximum combustion efficiency was obtained with retarded 1st injection and earlier 2nd injection, because of less over-mixing from the 1st injection and the higher combustion temperature of earlier 2nd injection. The thermal efficiency and indicated efficiencies were marginally higher and they were spread across a wider range of fuel injection timings.

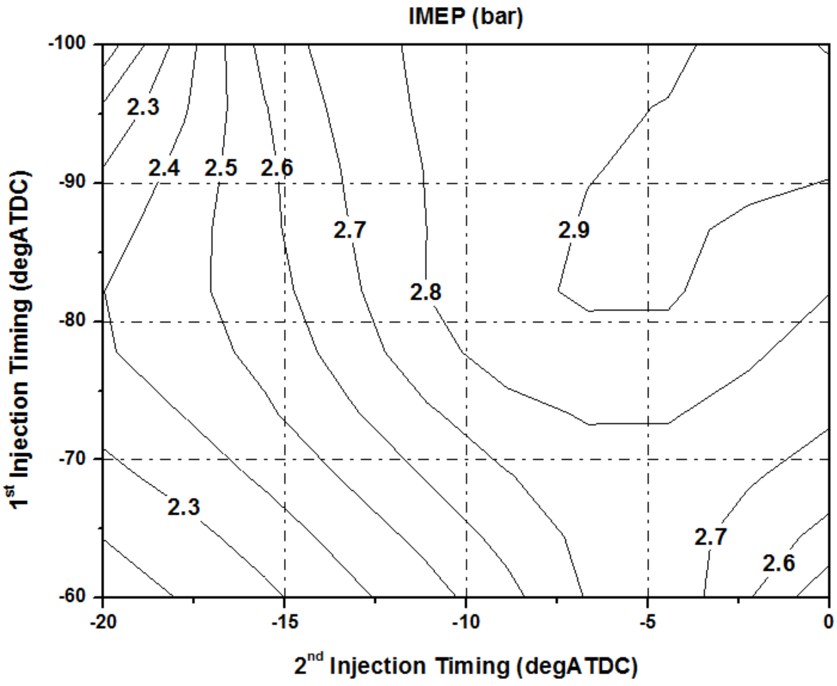

Figure 5.44 IMEP of 70:30 Fuel Distribution at 900 bar Injection Pressure

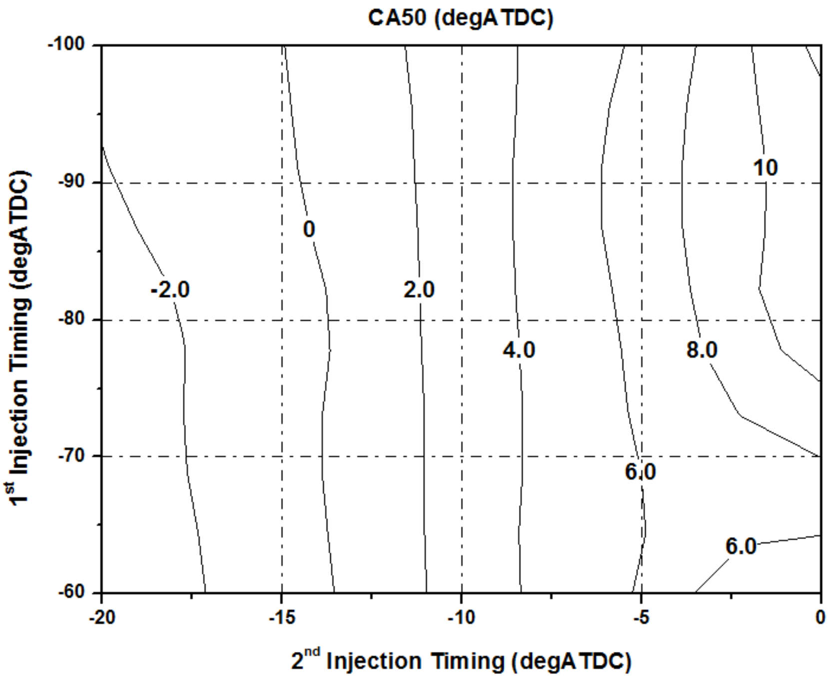

Figure 5.45 Combustion Phasing (CA50) of 70:30 Fuel Distribution at 900 bar Injection Pressure

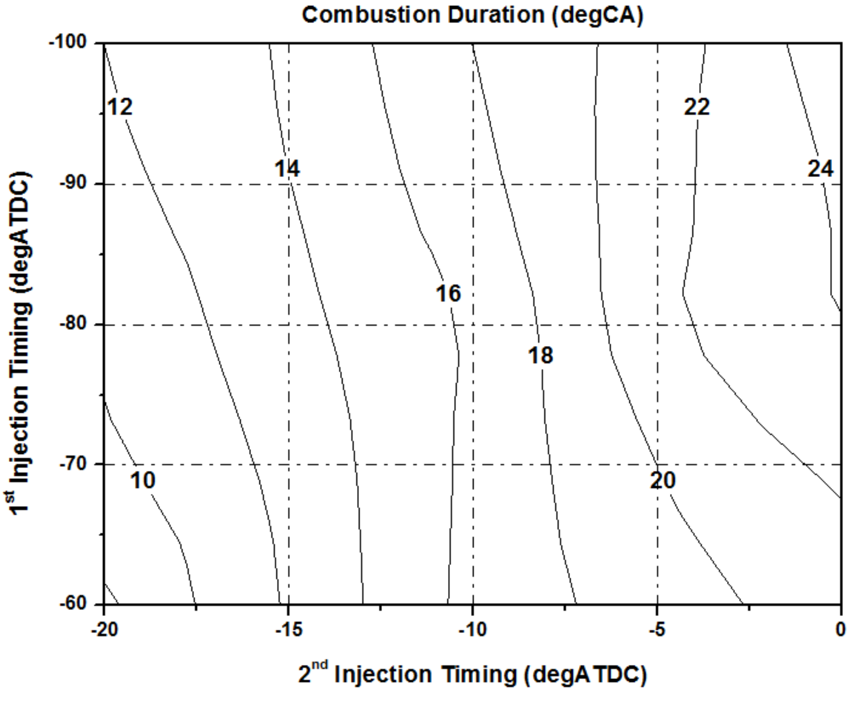

Figure 5.46 Combustion Duration (CA10-90) of 70:30 Fuel Distribution at 900 bar Injection Pressure

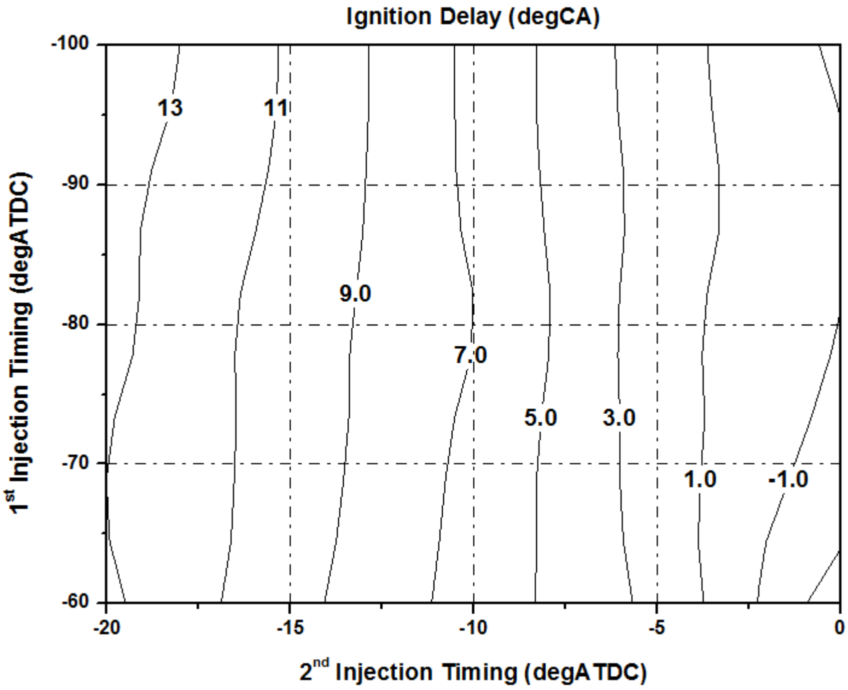

Figure 5.47 Ignition Delay (SOI_{2nd}-CA10) of 70:30 Fuel Distribution at 900 bar Injection Pressure

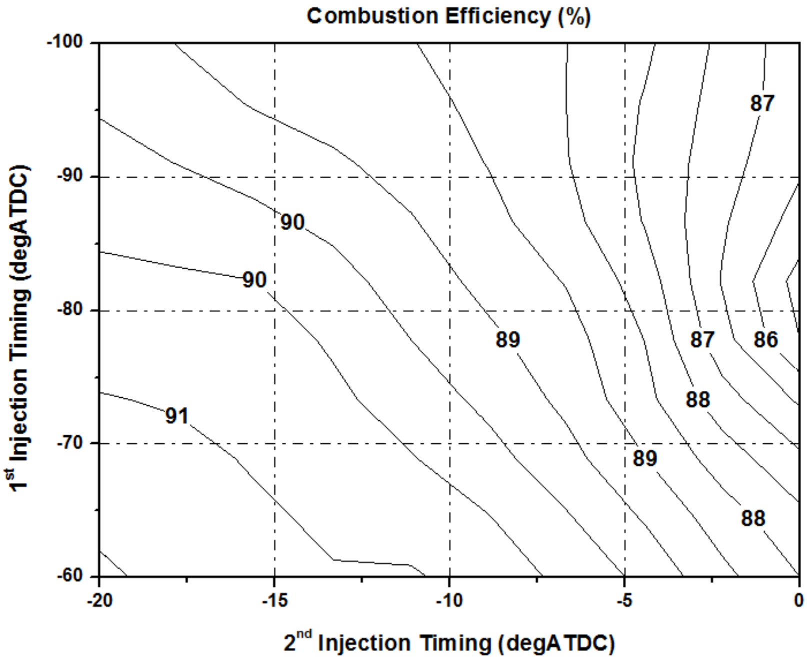

Figure 5.48 Combustion Efficiency of 70:30 Fuel Distribution at 900 bar Injection Pressure

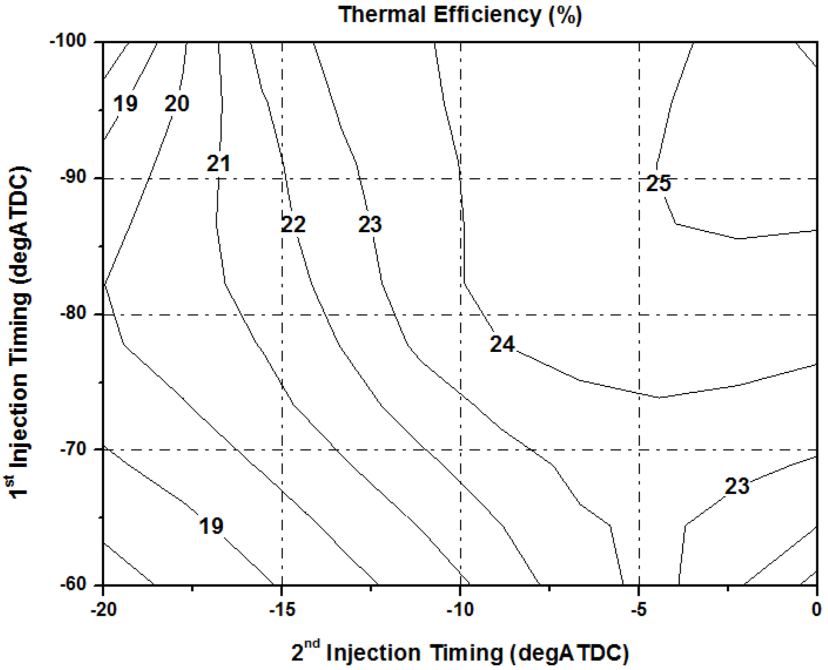

Figure 5.49 Thermal Efficiency of 70:30 Fuel Distribution at 900 bar Injection Pressure

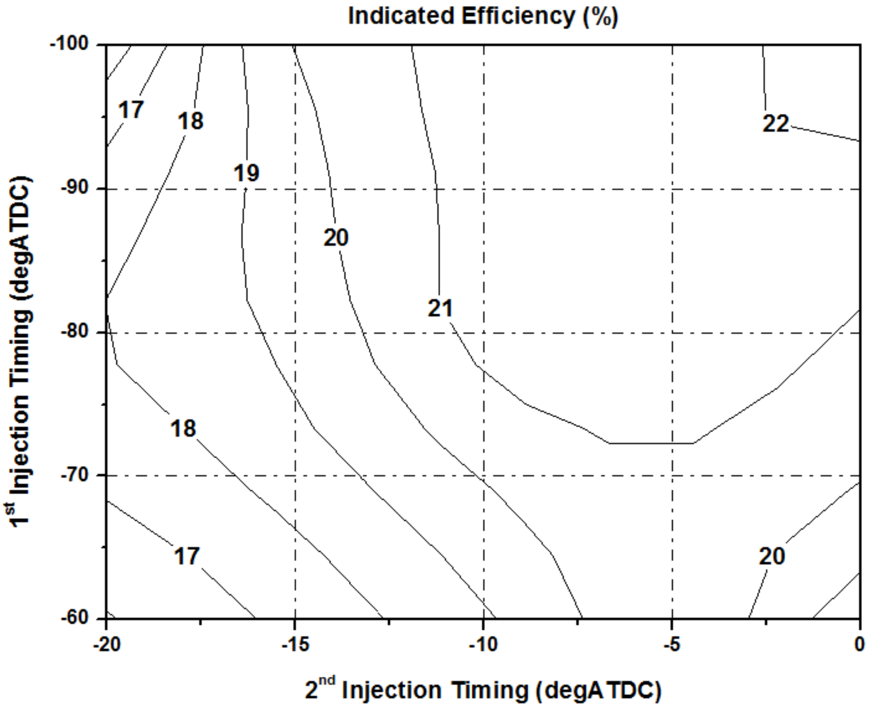

Figure 5.50 Indicated Efficiency of 70:30 Fuel Distribution at 900 bar Injection Pressure

5.4.6 Analysis of the Effect of Injection Timings on Emissions of 70:30 Double Injection at 900 bar Injection Pressure

As shown in Figures 5.51-5.53, exhaust emissions were primarily affected by 2nd injection timings. As 2nd injection was retarded more uHC were produced because of increased fuel rich region and lower oxidation rates at reduced combustion temperature. For the same reason, NOx emissions fell and soot emissions went up with the retarded 2nd injection. Compared to 50:50 injection at 900 bar (Figure 5.39), lower uHC emissions were generated during the late 2nd injections due to less fuel rich regions from smaller amount of 2nd injection. However, when the percentage of 1st injection was increased from 50% to 70% more soot was produced in the region with earlier 1st injection and late 2nd injection, which seemed to point to the presence of fuel rich (probably formed from fuel impingement) from 1st injection.

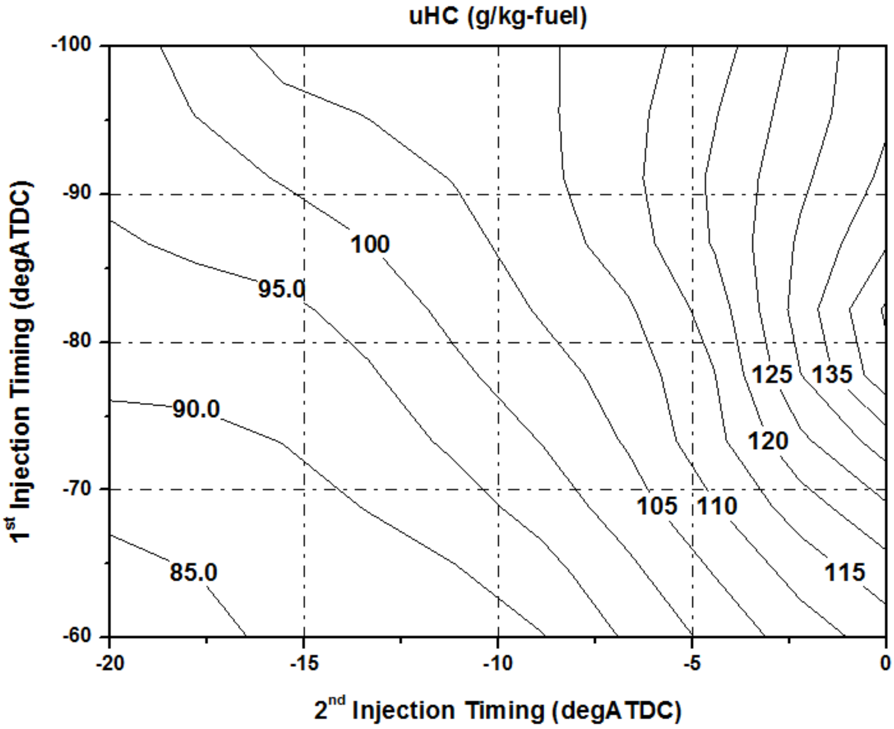

Figure 5.51 uHC Emissions of 70:30 Fuel Distribution at 900 bar Injection Pressure

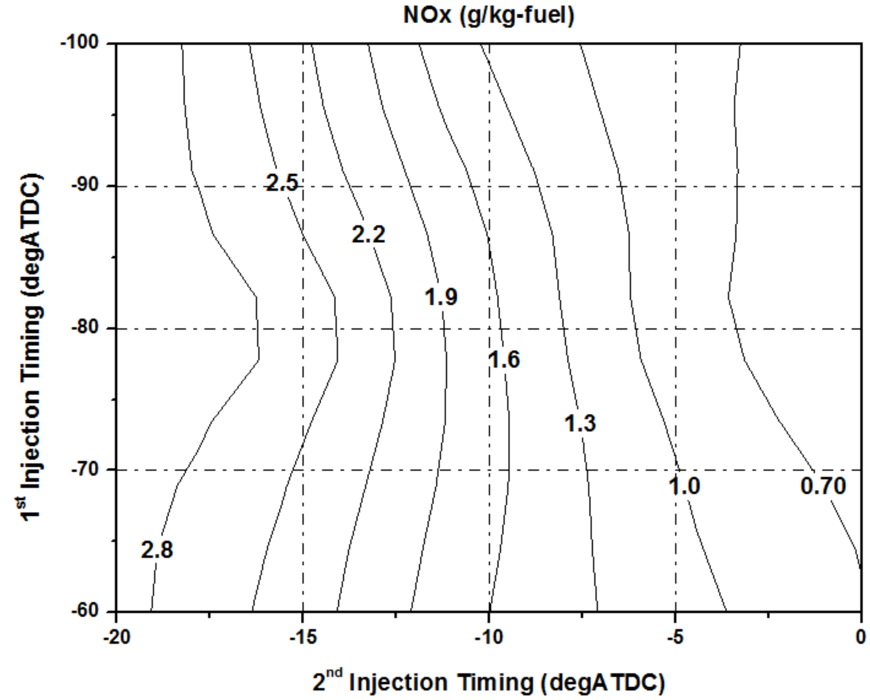

Figure 5.52 NOx Emissions of 70:30 Fuel Distribution at 900 bar Injection Pressure

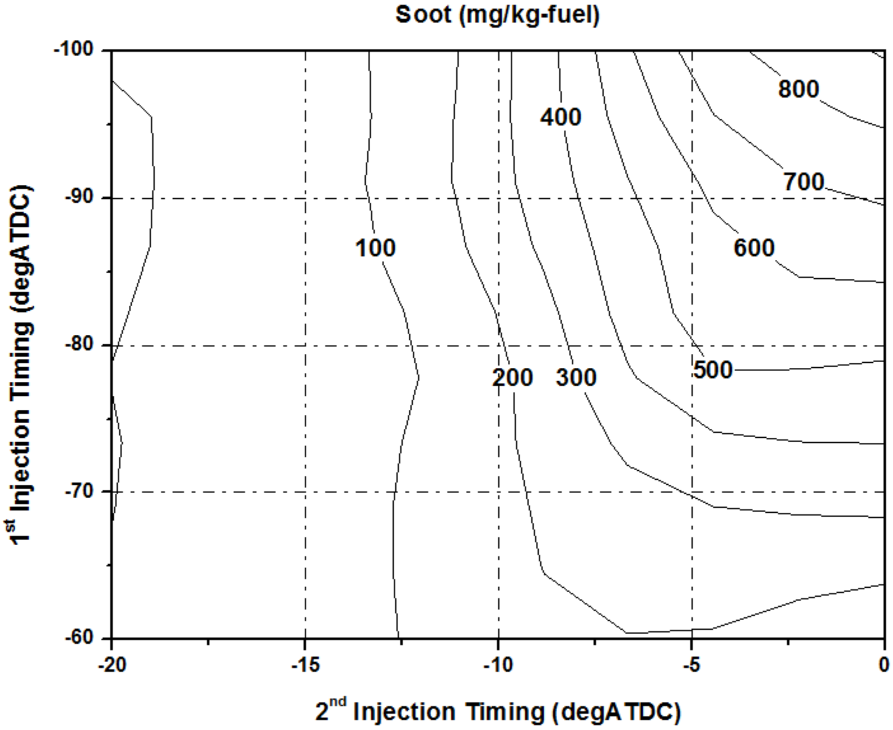

Figure 5.53 Soot Emissions of 70:30 Fuel Distribution at 900 bar Injection Pressure

5.5 Baseline Diesel Combustion at Injection Pressure of 1200bar

The effect of injection timing on combustion characteristics and emissions were investigated at injection pressure of 1200 bar. Pilot+Main injection strategy was implemented for baseline diesel experiment. 10% amount of fuel was injected as pilot injection while rest of fuel was injected in main injection. The dwell angles between injections was categorised as 10, 15 and 20 °CA, respectively. In Figure 5.54, the tested points for all diesel baseline strategies have been plotted in an operation map as a function of injection timings. Only strategy F (dwell 10 ° CA) was discussed in the following section to illustrate the salient features of standard diesel combustion. The combustion characteristics and exhaust emissions were analysed for all the strategies.

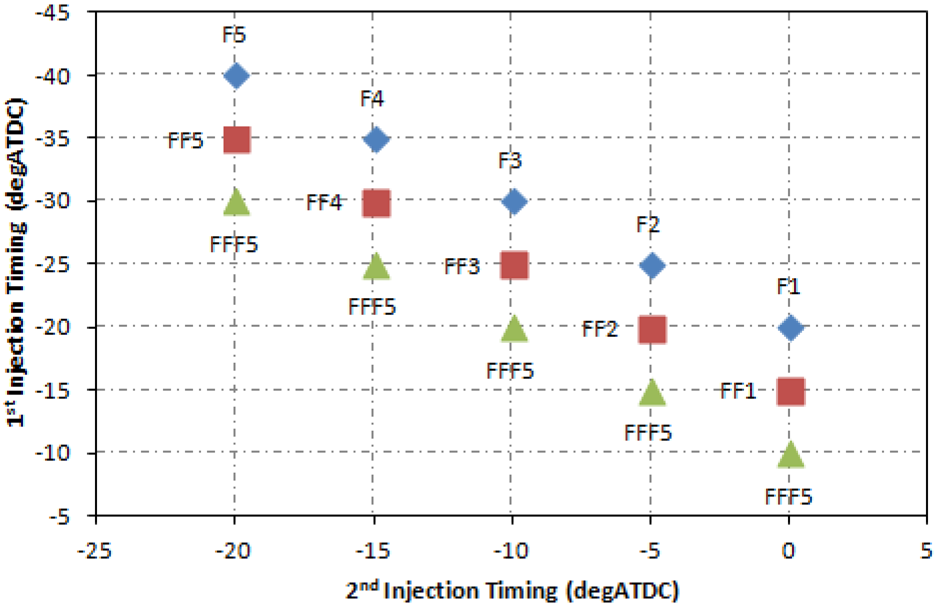

Figure 5.54 Diesel Baseline Injection Strategy

5.5.1 In-Cylinder Pressure and Heat Release Rate Analysis for Strategy F (10:90 fuel distribution with a fixed dwell angle of 20 ° CA ATDC at 1200 bar injection pressure)

The in-cylinder pressure traces and the corresponding heat release rates of baseline diesel combustion operations with a fixed dwell angle are shown Figure 5.55 and Figure 5.56, respectively. Although the first injection was much later and less than that of the high octane PRF, the diesel combustion shared similar trends in its heat release process to the high octane and volatile fuel. With the retarded main injection, a small amount of heat release from the pilot injection was observed. As both the pilot and main injection were advanced, the heat release rate showed only one peak because of the relative longer ignition delay of the 1st injection. The rate of heat release and peak cylinder pressure became higher with the advanced timing as combustion took place closer to TDC.

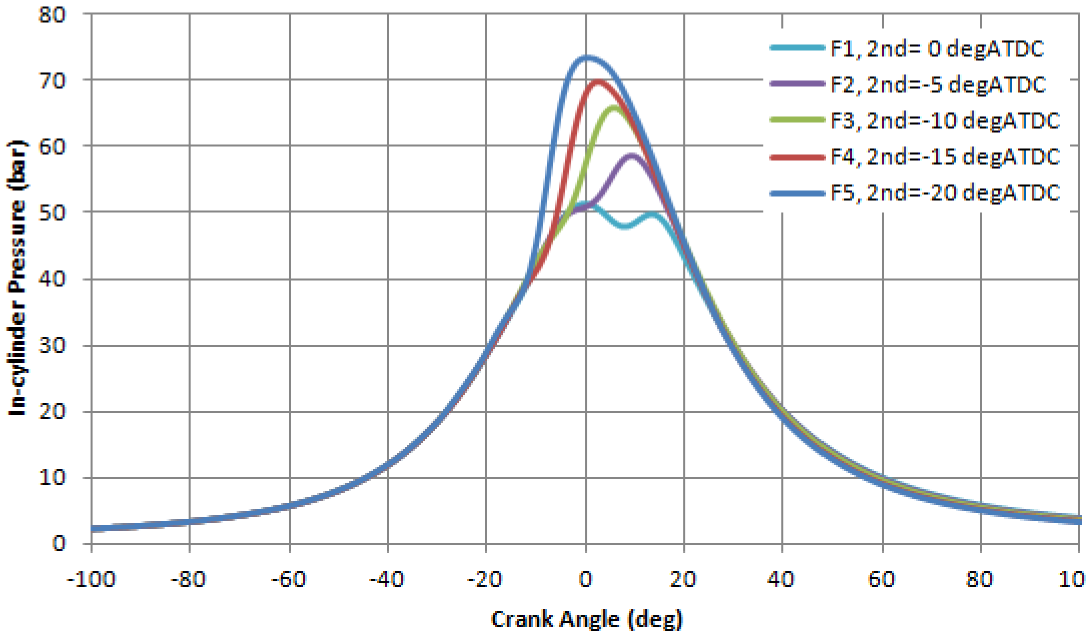

Figure 5.55 In-Cylinder Pressure Traces for Strategy F (fixed dwell angle of 20 ° CA)

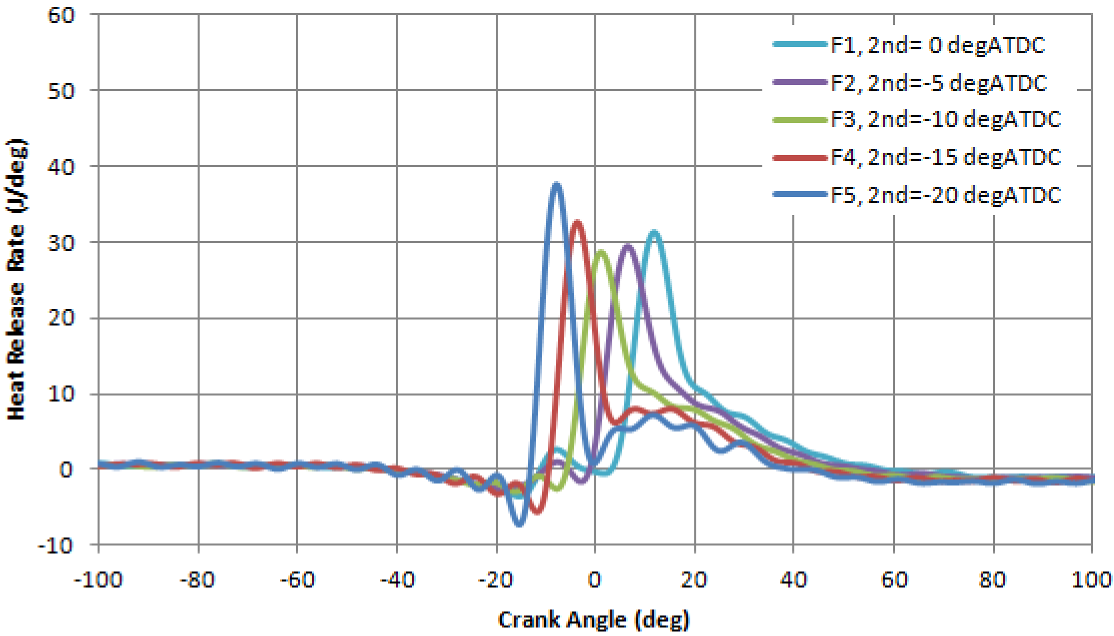

Figure 5.56 Heat Release Rate Traces for Strategy F (fixed dwell angle of 20 °CA)

5.5.2 Analysis of the Effect of Injection Timings on Performance and Combustion of 10:90 Double Injection with Different Dwell Angle at 1200 bar Injection Pressure

The IMEP values for diesel baseline strategies are presented in Figure 5.57. It is noted that diesel baseline operations produced significantly higher IMEP values with a maximum value of 4.4 bar compared to 3.1 bar of gasoline PPC combustion at 900 bar injection pressure. IMEP gradually decreased when injection timings were advanced since combustion phasing was moved away from optimized position. The combustion phasing (CA50) shown in Figure 5.58 was progressively retarded when main injection timing was closer to TDC, and same trend can be observed with retarded pilot injection timing. In terms of combustion duration (CA10-90) in Figure 5.59, the longest combustion process was obtained at early main injection timings while more rapid combustion process was achieved when main injection timing was closer to TDC since higher surrounding temperature and pressure at TDC substantially promoted combustion speed. However, the pilot injection timing had little influence on combustion duration. As shown in Figure 5.60, ignition delay was prolonged when injection timings were advanced.

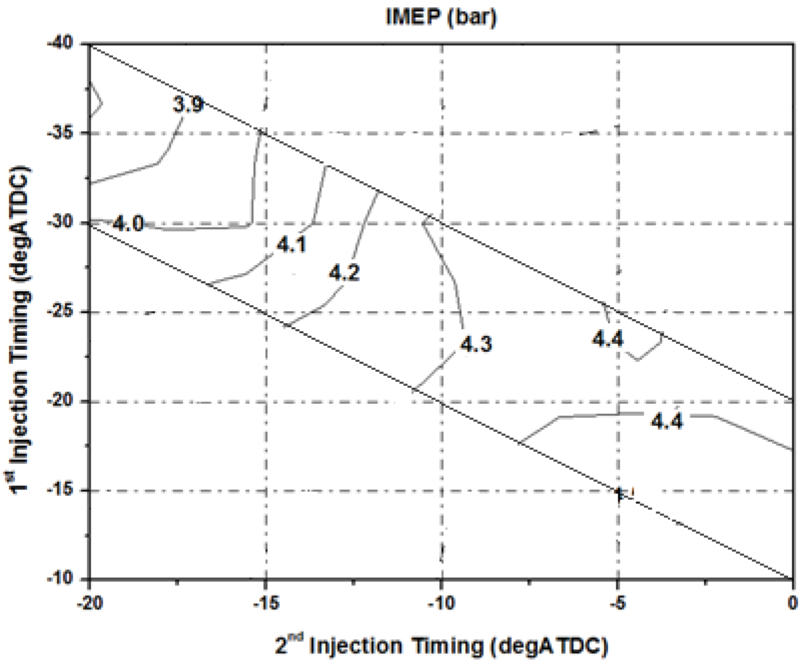

Figure 5.57 IMEP of 10:90 Fuel Distribution at 1200 bar Injection Pressure (diesel)

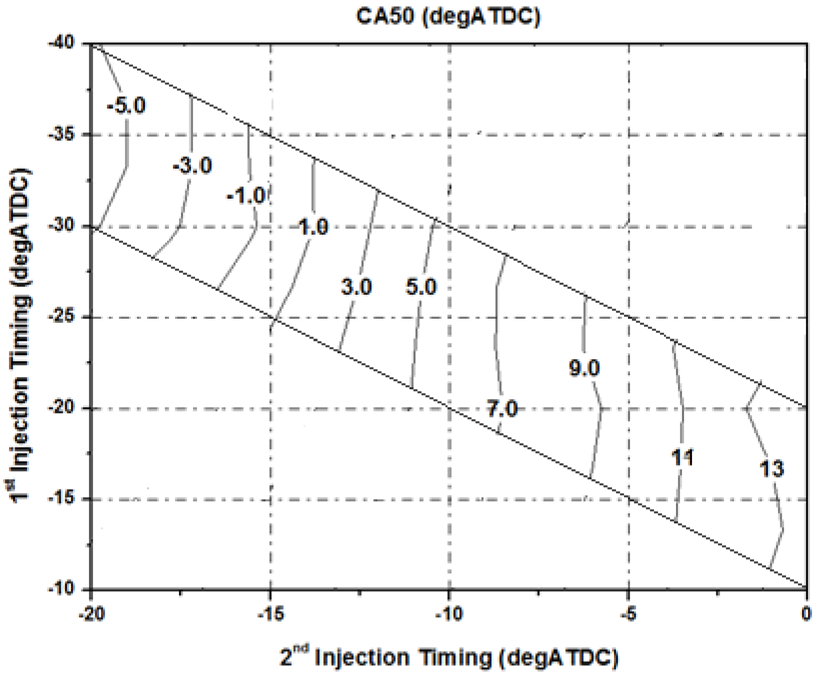

Figure 5.58 Combustion Phasing (CA50) of 10:90 Fuel Distribution at 1200 bar Injection Pressure (diesel)

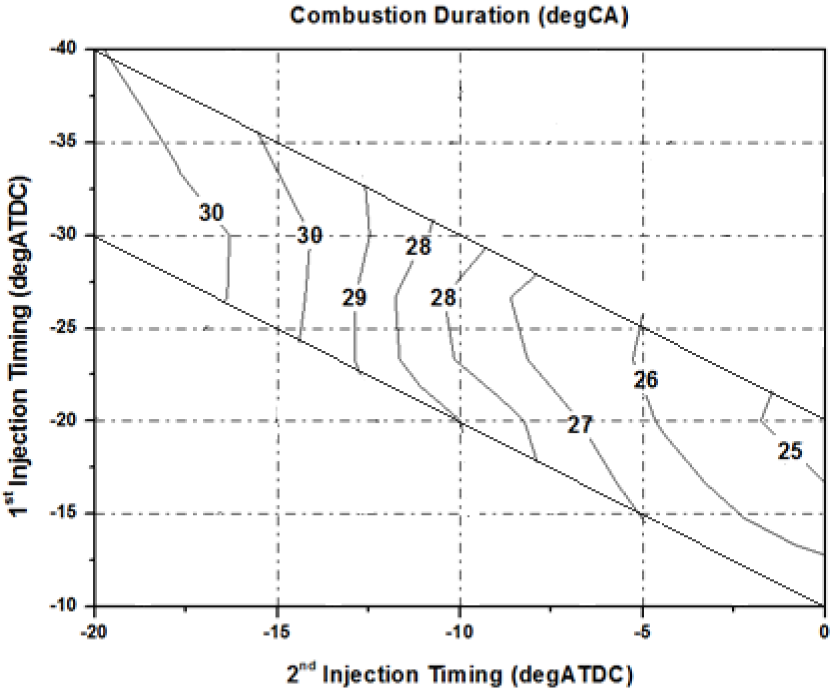

Figure 5.59 Combustion Duration (CA10-90) of 10:90 Fuel Distribution at 1200 bar Injection Pressure (diesel)

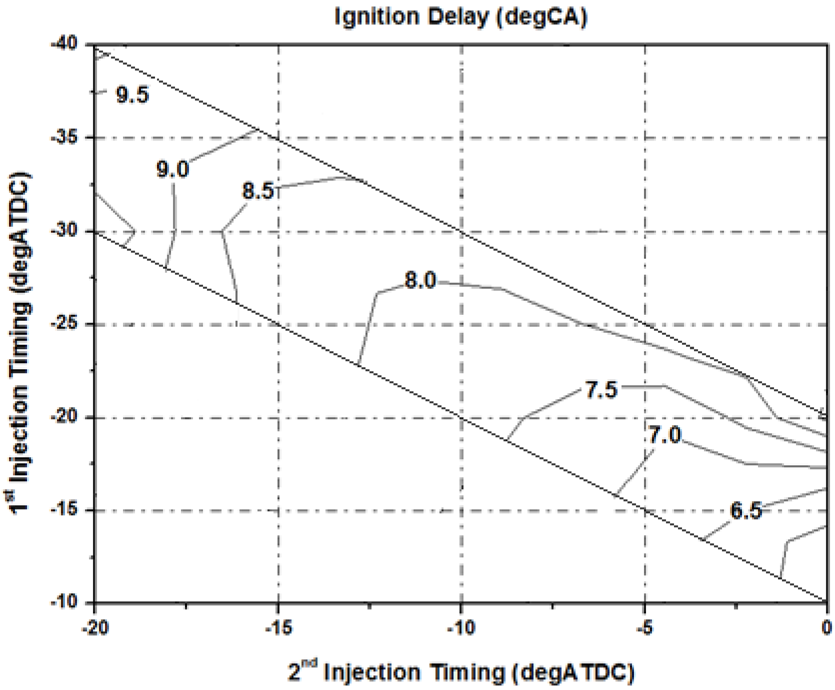

Figure 5.60 Ignition Delay (SOI_{2nd}-CA10) of 10:90 Fuel Distribution at 1200 bar Injection Pressure (diesel)

The combustion efficiency in Figure 5.61 demonstrated that diesel combustion was characterized by excellent combustion efficiency of over 98% throughout the operating range. In comparison, gasoline PPC combustion was limited to typically 90% combustion efficiency. As shown in Figure 5.62, maximum thermal efficiency of 34% was achieved at late injection timings (-25 to -10 °CA ATDC for 1st injection; -10 to 0 °CA ATDC for 2nd injection) due to lowered combustion temperature caused by retarded combustion phasing (CA50). Indicated efficiency shown in Figure 5.63 presented the same trend with varied injection timings. Compared to thermal efficiency, 1% lower of indicated efficiency was detected due to little incomplete combustion.

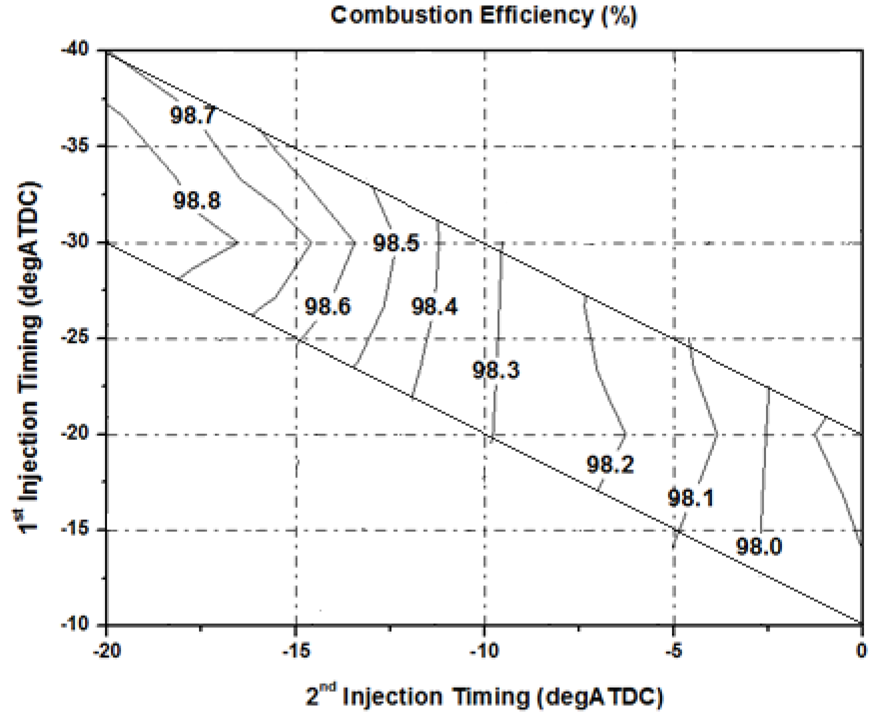

Figure 5.61 Combustion Efficiency of 10:90 Fuel Distribution at 1200 bar Injection Pressure (diesel)

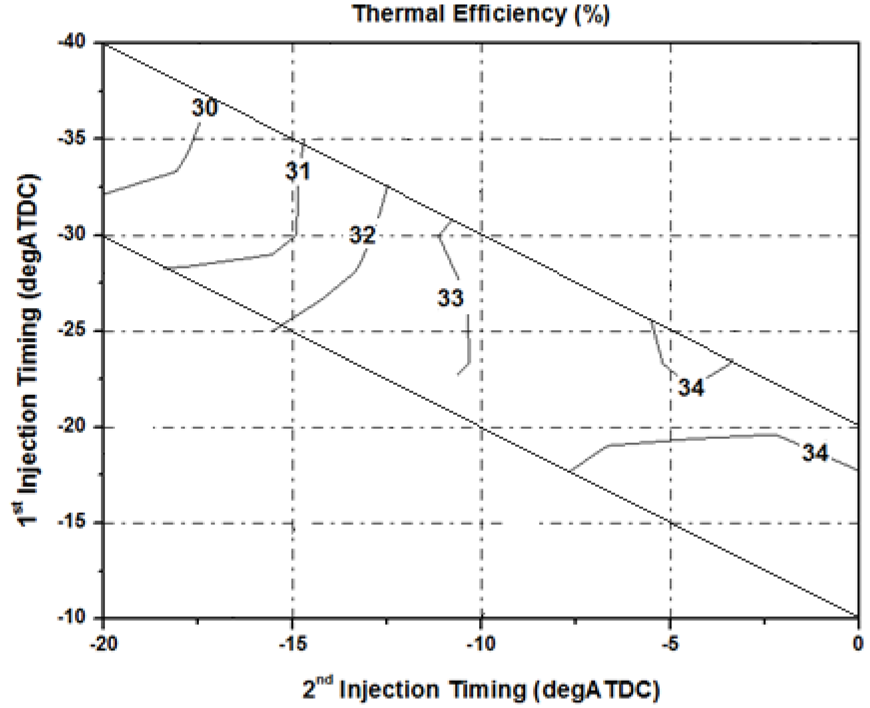

Figure 5.62 Thermal Efficiency of 10:90 Fuel Distribution at 1200 bar Injection Pressure (diesel)

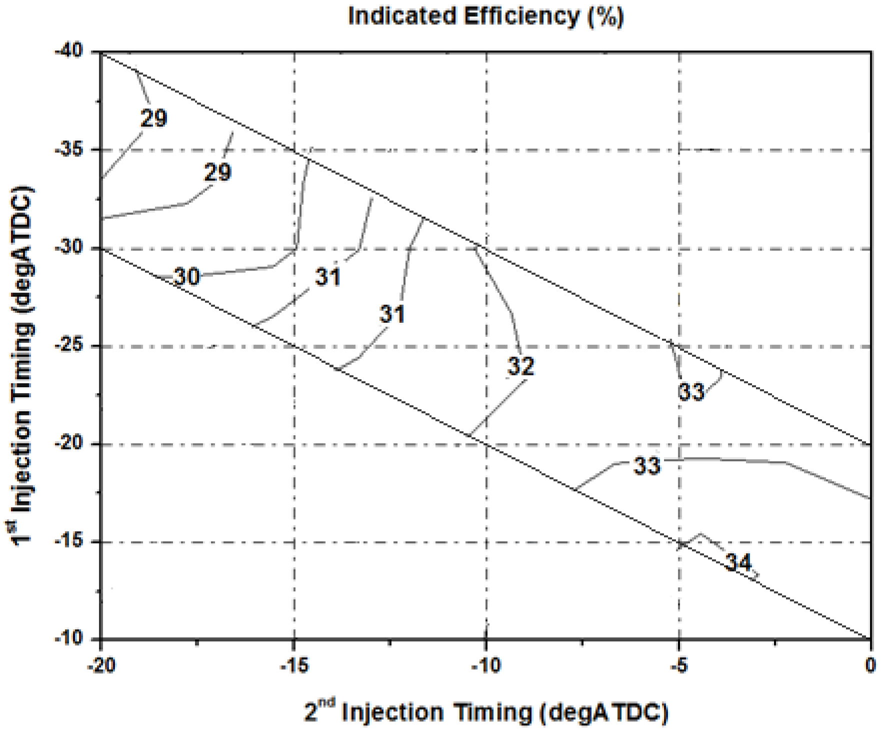

Figure 5.63 Indicated Efficiency of 10:90 Fuel Distribution at 1200 bar Injection Pressure (diesel)

5.5.3 Analysis of the Effect of Injection Timings on Emissions of 10:90 Double Injection with Different Dwell Angle at 1200 bar Injection Pressure

Compared to gasoline PPC operations, the uHC emissions shown in Figure 5.64 demonstrated that diesel combustion produced around 50 times less uHC emission. Such low uHC emissions are caused by the reduced over-mixing, more complete combustion and unburned hydrocarbon oxidations at higher temperature, as well as the absence of premixed charge trapped in the crevices which were more significant in the optical engine. However, diesel combustion emits much more NOx emissions due to higher combustion temperature of stratified near-stoichiometric diesel charge. The increase in NOx emission with advanced injection timing could be explained by the higher combustion temperature. Finally, diesel combustion produced two orders of magnitude higher soot emissions because of the fuel rich mixtures formed from the main injection and shorter ignition delay period. The diesel soot emissions went up with the retarded injection timing as the ignition delay became longer.

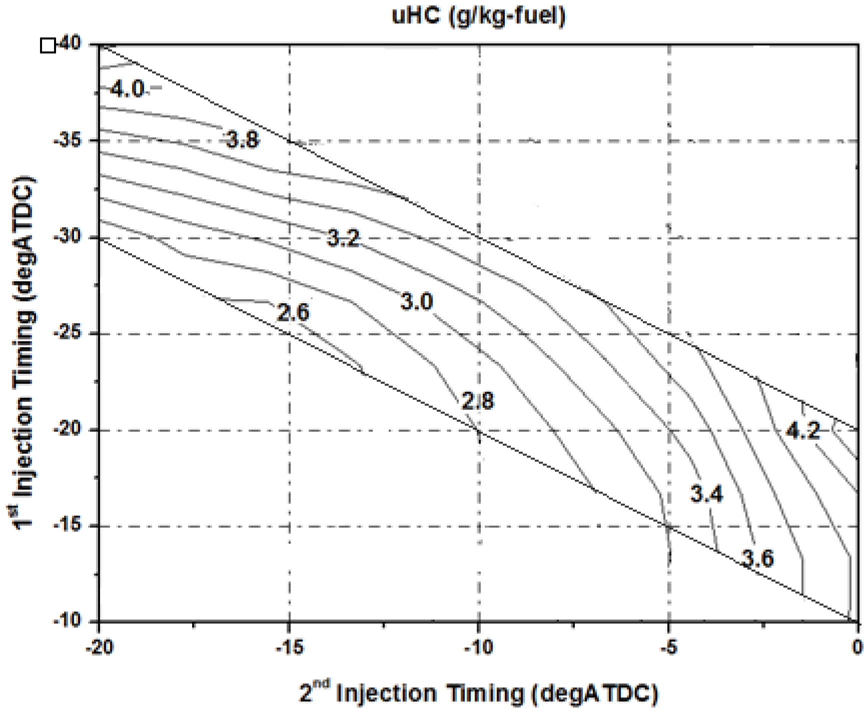

Figure 5.64 uHC Emissions of 10:90 Fuel Distribution at 1200 bar Injection Pressure (diesel)

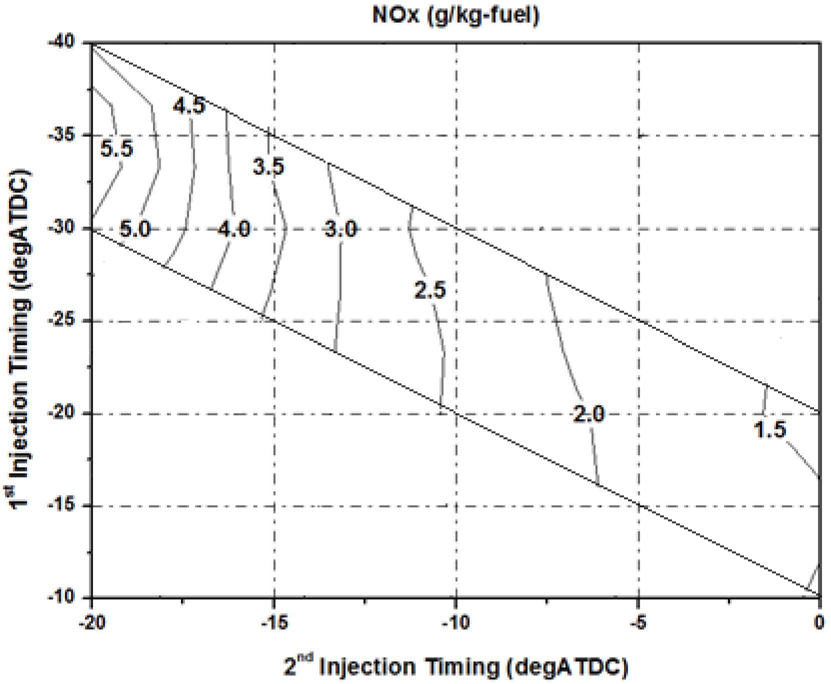

Figure 5.65 NOx Emissions of 10:90 Fuel Distribution at 1200 bar Injection Pressure (diesel)

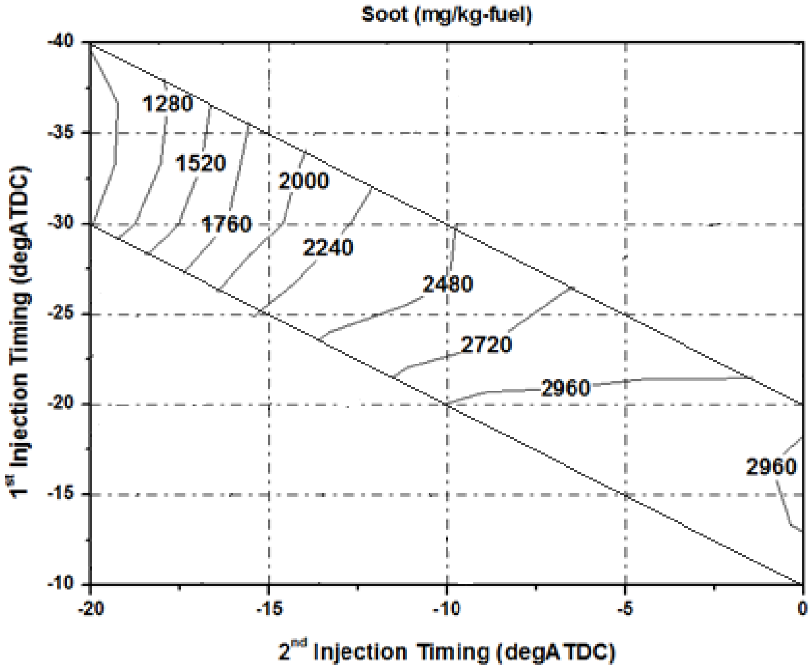

Figure 5.66 Soot Emissions of 10:90 Fuel Distribution at 1200 bar Injection Pressure (diesel)

5.6 Analysis of the Effect of Injection Pressure for Gasoline PPC (900 vs 1200 bar injection pressure at 70:30 fuel distribution strategy)

In order to assess the effect of injection pressure on gasoline PPC, two operating points of the same fuel injection strategies (70:30 injection split, 1st/2nd injection at -80,-5 CA ATDC) were selected: BB2 at 1200 bar injection pressure and EE2 at 900 bar. As shown in Figure 5.67, by reducing injection pressure from 1200 bar to 900 bar, strategy EE2 produced more smoothed pressure rise than strategy BB2. Moreover, the peak in-cylinder pressure value for strategy EE2 was a few crank angles earlier than BB2. As the injection pressure was lowered, the injection duration would have to be prolonged to maintain the amount of fuel injected. The less homogeneous air-fuel mixture created by 1st injection at a lower injection pressure in strategy EE2 could result in earlier auto-ignition, as Figure 5.68 shows.

In terms of heat release rate results in figure 5.68, fairly different heat release processes took place in these two strategies. Strategy BB2 at higher injection pressure indicated a dominating premixed combustion coupling with subtle diffusion combustion sign at the end of combustion event. With strategy EE2 the combustion process was characterized with twin peaks, the first peak just by heat release from 1st injection and the second one after TDC due to heat release of 2nd injection. The maximum heat release rate was substantially reduced in strategy EE2 as the result of late fuel energy release during the expansion stroke. Accordingly strategy EE2 produced approximately 40% longer combustion duration than strategy BB2 due to increased injection duration.

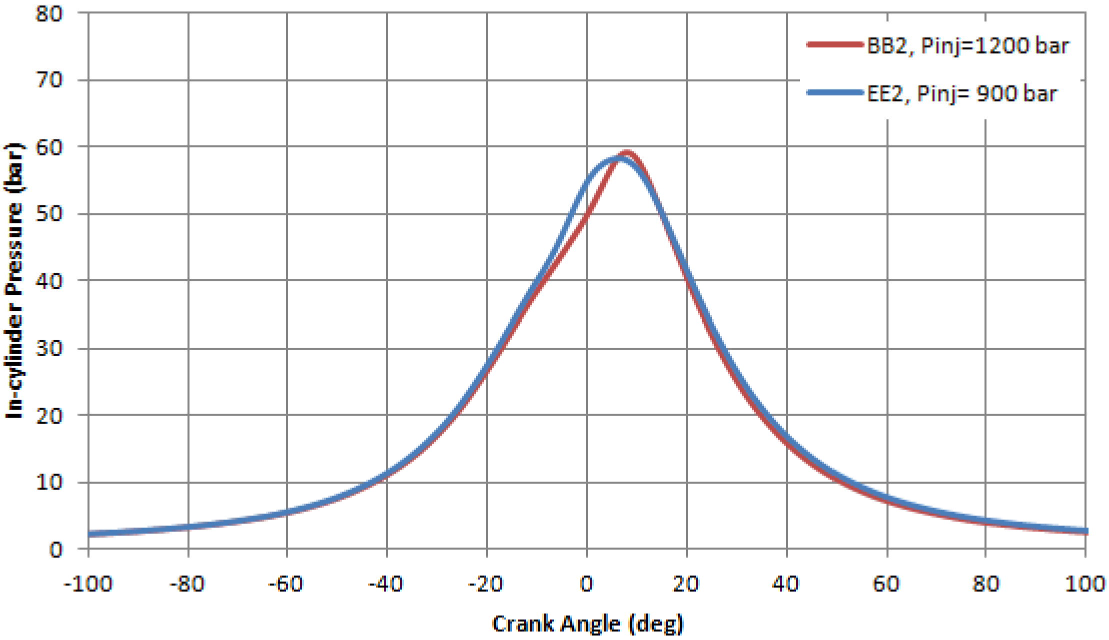

Figure 5.67 Comparison of In-Cylinder Pressure Traces for Strategy BB2 and EE2

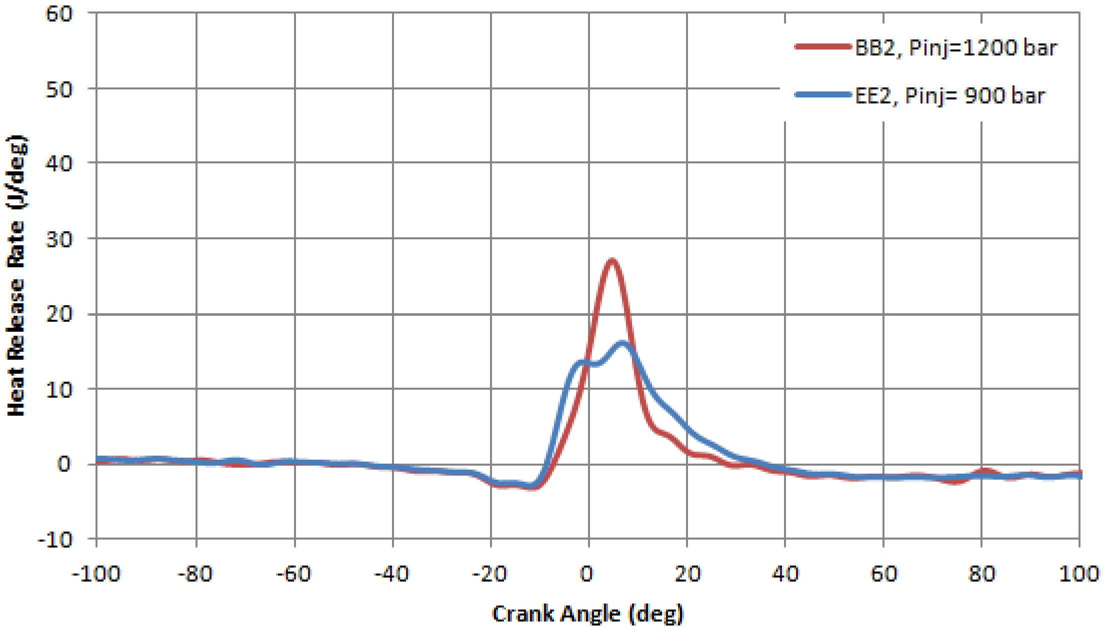

Figure 5.68 Comparison of Heat Release Rate Traces for Strategy BB2 and EE2

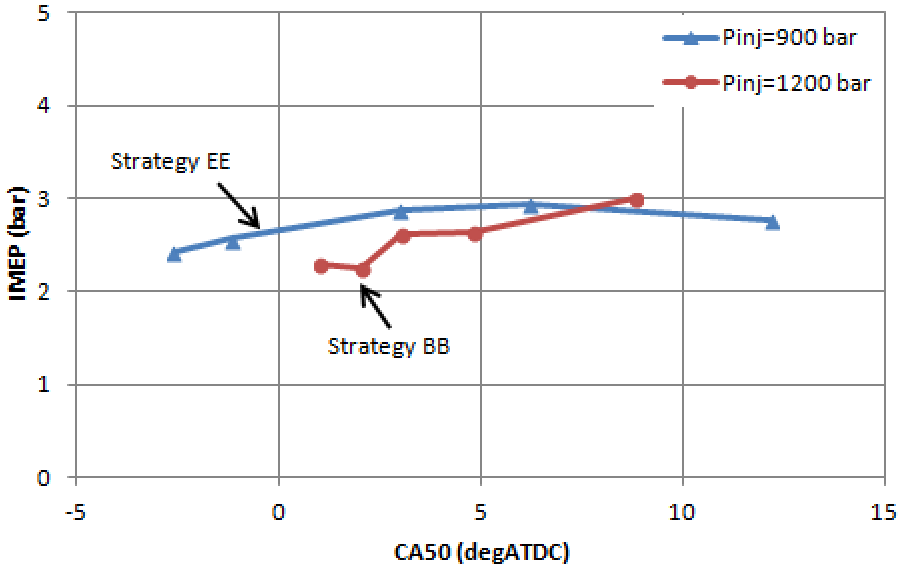

Figure 5.69 Comparison of Combustion Phasing (CA50) between 900 and 1200 bar Injection Pressure

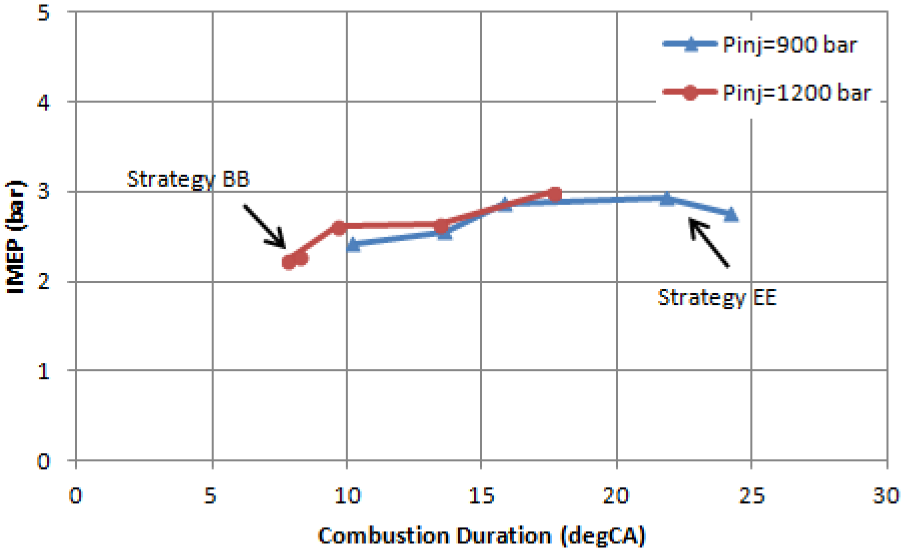

Figure 5.70 Comparison of Combustion Duration (CA10-90) between 900 and 1200 bar Injection Pressure

Effects of injection pressure on the overall gasoline PPC operations at different injection timings are shown in Figures 5.69 to 5.73. It is noted that the IMEP values were less sensitive to the combustion phasing (CA50) and combustion duration at 900 bar injection pressure than higher injection pressure at 1200 bar. Thus, more flexible positioned combustion control can be achieved by lower injection pressure without losing output work. As shown in Figure 5.70, lower injection pressure extended combustion duration by approximately 20%. This was mainly attributed to increased injection duration at 900 bar injection pressure. Figure 5.71 shows that higher injection pressure extended ignition delay due to probably more homogeneous charge formed prior to onset of combustion.

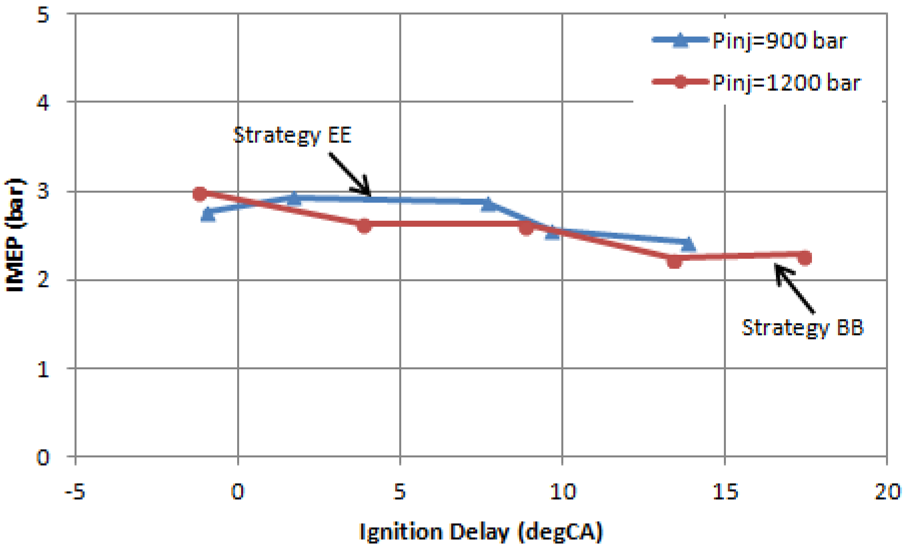

Figure 5.71 Comparison of Ignition Delay (SOI_{2nd}-CA10) between 900 and 1200 bar Injection Pressure

Figure 5.72 shows that dramatic reduction in soot emissions was achieved at higher injection pressure 1200 bar. The high injection pressure substantially promoted fuel-air mixing process and hence homogeneous charge was generated before the combustion took place. In addition, prolonged injection duration of 900 bar case led the extended combustion progress during the fuel injection event resulted in diffusion combustion thereby created excessive soot formation. However, NOx emissions were remained at very low level due to overall low temperature combustion. As shown in Figure 5.73, the uHC emissions were similar at the two injection pressures. However uHC emissions were more sensitive to injection timings at 900 bar injection pressure than at 1200 bar injection.

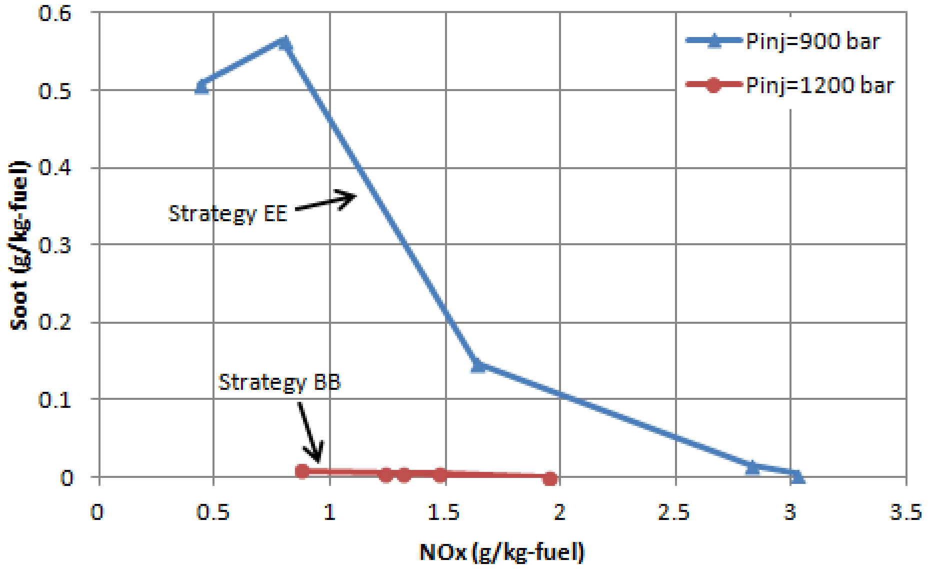

Figure 5.72 Comparison of Soot and NOx Emissions between 900 and 1200 bar Injection Pressure

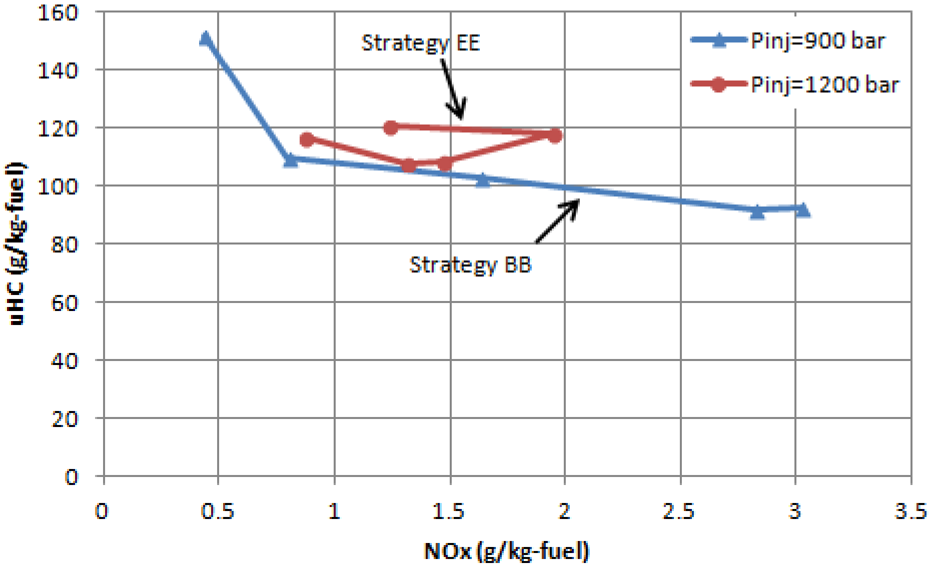

Figure 5.73 Comparison of uHC and NOx Emissions between 900 and 1200 bar Injection Pressure

5.7 Analysis of the Effect of Fuel Distribution for Gasoline PPC (50:50 vs 70:30 strategy at 1200 bar injection pressure)

In order to evaluate the effect of fuel quantity in each of the double injections, equally split injection quantity (50:50) strategy AA and 70:30 fuel quantity distributions strategy BB have been selected for comparison.

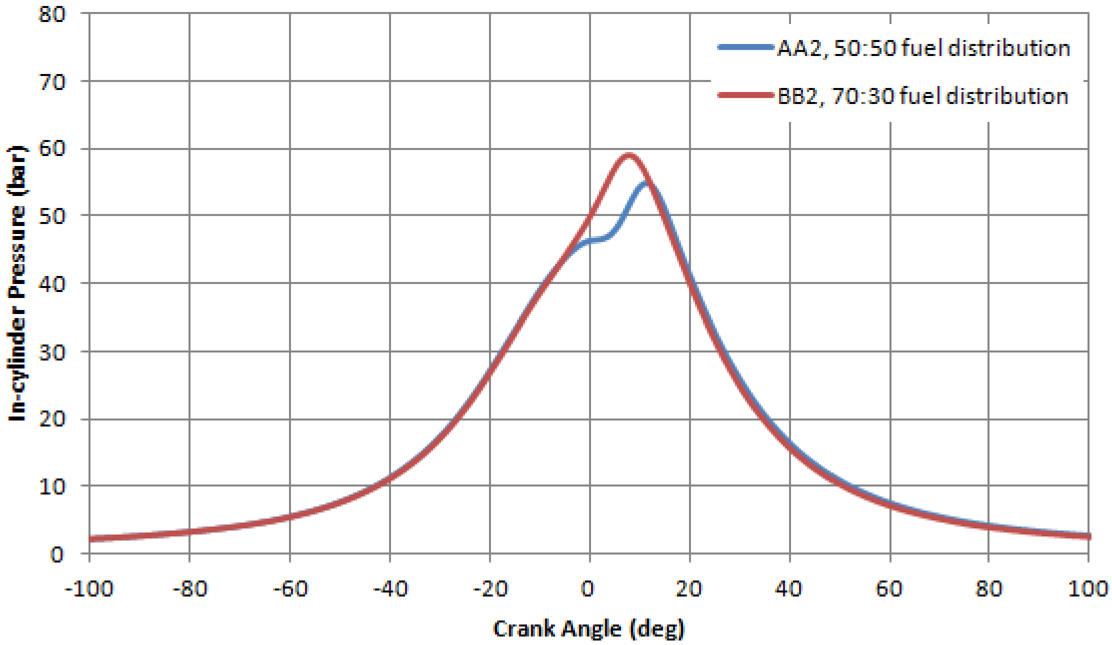

Figure 5.74 Comparison of In-Cylinder Pressure Traces for Strategy AA2 and BB2

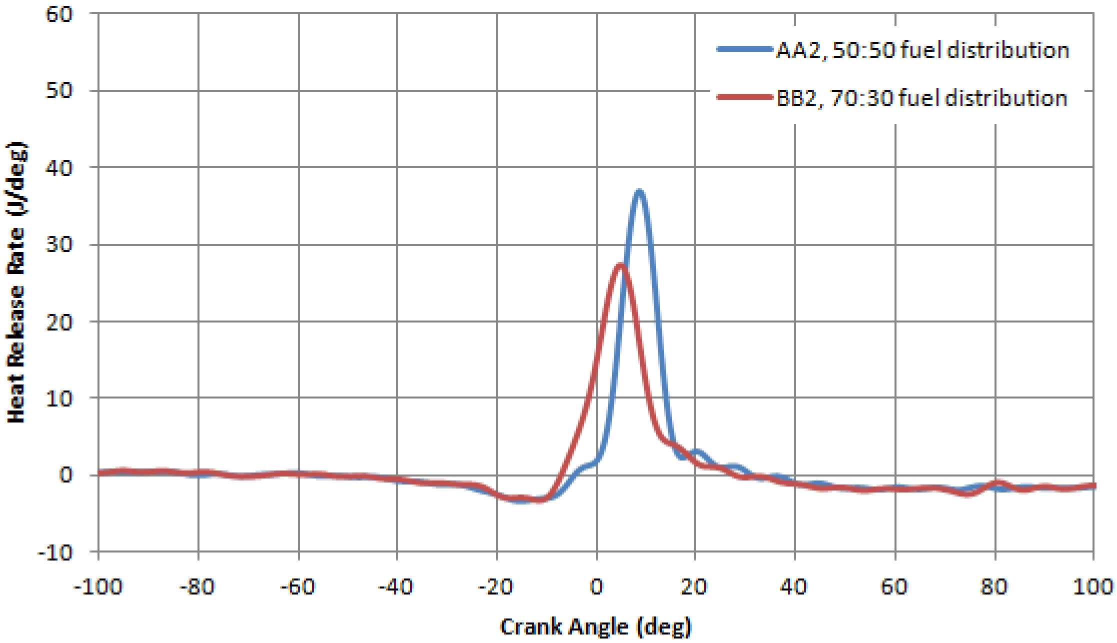

Figure 5.75 Comparison of Heat Release Rate Traces for Strategy AA2 and BB2

As shown in Figure 5.74, the BB2 case (injection timings at -80,-5 ° CA ATDC) was characterized with earlier, faster and higher pressure rise than the AA2 case. This was attributed to more fuel injected during 1st injection of strategy BB2, which led the formation of more near stoichiometric fuel-air mixture and hence earlier auto-ignition. Correspondingly, the heat release rate for strategy BB2 initiated earlier at the end of compression stroke than strategy AA2. In addition, the short ignition delay after 2nd injection in BB2 slowed down the heat release rate as more diffusion combustion took place.

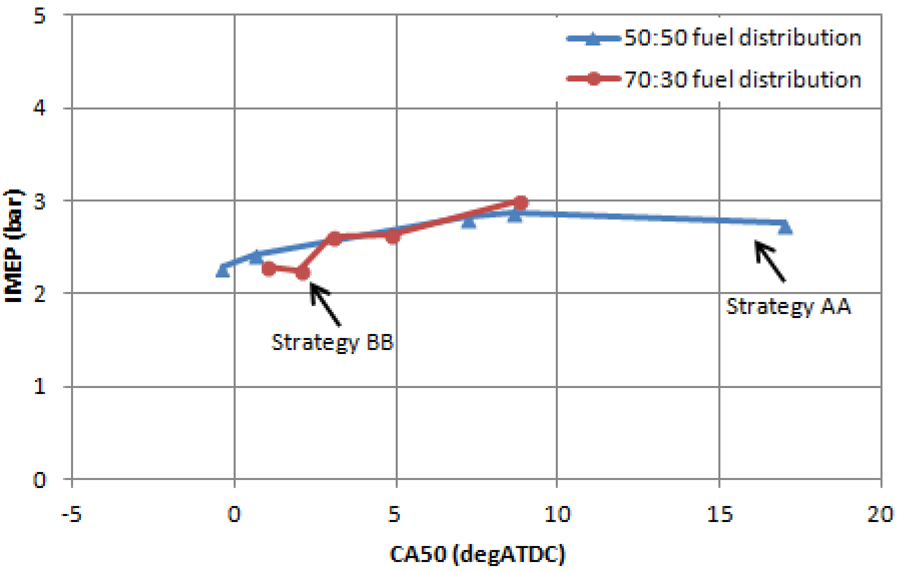

Figure 5.76 Comparison of Combustion Phasing (CA50) between 50:50 and 70:30 Fuel Distribution Strategy

As shown in Figure 5.76, combustion phasing (CA50) was spread over a wide range of TDC 17 ° CA ATDC for 50:50 fuel injections and is was limited between 0 to 10 ° CA ATDC for 70;30 fuel injections. But the spread of combustion durations (CA10-90) of the two injection strategies were almost the same. Figure 5.78 shows that the ignition delay of 70:30 strategy was more sensitive to the fuel injection timings than 50:50 strategy. Shorter ignition delays were found with 70:30 injections when 2nd injection was retarded, because of the higher charge temperature at the start of 2nd junction due to the more heat released from increased 1st injection.

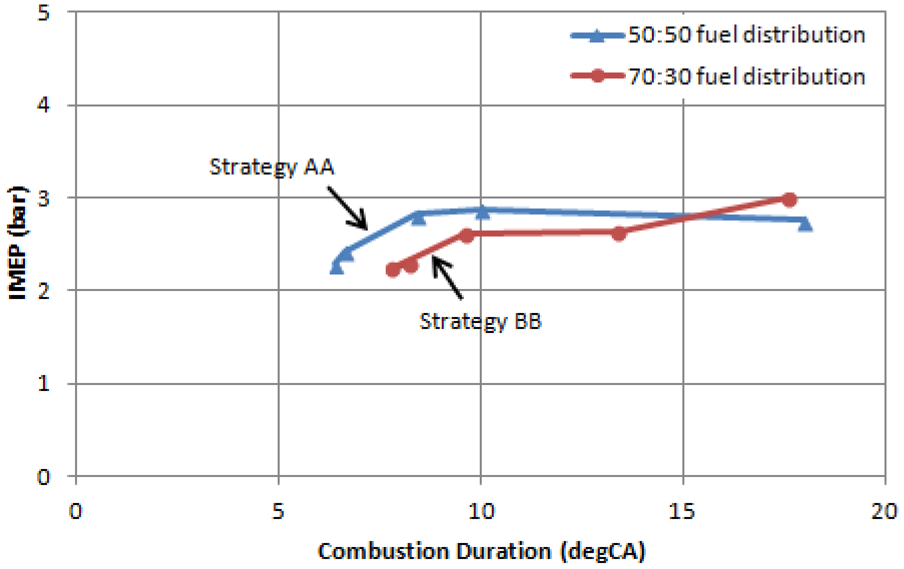

Figure 5.77 Comparison of Combustion Duration (CA10-90) between 50:50 and 70:30 Fuel Distribution Strategy

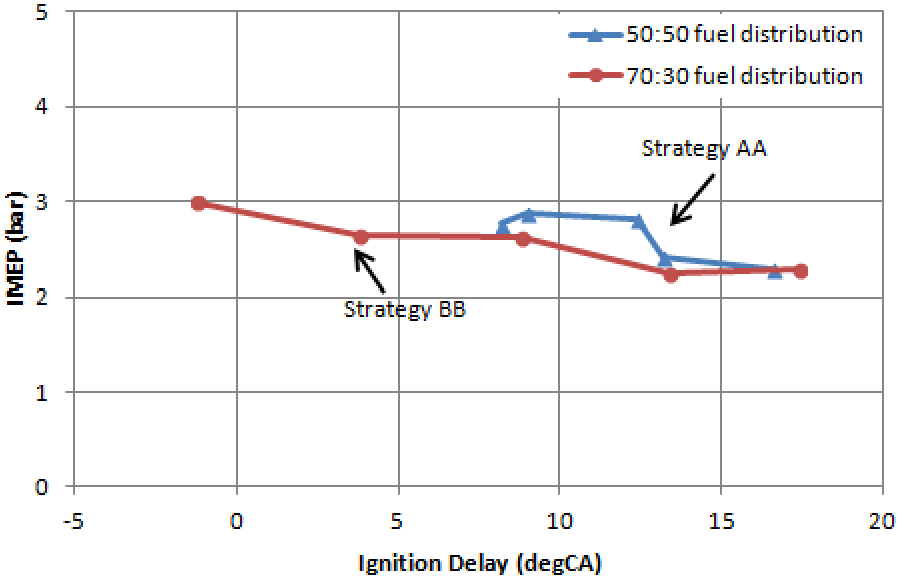

Figure 5.78 Comparison of Ignition Delay (SOI_{2nd}-CA10) between 50:50 and 70:30 Fuel Distribution Strategy

The exhaust emissions and soot concentration for the 50:50 and 70:30 injection strategies are shown in Figures 5.79 and 5.80, respectively. The soot concentration for both strategies stayed at ultra-low level due to lean premixed combustion. Increased amount of 1st injection tended to produce more soot, probably because of poor atomisation and more fuel impingement during the 1st injection, and lower oxidation rate at lower combustion temperature. In addition, uHC emissions during 50:50 fuel injection operations showed more variation with injection timings. Furthermore, 50:50 strategy resulted in some increase in NOx emissions due to higher combustion temperature.

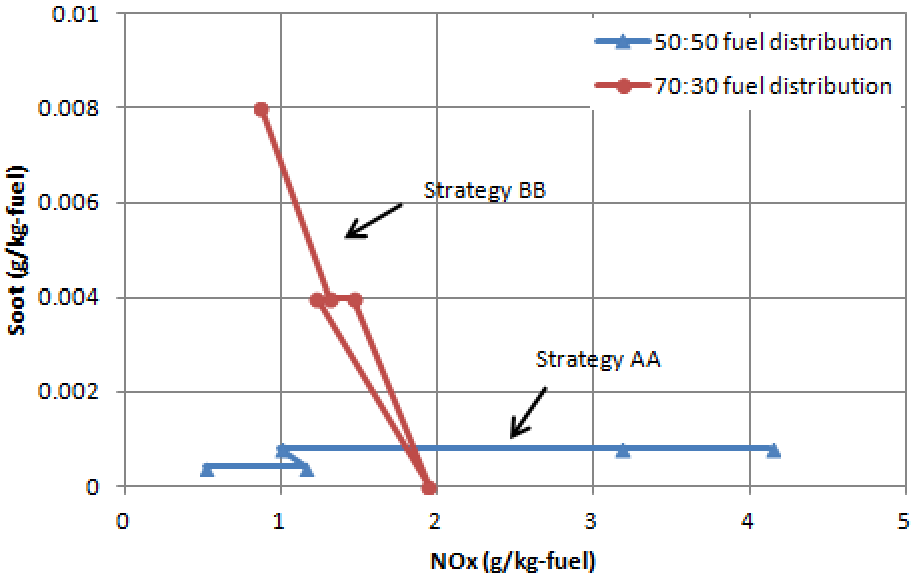

Figure 5.79 Comparison of Soot and NOx Emissions between 50:50 and 70:30 Fuel Distribution Strategy

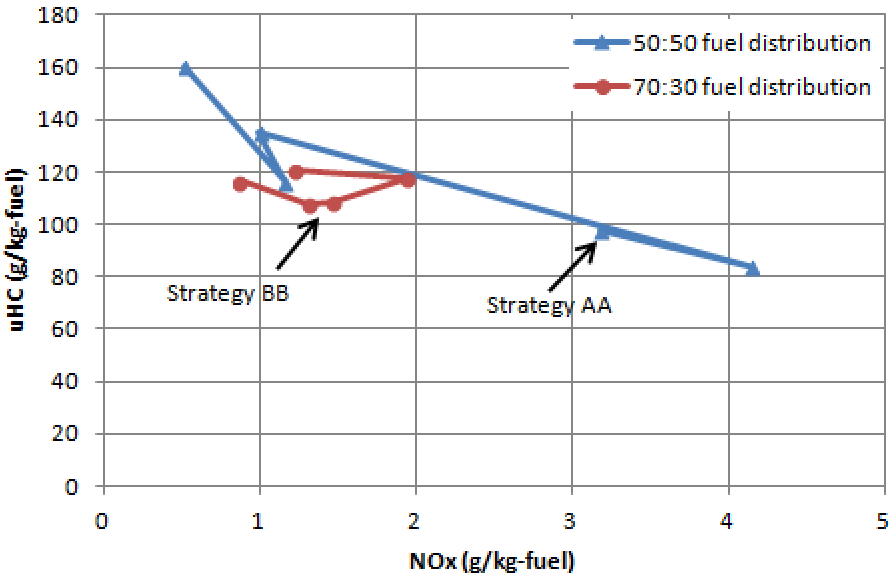

Figure 5.80 Comparison of uHC and NOx Emissions between 50:50 and 70:30 Fuel Distribution Strategy

5.8 Analysis of the Effect of Fuel Type (gasoline PPC vs diesel baseline at 1200bar injection pressure)

The effects of different fuels on combustion and emission are discussed in this section. Figure 5.81 and Figure 5.82 plot the in-cylinder pressure, heat release rate and injection drive signal for PRF (strategy BB2) and diesel fuel (strategy F2), respectively. These results were obtained at nearly identical engine running conditions. Lambda value and EGR concentration were controlled at the same level in order to achieve the identical overall mixture compositions. The intake temperature was increased from 100 to 150 degree for PRF in order to achieve stable combustion operations. In terms of mixture formation and combustion processes, partially premixed combustion was utilised for high octane fuel while typical pilot+main injection strategy was employed in diesel operations. The injection timings for both cases were indicated by injection drive signal in Figures 5.81 and 5.82.

By setting the injection timings at -80 and -5 ° CA ATDC, the partially premixed combustion was achieved for gasoline case (strategy BB2). Relative homogeneous charge was generated under the effect of 1st injection while 2nd injection was placed around TDC to trigger the main combustion event. The auto-ignition of the premixed fuel/air mixture appeared 70 ° CA after the start of 1st injection due to the high octane number of PRF and the lower charge temperature. In comparison, auto-ignition was detected shortly after the end of the pilot injection of diesel because of the high cetane number and hotter charge temperature. In addition, it is noted that diesel combustion was characterized with a larger portion of diffusion combustion as indicated by the slower heat release rate during the latter part of the heat release process.

As shown in Figure 5.83, the combustion phasing (CA50) were evenly distributed in the range of -5 to 20 ° CA ATDC for both cases as the injection timings were varied. However, Figure 5.84 shows that combustion durations (CA10-90) of PPC operations were considerably shortened compared to diesel combustion, due to rapid premixed combustion after longer ignition delays following the 1st injection and 2nd injections. In Figure 5.85, it can be seen that the ignition started 5 °CA before to 20 °CA after as the start of 2nd injection was advanced from TDC to -20 °CA ATDC.

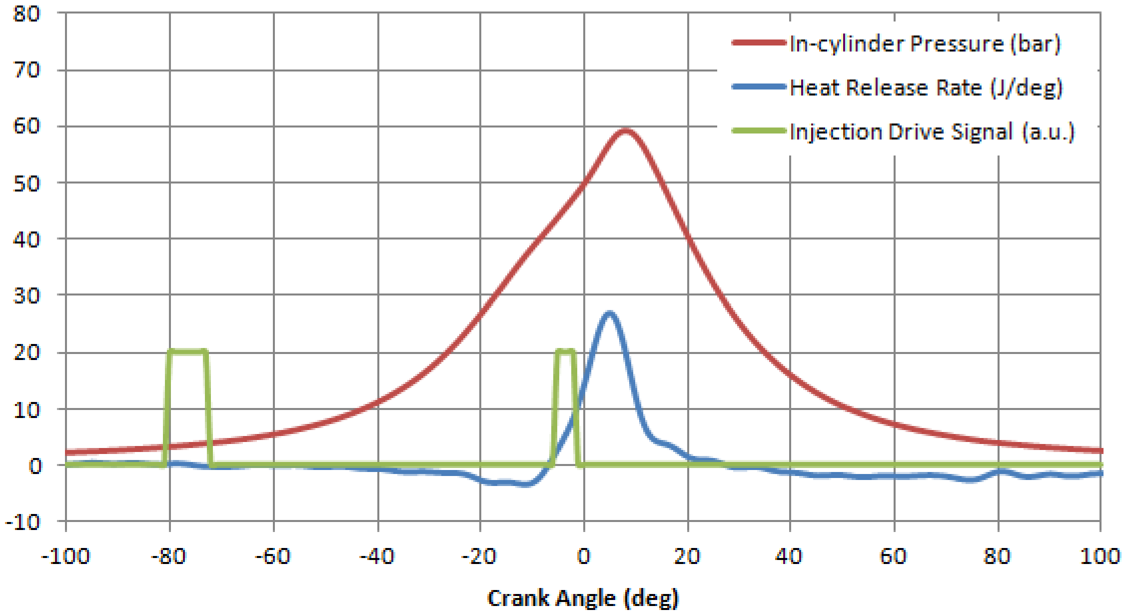

Figure 5.81 In-cylinder Pressure, Heat Release Rate and Injection Signal for Gasoline PPC (strategy BB2)

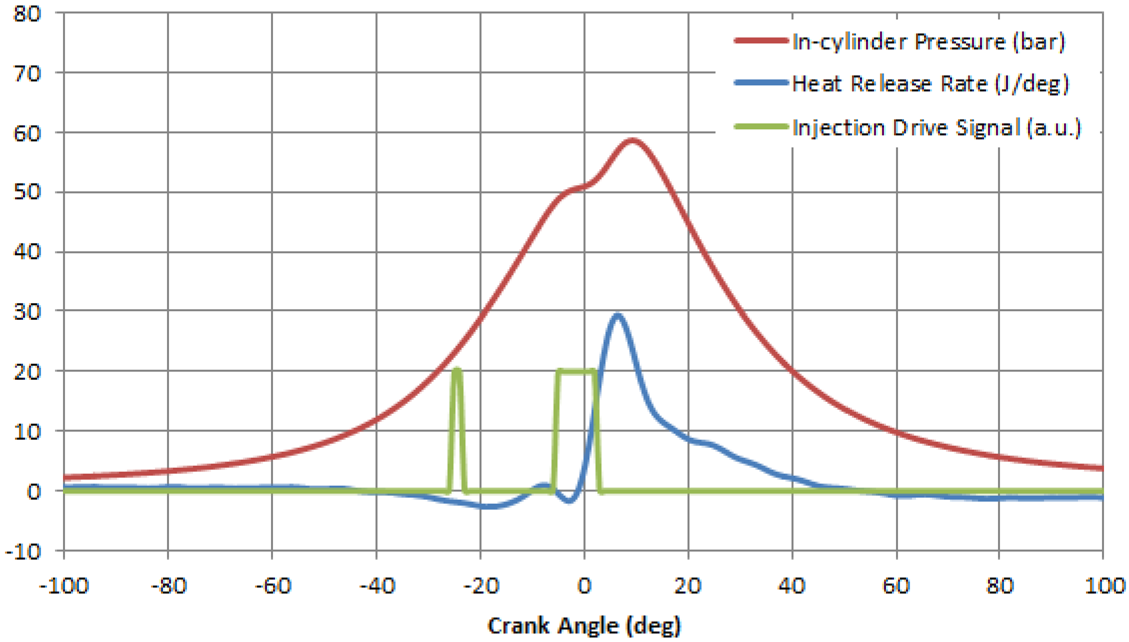

Figure 5.82 In-cylinder Pressure, Heat Release Rate and Injection Signal for Diesel Baseline (strategy F2)

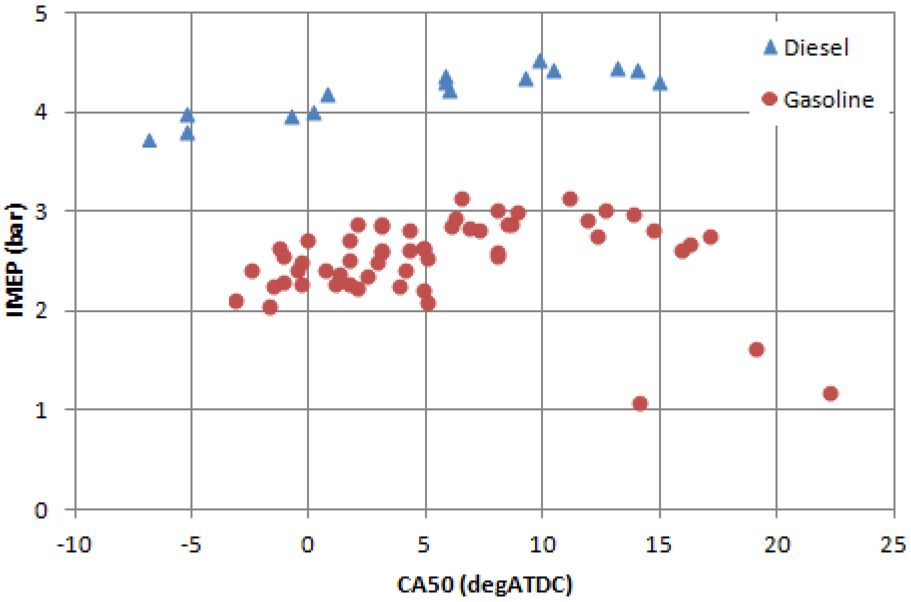

Figure 5.83 Comparison of Combustion Phasing (CA50) between Gasoline PPC and Diesel Baseline

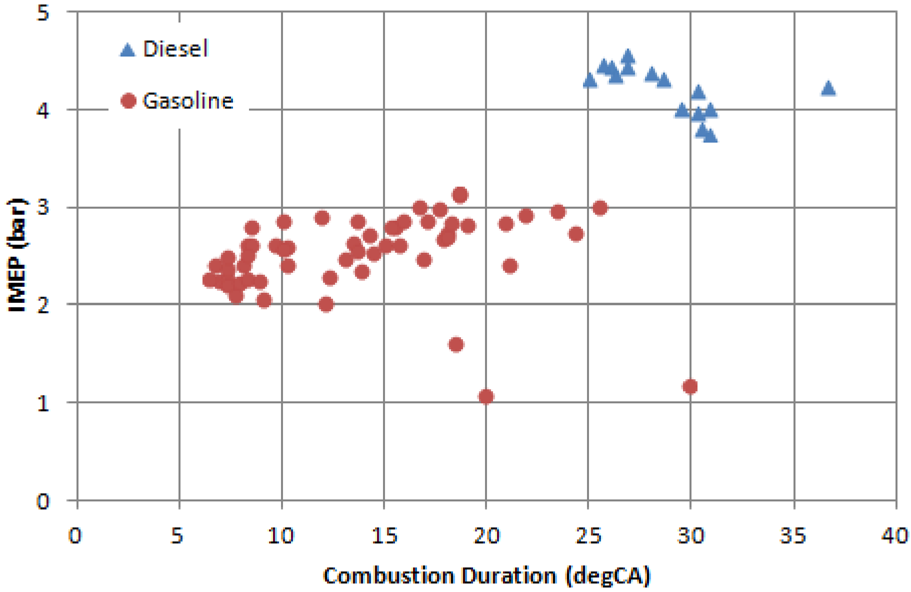

Figure 5.84 Comparison of Combustion Duration (CA10-90) between Gasoline PPC and Diesel Baseline

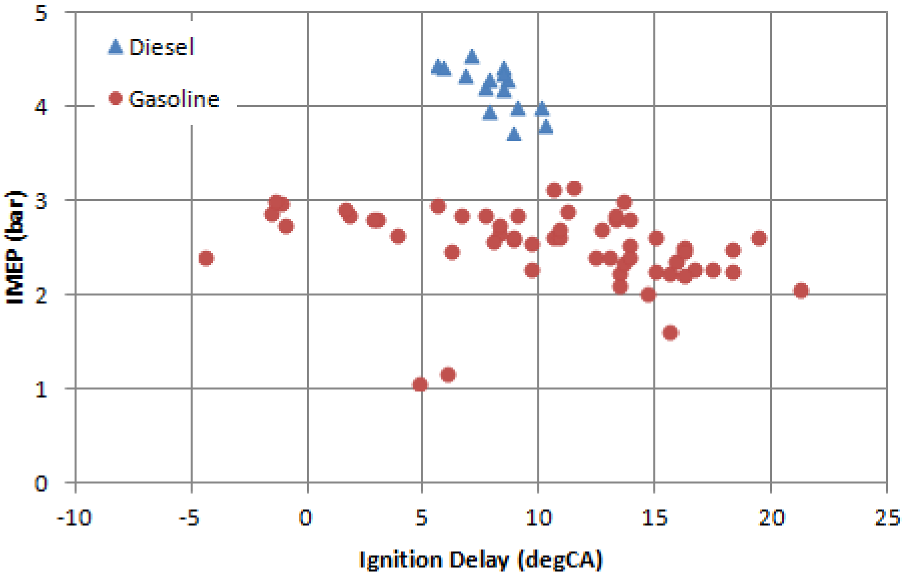

Figure 5.85 Comparison of Ignition Delay (SOI_{2nd}-CA10) between Gasoline PPC and Diesel Baseline

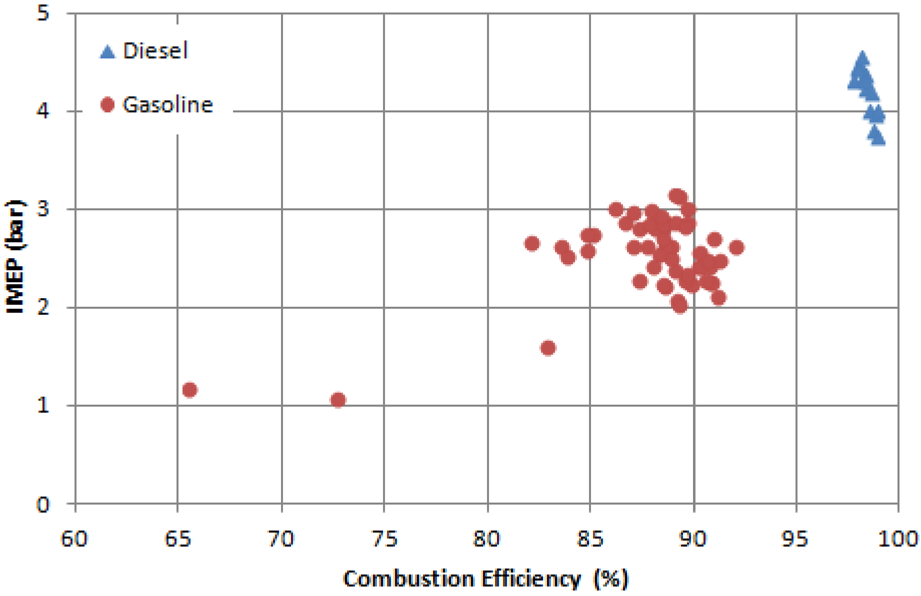

Figure 5.86 Comparison of Combustion Efficiency between Gasoline PPC and Diesel Baseline

Figure 5.86 shows that diesel baseline combustion efficiency was at least 8% higher than gasoline PPC, due to the absence of premixed mixture in crevices, less over-mixing and fuel impingement from 1st injection, and reduced oxidation reactions at lower combustion temperature. In addition, the blow-by in an optically engine tended to be higher, which would have greater impact to premixed charge operations. As a consequence, the PPC operations had lower engine efficiencies as shown in Figure 5.87 and Figure 5.88.

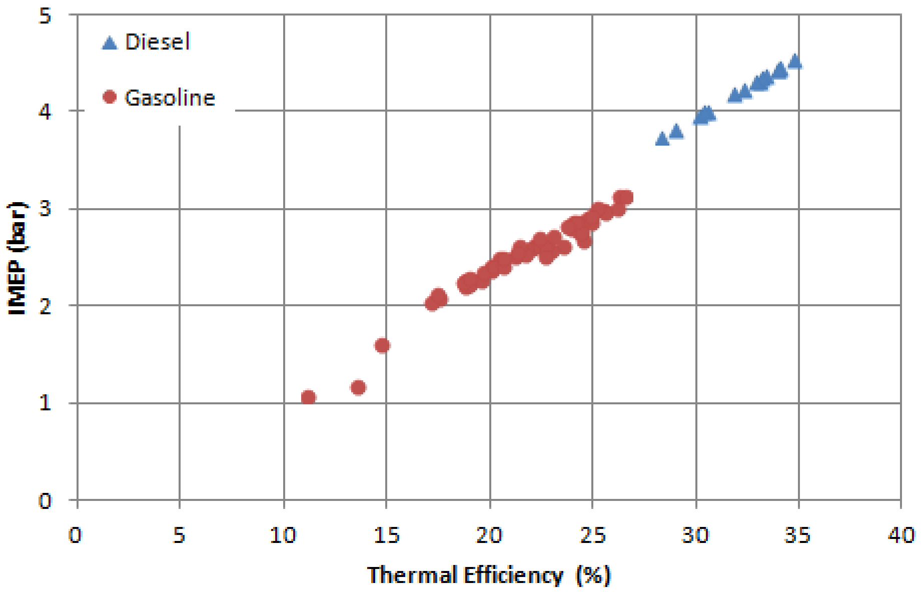

Figure 5.87 Comparison of Thermal Efficiency between Gasoline PPC and Diesel Baseline

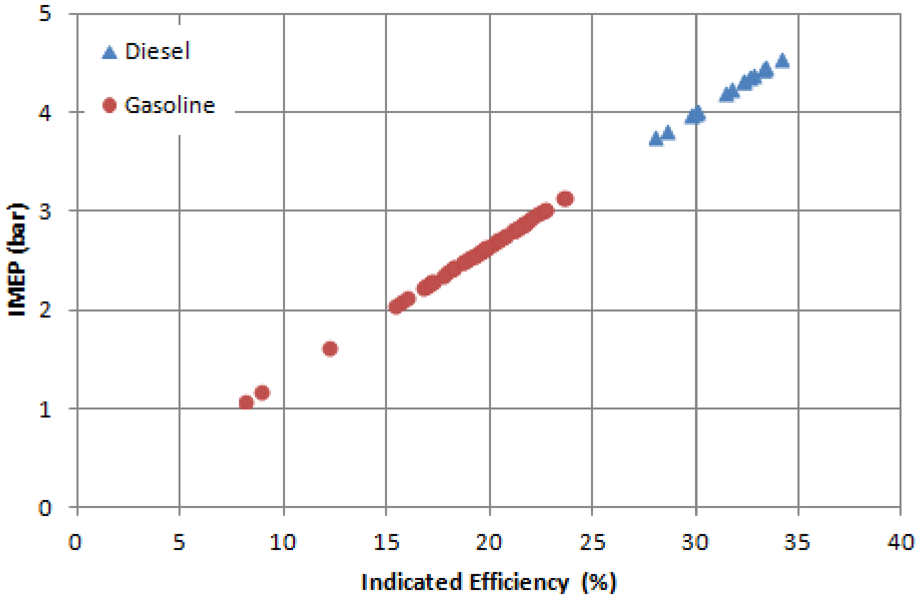

Figure 5.88 Comparison of Indicated Efficiency between Gasoline PPC and Diesel Baseline

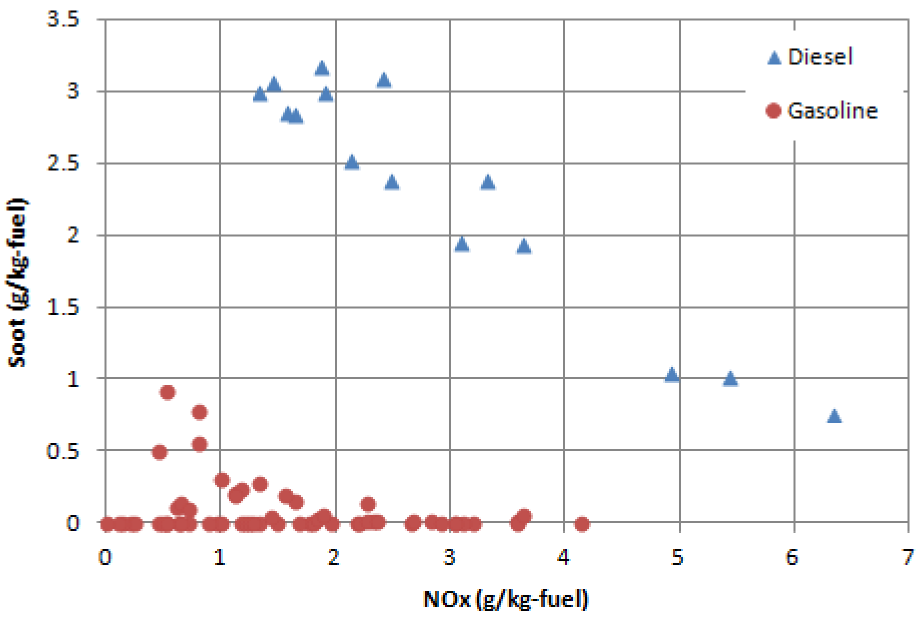

Figure 5.89 Comparison of Soot and NOx Emissions between Gasoline PPC and Diesel Baseline

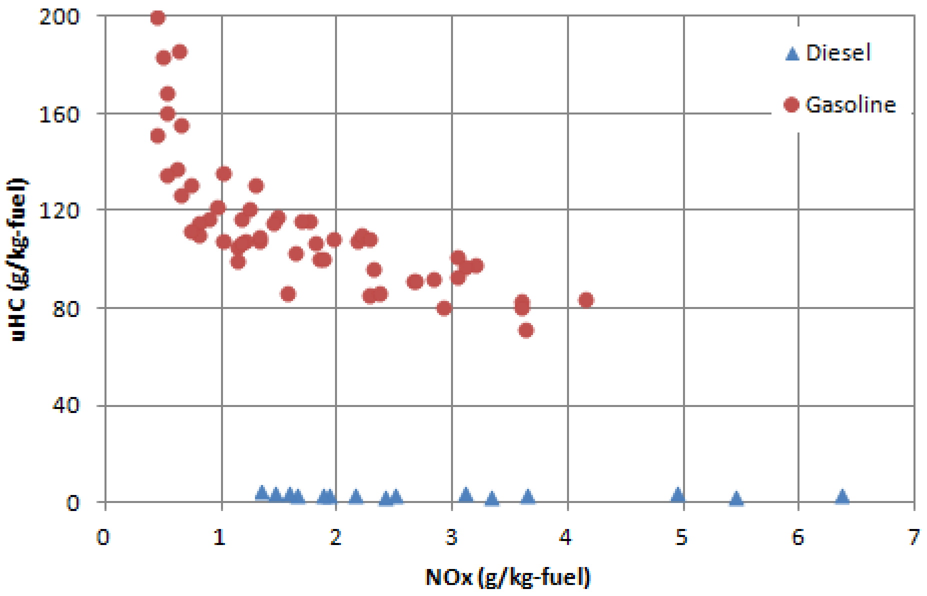

Figure 5.90 Comparison of uHC and NOx Emissions between Gasoline PPC and Diesel Baseline

The comparison of exhaust emissions and soot concentrations between gasoline PPC and diesel baseline combustion can be found in Figures 5.89 and 5.90. Simultaneous reduction of soot and NOx emissions were achieved for gasoline PPC. In comparison, excessive soot emission was experienced in diesel combustion. The simultaneous ultra-low soot and NOx emissions were achieved during the homogeneous lean combustion at low temperature by introduction of EGR and early fuel injection and longer ignition delay of a high octane and high volatility fuel therefore governing charge concentration has been turned to the key point for improving soot emissions. But the downside was the huge increase in uHC emissions as a result of low temperature combustion of premixed lean mixture.

5.9 Optimization of Gasoline PPC Operation

In this section, the optimum gasoline PPC operation regime was extracted for the different operation strategies.

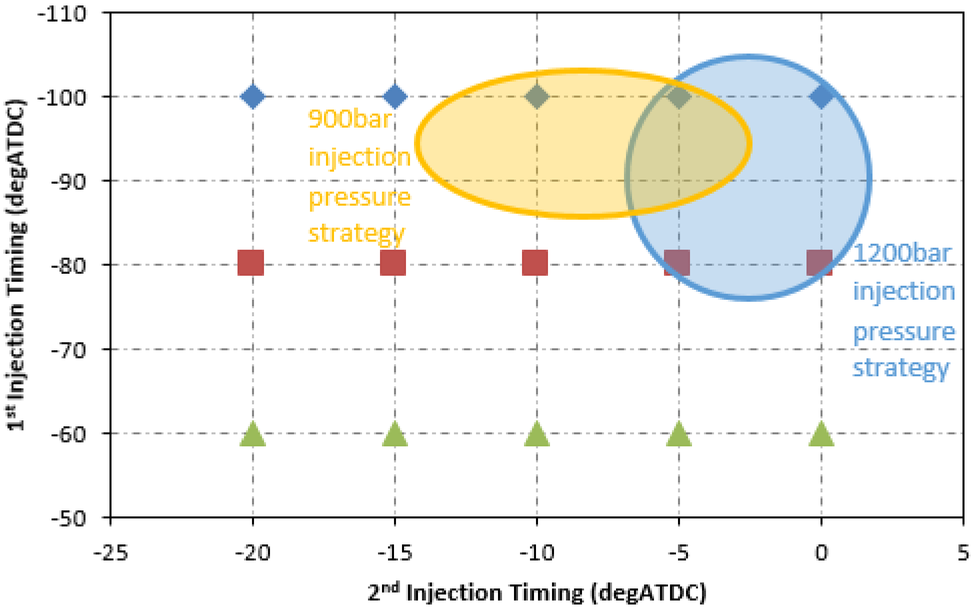

Figure 5.91 Optimized Engine Operation Regime for Gasoline PPC

As shown in Figure 5.91, the coloured area represents optimum engine operation regime for 1200 and 900 bar injection pressure strategies, respectively. In the blue circle (1200 bar injection pressure strategy), higher IMEP and thermal efficiency were achieved for both 50:50 and 70:30 fuel quantity split strategies. In the meantime, NOx and soot emissions were kept at fairly low level with the penalty of uHC emissions. Although this optimized area can be moved towards to the left direction horizontally to improve the uHC emissions thereby increasing the combustion efficiency, the entire engine efficiencies will be deteriorated with the increase of NOx and soot emissions. In terms of 900 bar injection strategy case (yellow area), the best engine efficiencies were achieved at combination of early 1st injection timing and 2nd injection timing between -

13 to -3 ° CA ATDC. In this yellow case (900 bar injection pressure strategy), 2^{nd} injection timing was advanced to achieve optimum engine operation regime compared to previous blue case (1200 bar injection pressure strategy). This was mainly attributed to the misfiring took place at retarded 2^{nd} injection timings for 50:50 fuel quantity split strategy.

In summary, the optimum engine operation regime for this gasoline PPC study can be defined at top right area where the high engine efficiencies and simultaneous reduction of NOx and soot emissions were achieved.

5.10 Summary

In this chapter, the thermodynamic analysis for gasoline type PPC and diesel baseline combustion were presented and discussed. Detailed results were analysed based on in-cylinder pressure, heat release rate, exhaust emissions and soot concentrations. The experimental strategies were divided into six categories according to the fuel type (gasoline and diesel), fuel injection patterns (50:50, 70:30, 30:70 and 10:90 at different injection timings) and injection pressures (1200 and 900 bar).

The results for gasoline PPC demonstrated that better output performance was obtained when combustion phasing was properly adjusted by injection timings. The uHC emissions remained at high level while NOx emissions were kept very low for all cases because of diluted lean combustion at low temperature. In the meantime, the soot concentrations were substantially suppressed at ultra low level due to improved fuel-air mixing process of gasoline PPC.

Comprehensive comparisons were made between injection pressures, fuel injection patterns and fuel types at the same energy input. In the case of gasoline type PPC, the soot concentration was significantly reduced under higher injection pressure with 70:30 fuel distribution strategy. It was found that diesel combustion produced approximately 12% higher indicated efficiency than gasoline case mainly owing to enhanced combustion efficiency and lower uHC emissions. Because of presence of EGR, NOx emissions of diesel combustion remained low. However soot concentrations from diesel combustion were a few orders of magnitude higher than gasoline type PPC operations.

CHAPTER 6

In-cylinder Visualization Studies of Gasoline PPC

6.1 Introduction

In this chapter, the visualization of fuel spray formation and the evaporation process for gasoline PPC was investigated by means of simultaneous Mie and LIF techniques. Images of liquid fuel distribution were detected by Mie scattering while vapour fuel distribution was identified by subtracting the Mie scattering image (liquid) from the LIF image where both liquid and vapour signals were generated. In addition, the fuel spray development and combustion processes were analysed by means of high speed imaging. It is noted that although crank angle resolved information was provided by the high speed images, only selected pictures were presented at particular crank angles, selected according to the heat release rate analysis. The results for diesel baseline combustion were also discussed for the purposes of comparison.

6.2 Test Conditions

Following thermodynamic analysis in Chapter 5, all the experiments were carried out under the same condition shown in Table 5.1. For each strategy, only one operation condition of the best IMEP value was chosen for the in-cylinder studies due to the time-consuming nature of the optical measurements involved. The detailed test plan was summarised in Section 5.2.3 and Table 5.2.

6.3 Results and Discussion

The image sequence of Mie-LIF and high speed video are exhibited in this section, categorised by fuel quantity distribution (50:50, 70:30), injection pressure (1200 bar, 900 bar) and fuel type (PRF, diesel). The 2nd injection timing was fixed at -5 degrees CA ATDC while the 1st injection timing was swept from -100 to -60 degrees CA ATDC.

6.3.1 Strategy A2 (PRF 50:50 distribution at 1200 bar injection pressure, 1st injection timing=-100degATDC, 2nd injection timing=-5degATDC)

6.3.1.1 Fuel Spray Images for Liquid and Vapour Phases

The temporal evolution of fuel liquid and vapour images of PRF for strategy A2 are presented in Figure 6.1. It is noted that five images were taken at the same crank angle for both fuel spray and background from where the subtraction of averaged image calculated. It can be seen that the fuel liquid phases at 60, 140 and 220μs ASOI$_{1st}$ showed increased concentration as more fuel was injected, while a slight reduction was observed at 300 and 380μs ASOI$_{1st}$, as a large proportion of fuel evaporated at the later stage of injection. It is noted that the asymmetry of the fuel spray was formed at the initial stage of injection due to inherent characteristic of the VCO (Valve Covered Orifice) injector. The fuel distribution became increasingly even as injection progressed. In terms of the fuel vapour results, they demonstrated a similar pattern to those of the fuel liquid spray through the early stages of injection, while an enlarged contour can be detected as the injection continued. According to the comparison between liquid and vapour phases, it can be concluded that the fuel evaporating process was substantially promoted by injecting gasoline fuel under the high injection pressure, which benefited soot emission results shown in Chapter 5. In the image at 380μs ASOI$_{1st}$, the fully developed fuel vapour spray nearly reached the extent of the window, leading to impingement.

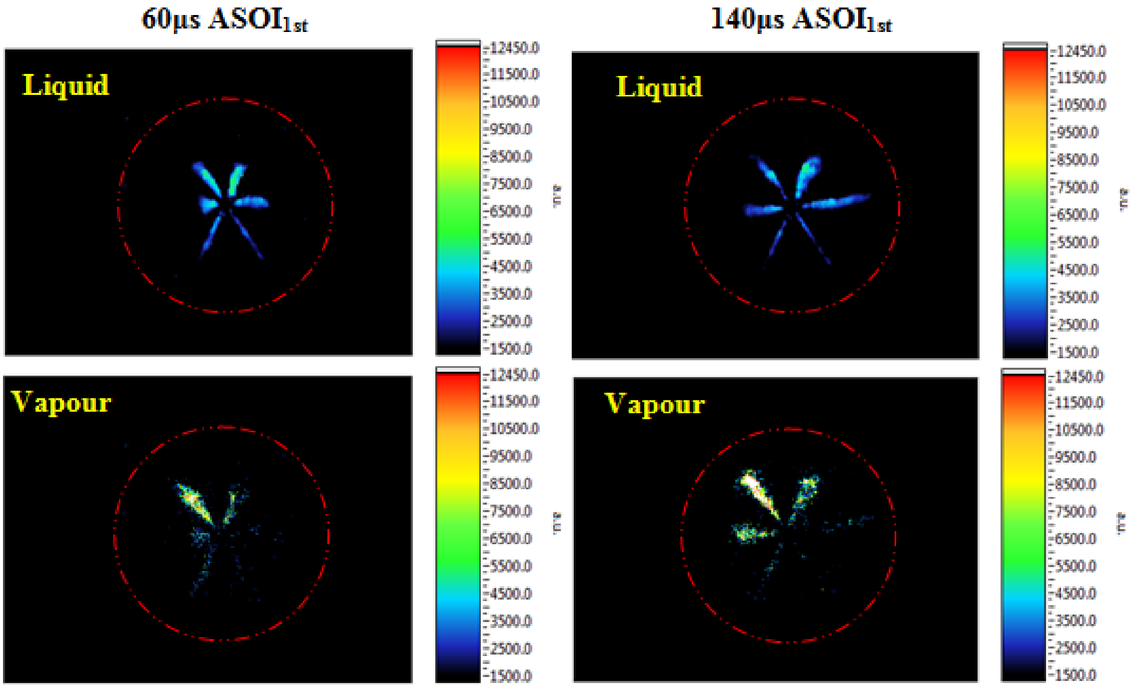

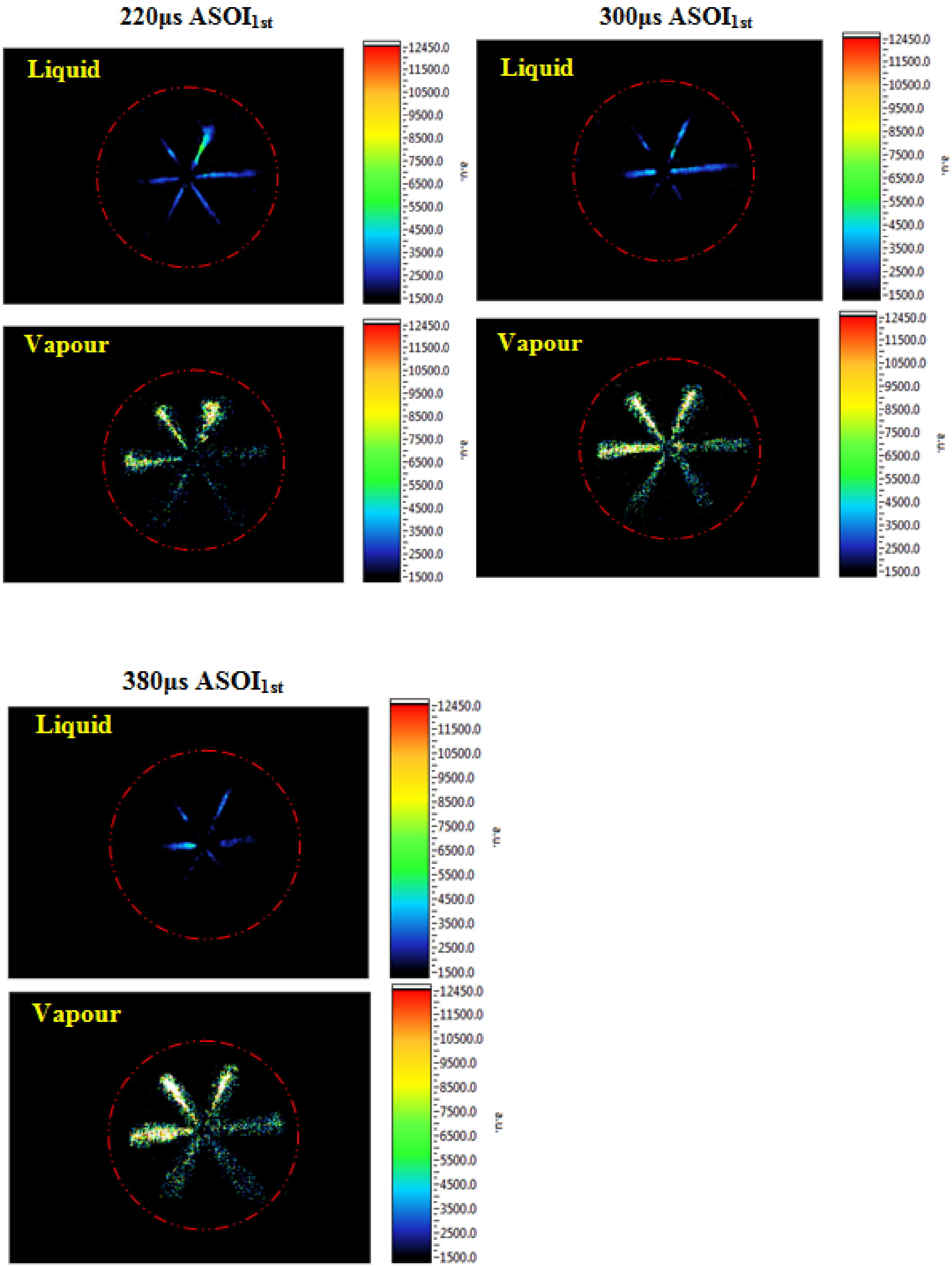

Figure 6.1 Sequence of Liquid and Vapour Images for Strategy A2 (P_{inj}=1200bar, 50:50 fuel quantity distribution, 1st injection timing=-100degATDC)

6.3.1.2 Fuel Injection and Combustion Visualisation

Figure 6.2 shows the image sequence of fuel spray and combustion for strategy A2 by utilizing the high speed imaging technique. The first three images showed the liquid fuel from Mie scattering of the copper vapour laser and they demonstrated fuel spray development from the start until the end of the 1st injection. It is worth noting that asymmetry of the fuel spray appeared in the frame of -100 degrees ATDC, consistent with the Mie-LIF image in the previous section. In the last frame, at -95.5 degrees ATDC, the fuel spray had almost completely evaporated. During the 2nd fuel injection shown in frames -5, -2.3 and -0.5 degrees ATDC, the contour of fuel spray was dramatically shrunk compared to the 1st injection, even though an identical injection quantity was used. This was mainly attributed to most of the injected fuel evaporating immediately after injection, due to the high surrounding temperature and pressure.

The first appearance of visible combustion was detected at 2.2 degrees ATDC, showing good agreement with heat release rate data in section 5.3.1. As seen in frames at 5.8 and 10.3 degrees ATDC, the flame was progressively propagated from the tip of fuel sprays and spread along the periphery of the combustion chamber, where the highly concentrated fuel vapour was. It can be seen that the flame progressively formed a mushroom like shape in the region of fuel injection, since fuel concentration was much higher in this area. In the next two frames, at 15.7 and 21.1 degrees ATDC, numerous small ignition sites were observed evenly distributed throughout the combustion chamber, which suggests relatively homogeneous charge combustion. At 21.1 and 31 degrees ATDC, the flames gradually became weaker with slight clockwise motion, due to in-cylinder swirl. In this strategy, the separation between the end of injection and start of combustion was achieved, which was the reason for considerably improved soot emissions. Moreover, no obvious diffusion combustion can be detected in the frames, although heat release rate data presented a slight fluctuation at the end of the heat release process.

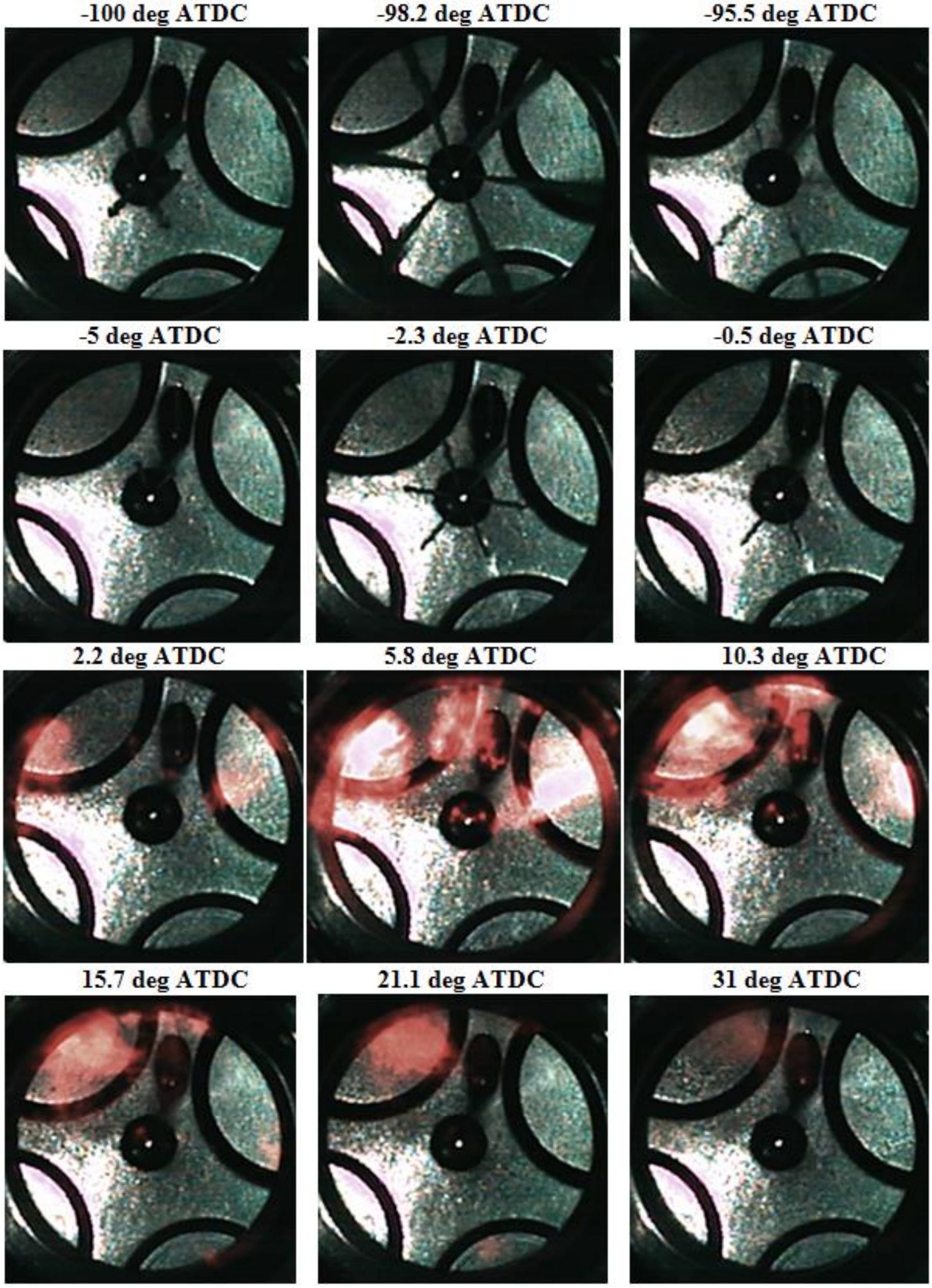

Figure 6.2 Sequence of Combustion Images for Strategy A2 (P_{inj}=1200bar, 50:50 fuel quantity distribution, 1st injection timing=-100degATDC, 2nd injection timing=-5degATDC)

6.3.2 Strategy AA2 (PRF 50:50 distribution at 1200 bar injection pressure, 1st injection timing=-80degATDC, 2nd injection timing=-5degATDC)

6.3.2.1 Fuel Spray Images for Liquid and Vapour Phases

Figure 6.3 demonstrates the image sequence of fuel liquid and vapour for strategy AA2. In the first two images, at 60 and 140µs ASOI$_{1st}$, the asymmetry of the fuel spray was detected for both liquid and vapour phases, due to utilization of a VCO injector. The fuel liquid spray steadily developed until 220µs ASOI$_{1st}$ because of increased injected fuel. However, the gradual reduction of fuel spray length and thickness was encountered at 300µs and 380µs ASOI$_{1st}$. This was mainly attributed to a portion of liquid fuel evaporating during the fuel injection. This trend was magnified in the gasoline case, compared to the diesel case, due to the better evaporative properties of gasoline fuel. The fuel vapour image presented the same contour as the fuel liquid phase during the initial stage of injection, but the difference increased as injection developed after 140µs ASOI$_{1st}$, since fuel evaporation was accelerated during the injection process. A slight impingement on the cylinder wall can be observed in the last frame at 380µs ASOI$_{1st}$, owing to the fully developed fuel spray.

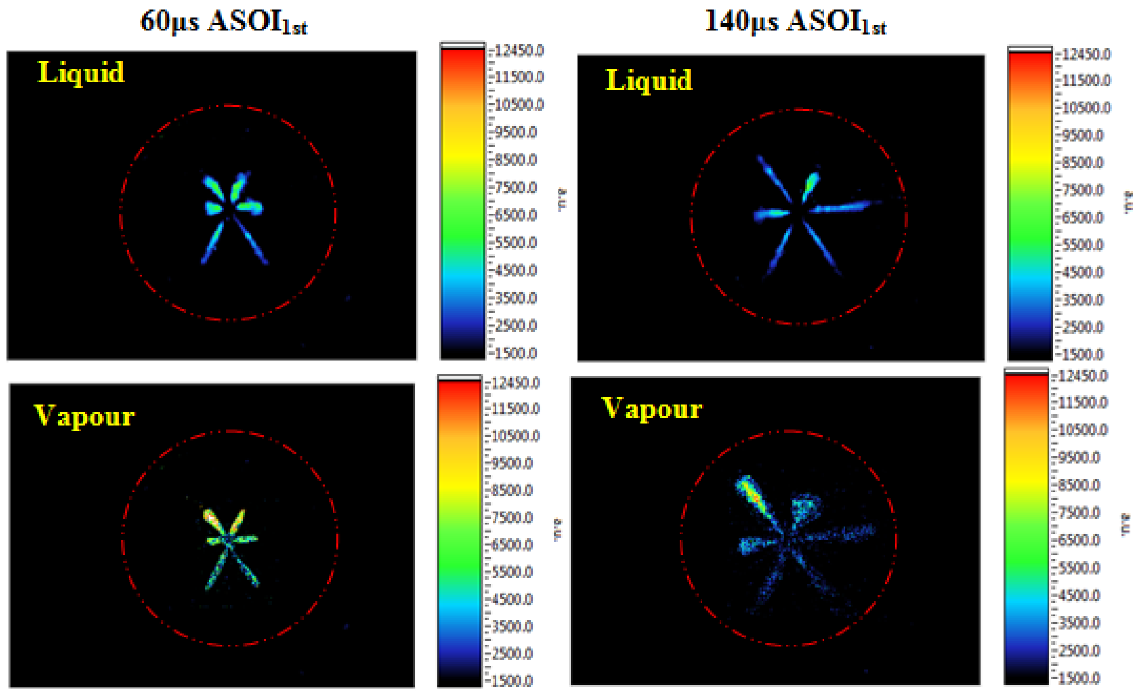

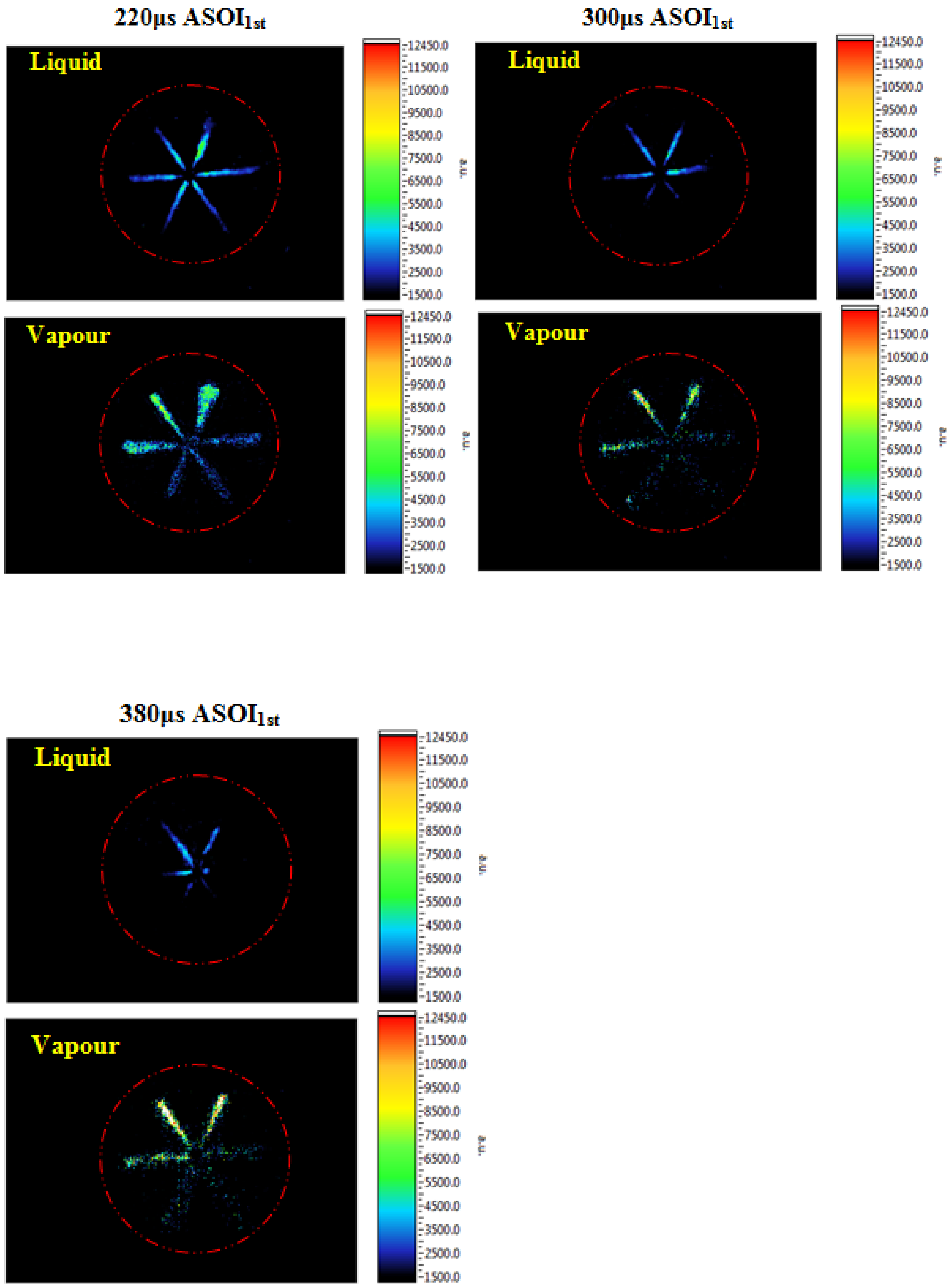

Figure 6.3 Sequence of Liquid and Vapour Images for Strategy AA2 (P_{inj}=1200bar, 50:50 fuel quantity distribution, 1st injection timing=-80degATDC)

6.3.2.2 Fuel Injection and Combustion Visualisation

The time evolution of fuel spray and combustion process for strategy AA2 are presented in Figure 6.4. Compared to strategy A2, retarded 1st injection timing at -80 degrees ATDC was used for strategy AA2. The first three frames, at -80, -78.2 and -76.4 degrees ATDC, show the evolution of the 1st injection. Asymmetry of the fuel spray was detected at -80 degrees ATDC and fuel evaporation can be clearly seen at the tip of the jet at -76.4 degrees ATDC. The image sequences of 2nd injection are shown in frames at -5, -3.2 and -1.4 degrees ATDC. It is evident that the fuel spray size and penetration were considerably reduced compared to the 1st injection, due to higher interaction with the ambient gases when the chamber density and temperature increased.

The first appearance of visible combustion was observed at 2.2 degrees ATDC, which is slightly early than CA10 (10% mass fraction burned) at 4 degrees ATDC. The flame subsequently propagated from the periphery of initiated ignition points and spread along the outer-ring of the combustion chamber, where the premixed mixture of air and fuel vapour was. The most intense flame propagation took place around 7 degrees ATDC, approximately where the maximum heat release rate occurred under the premixed combustion control. After that, the flame intensity gradually diminished during the expansion stroke shown in frames at 13, 17.5 and 22.9 degrees ATDC and the clockwise movement of the weakened flame can be seen, due to the swirl motion. It is noted that the flame propagation was not occupying the full view of the chamber, but only the right half side, even when the combustion process was most intense. The low combustion luminosity indicated the absence of diffusion combustion and soot formation, because of the burning of premixed mixture formed during the longer ignition delay between the end of injection and the start of combustion and the low combustion temperature due to EGR. Therefore, simultaneous reduction of soot and NOx emissions were achieved thanks to this moderate combustion process.

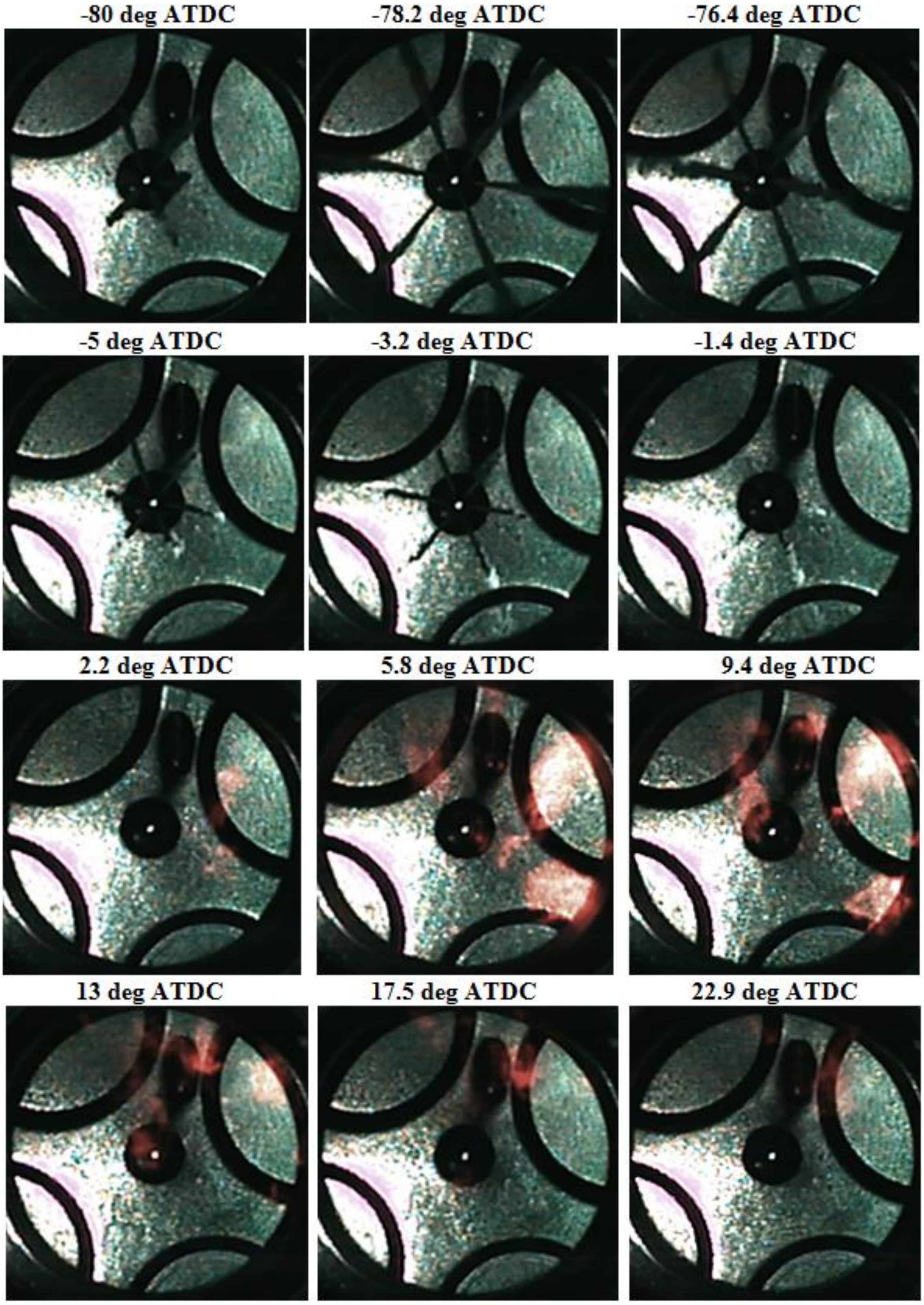

Figure 6.4 Sequence of Combustion Images for Strategy AA2 (P_{inj}=1200bar, 50:50 fuel quantity distribution, 1st injection timing=-80degATDC, 2nd injection timing=-5degATDC)

6.3.3 Strategy B2 (PRF 70:30 distribution at 1200 bar injection pressure, 1^{st} injection timing=-100degATDC, 2^{nd} injection timing=-5degATDC)

6.3.3.1 Fuel Spray Images for Liquid and Vapour Phases

Figure 6.5 shows the image sequence of fuel liquid and vapour for strategy B2. Compared to strategies discussed above, the fuel quantity distribution was changed from 50:50 to 70:30 and the fuel spray images data below was acquired with the 1^{st} injection at -100 degrees ATDC. For the fuel liquid image at 80µs ASOI$_{1st}$, an obviously asymmetrical fuel spray was detected owing to the inherent characteristic of the VCO injector. The liquid spray progressively developed until 280µs ASOI$_{1st}$ as more fuel was injected, while, in the same manner as with previous strategies, the intensity and length of the liquid spray was reduced at later stages of injection. This was mainly attributed to improved evaporation characteristics of gasoline fuel, turning liquid fuel into vapour. In terms of fuel vapour results, similar spray contours can be seen only at the early injection stage of 80µs ASOI$_{1st}$ and larger surroundings were observed in the rest of the vapour images. This can be understood by considering the rapid fuel evaporating process when injection approached the end. The fuel vapour concentration gradually increased from 200µs ASOI$_{1st}$ until the end of injection at 440µs ASOI$_{1st}$ as more fuel was evaporated. Compared to 50:50 fuel quantity distribution strategies, 70:30 strategy apparently injected more fuel in 1^{st} injection so that a more concentrated fuel vapour signal can be seen in the final stage of injection.

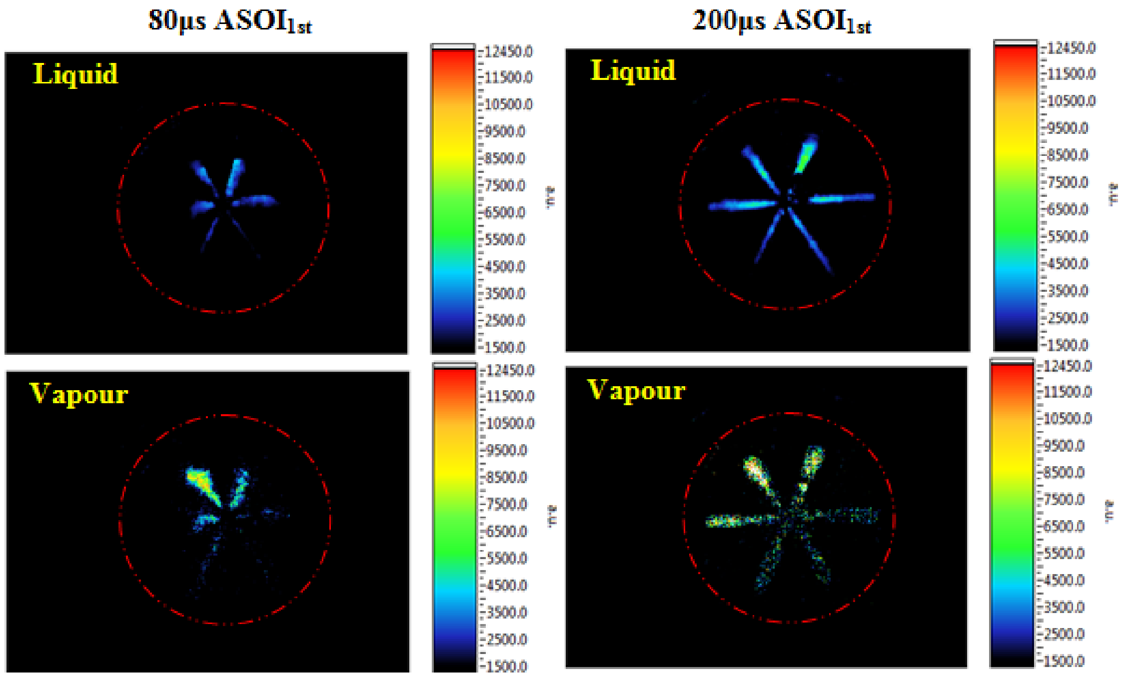
80µs ASOI$_{1st}$ 200µs ASOI$_{1st}$

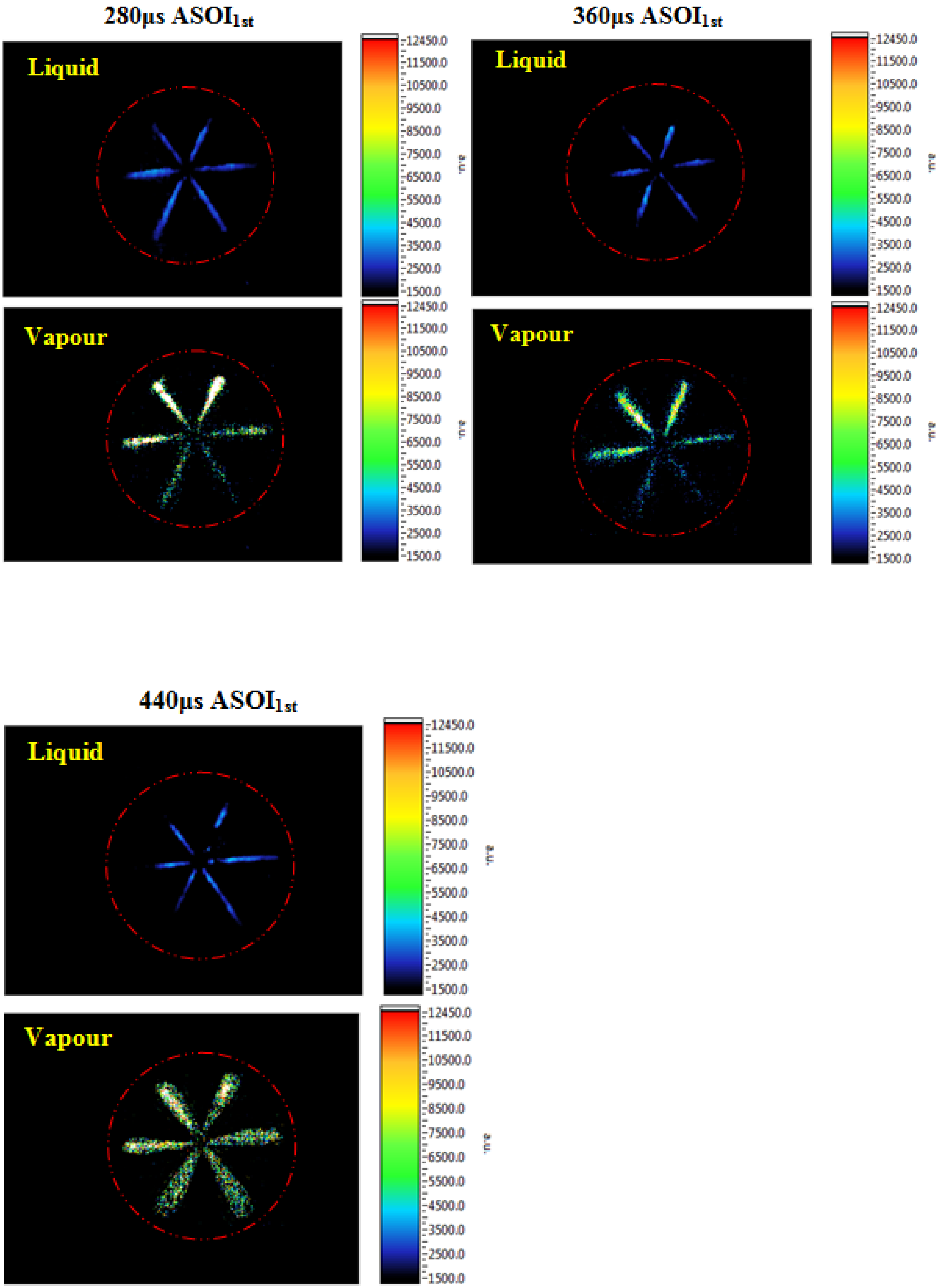

Figure 6.5 Sequence of Liquid and Vapour Images for Strategy B2 (P_{inj}=1200bar, 70:30 fuel quantity distribution, 1st injection timing=-100degATDC)

6.3.3.2 Fuel Injection and Combustion Visualisation

The image sequence of fuel spray and combustion for strategy B2 are shown in Figure 6.6. The first three frames show the image sequence from the start to the end of the 1st injection. It is evident that longer injection duration was obtained compared to previous strategies, as more fuel was injected during 1st injection. The asymmetry of the fuel spray was observed at the initial injection stage of -100 degrees ATDC and decent fuel evaporating process can be seen at the tip of the jet at final injection period of -95.5 degrees ATDC. The 2nd injection process is presented in the next three frames, at -5, -2.3 and -0.5 degrees ATDC. A fairly small fuel spray jet is detected at the first two frames since only 30% of the total amount of fuel was injected during 2nd injection. It is noted that visible combustion started appearing at the end of 2nd injection which was much quicker than under the 50:50 fuel distribution strategy. This can be understood by considering that a more concentrated fuel-air mixture was created before the onset of the 2nd injection, resulting in earlier ignition. In the next frame, at 2.2 degrees ATDC, more visible flame can be detected and several ignition sites were present due to premixed combustion. The most intense flame took place at 4.9 degrees ATDC, corresponding to the peak heat release rate at around 4.2 degrees ATDC. Subsequently, the flame gradually diminished over the rest of the frames, with clockwise direction movement due to swirl motion. Generally, more intense flame propagation for the 70:30 strategy was achieved compared to the 50:50 strategy.

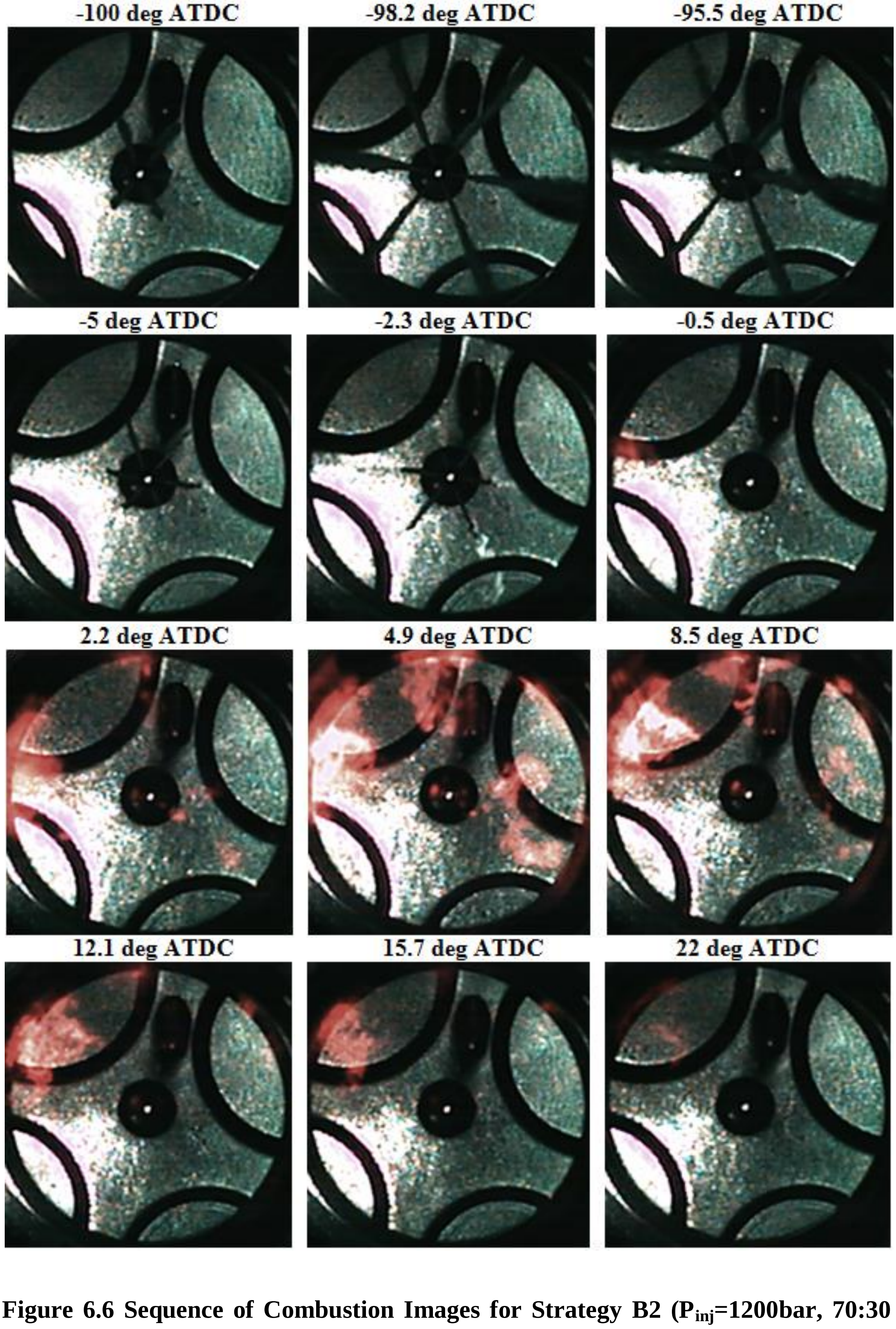

Figure 6.6 Sequence of Combustion Images for Strategy B2 (P_{inj}=1200bar, 70:30 fuel quantity distribution, 1st injection timing=-100degATDC, 2nd injection timing=-5degATDC)

6.3.4 Strategy BB2 (PRF 70:30 distribution at 1200 bar injection pressure, 1st injection timing=-80degATDC, 2nd injection timing=-5degATDC)

6.3.4.1 Fuel Spray Images for Liquid and Vapour Phases

Figure 6.7 shows the image sequence of fuel liquid and vapour for strategy BB2. In this strategy, both 1st and 2nd injections are discussed in order to have better understanding of integral fuel injecting and evaporating processes. For fuel liquid images, an asymmetrical fuel spray was obtained at an early stage of injection due to the inherent characteristic of the VCO injector. The liquid spray afterwards developed until 380μs $ASOI_{1st}$ reaching the maximum concentration. After this peak, the liquid spray intensity slightly weakened through the final stage of the 1st injection (460μs $ASOI_{1st}$) owing to acceleration of the fuel evaporation process. The fuel vapour spray demonstrated identical contours to the fuel liquid phase at 30μs $ASOI_{1st}$ and progressively expanded as injection progressed. In the same manner as previous strategies, the fuel vapour phases covered larger areas than the fuel liquid phases as fuel injection was developing. This indicated that the fuel-air mixing process was promoted by rapidly evaporated gasoline fuel. At the final injection stage of 460μs $ASOI_{1st}$, a slight impingement on the cylinder wall can be recognized due to the fully developed injection event.

During the 2nd injection, the consistent contours can be seen between fuel liquid and vapour images at 100 and 140μs $ASOI_{2nd}$. However, enhanced evaporation was apparent over the next two frames, 240 and 340μs $ASOI_{2nd}$, respectively. The concentration of fuel liquid gradually declined, while that of fuel vapour was dramatically magnified. This was mainly attributed to higher surrounding temperature and pressure, which substantially promoted the fuel evaporation process.

30µs ASOI$_{1st}$

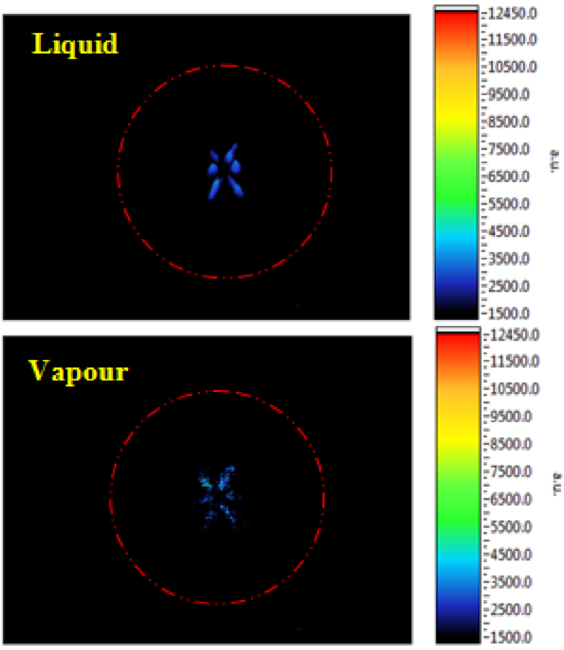

180µs ASOI$_{1st}$

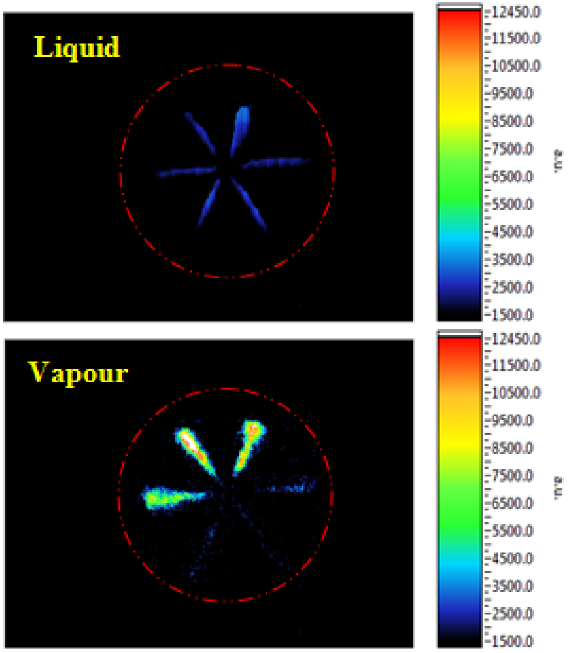

260µs ASOI$_{1st}$

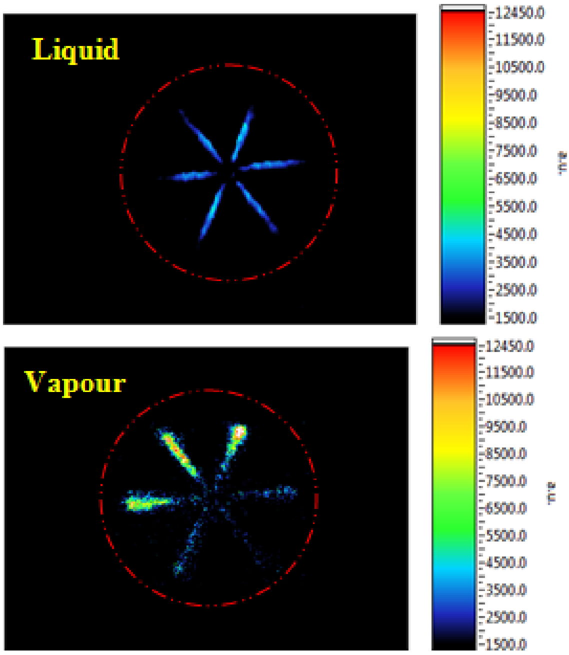

380µs ASOI$_{1st}$

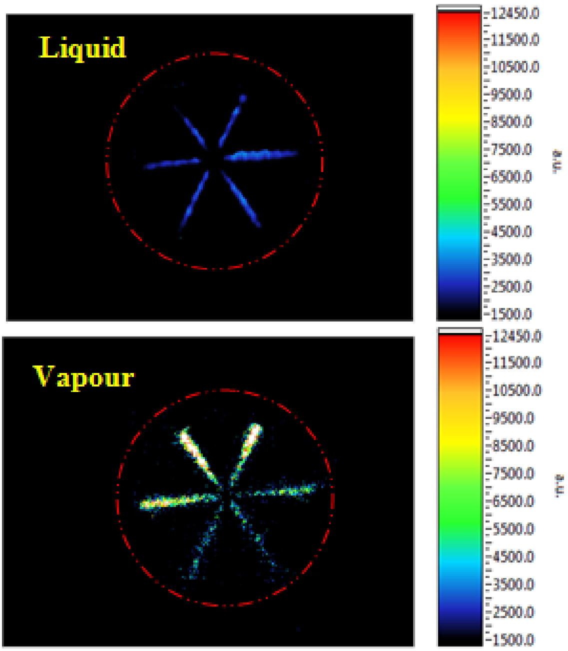

460μs ASOI$_{1st}$

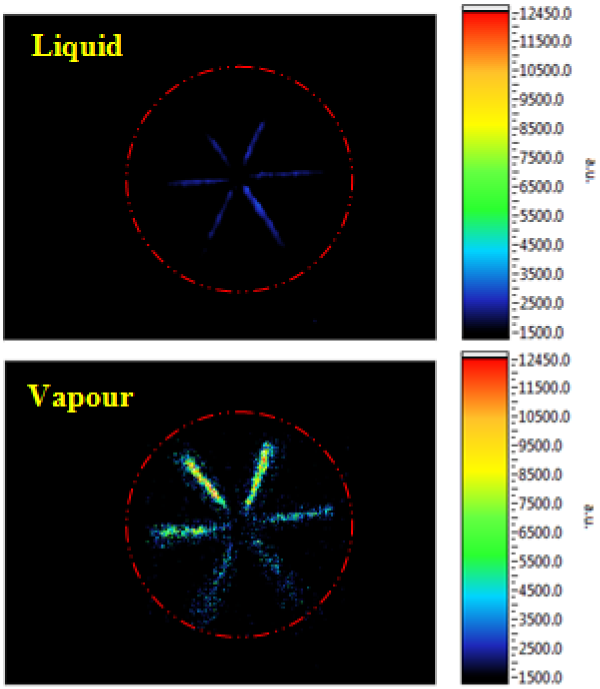

100μs ASOI$_{2nd}$

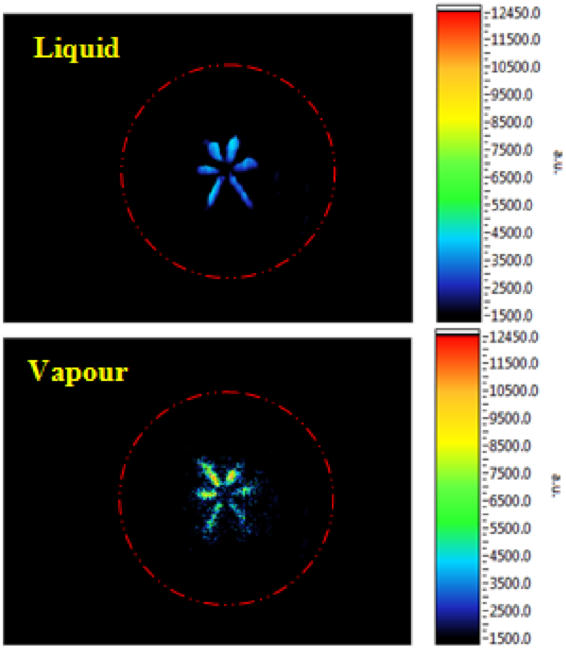

140μs ASOI$_{2nd}$

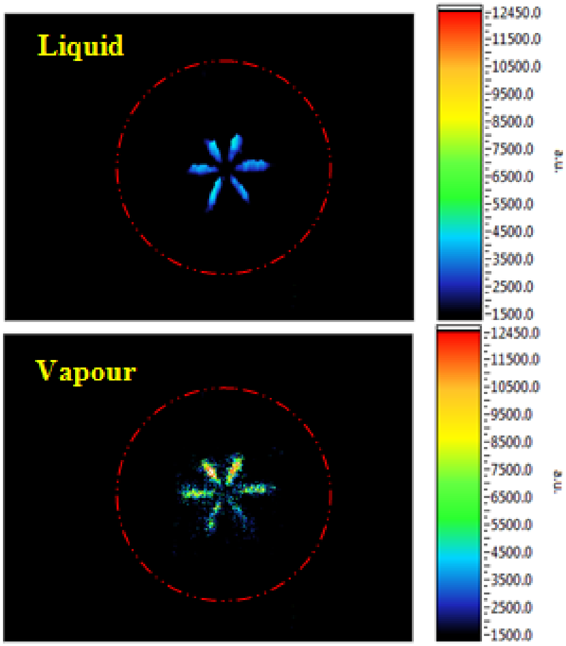

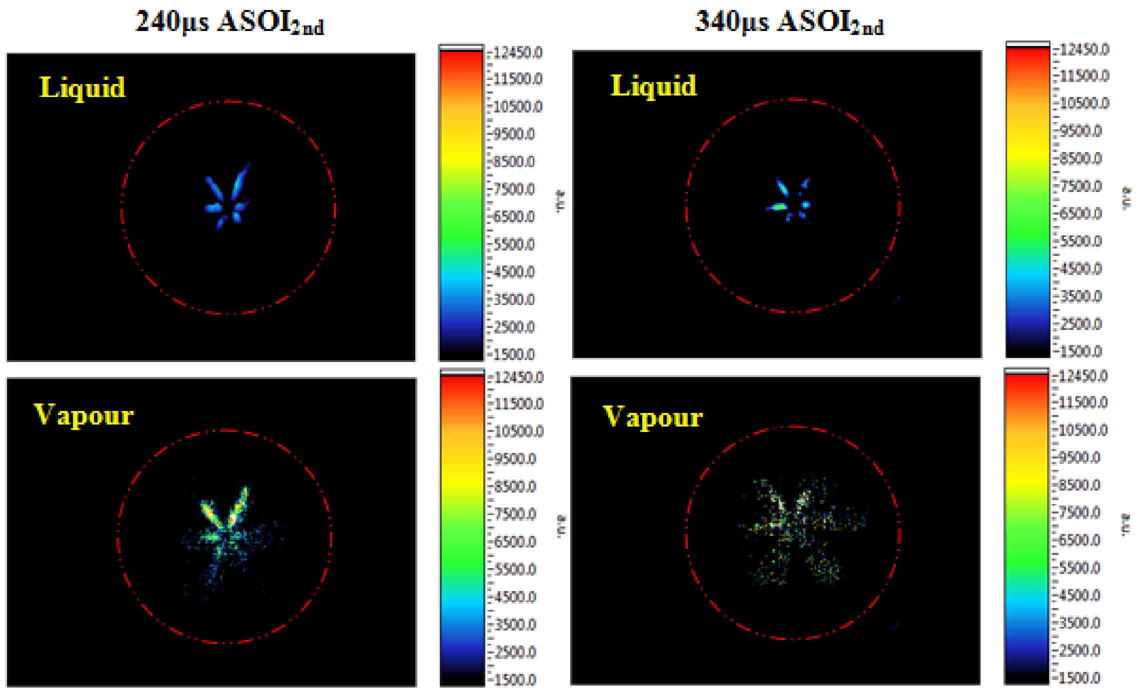

Figure 6.7 Sequence of Liquid and Vapour Images for Strategy BB2 (P_{inj}=1200bar, 70:30 fuel quantity distribution, 1st injection timing=-80degATDC, 2nd injection timing=-5degATDC)

6.3.4.2 Fuel Injection and Combustion Visualisation

The image sequence of fuel spray and combustion for strategy BB2 are demonstrated in Figure 6.8. The frames at -80, -78.2 and -75.5 degrees ATDC show fuel spray development from the start to the end of the 1st injection. The asymmetry of the fuel jet can be seen in the first frame owing to utilization of a VCO injector, and the evaporated tip of the spray was observed in last image. Subsequently the entire 2nd fuel injection process is indicated in the next three frames, at -5, -2.3 and 0.4 degrees ATDC. A fairly small fuel jet was obtained in these frames because only 30% of the total amount of fuel was injected during the 2nd injection. The first visible combustion spots appeared surrounding the injector at 0.4 degrees ATDC, as soon as the 2nd injection finished. The next frame, shown at 3.1 degrees ATDC, presented more visible flame distribution around the first initiated ignition points. The most intense flame was found at 5.8 degrees ATDC which corresponds to the peak heat release rate of 28 J/deg. The frame at 8.5 degrees ATDC indicated that the flame propagation had developed towards the edge of the cylinder wall, where more concentrated fuel vapour was. In the subsequent frames, at 11.2, 14.8 and 19.3 degrees ATDC, the flame was gradually diminished during the expansion stroke with clockwise direction movement demonstrating swirl motion.

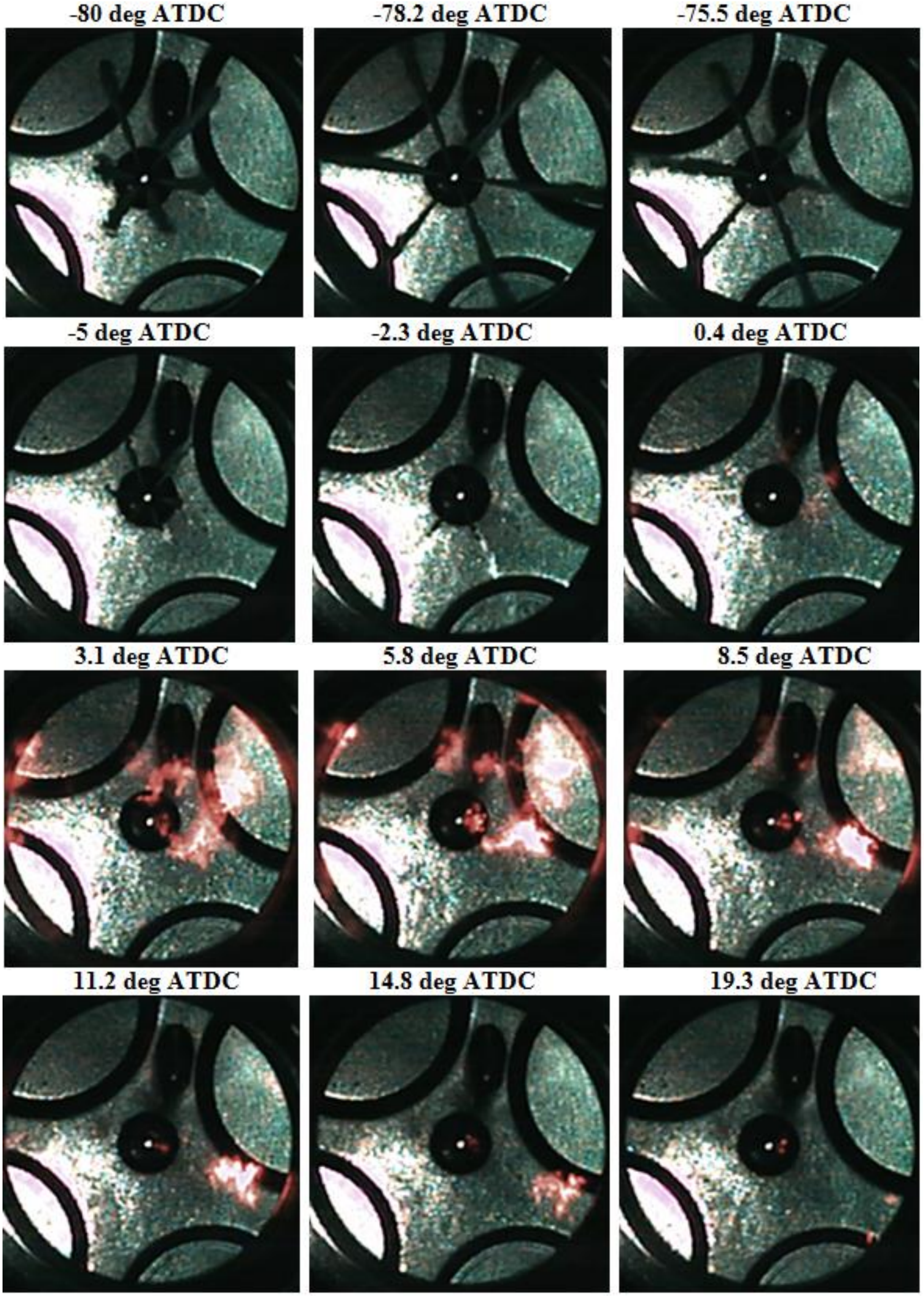

Figure 6.8 Sequence of Combustion Images for Strategy BB2 (P_{inj}=1200bar, 70:30 fuel quantity distribution, 1st injection timing=-80degATDC, 2nd injection timing=-5degATDC)

6.3.5 Strategy D2 (PRF 50:50 distribution at 900 bar injection pressure, 1st injection timing=-100degATDC, 2nd injection timing=-5degATDC)

6.3.5.1 Fuel Spray Images for Liquid and Vapour Phases

The image sequence of fuel liquid and vapour for strategy D2 are shown in Figure 6.9. In this strategy, the injection pressure was decreased from 1200 bar to 900 bar in order to investigate the effect of different injection pressure on fuel spray formation. Since the injection quantity was kept the same for all of the strategies, the injection duration at 900 bar injection pressure needed to be increased to reach the desired injected fuel amount. Consequently, longer injection duration can be seen for 900 bar injection pressure strategies compared to the 1200bar cases.

It can be seen in the first three frames, at 60, 90 and 160μs $ASOI_{1st}$, that the asymmetry of the fuel spray was formed for both fuel liquid and vapour images, owing to the inherent characteristics of the VCO injector. This phenomenon gradually diminished after 240μs $ASOI_{1st}$ as the injector needle was fully open. The liquid spray progressively developed in the rest of images with a slight drop in image intensity in the last frame at 620μs $ASOI_{1st}$. It differs from the noticeable concentration reduction of liquid spray for the 1200 bar injection pressure strategies. This can be understood by considering the deteriorated evaporating effect under lowered injection pressure, which resulted in more fuel liquid remaining during the injection process.

In terms of fuel vapour results, the larger coverage can be seen compared to fuel liquid images when the fuel spray was developing. It is evident that plenty of fuel vapour was generated, spreading to the periphery of the fuel liquid spray, indicative of the fuel-air mixing process. In the final stage of injection at 520 and 620μs $ASOI_{1st}$, a slight impingement can be recognized due to the fully developed fuel spray.

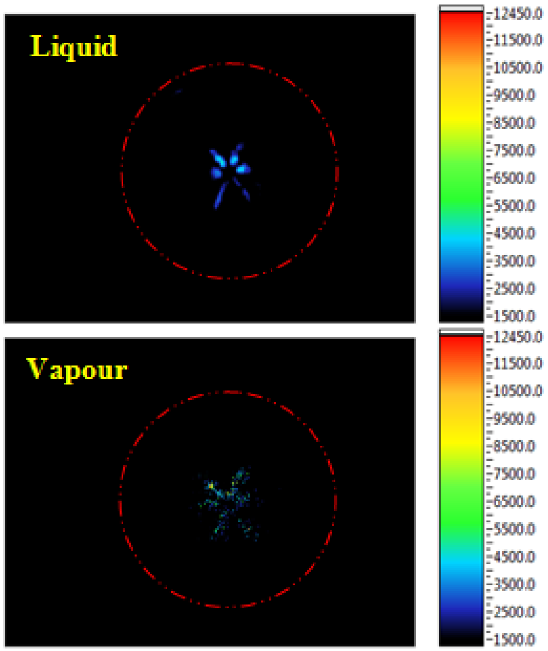
60μs ASOI$_{1st}$

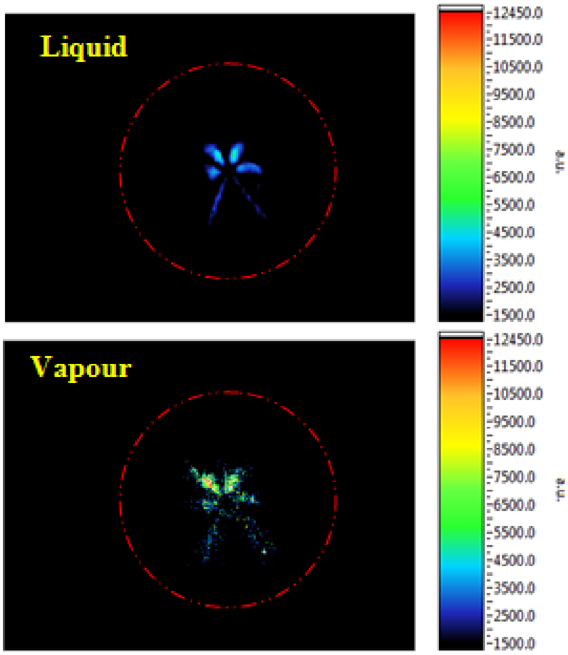
90μs ASOI$_{1st}$

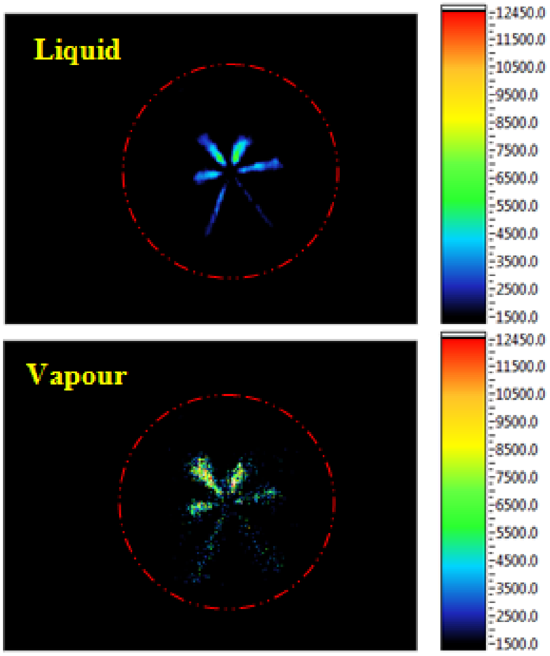
160μs ASOI$_{1st}$

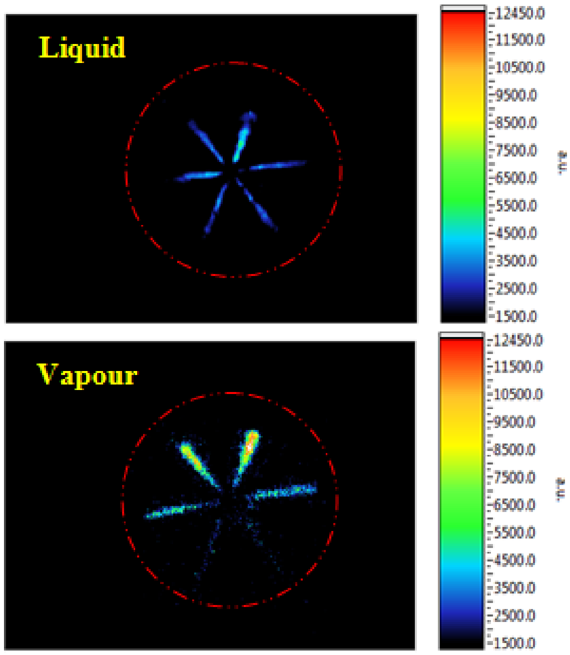
240μs ASOI$_{1st}$

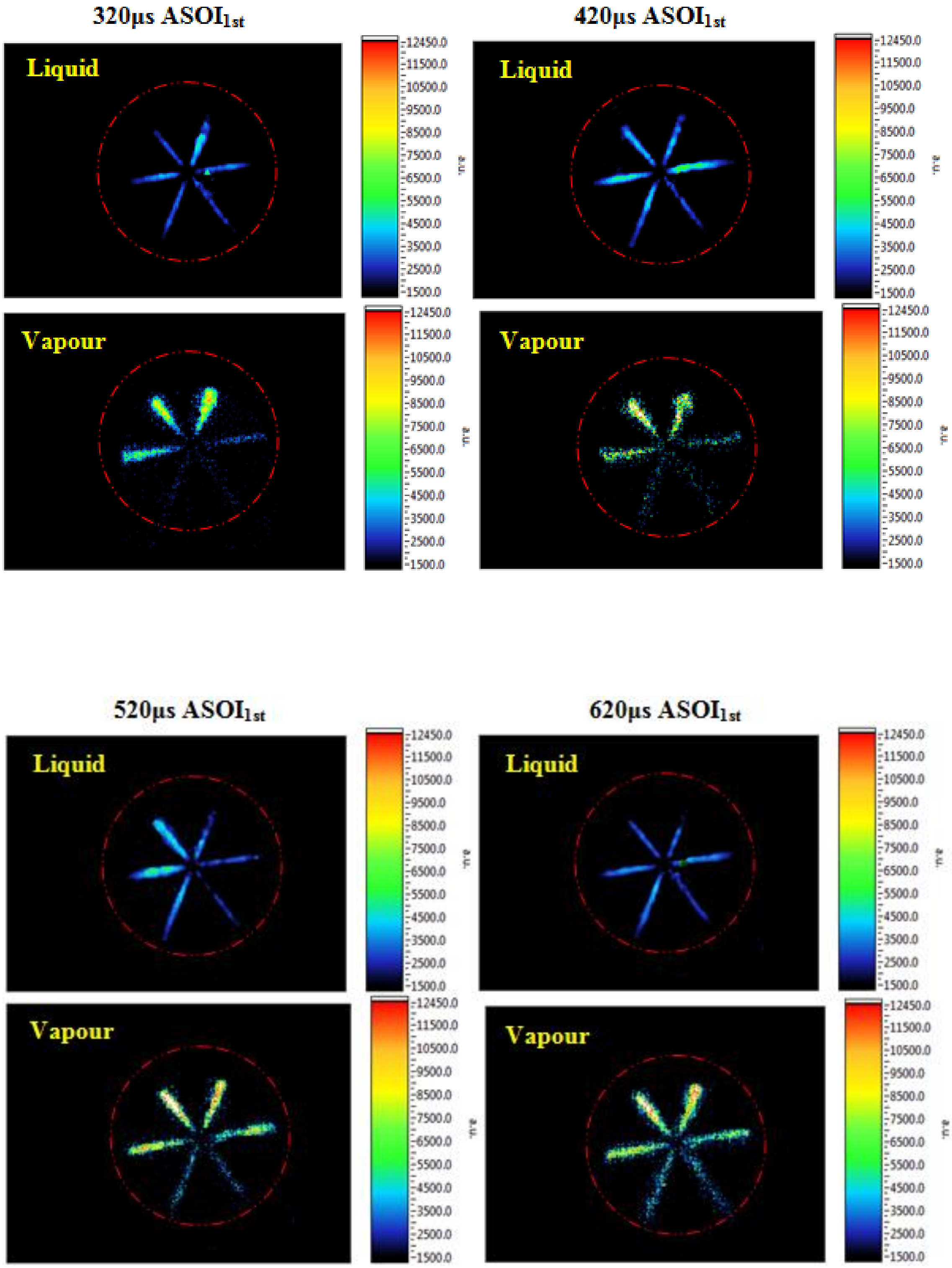

Figure 6.9 Sequence of Liquid and Vapour Images for Strategy D2 (P_{inj}=900bar, 50:50 fuel quantity distribution, 1st injection timing=-100degATDC, 2nd injection timing=-5degATDC)

6.3.5.2 Fuel Injection and Combustion Visualisation

Figure 6.10 demonstrates the image sequence of fuel spray and combustion for strategy D2. As shown in the first three images at -100, -97.3 and -93.7 degrees ATDC, the injection duration of the 1st injection was considerably prolonged in order to compensate for the reduced injection quantity caused by the reduction in injection pressure. The asymmetry of the fuel spray can be clearly seen at -100 degrees ATDC, due to employment of a VOC injector, and the fuel spray was almost evaporated afterwards, at -93.7 degrees ATDC. From the start to the end of the 2nd injection is depicted in the subsequent three frames, at -5, -2.3 and 1.3 degrees ATDC. A larger fuel spray contour was present than that of the 1200 bar injection pressure, due to the longer injection duration. However, it was still much weaker than the fuel spray jet shown in the 1st injection, since the majority of liquid fuel evaporates soon after injection, due to high surrounding temperature and pressure. The first visible ignition spots appeared at the end of the 2nd injection, around 1.3 degrees ATDC. The flame subsequently propagated from the edge of cylinder wall, where highly concentrated fuel vapour was present. Meanwhile, several ignition spots can also be observed over the whole view of the combustion chamber. This spontaneous ignition might be promoted by enhanced temperature from where the initial ignition point was. In the next three frames, at 5.8, 9.4 and 14.8 degrees ATDC, intense flame propagation further developed at the periphery of the piston wall since premixed fuel and air were concentrated at those areas. The most intense flame can be seen around 10 degrees ATDC, corresponding to where the maximum heat release rate occurred. According to heat release rate data of strategy D2, a small quantity of diffusion combustion can be found at the end of premixed combustion. The presence of several combustion sites in frames 14.8 and 22.9 degrees ATDC proved the existence of the aforementioned diffusion combustion. The diminished flame can be seen in the last two frames, with clockwise direction movement indicating swirl motion evolution.

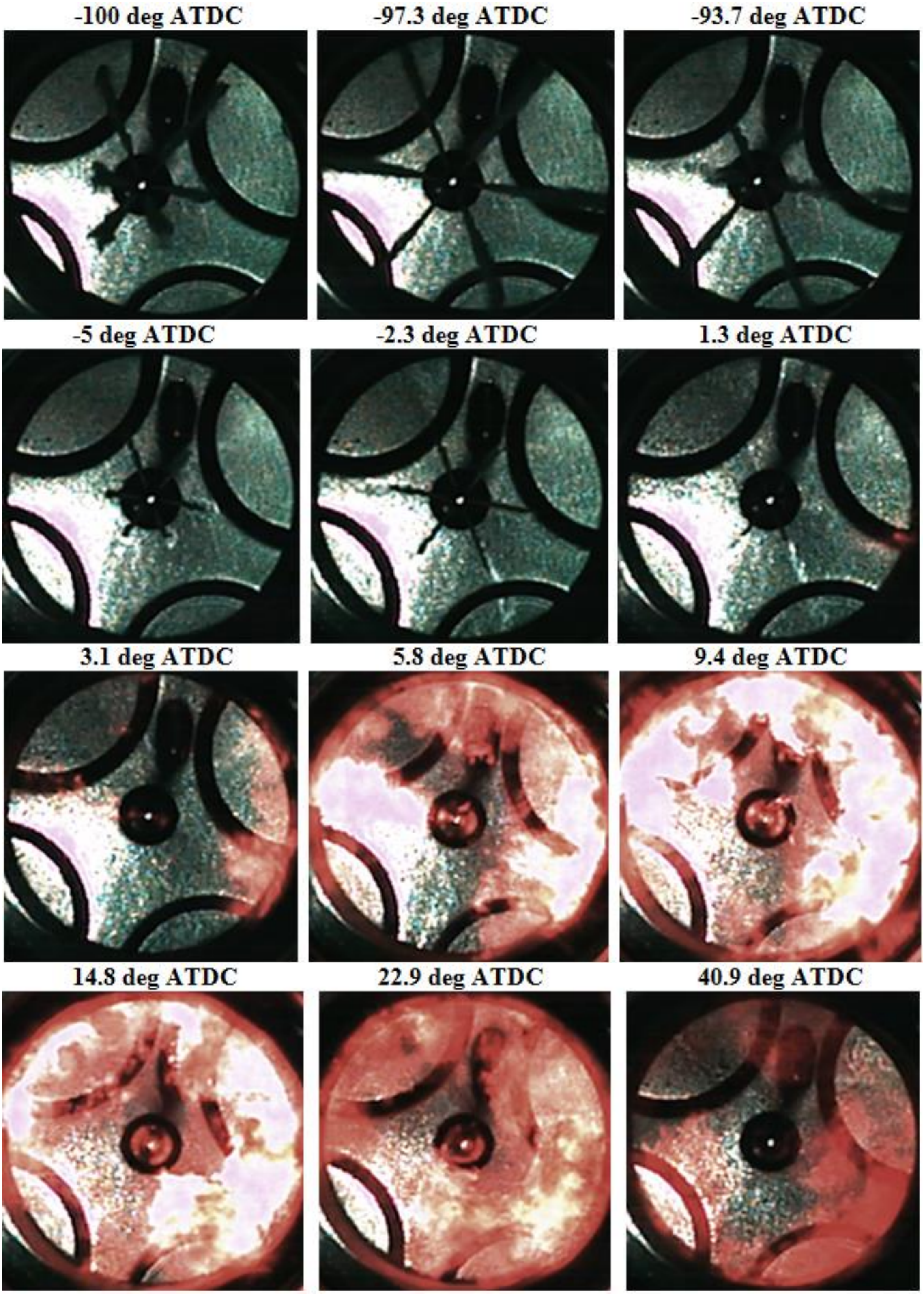

Figure 6.10 Sequence of Combustion Images for Strategy D2 (P_{inj}=900bar, 50:50 fuel quantity distribution, 1st injection timing=-100degATDC, 2nd injection timing=-5degATDC)

6.3.6 Strategy DD2 (PRF 50:50 distribution at 900 bar injection pressure, 1st injection timing=-80degATDC, 2nd injection timing=-5degATDC)

6.3.6.1 Fuel Spray Images for Liquid and Vapour Phases

The image sequence of fuel spray liquid and vapour phases for strategy DD2 are presented in Figure 6.11. The asymmetry of the fuel spray can be seen in the first two liquid and vapour frames at 60 and 120μs ASOI$_{1st}$, since inherent characteristics of the VCO injector caused uneven fuel jet distribution. The fuel liquid spray progressively developed as the injection continued until 420μs ASOI$_{1st}$, and weakened intensity of the spray image was observed in last two frames, at 520 and 620μs ASOI$_{1st}$. This was mainly attributed to more fuel liquid having evaporated into vapour phases at the final stage of injection. The fuel vapour spray was developing in the same manner as the liquid case, but with wider distribution at the periphery of the liquid spray due to evolution of the process of fuel evaporation. This trend became more noticeable as the injection process approached its conclusion. Generally, compared to strategy D2, the fuel vapour image for strategy DD2 presented a more widely spread trend, since the injection timing was retarded to where higher temperature and pressure were present, resulting in an improved fuel-air mixing process. The fuel vapour spray impingement can be recognized after 520μs ASOI$_{1st}$, indicating the place of potential ignition starting spots due to the presence of a highly concentrated fuel-air mixing area.

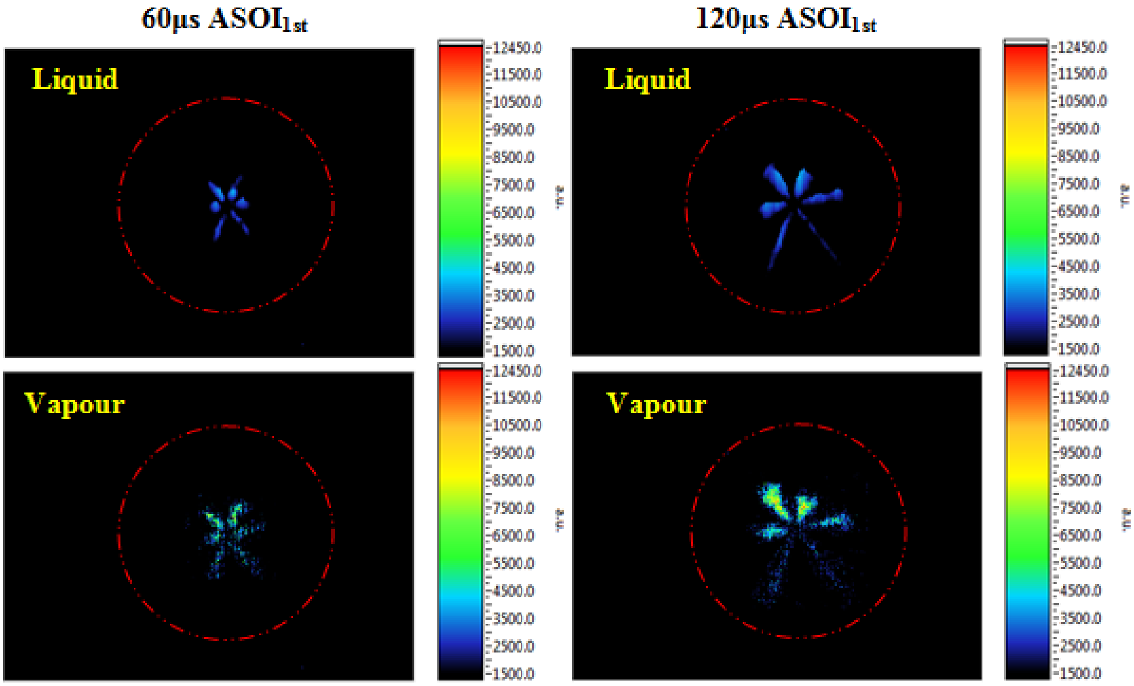
60μs ASOI$_{1st}$

120μs ASOI$_{1st}$

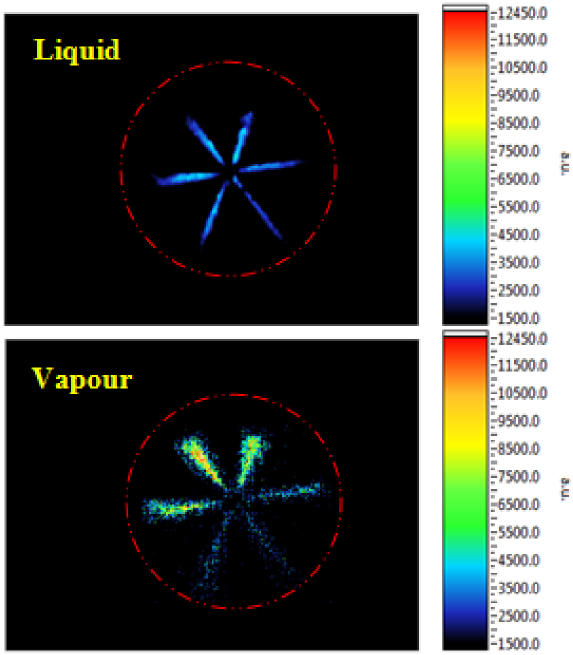

220µs ASOI$_{1st}$

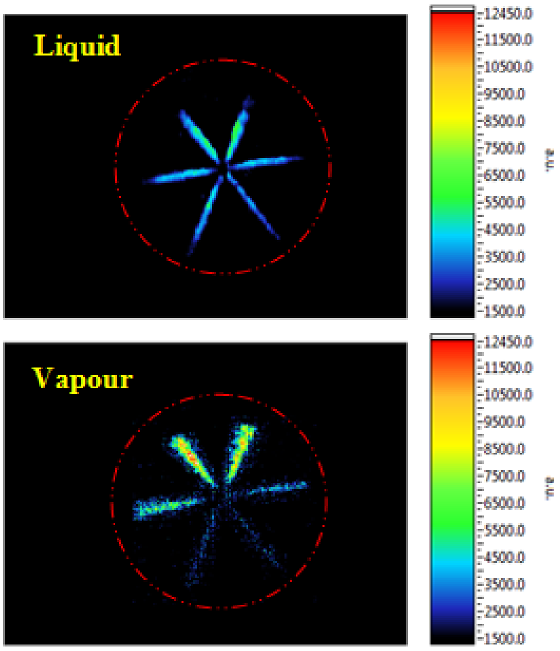

320µs ASOI$_{1st}$

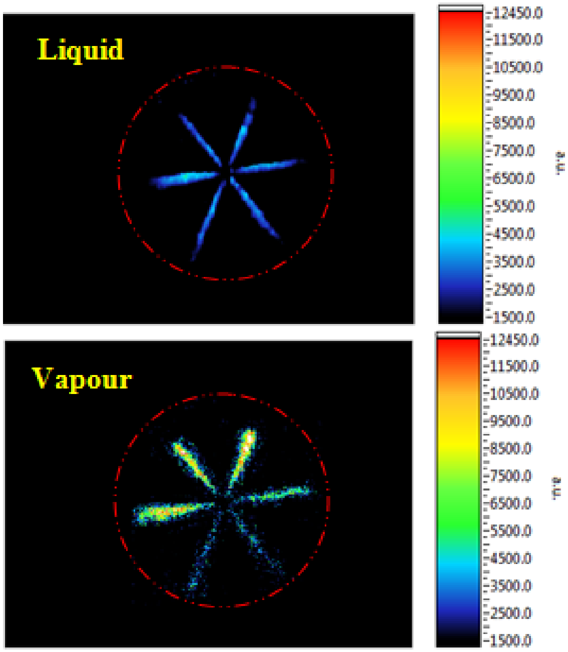

420µs ASOI$_{1st}$

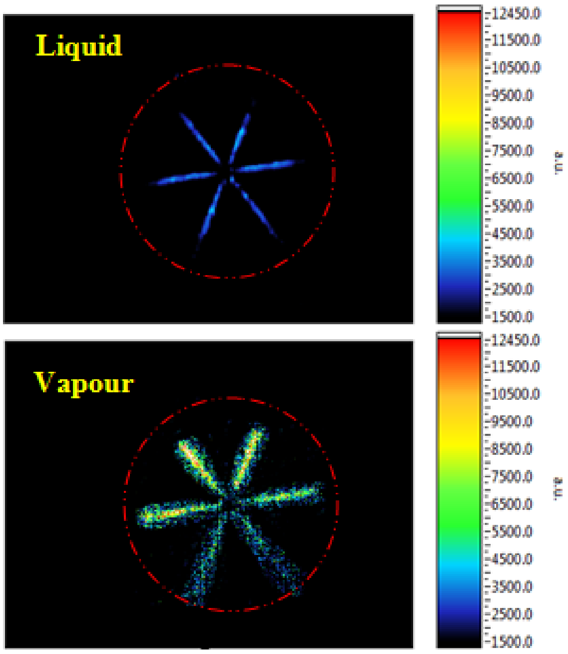

520µs ASOI$_{1st}$

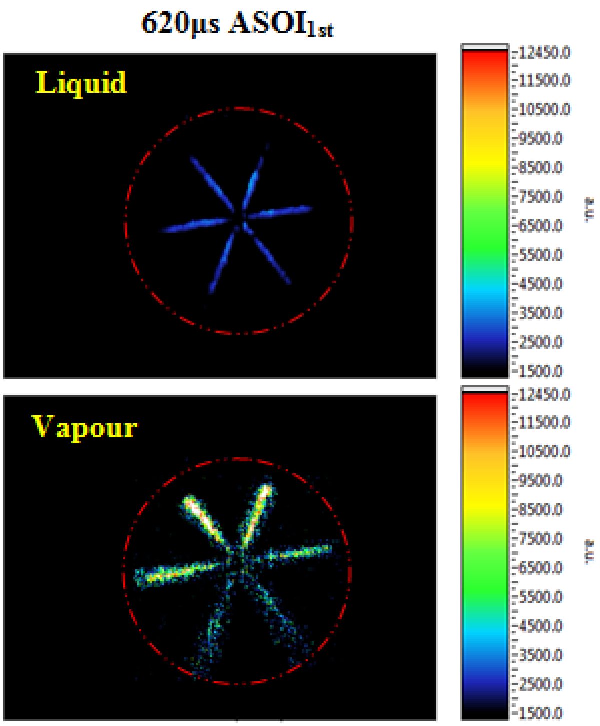

Figure 6.11 Sequence of Liquid and Vapour Images for Strategy DD2 (P_{inj}=900bar, 50:50 fuel quantity distribution, 1st injection timing=-80degATDC, 2nd injection timing=-5degATDC)

6.3.6.2 Fuel Injection and Combustion Visualisation

Figure 6.12 indicates the image sequence of fuel spray and combustion for strategy DD2. As shown in first three frames, at -80, -77.3 and -73.7 degrees ATDC, from the start to the end of the 1st injection can be clearly seen. The asymmetry of the fuel spray coinciding with the Mie-LIF image can be observed at -80 degrees ATDC, and the fuel spray was almost evaporated by -73.7 degrees ATDC. In the next three frames, at -5, -1.4 and 2.2 degrees ATDC, the 2nd injection with shrunken fuel spray contour can be observed. The higher in-cylinder pressure and temperature substantially promoted the process of fuel evaporation since the 2nd injection was placed closed to TDC. The first appearance of visible combustion can be seen by the end of the 2nd injection at 2.2 degrees ATDC, and the ignition spots occurred at the tip of the injection jet. It differed from the onset of the combustion flame in strategy D2, which had weaker initiated ignition points. It can be understood by considering the effect of more complete fuel-air mixture under the retarded 1st injection timing. In the next frame, at 4 degrees ATDC, four developing flames can be detected in the area where fuel spray jets used to be, indicating a more concentrated fuel-air mixture region. The flame propagated rapidly, spreading to peripheral regions of the combustion chamber with fairly bright colour. The most intense flame can be found at 13.9 degrees ATDC corresponding to where the maximum heat release rate occurred. Although there was little evidence for diffusion combustion on the basis of the heat release rate data shown in Figure 5.31, the several presented combustion sites can be recognized as the existence of diffusion combustion. The flame was gradually diminished in subsequent frames at 21.1, 29.2 and 39.1 degrees ATDC with the clockwise direction movement due to the swirl motion.

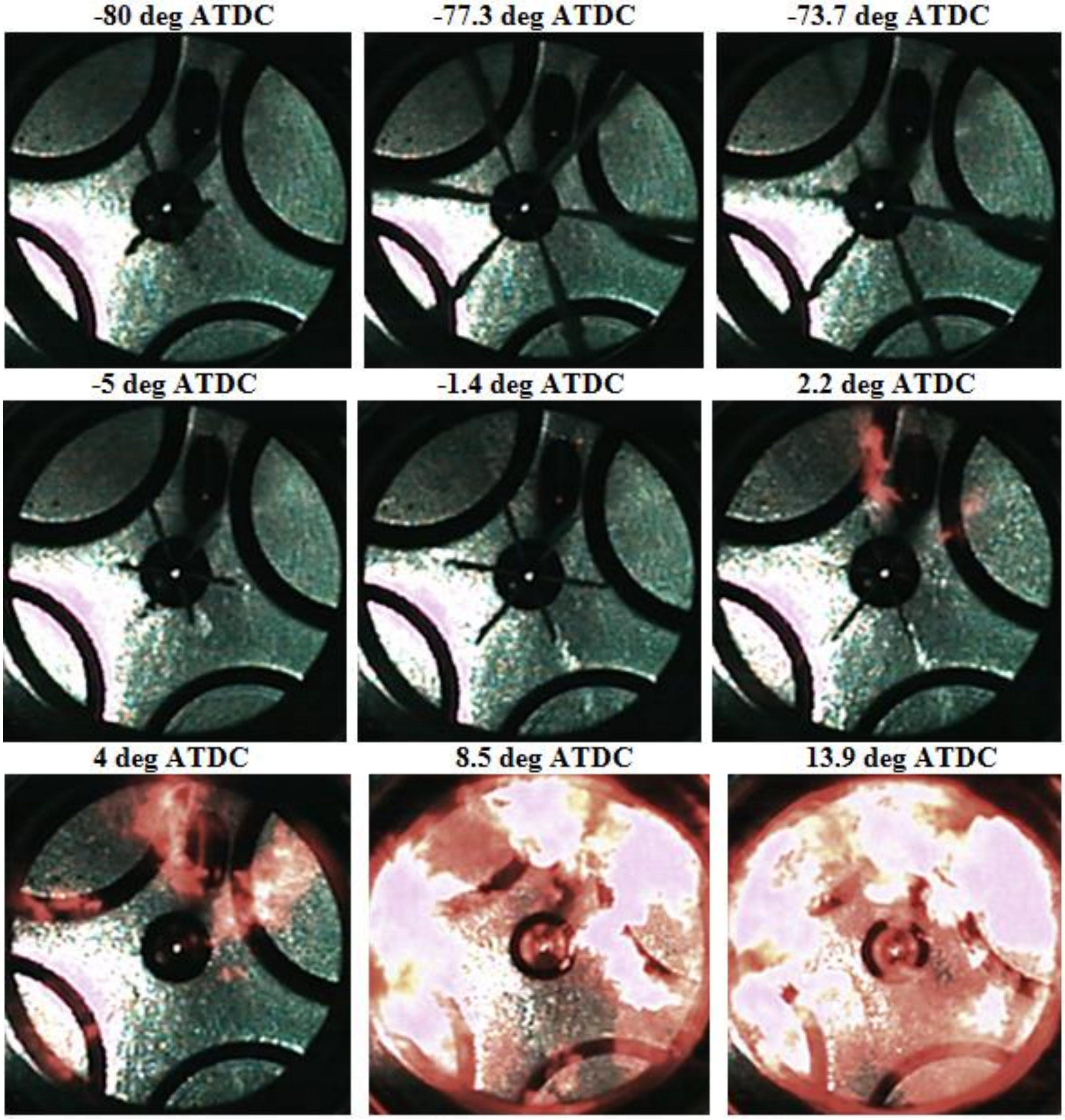

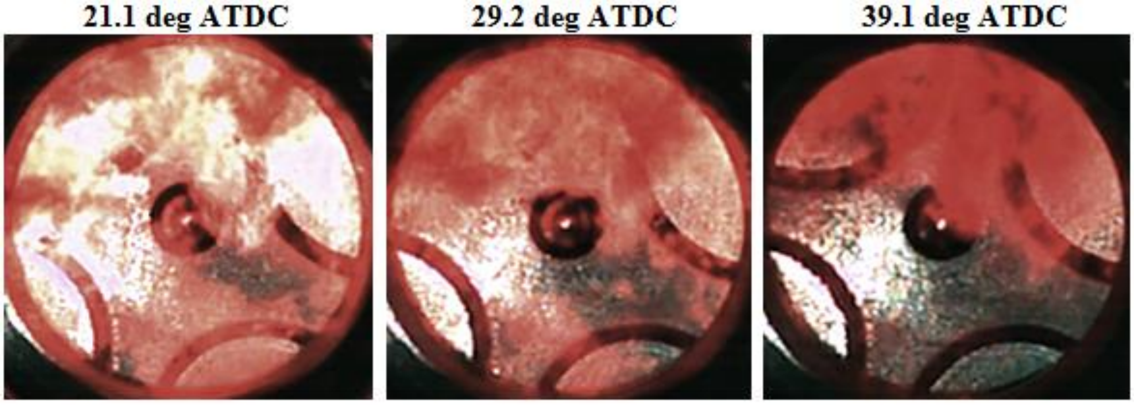

Figure 6.12 Sequence of Combustion Images for Strategy DD2 (P_{inj}=900bar, 50:50 fuel quantity distribution, 1st injection timing=-80degATDC, 2nd injection timing=-5degATDC)

6.3.7 Strategy E2 (PRF 70:30 distribution at 900 bar injection pressure, 1st injection timing=-100degATDC, 2nd injection timing=-5degATDC)

6.3.7.1 Fuel Spray Images for Liquid and Vapour Phases

The image sequence of fuel spray liquid and vapour phases for strategy E2 are presented in Figure 6.13. Since a 70:30 fuel quantity distribution at 900 bar injection pressure was used in this strategy, the longest injection duration was experienced for the 1st injection. It is similar to previous strategies, in that asymmetry of the fuel spray was observed for both liquid and vapour phases at an early stage of injection, 80 and 160μs $ASOI_{1st}$, due to utilization of a VCO injector. The fuel liquid spray gradually developed until 620μs $ASOI_{1st}$ and intensity reduction was encountered in the last two frames, at 700 and 800μs $ASOI_{1st}$. This was mainly due to large amounts of fuel liquid transitioning to the vapour phase. In terms of fuel vapour images, enlarged fuel jets were formed, indicating the process of fuel evaporation. The difference between fuel liquid and vapour phases progressively increased; since the fuel evaporation was accelerated as injection progressed. Spray impingement was detected in fuel vapour images from 620μs $ASOI_{1st}$ until the end of fuel injection, owing to prolonged injection duration.

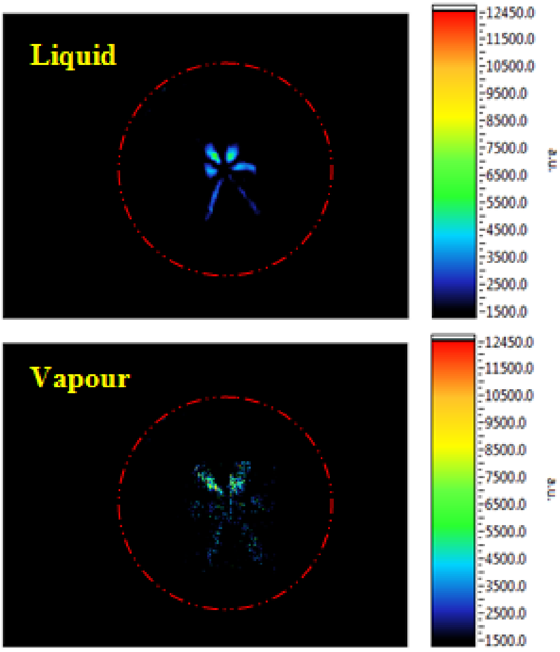

80μs ASOI$_{1st}$

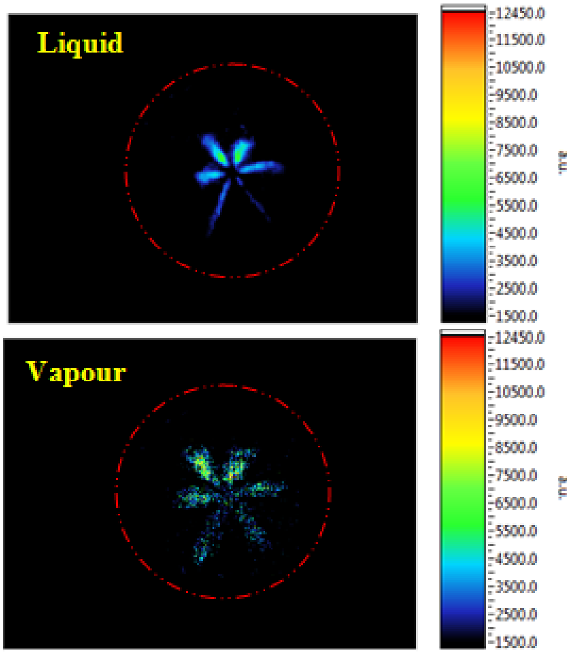

160μs ASOI$_{1st}$

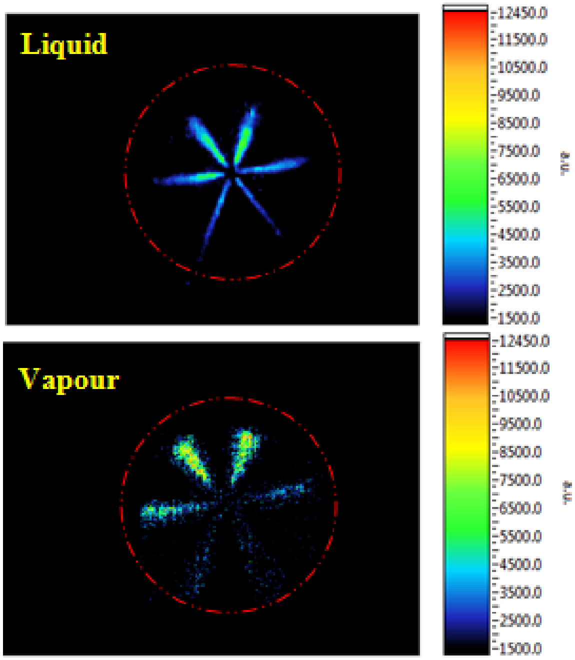

240μs ASOI$_{1st}$

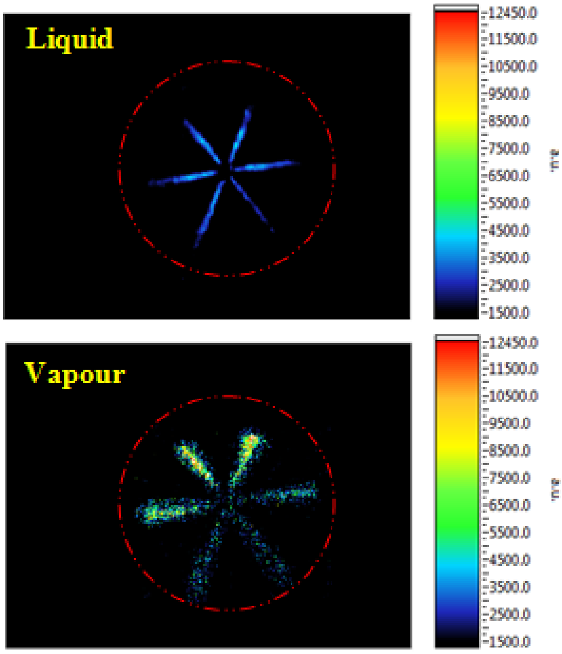

320μs ASOI$_{1st}$

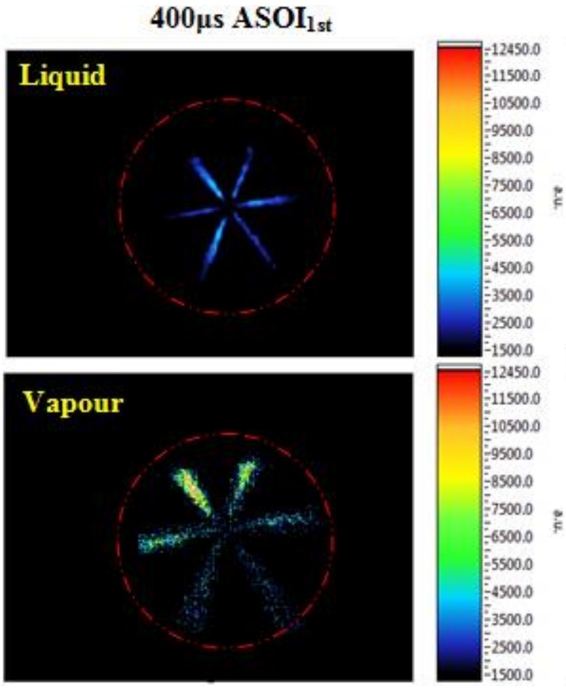
400μs ASOI$_{1st}$

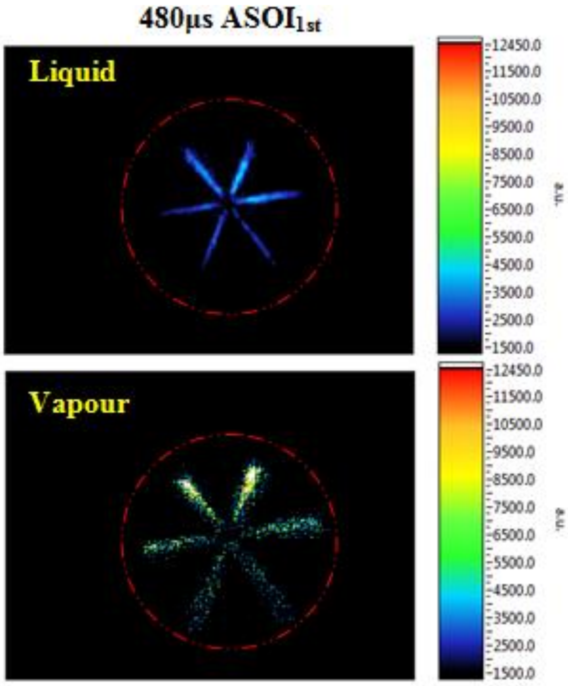
480μs ASOI$_{1st}$

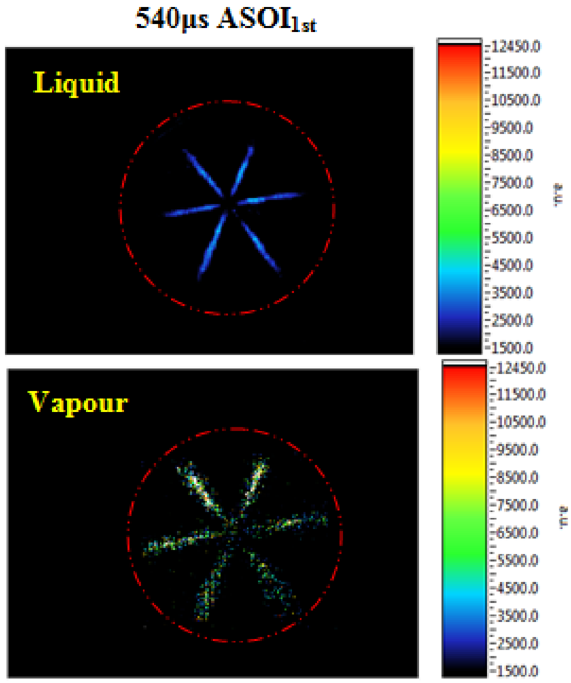
540μs ASOI$_{1st}$

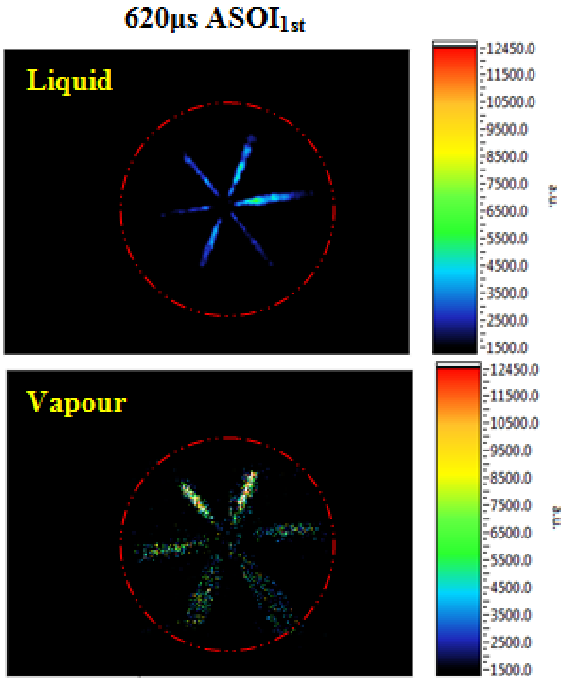
620μs ASOI$_{1st}$

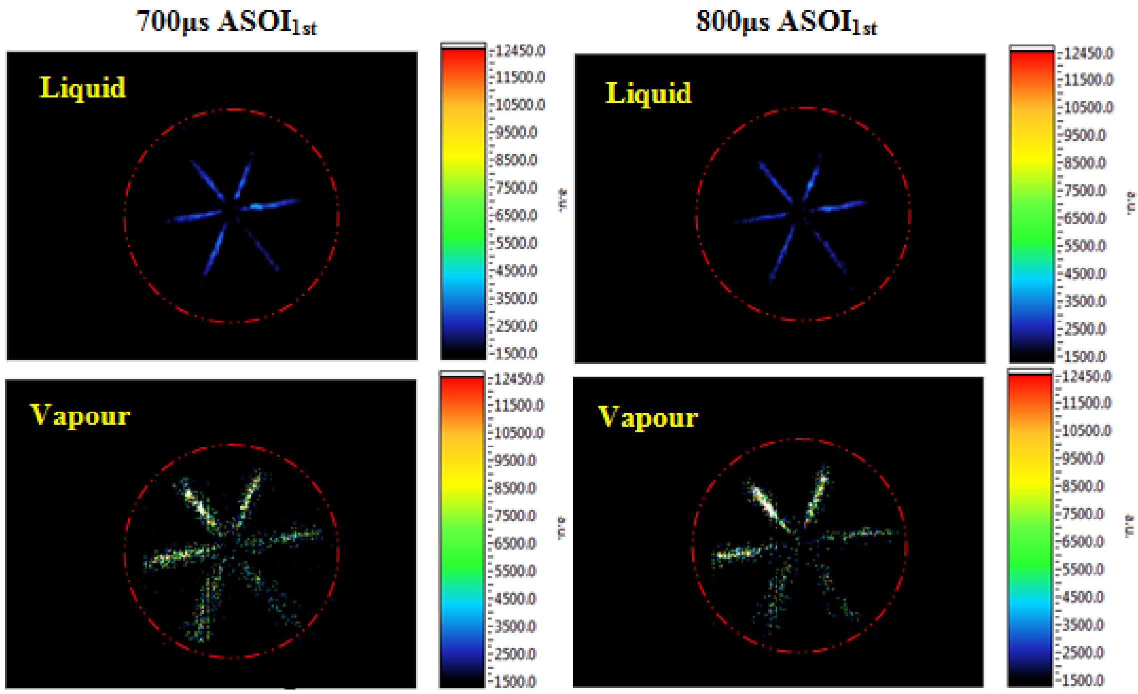

Figure 6.13 Sequence of Liquid and Vapour Images for Strategy E2 (P_{inj}=900bar, 70:30 fuel quantity distribution, 1st injection timing=-100degATDC, 2nd injection timing=-5degATDC)

6.3.7.2 Fuel Injection and Combustion Visualisation

Figure 6.14 shows the image sequence of fuel spray and combustion for strategy E2. The further increased injection duration for the 1st injection can be seen in the first three frames, from -100 to -89.2 degrees ATDC. The asymmetry of the fuel spray is apparent in the first image, and almost evaporated spray can be detected in the last frame. In the next three frames at -5, -2.3 and 0.4 degrees ATDC, the start to the end of the 2nd injection is presented. It is evident that the visible fuel spray was quite short since only 30% of the total amount of fuel was injected during the 2nd injection. It is noted that the first appearance of the combustion flame was presented in the middle of the 2nd injection at -2.3 degrees ATDC. This was mainly attributed to well premixed fuel-air mixture having been generated by the large amount of injected fuel in the 1st injection, so that the ignition boundary was reached once the 2nd injection took place. The combustion flame was initiated at one of the injection jets, with several tiny ignition spots spreading over the combustion chamber. In the next frame, at 0.4 degrees ATDC, four mushroom like flames can be clearly seen, indicating the developing flame propagation. The flame subsequently propagated at the tip of sprays spreading to the periphery of the piston wall, where the more concentrated fuel-air mixture was. The most intense flame was obtained at 7.6 degrees ATDC, where the maximum heat release rate also occurred. The intense flame was extended to 13 degrees ATDC, with the trend spreading to the central region of the combustion chamber. In the last three frames, at 18.4, 26.5 and 35.5 degrees ATDC, the flame gradually diminished with several combustion sites representing some diffusion combustion.

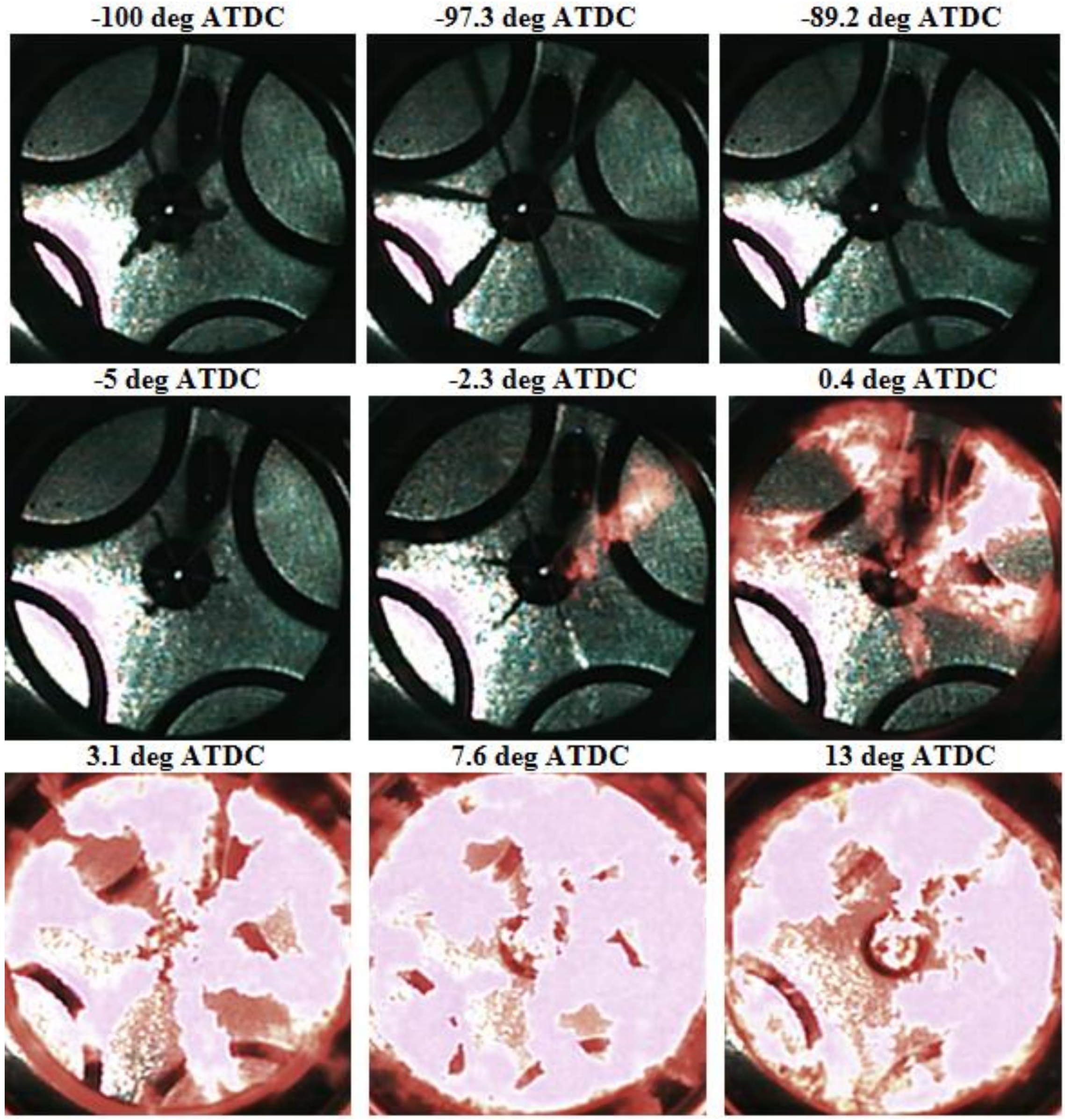
-100 deg ATDC
-97.3 deg ATDC
-89.2 deg ATDC
-5 deg ATDC
-2.3 deg ATDC
0.4 deg ATDC
3.1 deg ATDC
7.6 deg ATDC
13 deg ATDC

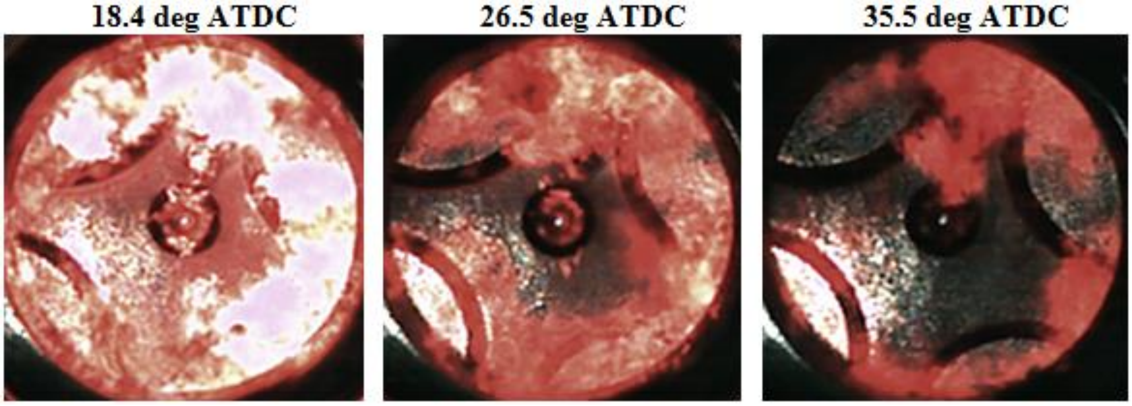

Figure 6.14 Sequence of Combustion Images for Strategy E2 (P_{inj}=900bar, 70:30 fuel quantity distribution, 1st injection timing=-100degATDC, 2nd injection timing=-5degATDC)

6.3.8 Strategy EE2 (PRF 70:30 distribution at 900 bar injection pressure, 1st injection timing=-80degATDC, 2nd injection timing=-5degATDC)

6.3.8.1 Fuel Spray Images for Liquid and Vapour Phases

The image sequence of fuel spray liquid and vapour phases for strategy EE2 are shown in Figure 6.15. For the fuel liquid images, asymmetry of the fuel spray can be seen, as expected owing to the inherent characteristic of the VCO injector. The fuel liquid jets subsequently grew up as the injection progressed, until 540μs ASOI$_{1st}$; weakened fuel spray intensity was observed at later stages of injection, after 620μs ASOI$_{1st}$, due to more evaporated fuel having been generated. In terms of fuel vapour results, enlarged coverage can be detected compared to fuel liquid jets, indicating the fuel evaporation process. It is noted that a slightly growing trend for fuel vapour jet size was observed compared to strategy E2. This was mainly attributed to the fuel evaporating process having been promoted by placing the 1st injection timing closed to TDC, where higher in-cylinder temperature and pressure are reached. The fuel spray impingement shown in the last three frames took place after 540μs ASOI$_{1st}$.

For the purposes of comparison, the image sequence for the 2nd injection was presented, followed by the 1st injection. It can be seen in 2nd injection that the asymmetry of the fuel spray was considerably reduced in both liquid and vapour results. The fuel liquid jets showed tiny contours throughout the whole injection, since less fuel was injected during the 2nd injection. However, the fuel vapour sprays progressively developed until the end of the 2nd injection, demonstrating an effective fuel evaporation process, owing to the contribution of further increased in-cylinder temperature and pressure.

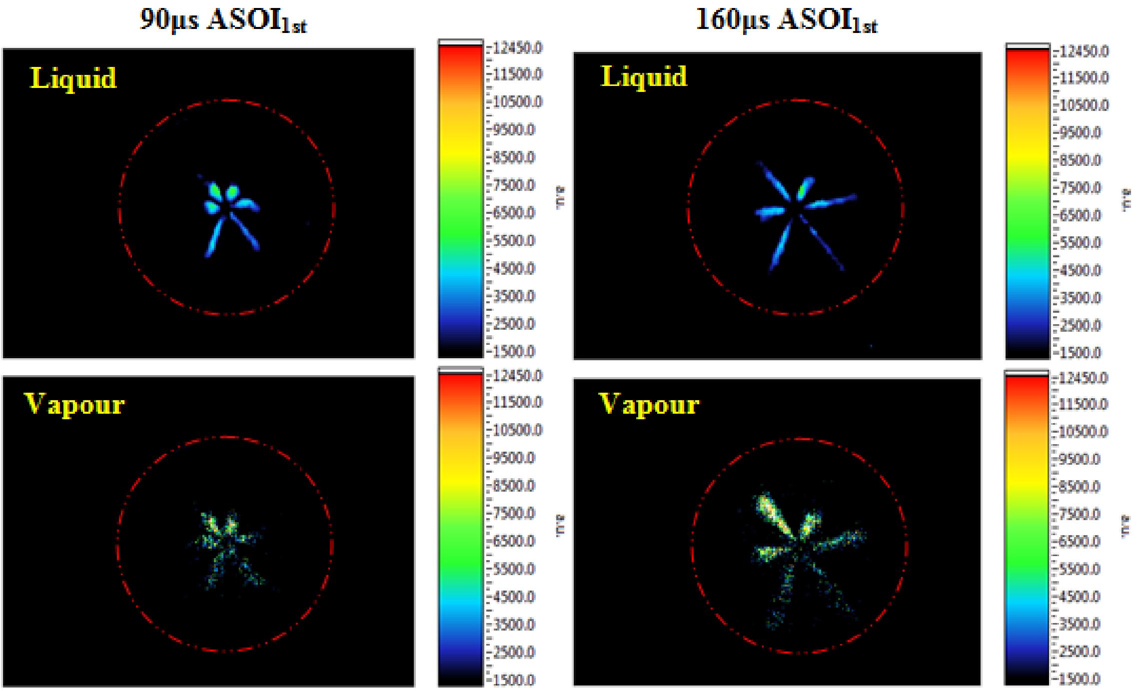

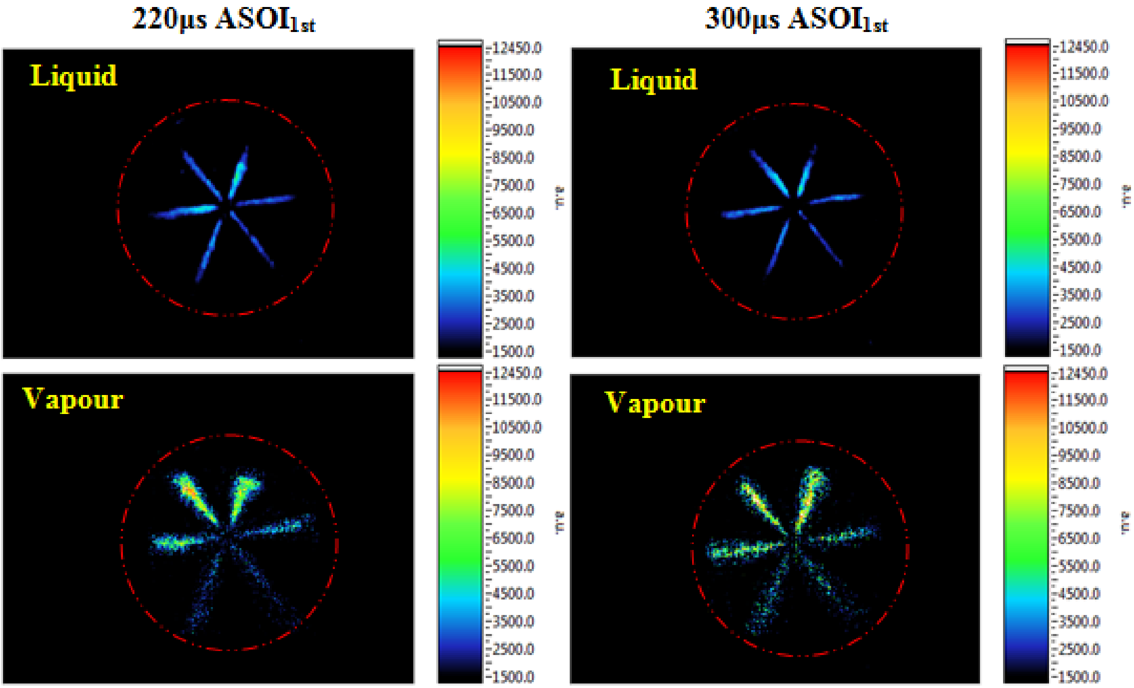

380μs ASOI$_{1st}$

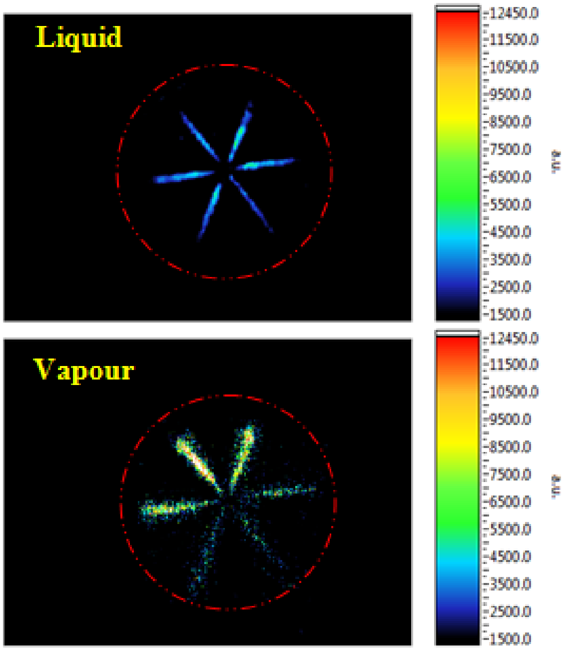

460μs ASOI$_{1st}$

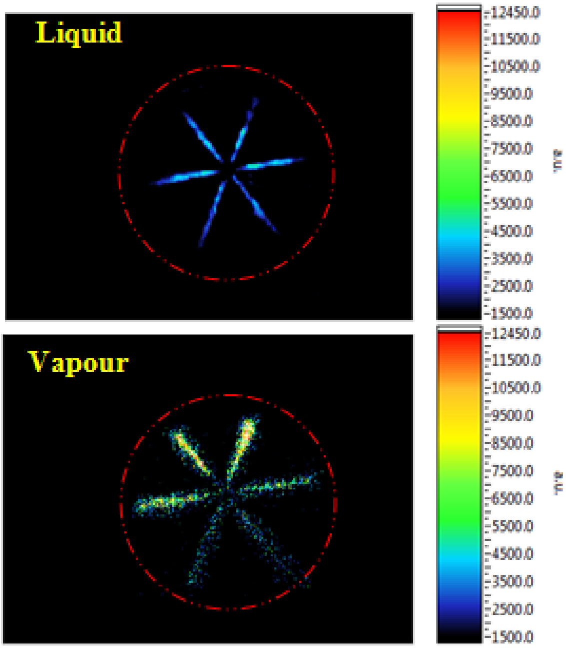

540μs ASOI$_{1st}$

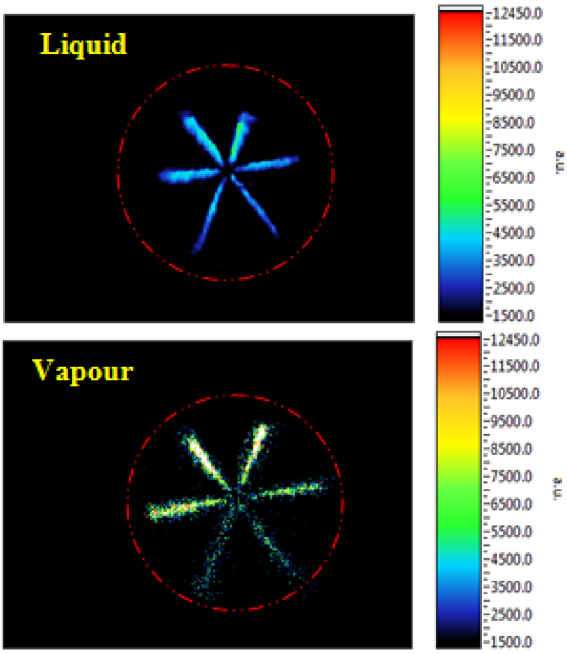

620μs ASOI$_{1st}$

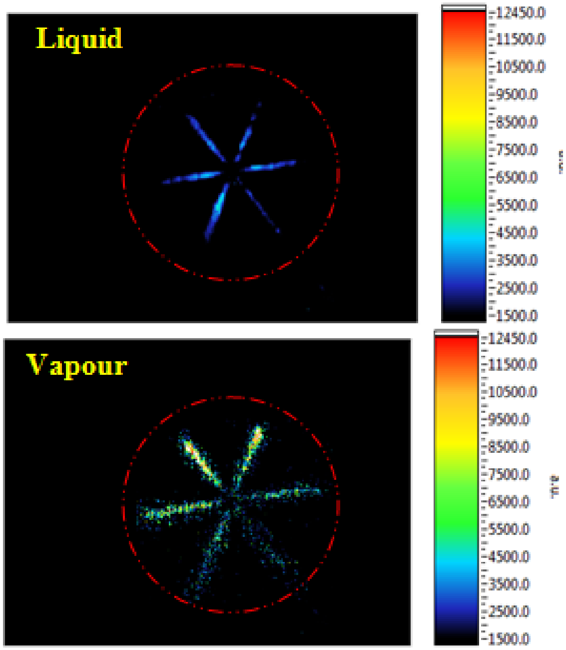

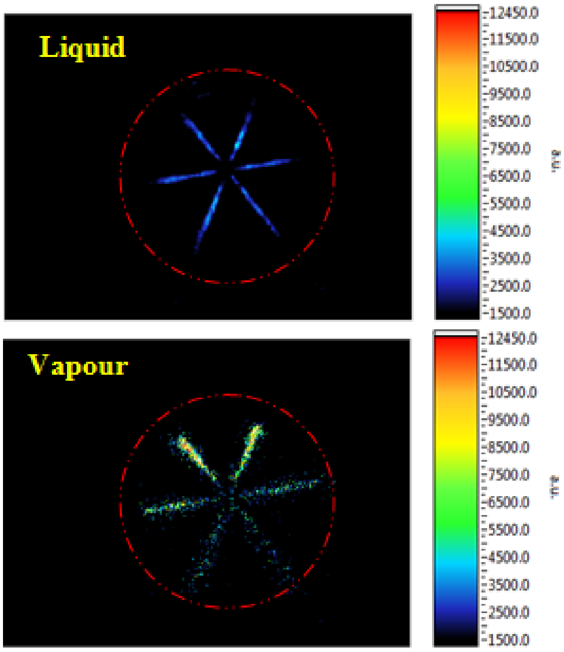

700µs ASOI$_{1st}$

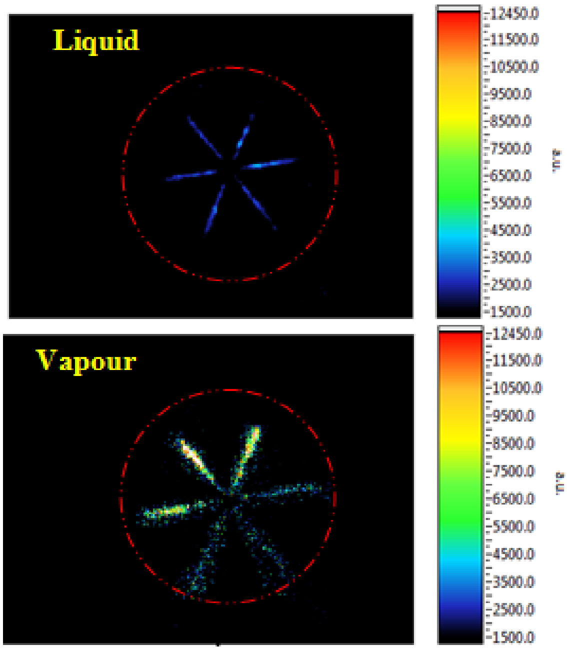

800µs ASOI$_{1st}$

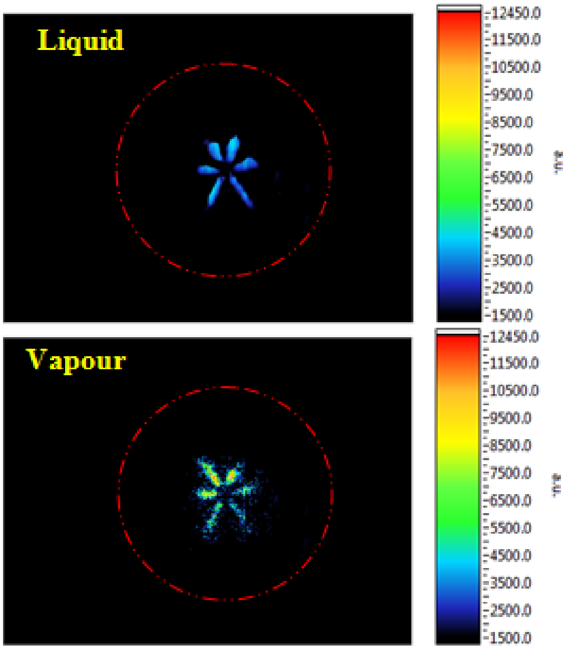

100µs ASOI$_{2nd}$

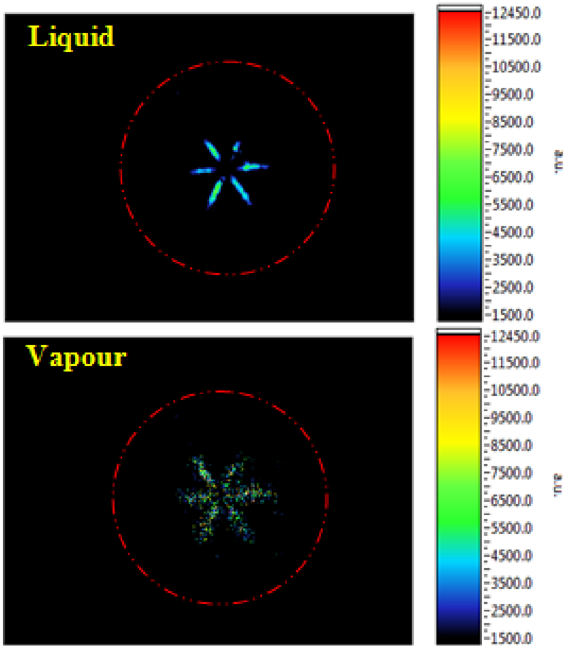

150µs ASOI$_{2nd}$

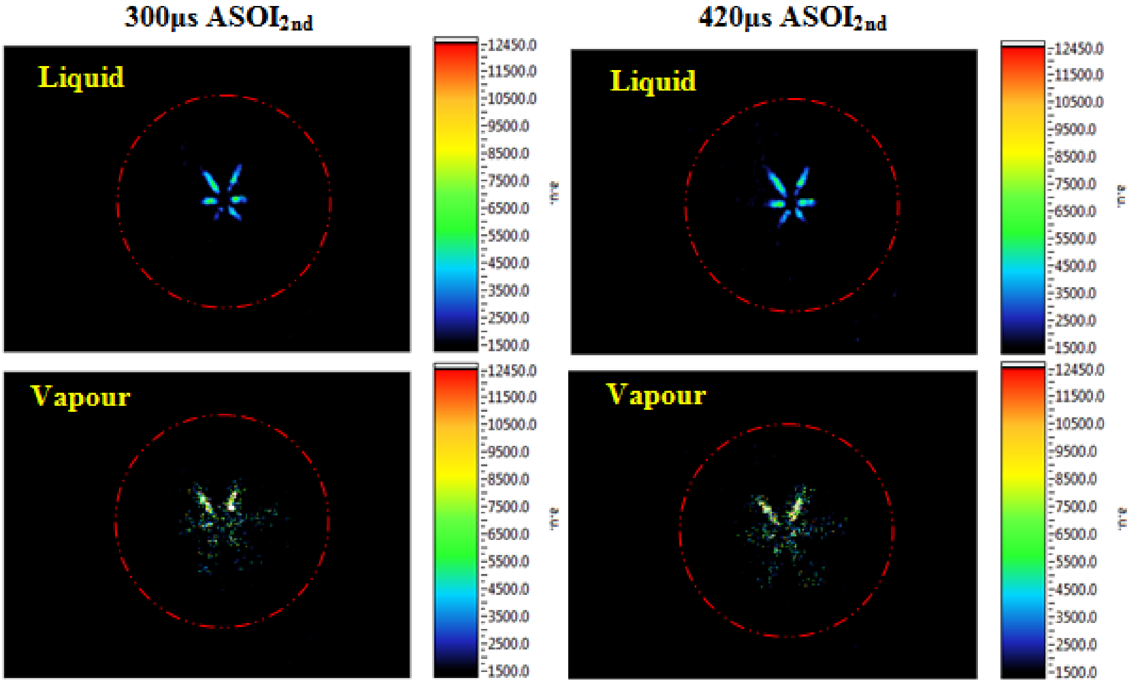

Figure 6.15 Sequence of Liquid and Vapour Images for Strategy EE2 (P_{inj}=900bar, 70:30 fuel quantity distribution, 1st injection timing=-80degATDC, 2nd injection timing=-5degATDC)

6.3.8.2 Fuel Injection and Combustion Visualisation

Figure 6.46 demonstrates the image sequences of fuel spray and combustion for strategy EE2. The 1st injection evolution is presented in the first three frames, where the asymmetry of the initiated fuel spray became apparent at -80 degrees ATDC, and almost evaporated fuel jet was present at -70.1 degrees ATDC. In the next three frames, at -5, -1.4 and 1.3 degrees ATDC, the 2nd injection showed fairly small fuel jets as only 30% of the total amount of fuel was injected. The first visible combustion flame appeared during the 2nd injection at -1.4 degrees ATDC, indicating an early onset of heat release for this strategy. The flame rapidly developed in subsequent frames at 1.3 and 4 degrees ATDC, showing mushroom shape profiles. It is worth noting that only four visible flames presented at the right side view of the combustion chamber, with a relatively blank area on left side view. This can be understood by considering the existence of incomplete combustion for this strategy. The most intense flame was obtained at 8.5 degrees ATDC, corresponding to where the maximum heat release rate took place. The combustion flames gradually diminished after 13.9 degrees ATDC, with the appearance of several combustion sites indicating the existence of diffusion combustion. Clockwise direction movements can be seen in the last two frames, due to swirl motion evolution.

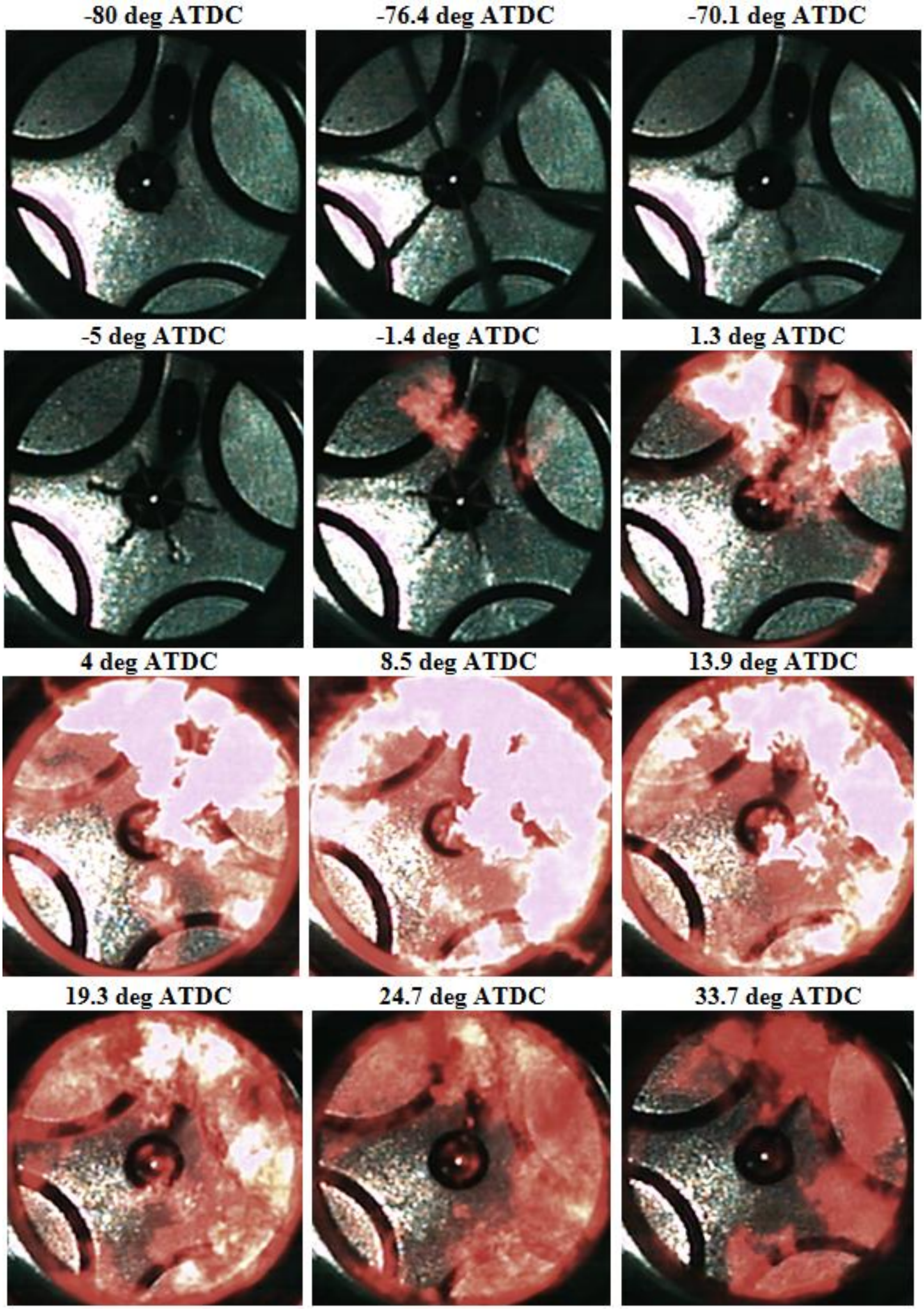

Figure 6.16 Sequence of Combustion Images for Strategy EE2 (P_{inj}=900bar, 70:30 fuel quantity distribution, 1st injection timing=-80degATDC, 2nd injection timing=-5degATDC)

6.3.9 Strategy F2 (diesel 10:90 distribution at 1200 bar injection pressure, 1st injection timing=-25degATDC, 2nd injection timing=-5degATDC)

6.3.9.1 Diesel Fuel Spray Images for Liquid and Vapour Phases

The image sequence of diesel fuel spray liquid and vapour for strategy F2 are shown in Figure 6.17. The results for the 1st injection (pilot injection) indicated an asymmetrical fuel spray at the initial injection stage before 100μs ASOI_{1st}, and the fuel spray became evenly distributed as the injection progressed. In this diesel injection strategy, noticeable differences between the fuel liquid and vapour images can only be seen when the injection was approaching the end, at 250μs ASOI_{1st}, demonstrating its slower fuel evaporating process. In terms of results for 2nd injection (main injection), the uneven fuel spray distribution was not as obvious as for the pilot injection. The fuel liquid spray progressively developed as the injection went along, without seeing any intensity reduction, which differed from the results shown in the gasoline cases. This was to some extent due to the weaker evaporation ability of diesel fuel. It can also be proved by considering the slow growing rate of fuel vapour jets, which presented almost the same spray contour as liquid phases. The fuel spray impingement can be clearly detected from 450μs ASOI_{2nd} until the end of injection at 580μs ASOI_{2nd}, since the fuel sprays were fully developed. The mushroom type shapes were formed between the tip of injection jet and the edge of cylinder wall for both fuel liquid and vapour phases. It is worth noting that more fuel vapour was generated at late stage of injection due to fuel spray impingement.

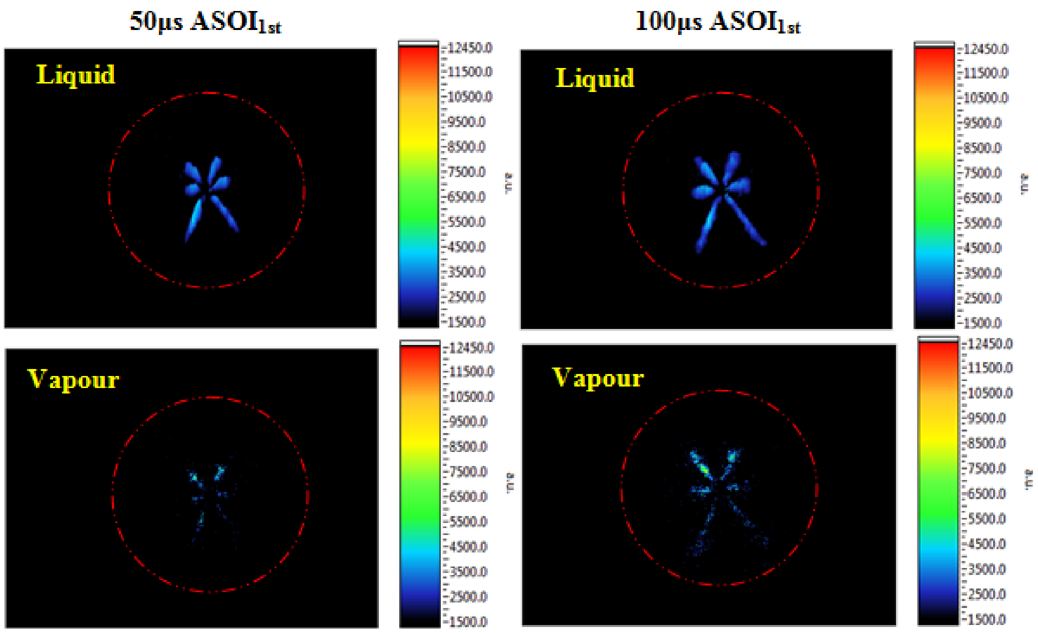

150μs ASOI$_{1st}$

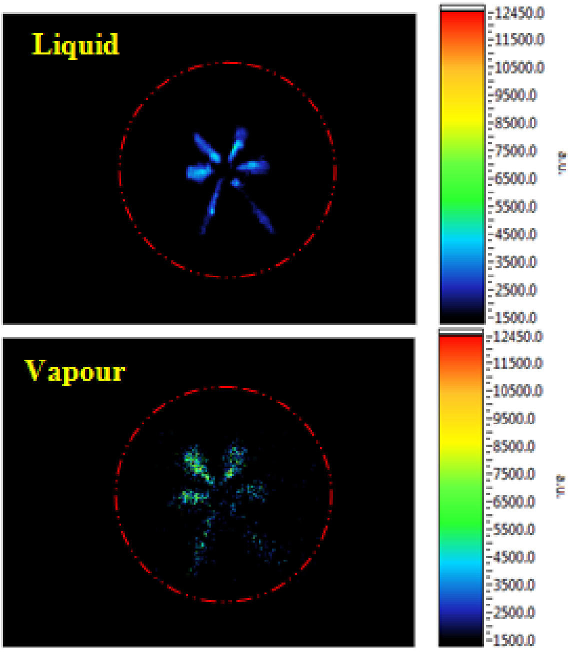

200μs ASOI$_{1st}$

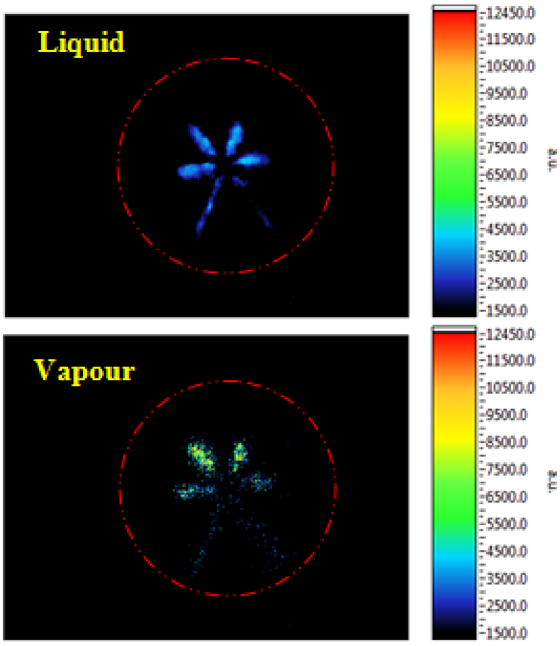

250μs ASOI$_{1st}$

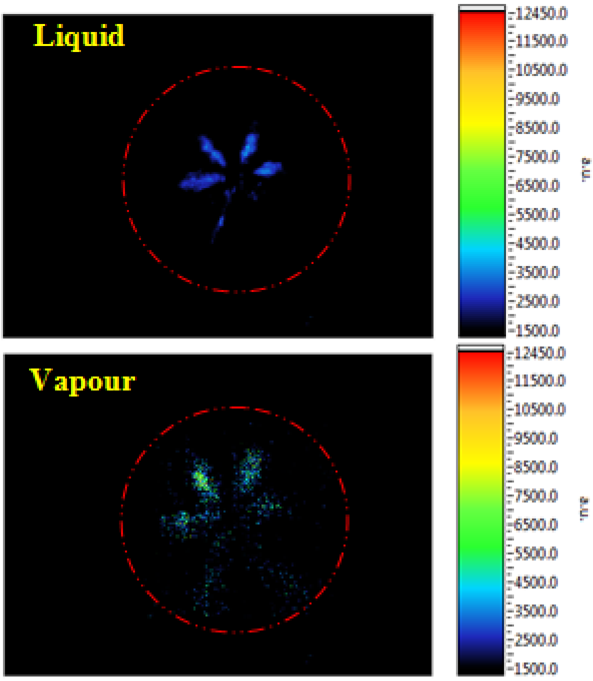

30μs ASOI$_{2nd}$

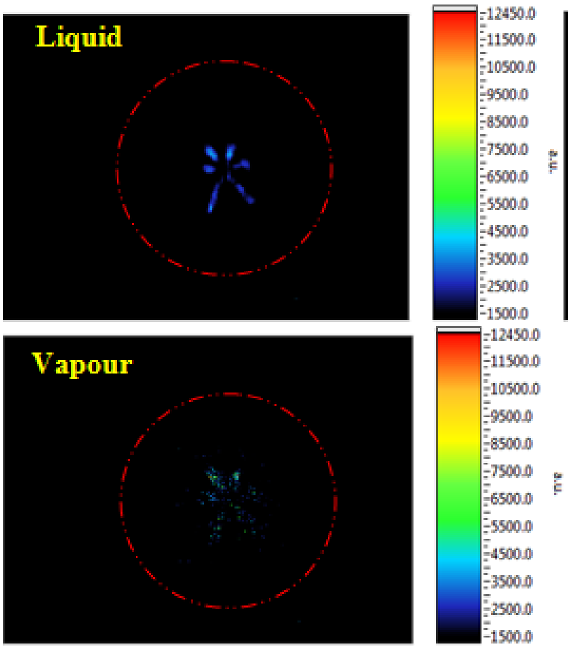

60μs ASOI$_{2nd}$

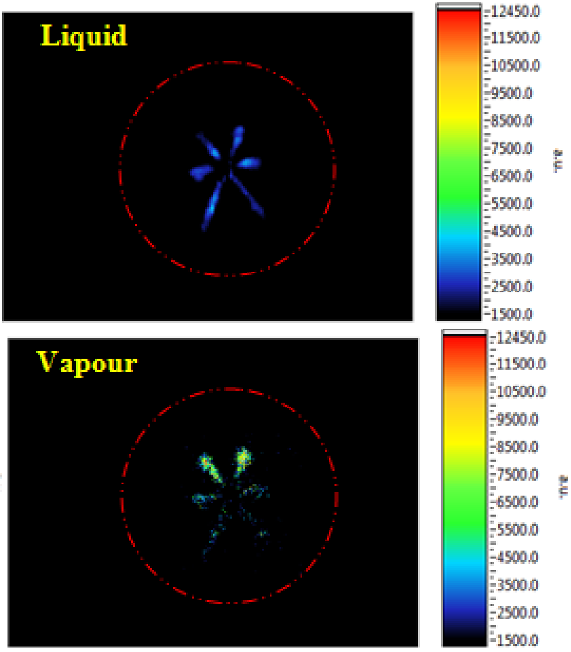

150μs ASOI$_{2nd}$

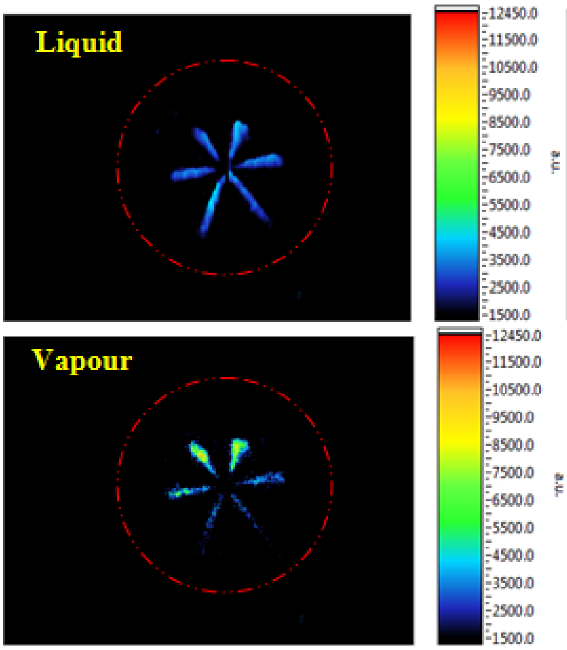

200μs ASOI$_{2nd}$

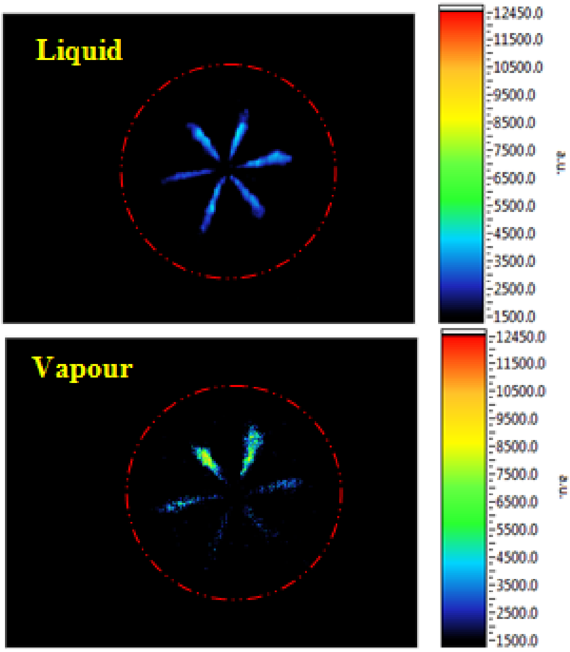

250μs ASOI$_{2nd}$

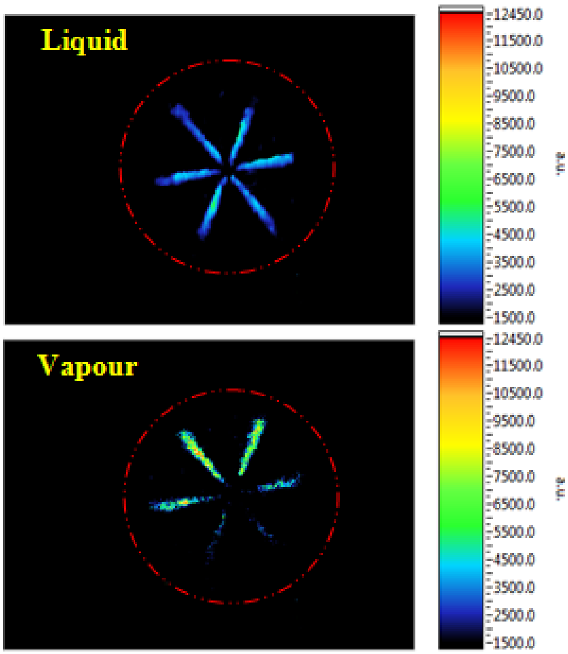

300μs ASOI$_{2nd}$

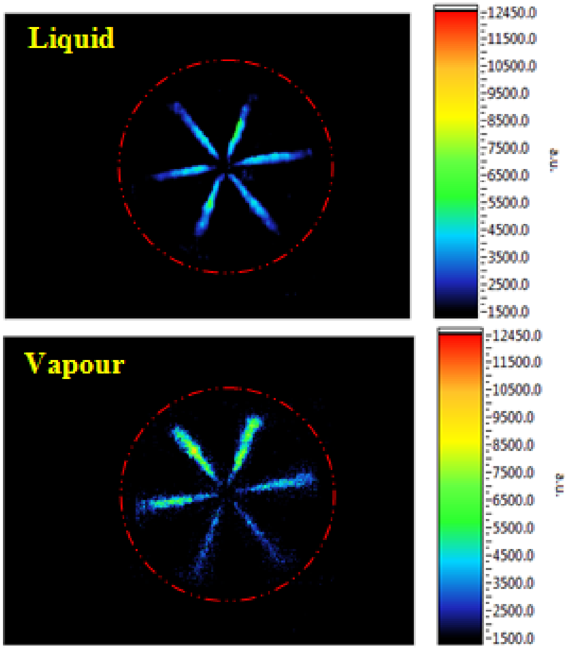

350μs ASOI$_{2nd}$

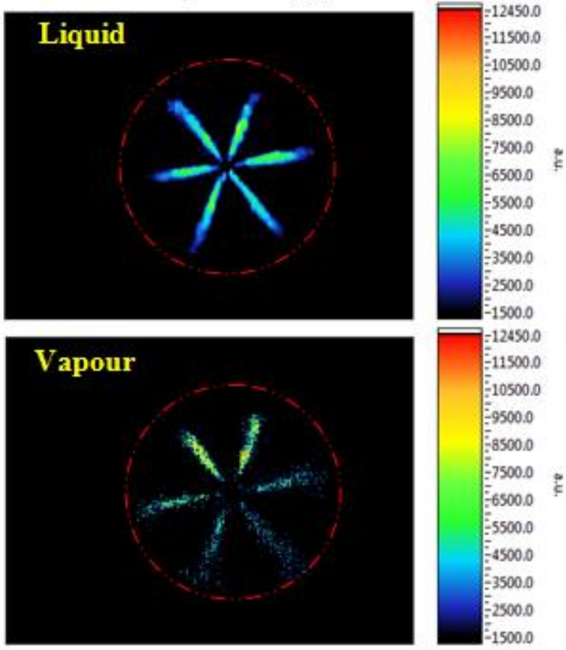

400μs ASOI$_{2nd}$

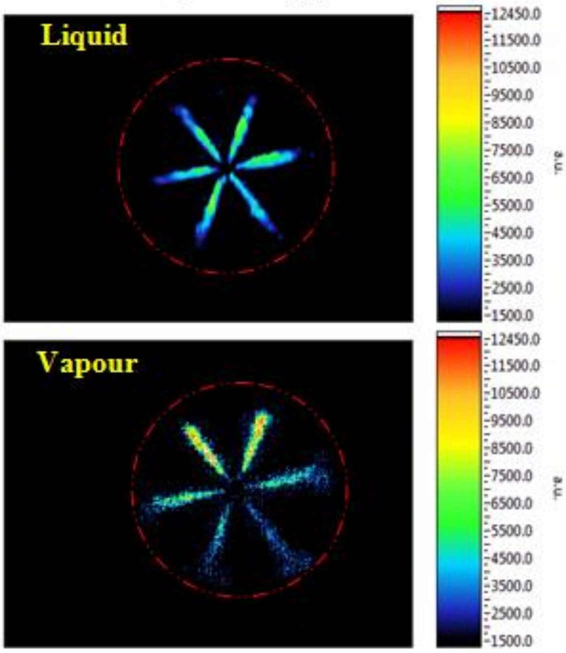

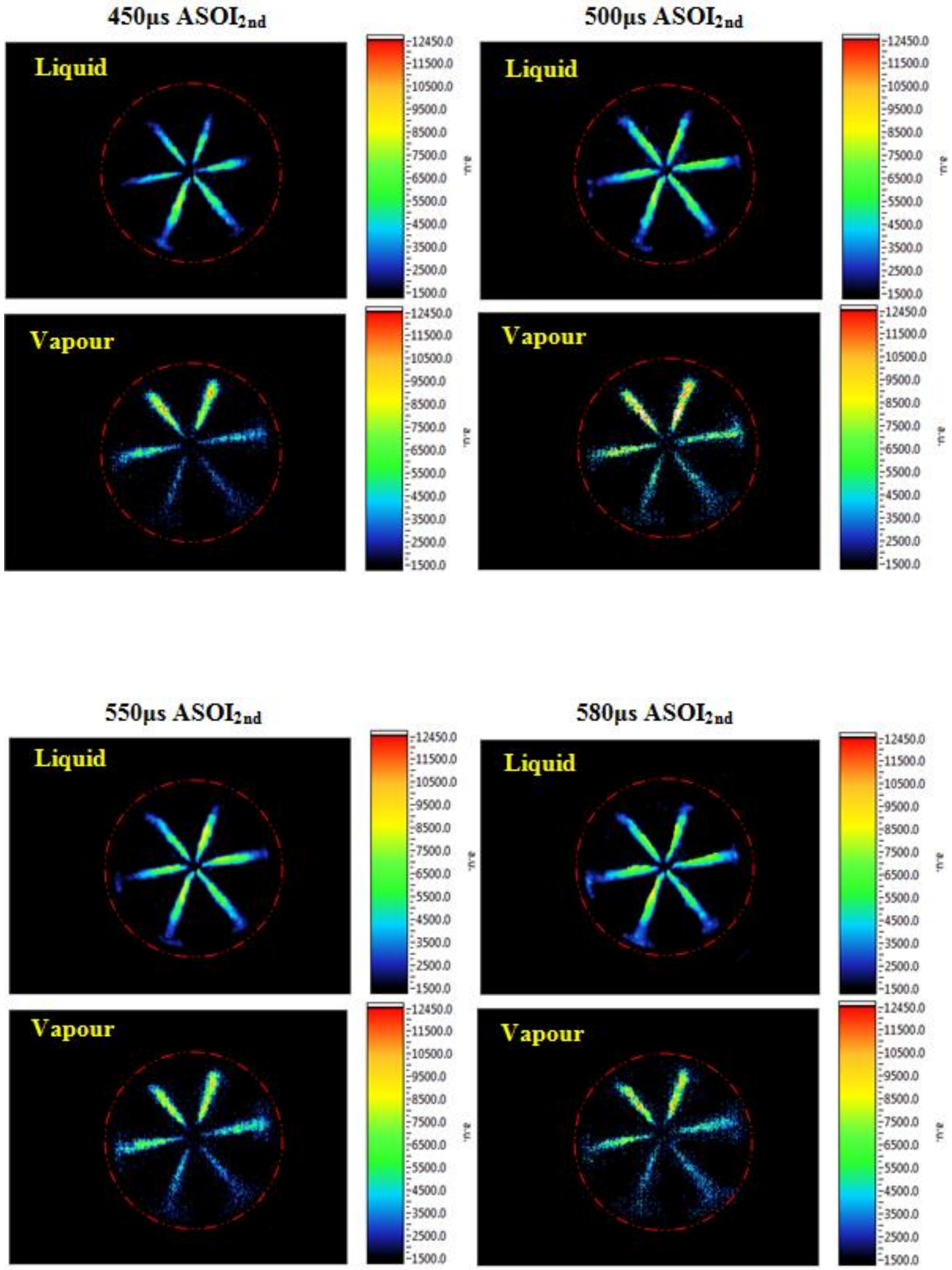

Figure 6.17 Sequence of Diesel Spray Liquid and Vapour Images for Strategy F2 (P_{inj}=1200bar, 10:90 fuel quantity distribution, 1st injection timing=-25degATDC, 2nd injection timing=-5degATDC)

6.3.9.2 Diesel Fuel Injection and Combustion Visualisation

Figure 6.18 indicates the image sequence of fuel spray and combustion for strategy F2. As seen in first three frames, the 1st injection (pilot injection) presented an asymmetrical fuel spray at -25 degrees ATDC, and an almost evaporated injection jet at -23.2 degrees ATDC. In the next four frames, which showed the development of 2nd injection, fuel spray impingement can be clearly seen at -0.5 degrees ATDC, since 90% of the total amount of fuel was injected during the 2nd injection. The first visible ignition spots can be detected during the 2nd injection (main injection) at -2.3 degrees ATDC. In the next two frames at -0.5 and 1.3 degrees ATDC, the flame propagated from the tip of the fuel injection jet, where the more highly concentrated fuel vapour was. Subsequently, the flame spread to the periphery of the combustion chamber because of impingement on the cylinder wall. Afterwards, the flame became more intense, showing bright colour at 12.1 degrees ATDC, which corresponded to where the maximum heat release rate occurred. In the frame at 21.1 degrees ATDC, the flame propagated towards to the centre of the combustion chamber, indicating the appearance of diffusion combustion. Lastly, the flame gradually diminished, with clockwise movement due to swirl motion evolution. When compared with the combustion images of gasoline type primary reference fuel, the diesel combustion is characterised with much brighter luminosity due to soot particles.

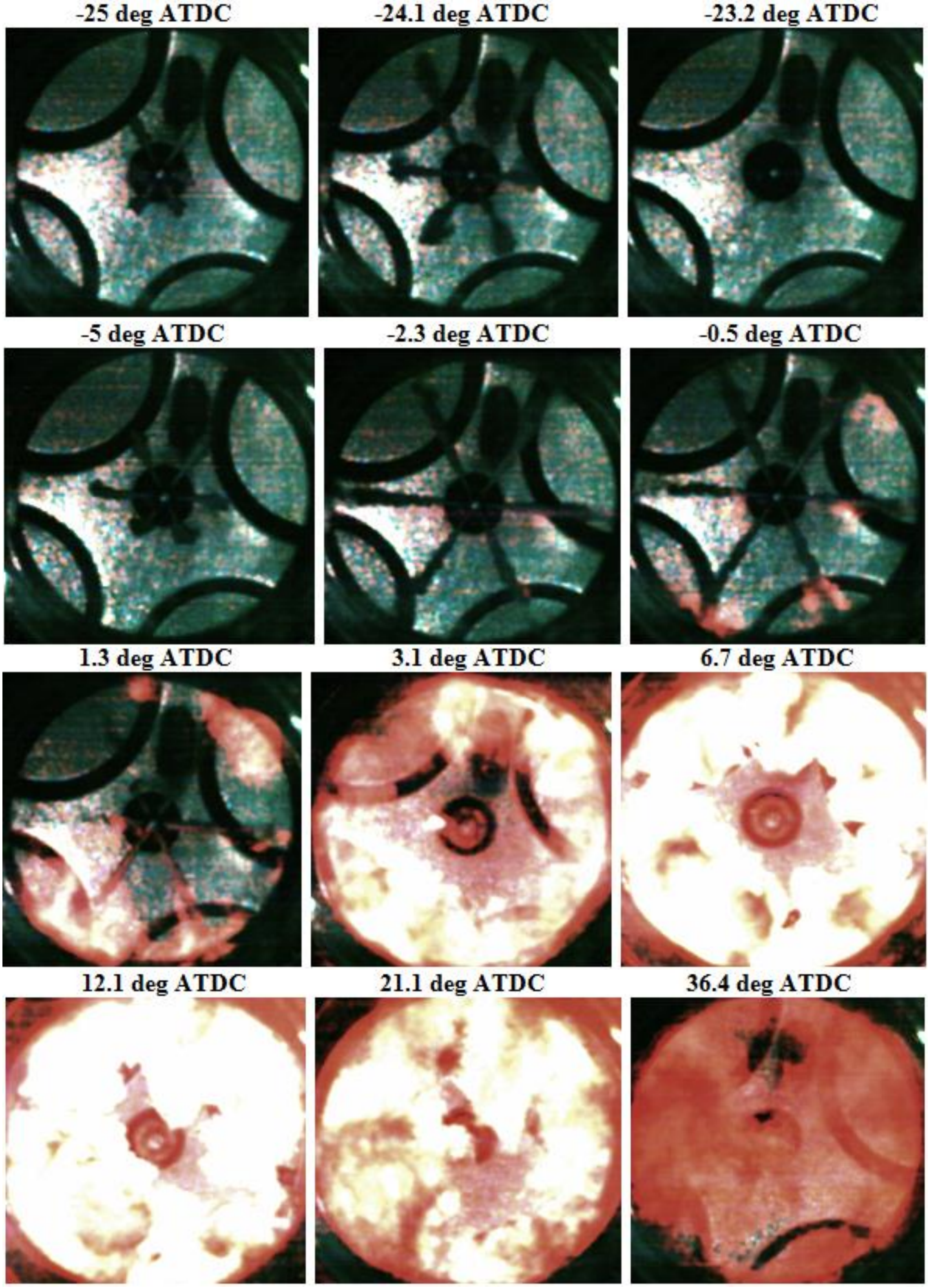

Figure 6.18 Sequence of Combustion Images for Strategy F2 (P_{inj}=1200bar, 10:90 fuel quantity distribution, 1st injection timing=-25degATDC, 2nd injection timing=-5degATDC)

6.3.10 Mie-LIF Results for Strategy BB2 by Diesel Fuel (70:30 fuel distribution strategy at 1200 bar injection pressure, 1st injection timing=-80degATDC, 2nd injection timing=-5degATDC)

In order to compare the fuel spray formations and their penetrations between different fuels under the same condition, strategy BB2 was repeated using diesel fuel. As shown in Figure 6.19, the liquid spray gradually developed until 240μs ASOI$_{1st}$ reaching the maximum concentration. Afterwards, slightly weakened liquid spray intensity can be observed through the later stage of the 1st injection (450μs ASOI$_{1st}$) due to acceleration of the fuel evaporation process. The fuel vapour spray progressively expanded as injection progressed with identical intensities and slightly larger contours can be seen compared to the fuel liquid spray. It is noted that the difference between the diesel fuel liquid and the diesel fuel vapour is smaller than PRF results. This can be understood by considering slower evaporating process of diesel fuel than PRF. During the 2nd injection, the fuel liquid spray showed gradually weakened contour and intensity as fuel injection was developing. In the meantime, compared to the fuel liquid spray, considerably larger contour of the fuel vapour spray can be obtained. This was attributed to later injection timing of -5 degrees ATDC promoted the fuel evaporation process.

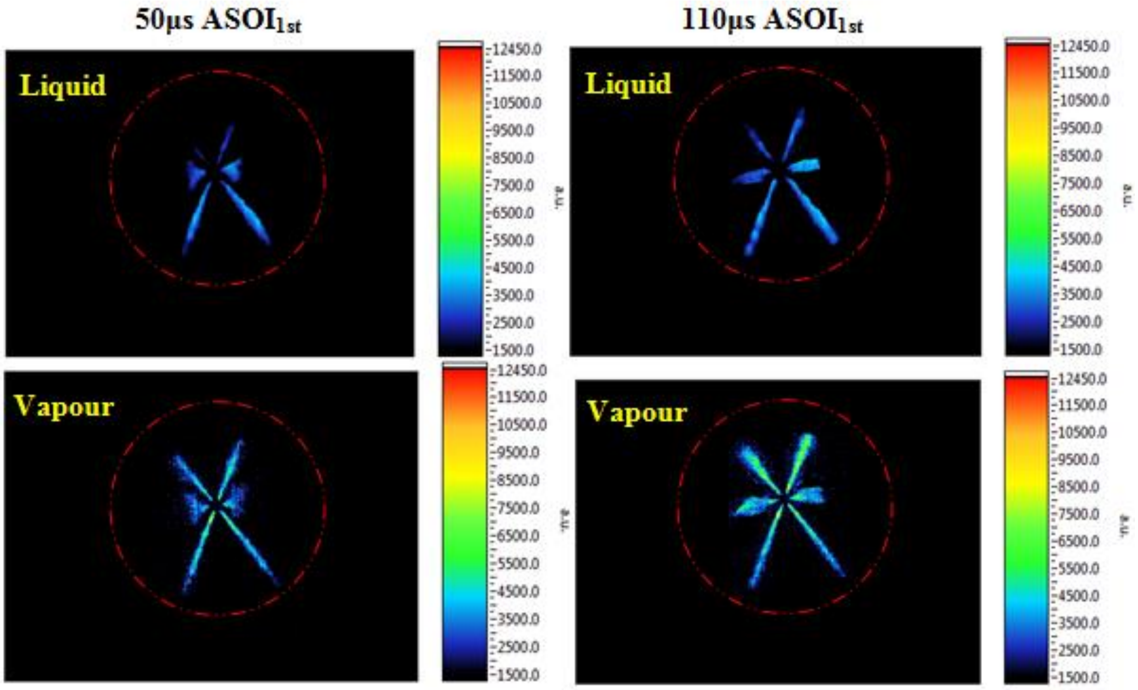

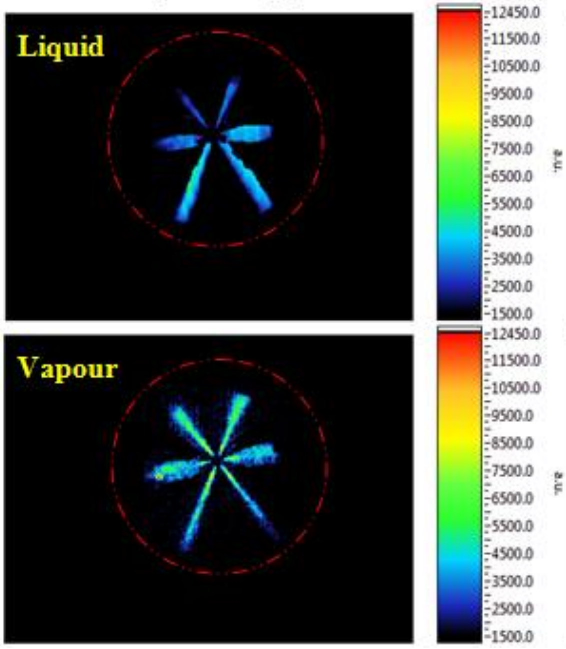
160µs ASOI$_{1st}$

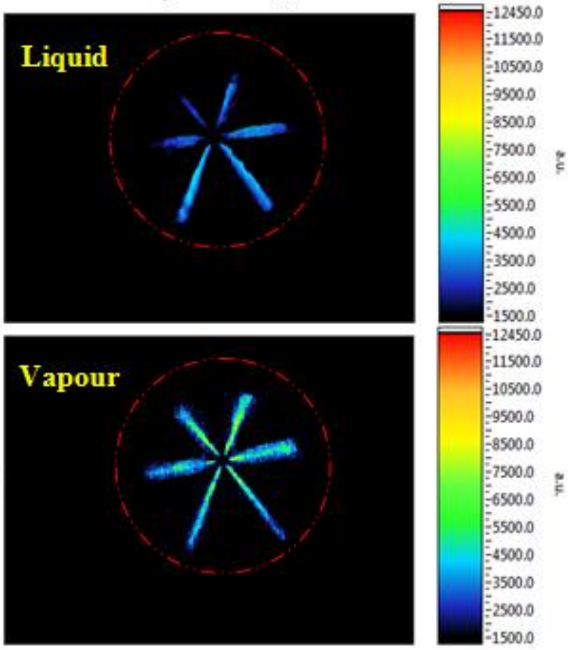
210µs ASOI$_{1st}$

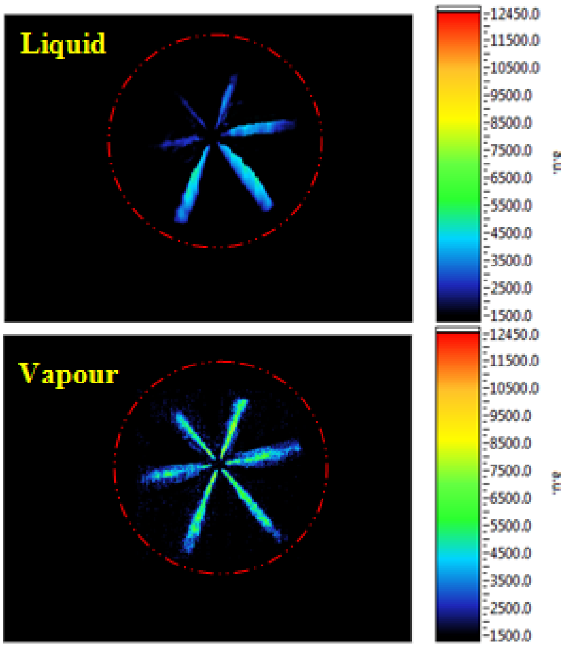
240µs ASOI$_{1st}$

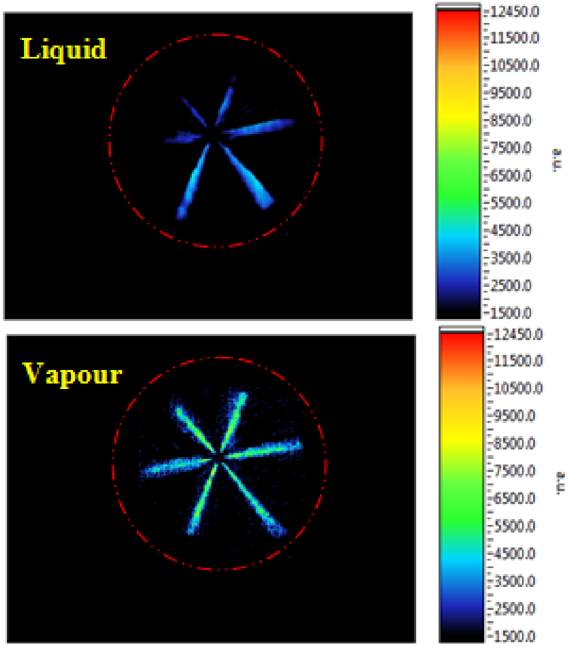
320µs ASOI$_{1st}$

360μs ASOI$_{1st}$

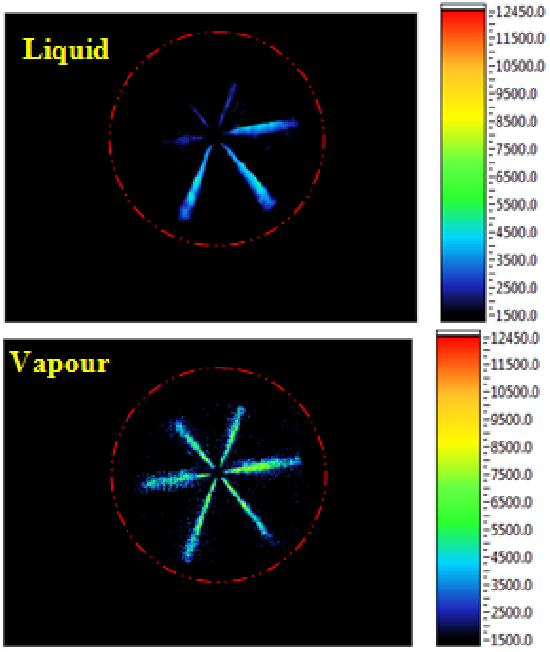

450μs ASOI$_{1st}$

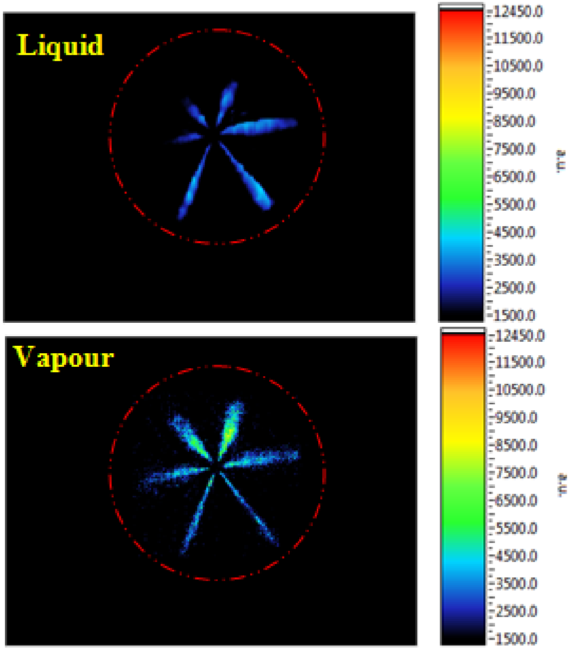

60μs ASOI$_{2nd}$

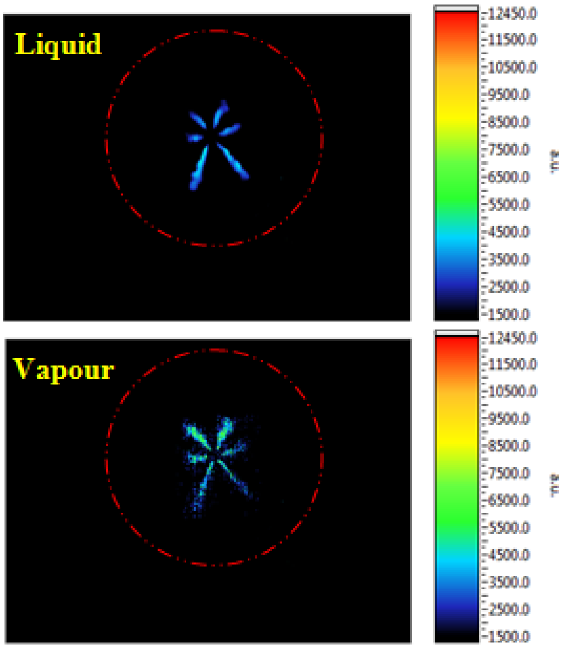

120μs ASOI$_{2nd}$

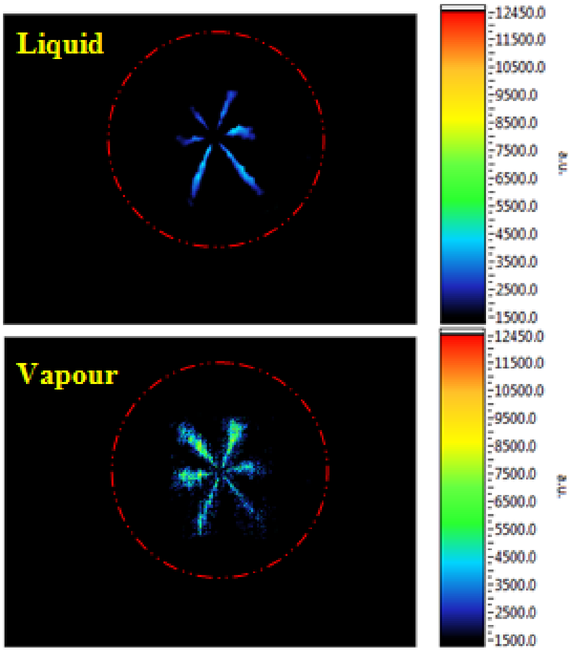

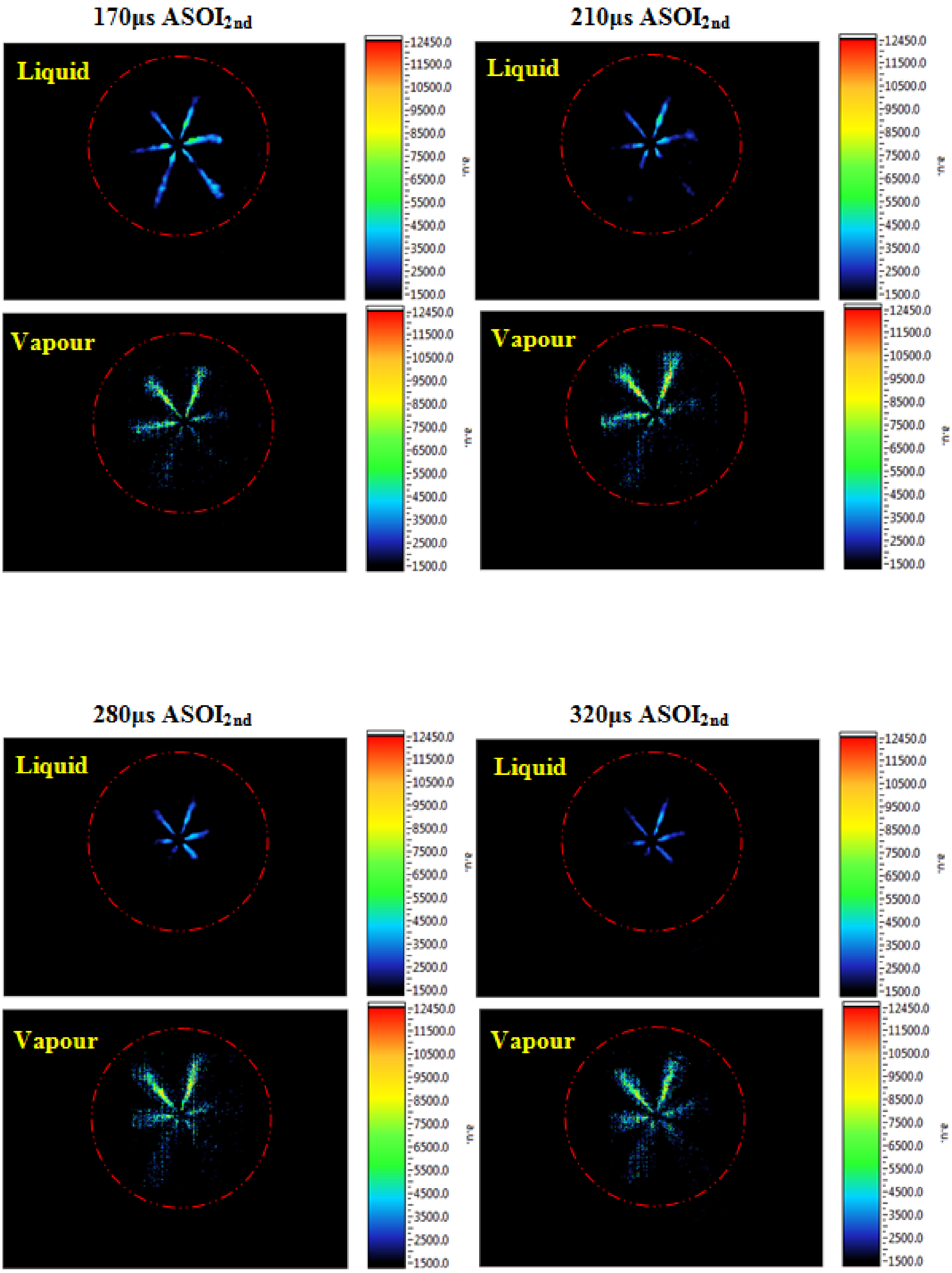

170μs ASOI$_{2nd}$

210μs ASOI$_{2nd}$

280μs ASOI$_{2nd}$

320μs ASOI$_{2nd}$

Figure 6.19 Sequence of Diesel Spray Liquid and Vapour Images for Strategy BB2 (P_{inj}=1200bar, 70:30 fuel quantity distribution, 1st injection timing=-80degATDC, 2nd injection timing=-5degATDC)

6.3.11 Mie-LIF Results for Strategy BBB2 by Diesel Fuel (70:30 fuel distribution strategy at 1200 bar injection pressure, 1st injection timing=-60degATDC, 2nd injection timing=-5degATDC)

Figure 6.20 shows the image sequence of diesel fuel liquid and vapour at injection timing of -60 degrees ATDC. Compared to the fuel vapour results for earlier injection timing (-80 degrees ATDC), slightly larger coverage can be recognized due to retarded injection timing. However, in terms of the fuel liquid spray, no obvious difference can be observed between different injection timings.

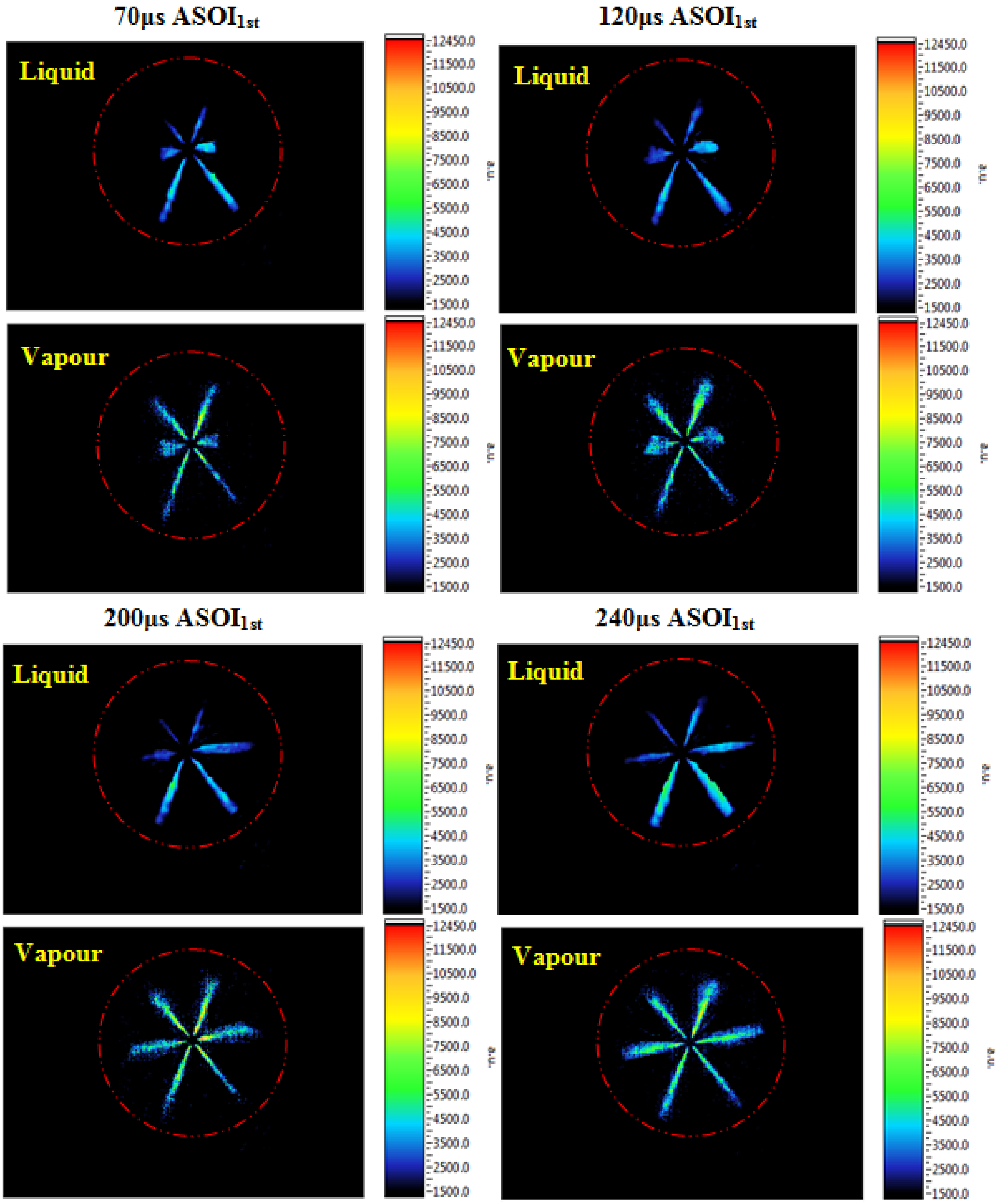

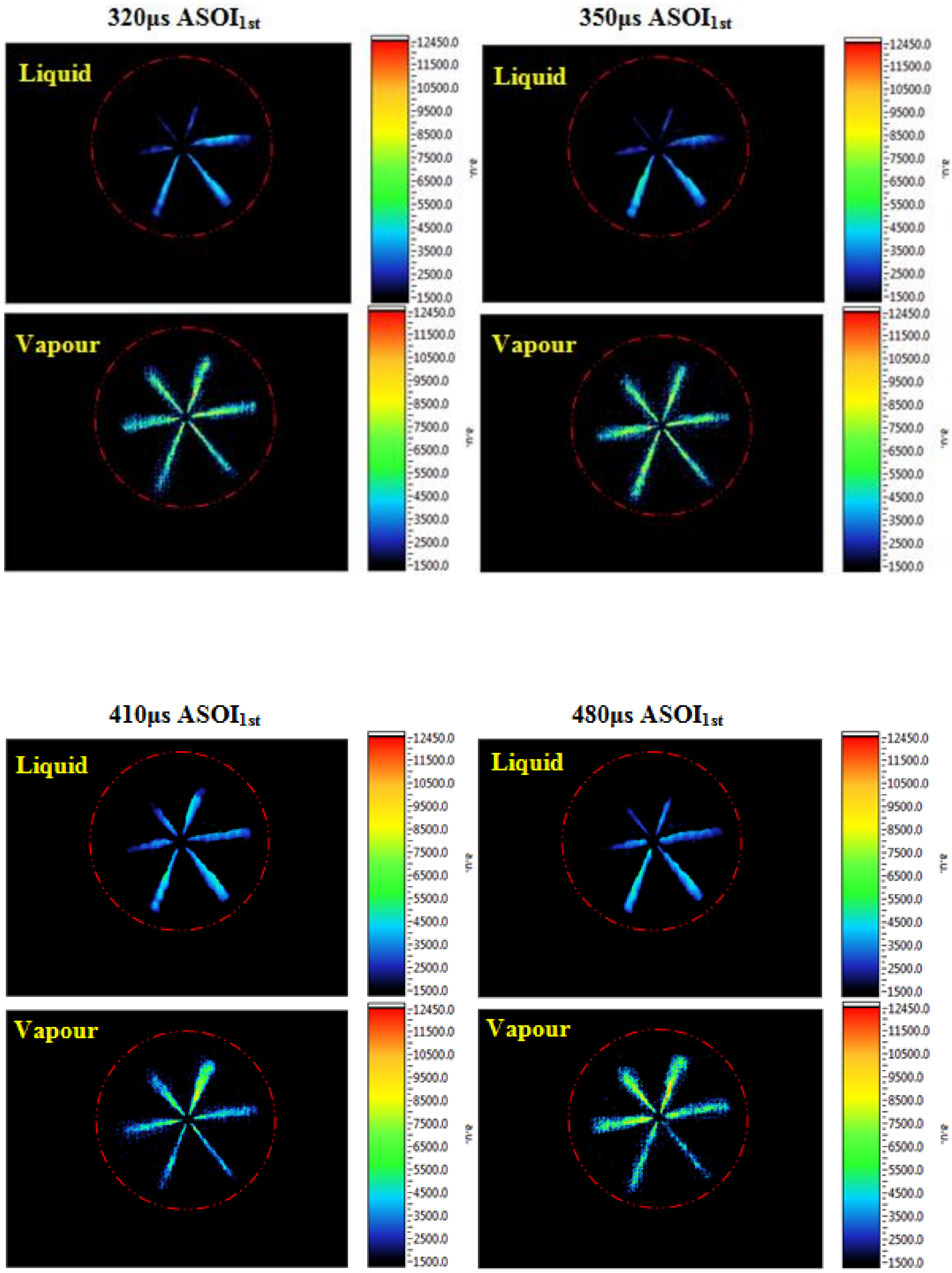
320µs $ASOI_{1st}$

350µs $ASOI_{1st}$

410µs $ASOI_{1st}$

480µs $ASOI_{1st}$

Figure 6.20 Sequence of Diesel Spray Liquid and Vapour Images for Strategy BBB2 (P_{inj}=1200bar, 70:30 fuel quantity distribution, 1st injection timing=-60degATDC, 2nd injection timing=-5degATDC)

6.3.12 Fuel Spray Penetration Analysis of Different Fuels and Injection Strategies

The speed and extent of fuel spray development in the combustion chamber have a crucial influence on air utilization and the fuel-air mixing rate. Therefore, it is important to evaluate spray penetration in order to obtain a better understanding of fuel-air mixing processes. In the following section, the effect of injection timing and pressure on spray penetration will be discussed.

Figure 6.21 demonstrates the sensitivity of the vapour spray tip position to the injection timing by showing penetration length as a function of time, for a variety of injection timings and pressures of PRF and diesel. The varied injection timing represents different ambient gas states during the fuel injection process – namely, in-cylinder pressures, density and temperatures. The results show that the initial spray tip penetration increased linearly with time, and the gradient declined as injection progressed due to the breakup of the jets. It is evident that the penetration length became slightly shorter with more retarded injection timing. This was mainly attributed to the higher environment density that was formed when piston was in close proximity to TDC, resulting in suppressed spray penetration. It is noted that the spray penetration for the diesel case was further reduced compared to the gasoline cases, since the injection took place almost at TDC. The effect of ambient temperature on spray penetration was not clarified in this study due to the limitations of the measurement method.

As shown in Figure 6.22, variation of the injection pressure seems to have had a greater significant effect on spray penetration. By applying different injection pressures of 900 and 1200 bar, the change in penetration profile can be clearly recognized. The tip of the vapour fuel spray jet spread further under the higher injection pressure of 1200 bar compared to its counterpart at 900 bar injection pressure. By using different fuel quantity distribution strategies under the same injection pressure, identical vapour penetration length results can be obtained. In terms of comparison between gasoline and diesel fuel, at the same injection timing, the reduction of vapour penetration length can be observed for the diesel case at a 1200 bar injection pressure. This was mainly because of the relatively slow injection velocity of diesel fuel, attributable to its high viscosity. It is worth noting that fairly consistent results can be obtained between gasoline spray at 900 bar injection pressure and diesel spray at 1200 bar injection pressure. It can be understood by considering the compensation between injection pressure and fuel velocity. In order to compare the difference between vapour and liquid fuel spray penetration, the liquid fuel spray length was measured at the same strategies. The results demonstrate that the vapour fuel has a longer spray length than the liquid fuel due to bigger spray surroundings for the vapour fuel. This can be proved in every Mie-LIF case study.

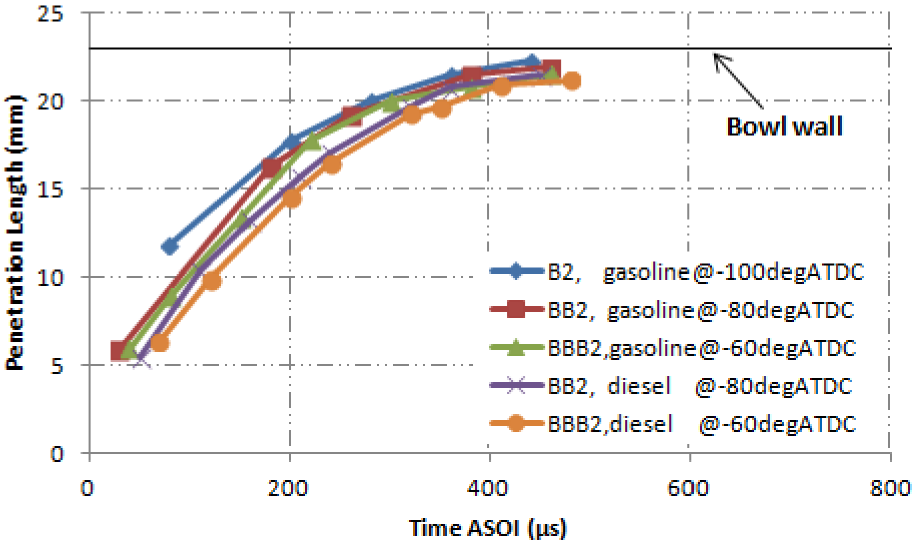

Figure 6.21 Comparison of Fuel Vapour Spray Penetration at 1200bar Injection Pressure based on Different Injection Timing

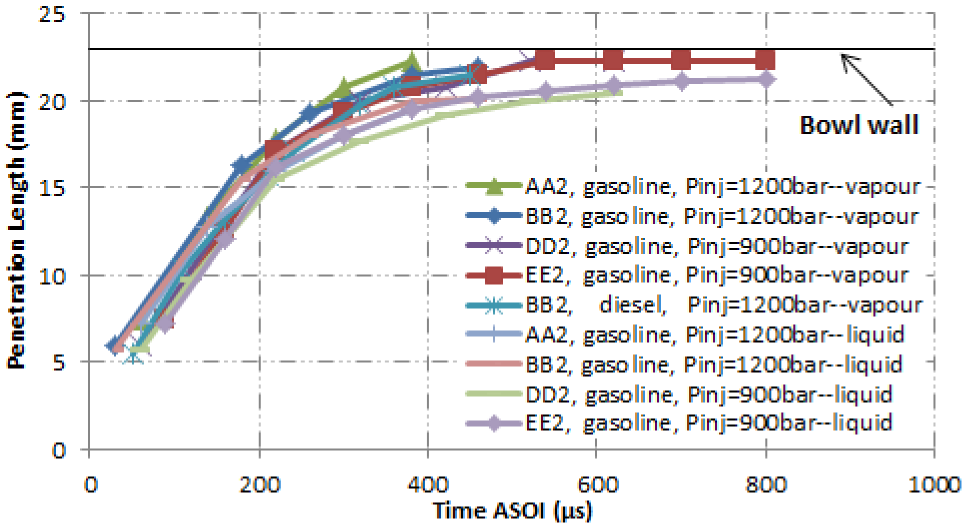

Figure 6.22 Comparison of Fuel Spray Penetration （vapour and liquid） at Injection Timing of -80degATDC based on Different Injection Pressure

6.4 Summary

In this chapter, an investigation of in-cylinder visualization for gasoline PPC and baseline diesel operation was carried out, by means of Mie-LIF imaging and high speed video. The fuel liquid and vapour formation were detected by a simultaneous Mie-LIF technique, while the fuel spray and combustion processes were analysed by high speed imaging.

The Mie-LIF images show that gasoline type fuel exhibited a wider distribution of fuel vapour than fuel liquid towards the end of the first fuel injection in the early part of the compression process. The difference between fuel liquid and vapour was unnoticeable early in the injection process, but it became more significant at later stages of the injection event. For liquid images, the intensity of fuel spray was stronger at an early stage but became weaker as the injection progressed in PRF cases, while the intensity of the spray was constant for diesel cases. In terms of the effect of injection timing, the fuel liquid spray was weaker when injection timing was closer to TDC. The injection pressure (1200 and 900 bar) seems to have no obvious influence on PRF fuel liquid results. For fuel vapour images, the spray contour was growing and intensity was weaker when the injection process approached the end. Retarded injection timing produced larger fuel vapour spray jets and higher injection pressure promoted a better evaporative process. Generally, diesel fuel generated less fuel vapour compared to gasoline fuel.

According to high speed imaging results, a less luminous combustion process was observed at 1200 bar injection pressure than 900 bar injection pressure. The premixed combustion of weak images was dominant in 1200 bar injection pressure cases, while more luminous diffusion combustion took place in 900 bar injection pressure strategies. Compared to the 50:50 fuel quantity distribution strategy, the 70:30 strategy improved the efficacy of the fuel-air mixing process and resulted in a more intense combustion flame. Diesel fuel burned via a combination of premixed combustion and diffusion combustion, while gasoline underwent partially premixed combustion. The retarded 1st injection timing led to an early onset of ignition, which might promote more diffusion combustion.

The results for fuel vapour spray penetration demonstrated that the penetration length was shortened under the higher ambient pressure and increased by using higher injection pressure. Gasoline fuel demonstrated a longer penetration length compared to diesel fuel, due to lower viscosity of the former. At the same condition, liquid fuel spray presented longer penetration length than vapour fuel spray because of the fuel evaporating process.

CHAPTER 7

Conclusions and Recommendations for Future Work

7.1 Conclusions

In this study, gasoline (PRF) partially premixed combustion (PPC) was achieved and investigated in an optical single cylinder direct injection diesel engine. The effects of injection timing, fuel quantity distribution and injection pressure on combustion and emissions characteristics were discussed by means of thermodynamic and optical analysis. The fuel injection quantity calibration and lambda determination were completed prior to the engine experiments. In the thermal dynamic study, in-cylinder pressure measurements were conducted for the combustion characteristics analysis. In addition, the exhaust gaseous pollutions and soot concentrations were measured for emission analysis. In the optical experiments, a simultaneous Mie-LIF technique was developed and used for fuel liquid and vapour spray visualization. In addition, a high speed imaging technique was utilized for fuel spray and combustion visualisation.

7.1.1 Thermodynamic Analysis of Gasoline PPC

Combustion and emissions characteristics of gasoline type fuel partially premixed combustion were investigated. At the engine speed of 1500 rpm, the effects of injection parameters were studied using primary reference fuel (PRF70) at lambda=2.3 and EGR=22%. The experimental strategies were divided into five categories according to fuel injection patterns (50:50, 70:30 and 30:70 at different injection timings) and injection pressures (1200 and 900 bar). Furthermore, diesel baseline combustion (10:90 at different injection timings) was added for the purpose of comparison.

The conclusions can be summed up as follows:

1. The results for gasoline PPC demonstrated that better output performance was obtained when combustion phasing was properly adjusted by injection timings. For most of the strategies, higher IMEP values can be achieved when the 2nd injection timing was at -5 degrees ATDC while IMEP was almost independent of the 1st injection timings. Within the operation range, the retarded 2nd injection timings resulted in shortened combustion duration (CA10-90), retarded

combustion phasing (CA50) and shorter ignition delay (SOI_{2nd}-CA10). Generally, better combustion efficiency (up to 92%) was obtained at the regime of early 1st injection timings and early 2nd injection timings, while good thermal efficiency (up to 25%) was achieved when the 1st injection timing was set at the early stage of the compression stroke, with 2nd injection timing was closed to TDC. In terms of exhaust emissions, NOx emissions were reduced by retarding the 2nd injection timings; Soot concentrations were suppressed at ultra low level for most strategies; lower uHC emissions can be obtained in areas of higher combustion efficiency.

2. Comparable IMEP values can be obtained for different fuel distribution strategies (50:50, 70:30 and 30:70). However, it was found that the 30:70 strategy was lacking control (misfiring) under the injection timing sweeping. Compared to the 50:50 strategy, the 70:30 strategy presented more rapid ignition performance. At injection pressure of 1200 bar, the 50:50 strategy produced less soot emissions than the 70:30 strategy. Fuel quantity distribution did not have apparent effects on NOx and uHC emissions at similar combustion phasing (CA50).
3. Compared to the injection pressure of 900 bar, the 1200 bar injection pressure resulted in more rapid combustion processes (CA10-90) and lower soot emissions. But higher injection pressure did not cause longer ignition delay in most cases. NOx emissions deteriorated for some early 2nd injection strategies at 900 bar injection pressure. uHC emissions remained high independent of injection pressure.
4. Gasoline PPC and diesel baseline combustion showed distinguished combustion and emissions characteristics. Compared to gasoline PPC, diesel baseline combustion exhibited rapid auto-ignition after the end of the pilot injection and with a large portion of diffusion combustion at the late stage of the heat release process. A more rapid combustion process and longer ignition delay were obtained for gasoline PPC than diesel baseline combustion. Simultaneous reductions in NOx and soot emissions were achieved for gasoline PPC with the penalty of high uHC emissions. The high uHC emissions led to poor combustion efficiency and thermal efficiency for gasoline PPC.
5. According to the thermodynamic results, the optimum engine operation regime can be found at the combination of early 1st injection timings and late 2nd

injection timings. In this area, better engine efficiencies can be obtained with fairly low NOx and soot emissions.

7.1.2 In-Cylinder Visualization Studies of Gasoline PPC

The Mie-LIF technique was developed and implemented for simultaneous fuel liquid and vapour phases measurement. The Mie-LIF images showed that the difference between fuel liquid and vapour was not obvious at the early stage of the injection, but it became more significant at the late stage of the injection.

For fuel liquid images, more intensive spray can be observed at the early stage, but became weaker as the injection progressed in PRF cases. On the other hand, diesel spray did not exhibit a different intensity. When injection timing was closer to TDC, the fuel liquid spray became weaker for both fuels. At different injection pressure (900 bar and 1200 bar), no obvious difference can be recognized in PRF fuel liquid results. For fuel vapour images, the spray contour grew and intensity was weaker when the injection process approached the end. Retarded injection timing produced larger fuel vapour spray jets and higher injection pressure promoted a better evaporative process. Generally, gasoline type fuel (PRF70) presented a wider distribution of fuel vapour than diesel fuel.

High speed imaging was utilized for the fuel spray and the combustion processes visualization. The high speed imaging results showed that the more intense combustion flame was present for the 70:30 fuel distribution strategy compared to the 50:50 strategy at both injection pressures. Compared to 1200 bar injection pressure, more luminous combustion processes were detected for 900 bar injection pressure due to greater diffusion combustion. Diesel fuel burned via a combination of premixed combustion and diffusion combustion, while gasoline underwent partially premixed combustion. It was found that onset of ignition was advanced as the 1st injection timing was retarded.

The results for fuel vapour spray penetration demonstrated that the penetration length was shortened under the higher ambient pressure and increased when using higher injection pressure. At the same injection timing with 1200 bar injection pressure, gasoline fuel exhibited a longer penetration length compared to diesel fuel. In addition, liquid fuel spray presented longer penetration length than vapour fuel spray because of the fuel evaporating process.

7.2 Recommendations for Future Work

Although gasoline type fuel PPC has exhibited the potential for simultaneous reduction of NOx and soot emissions, optimization of control parameters will be required to overcome the difficulties associated with high uHC emissioins, poor combustion efficiencies and thermal efficiencies.

In this study, injection timings were swept under a selected lambda, EGR rate and intake conditions (temperature and pressure). As mentioned previously, the gasoline type fuel PPC operation is much more sensitive to lambda and EGR than diesel combustion. Thus, further studies will be needed to investigate the effects of lambda and EGR on combustion and emissions characteristics. By optimizing the combination of lambda and EGR rate with adjustment of injection timings, uHC emissions and engine efficiencies might be improved. In addition, NOx and soot emissions benefited from cold EGR gas throughout the experiments. Therefore, investigation of the effects of EGR temperature on combustion and emissions characteristics are recommended to get a better understanding of the intake temperature sensitivity of gasoline PPC operation.

The Mie-LIF measurement has enabled qualitative visualisation of the fuel liquid and vapour distribution in the cylinder. During the experiments, the Mie scattering images suffered from reflection by laser light scattering. Although the interferences were minimized by a usage of black painting, the image quality was still influenced by scattering noise. Therefore, other optical techniques such as LIEF and planar light source are recommended to eliminate background noise. In addition, quantitative measurement of fuel spray would be suggested in future work.

References

[1] Heywood, J.B., 1988. *Internal Combustion Engine Fundamentals* McGraw-Hill Science Engineering

[2] S. Onishi, S. H. Jo, K. Shoda, P. Do Jo and S. Kato, *Active Thermo-Atmosphere Combustion (ATAC)-a New Combustion Process for Internal Combustion Engines,* SAE Paper 790501.

[3] P. M. Najt and D. E. Foster, *Compression-Ignited Homogeneous Charge Combustion,* SAE Paper 830264.

[4] D. Goldman and A. S. Popel, "A computational study of the effect of capillary network anastomoses and tortuosity on oxygen transport," *J. Theor. Biol.,* vol. 206, pp. 181-194, 2000.

[5] N. Kaneko, H. Ando, H. Ogawa and N. Miyamoto, *Expansion of the Operating Range with in-Cylinder Water Injection in a Premixed Charge Compression Ignition Engine,* SAE Paper 2002-01-1743.

[6] M. Odaka, H. Suzuki, N. Koike and H. Ishii, *Search for Optimizing Control Method of Homogeneous Charge Diesel Combustion,* SAE Paper 1999-01-0184.

[7] H. Suzuki, N. Koike and M. Odaka, *Combustion Control Method of Homogeneous Charge Diesel Engines,* SAE Paper 980509.

[8] H. Ishii, N. Koike, H. Suzuki and M. Odaka, *Exhaust Purification of Diesel Engines by Homogeneous Charge with Compression Ignition Part 2: Analysis of Combustion Phenomena and NOx Formation by Numerical Simulation with Experiment,* SAE Paper 970315.

[9] H. Suzuki, N. Koike, H. Ishii and M. Odaka, *Exhaust Purification of Diesel Engines by Homogeneous Charge with Compression Ignition Part 1: Experimental Investigation of Combustion and Exhaust Emission Behavior Under Pre-Mixed Homogeneous Charge Compression Ignition Method,* SAE Paper 970313.

[10] Y. Iwabuchi, K. Kawai, T. Shoji and Y. Takeda, *Trial of New Concept Diesel Combustion System-Premixed Compression-Ignited Combustion,* SAE Paper 1999-01-0185.

[11] H. Akagawa, T. Miyamoto, A. Harada, S. Sasaki, N. Shimazaki, T. Hashizume and K. Tsujimura, *Approaches to Solve Problems of the Premixed Lean Diesel Combustion,* SAE Paper 1999-01-0183.

[12] Y. Takeda, N. Keiichi and N. Keiichi, *Emission Characteristics of Premixed Lean Diesel Combustion with Extremely Early Staged Fuel Injection,* SAE Paper 961163.

[13] N. Shimazaki, H. Akagawa and K. Tsujimura, *An Experimental Study of Premixed Lean Diesel Combustion,* SAE Paper 1999-01-0181.

[14] Y. Nishijima, Y. Asaumi and Y. Aoyagi, *Premixed Lean Diesel Combustion (PREDIC) using Impingement Spray System,* SAE Paper 2001-01-1982.

[15] H. Yokota, Y. Kudo, H. Nakajima, T. Kakegawa and T. Suzuki, *A New Concept for Low Emission Diesel Combustion,* SAE Paper 970891.

[16] B. Walter and B. Gatellier, *Development of the High Power NADI™ Concept using Dual Mode Diesel Combustion to Achieve Zero NOx and Particulate Emissions,* SAE Paper 2002-01-1744.

[17] Y. Mase, J. Kawashima, T. Sato and M. Eguchi, *Nissan's New Multivalve DI Diesel Engine Series,* SAE Paper 981039.

[18] S. Kimura, O. Aoki, Y. Kitahara and E. Aiyoshizawa, *Ultra-Clean Combustion Technology Combining a Low-Temperature and Premixed Combustion Concept for Meeting Future Emission Standards,* SAE Paper 2001-01-0200.

[19] H. Ogawa, S. Kimura, M. Koike and Y. Enomoto, *A Study of Heat Rejection and Combustion Characteristics of a Low-Temperature and Pre-Mixed Combustion Concept Based on Measurement of Instantaneous Heat Flux in a Direct-Injection Diesel Engine,* SAE Paper 2000-01-2792.

[20] U. Asad, M. Zheng, X. Han, G. Reader and M. Wang, *Fuel Injection Strategies to Improve Emissions and Efficiency of High Compression Ratio Diesel Engines.* SAE Tech Paper; 2008-01-2472, .

[21] U. Asad and M. Zheng, *Efficacy of EGR and Boost in Single-Injection Enabled Low Temperature Combustion,* SAE Paper 2009-01-1126.

[22] W. de Ojeda, P. Zoldak, R. Espinosa and R. Kumar, *Development of a Fuel Injection Strategy for Diesel LTC,* SAE Paper 2008-01-0057.

[23] J. Benajes, J. M. García-Oliver, R. Novella and C. Kolodziej, "Increased particle emissions from early fuel injection timing Diesel low temperature combustion," *Fuel,* vol. 94, pp. 184-190, 2012.

[24] J. Benajes, S. Molina, R. Novella and E. Belarte, "Evaluation of massive exhaust gas recirculation and Miller cycle strategies for mixing-controlled low temperature combustion in a heavy duty diesel engine," *Energy, volume 71,* 2014.

[25] K. Inagaki, T. Fuyuto, K. Nishikawa, K. Nakakita and I. Sakata, *Dual-Fuel PCI Combustion Controlled by in-Cylinder Stratification of Ignitability,* SAE Paper 2006-01-0028.

[26] J. E. Dec and M. Sjöberg, *Isolating the Effects of Fuel Chemistry on Combustion Phasing in an HCCI Engine and the Potential of Fuel Stratification for Ignition Control,* SAE Paper 2004-01-0557.

[27] W. d. Ojeda, "SuperTruck-Development and Demonstration of a Fuel-Efficient Class 8 Tractor & Trailer Engine Systems," *Presentation at US Department of Energy Merit Review,* 2013.

[28] C. De Boer, J. Chang and S. Shetty, *Transonic Combustion-A Novel Injection-Ignition System for Improved Gasoline Engine Efficiency,* SAE Paper 2010-01-2110.

[29] P. Zoldak, C. de Boer and S. Shetty, *Transonic Combustion-Supercritical Gasoline Combustion Operating Range Extension for Low Emissions and High Thermal Efficiency,* SAE Paper 2012-01-0702.

[30] Bowman, C. T.:"Kinetics of Pullutant Formation and Destruction in Combustion," *Prog. Energy Combust. Sci.,* vol. 1, pp. 33-45, 1975

[31] Lavoie, G. A., Heywood, J. B., and Keck, J. C.:"Experimental and Theoretical Investigation of Nitric Oxide Formation in Internal Combustion Engines," *Combus. Sci. Technol.,* vol. 1, pp. 313-326, 1970

[32] S. Shundoh, T. Kakegawa, K. Tsujimura and S. Kobayashi, *The Effect of Injection Parameters and Swirl on Diesel Combustion with High Pressure Fuel Injection,* SAE Paper 910489.

[33] S. Shundoh, M. Komori, K. Tsujimura and S. Kobayashi, *NOx Reduction from Diesel Combustion using Pilot Injection with High Pressure Fuel Injection,* SAE Paper 920461.

[34] Y. Kitamura, Ali Mohammadi, " Fundamental Investigation of NOx Formation in Diesel Combustion Under Supercharged and EGR Conditions," SAE Paper 2005-01-0364.

[35] Y. Oh, D. Lee, K. Jeong, S. Kim, D. Kim, C. S. Lee and S. Park, *Two-Stage Combustion Strategy for Reducing NOx Emissions in a Compression Ignition Engine,* SAE Paper 2011-32-0659.

[36] M. Jangi, T. Lucchini, G. D'Errico and X. Bai, "Effects of EGR on the structure and emissions of diesel combustion," *Proceedings of the Combustion Institute,* vol. 34, pp. 3091-3098, 2013.

[37] A. Maiboom, X. Tauzia and J. Hétet, "Experimental study of various effects of exhaust gas recirculation (EGR) on combustion and emissions of an automotive direct injection diesel engine," *Energy,* vol. 33, pp. 22-34, 2008.

[38] Y. Wakisaka, Y. Hotta, M. Inayoshi, K. Nakakita, I. Sakata and T. Takano, *Emissions Reduction Potential of Extremely High Boost and High EGR Rate for an HSDI Diesel Engine and the Reduction Mechanisms of Exhaust Emissions,* SAE Paper 2008-01-1189.

[39] D. Six, T. Van Herzele, L. Vervaeke, M. Bastiaen, J. Galle, R. Sierens and S. Verhelst, *Development and Testing of an EGR System for Medium Speed Diesel Engines,* SAE Paper 2012-01-0680.

[40] J. Lee, S. Choi, J. Lee, S. Shin, S. Lee, H. H. Song, K. Min and H. Choi, *Emission Reduction using a Close Post Injection Strategy with a Modified Nozzle and Piston Bowl Geometry for a Heavy EGR Rate,* SAE Paper 2012-01-0681.

[41] T. Li, H. Ogawa, R. Moriwaki and T. Suzuki, *Effects of EGR and Pilot Injection on Characteristics of Combustion and Emissions of Diesel Engines with Low Ignitability Fuel,* SAE Paper 2012-01-0853.

[42] D. B. Kittelson, "Engines and nanoparticles: a review," *J. Aerosol Sci.,* vol. 29, pp. 575-588, 1998.

[43] H. Suzuki, N. Koike, H. Ishii and M. Odaka, *Exhaust Purification of Diesel Engines by Homogeneous Charge with Compression Ignition Part 1: Experimental Investigation of Combustion and Exhaust Emission Behavior Under Pre-Mixed Homogeneous Charge Compression Ignition Method,* SAE Paper 970313.

[44] J. Senda, M. Ikeda, M. Yamamoto, B. Kawaguchi and H. Fujimoto, *Low Emission Diesel Combustion System by use of Reformulated Fuel with Liquefied CO2 and n-Tridecane,* SAE Paper 1999-01-1136.

[45] J. Senda and H. Fujimoto, *Multicomponent Fuel Consideration for Spray Evaporation Field and Spray-Wall Interaction,* SAE Paper 2001-01-1071.

[46] M. Matti Maricq, "Chemical characterization of particulate emissions from diesel engines: A review," *J. Aerosol Sci.,* vol. 38, pp. 1079-1118, 2007.

[47] N. Miyamoto, H. Ogawa, N. M. Nurun, K. Obata and T. Arima, *Smokeless, Low NOx, High Thermal Efficiency, and Low Noise Diesel Combustion with Oxygenated Agents as Main Fuel,* SAE Paper 980506.

[48] H. Chen, S. Shi-Jin and W. Jian-Xin, "Study on combustion characteristics and PM emission of diesel engines using ester–ethanol–diesel blended fuels," *Proceedings of the Combustion Institute,* vol. 31, pp. 2981-2989, 2007.

[49] Y. Xu and F. L. Chia-fon, *Study of Soot Formation of Oxygenated Diesel Fuels using Forward Illumination Light Extinction (FILE) Technique,* SAE Paper 2006-01-1415.

[50] P. Adomeit, M. Becker, H. Rohs, S. Pischinger, A. Greis and G. Grünefeld, *Potential Soot and CO Reduction for HSDI Diesel Combustion Systems,* SAE Paper 2006-01-1417.

[51] J. E. Dec, *Soot Distribution in a DI Diesel Engine using 2-D Imaging of Laser-Induced Incandescence, Elastic Scattering, and Flame Luminosity,* SAE Paper 920115.

[52] C. Espey and J. E. Dec, *Diesel Engine Combustion Studies in a Newly Designed Optical-Access Engine using High-Speed Visualization and 2-D Laser Imaging,* SAE Paper 930971.

[53] J. Senda, D. Choi, M. Iwamuro, H. Fujimoto and G. Asai, *Experimental Analysis on Soot Formation Process in DI Diesel Combustion Chamber by use of Optical Diagnostics,* SAE Paper 2002-01-0893.

[54] K. Inagaki, S. Takasu, K. Nakakita and S. Watanabe, *Quantitative Analysis of Soot Formation and Oxidation Process using Laser-Induced Incandescence,* SAE Paper 2003-01-1795.

[55] F. Tao, Y. Liu, B. H. Rempelewert, D. E. Foster, R. D. Reitz, D. Choi and P. C. Miles, *Modeling the Effects of EGR and Injection Pressure on Soot Formation in a High-Speed Direct-Injection (HSDI) Diesel Engine using a Multi-Step Phenomenological Soot Model,* SAE Paper 2005-01-0121.

[56] C. A. Idicheria and L. M. Pickett, *Soot Formation in Diesel Combustion Under High-EGR Conditions,* SAE Paper 2005-01-3834.

[57] J. O'Connor and M. Musculus, *Post Injections for Soot Reduction in Diesel Engines: A Review of Current Understanding,* SAE Paper 2013-01-0917.

[58] Han M, Assanis DN, Bohac SV. :"Sources of Hydrocarbon Emissions from Low-temperature Premixed Compression Ignition Combustion from a Common Rail Direct Injection Diesel Engine," *Combus. Sci. Technol.,* 181:496-517, 2009

[59] Opat R, Ra Y, Manuel A, Gonzalez D, Krieger R, Reitz RD, Foster DE, Durrett RP, Siewert RM,"*Investigation of Mixing and Temperature Effects on HC/CO Emissions for Highly Dilute Low Temperature Combustion in a Light Duty Diesel Engine*," SAE Paper 2007-01-0193

[60] Julian T. Kashdan, Sylvain Mendez, Gilles Bruneaux, "*On the origin of Unburned Hydrocarbon Emissions in a Wall Guided, Low NOx Diesel Combustion System*," SAE Paper 2007-01-1836

[61] Sylvain Mendez, Julian T. Kashan, "*Formation of Unburned Hydrocarbons in Low Temperature Diesel Combustion*," SAE Paper 2009-01-2729

[62] Ekoto, I.W., Colban, W.F., Miles, P.C., Park S. et al., "*Sources of UHC Emissions from a Light-Duty Diesel Engine Operating in a Partially Premixed Combustion Regime*," SAE Int. J. Engines 2(1): 1265-1289, 2009.

[63] Ekoto, I.W., Colban, W.F., Miles, P.C., Park S.W. et al., "*UHC and CO Emissions Sources from a Light-Duty Diesel Engine Undergoing Dilution-Controlled Low-Temperature Combustion*," SAE Int. J. Engines 2(2):411-430, 2009.

[64] Ekoto, I.W., Colban, W.F., Miles, P.C., Aronsson, U., Andersson, O., Park S.W., Foster, D.E., Reitz, R.D., Aronsson, U., Andersson, O., "UHC and CO Emissions Sources from a Light-Duty Diesel Engine Undergoing Late- Injection Low Temperature Combustion," *Proceedings of ASME ICEF2009, ICEF2009-14030, 2009.*

[65] Kim, D., Ekoto, I, Colban, W.F., and Miles, P.C., "*In-cylinder CO and UHC Imaging in a Light-Duty Diesel Engine During PPCI Low-Temperature Combustion*," SAE Int. J. Fuels Lubr. 1(1):933-956, 2008.

[66] Haskell, W. W., and Legate, C. E.:" *Exhaust Hydrocarbon Emissions from Gasoline Engines-Surface Phenomena,*" SAE Paper 720255, 1972.

[67] W. L. Hardy and R. Reitz, *A Study of the Effects of High EGR, High Equivalence Ratio, and Mixing Time on Emissions Levels in a Heavy-Duty Diesel Engine for PCCI Combustion,* SAE Paper 2006-01-0026.

[68] T. Kanda, T. Hakozaki, T. Uchimoto, J. Hatano, N. Kitayama and H. Sono, *PCCI Operation with Early Injection of Conventional Diesel Fuel,* SAE Paper 2005-01-0378.

[69] S. Lee and R. D. Reitz, *Spray Targeting to Minimize Soot and CO Formation in Premixed Charge Compression Ignition (PCCI) Combustion with a HSDI Diesel Engine,* SAE Paper 2006-01-0918.

[70] M. Lewander, K. Ekholm, B. Johansson, P. Tunestal, N. Milovanovic, N. Keeler, T. Harcombe and P. Bergstrand, *Investigation of the Combustion Characteristics with Focus on Partially Premixed Combustion in a Heavy Duty Engine,* SAE Paper 2008-01-1658.

[71] P. Risberg, G. Kalghatgi, H. Ångstrom and F. Wåhlin, *Auto-Ignition Quality of Diesel-Like Fuels in HCCI Engines,* SAE Paper 2005-01-2127.

[72] W. de Ojeda, P. Zoldak, R. Espinosa and R. Kumar, *Development of a Fuel Injection Strategy for Diesel LTC,* SAE Paper 2008-01-0057.

[73] B. Keeler and P. J. Shayler, *Constraints on Fuel Injection and EGR Strategies for Diesel PCCI-Type Combustion,* SAE Paper 2008-01-1327.

[74] S. Kook, C. Bae, P. C. Miles, D. Choi and L. M. Pickett, *The Influence of Charge Dilution and Injection Timing on Low-Temperature Diesel Combustion and Emissions,* SAE Paper 2005-01-3837.

[75] N. Horibe, K. Takahashi, S. Kee, T. Ishiyama and M. Shioji, *The Effects of Injection Conditions and Combustion Chamber Geometry on Performance and Emissions of DI-PCCI Operation in a Diesel Engine,* SAE Paper 2007-01-1874.

[76] R. M. Nevin, Y. Sun and R. D. Reitz, *PCCI Investigation using Variable Intake Valve Closing in a Heavy Duty Diesel Engine,* SAE Paper 2007-01-0903.

[77] W. F. Colban, P. C. Miles and S. Oh, *Effect of Intake Pressure on Performance and Emissions in an Automotive Diesel Engine Operating in Low Temperature Combustion Regimes,* SAE Paper 2007-01-4063.

[78] A. E. Klingbeil, H. Juneja, Y. Ra and R. D. Reitz, *Premixed Diesel Combustion Analysis in a Heavy-Duty Diesel Engine,* SAE Paper 2003-01-0341.

[79] S. Kimura, O. Aoki, H. Ogawa, S. Muranaka and Y. Enomoto, *New Combustion Concept for Ultra-Clean and High-Efficiency Small DI Diesel Engines,* SAE Paper 1999-01-3681.

[80] F. Zhang, H. Xu, S. Z. Rezaei, G. Kalghatgi and S. Shuai, *Combustion and Emission Characteristics of a PPCI Engine Fuelled with Dieseline,* SAE Paper 2012-01-1138.

[81] K. Kitano, R. Nishiumi, Y. Tsukasaki, T. Tanaka and M. Morinaga, *Effects of Fuel Properties on Premixed Charge Compression Ignition Combustion in a Direct Injection Diesel Engine*, SAE Paper 2003-01-1815.

[82] Y. Murata, J. Kusaka, M. Odaka, Y. Daisho, D. Kawano, H. Suzuki, H. Ishii and Y. Goto, *Achievement of Medium Engine Speed and Load Premixed Diesel Combustion with Variable Valve Timing,* SAE Paper 2006-01-0203.

[83] T. Kanda, T. Hakozaki, T. Uchimoto, J. Hatano, N. Kitayama and H. Sono, *PCCI Operation with Fuel Injection Timing Set Close to TDC,* SAE Paper 2006-01-0920.

[84] P. K. Karra, M. K. Veltman and S. Kong, "Characteristics of engine emissions using biodiesel blends in low-temperature combustion regimes," *Energy Fuels,* vol. 22, pp. 3763-3770, 2008.

[85] G. T. Kalghatgi, P. Risberg and H. Ångström, *Advantages of Fuels with High Resistance to Auto-Ignition in Late-Injection, Low-Temperature, Compression Ignition Combustion,* SAE Paper 2006-01-3385.

[86] G. T. Kalghatgi, P. Risberg and H. Angstrom, *Partially Pre-Mixed Auto-Ignition of Gasoline to Attain Low Smoke and Low NOx at High Load in a Compression Ignition Engine and Comparison with a Diesel Fuel,* SAE Paper 2007-01-0006.

[87] G. Kalghatgi, L. Hildingsson and B. Johansson, "Low NOx and low smoke operation of a diesel engine using gasolinelike fuels," *Journal of Engineering for Gas Turbines and Power,* vol. 132, pp. 092803, 2010.

[88] L. Hildingsson, G. Kalghatgi, N. Tait, B. Johansson and A. Harrison, *Fuel Octane Effects in the Partially Premixed Combustion Regime in Compression Ignition Engines,* SAE Paper 2009-01-2648.

[89] B. R. Petersen, I. W. Ekoto and P. C. Miles, *An Investigation into the Effects of Fuel Properties and Engine Load on UHC and CO Emissions from a Light-Duty Optical Diesel Engine Operating in a Partially Premixed Combustion Regime,* SAE Paper 2010-01-1470.

[90] V. Manente, B. Johansson, P. Tunestal and W. Cannella, *Effects of Different Type of Gasoline Fuels on Heavy Duty Partially Premixed Combustion,* SAE Paper 2009-01-2668.

[91] V. Manente, P. Tunestal, B. Johansson and W. J. Cannella, *Effects of Ethanol and Different Type of Gasoline Fuels on Partially Premixed Combustion from Low to High Load,* SAE Paper 2010-01-0871.

[92] H. Liu, Z. Wang, J. Wang and X. He, "Effects of gasoline research octane number on premixed low-temperature combustion of wide distillation fuel by gasoline/diesel blend," *Fuel,* vol. 134, pp. 381-388, 2014.

[93] C. Leermakers, P. Bakker, B. Nijssen, L. Somers and B. Johansson, "Low octane fuel composition effects on the load range capability of partially premixed combustion," *Fuel,*vol.135,pp.210-222, 2014.

[94] G. Kalghatgi, L. Hildingsson, A. Harrison and B. Johansson, "Autoignition quality of gasoline fuels in partially premixed combustion in diesel engines," *Proceedings of the Combustion Institute,* vol. 33, pp. 3015-3021, 2011.

[95] S. Zeraati Rezaei, F. Zhang, H. Xu, A. Ghafourian, J. M. Herreros and S. Shuai, "Investigation of two-stage split-injection strategies for a Dieseline fuelled PPCI engine," *Fuel,* vol. 107, pp. 299-308, 2013.

[96] A. Turkcan, A. N. Ozsezen and M. Canakci, "Effects of second injection timing on combustion characteristics of a two stage direct injection gasoline–alcohol HCCI engine," *Fuel,* vol. 111, pp. 30-39, 2013.

[97] M. Sellnau, J. Sinnamon, K. Hoyer and H. Husted, *Gasoline Direct Injection Compression Ignition (GDCI)-Diesel-Like Efficiency with Low CO2 Emissions,* SAE Paper 2011-01-1386.

[98] Y. Shi and R. D. Reitz, "Optimization of a heavy-duty compression–ignition engine fueled with diesel and gasoline-like fuels," *Fuel,* vol. 89, pp. 3416-3430, 2010.

[99] A. Weall and N. Collings, *Gasoline Fuelled Partially Premixed Compression Ignition in a Light Duty Multi Cylinder Engine: A Study of Low Load and Low Speed Operation,* SAE Paper 2009-01-1791.

[100] Y. Yang, J. Dec, N. Dronniou and W. Cannella, *Boosted HCCI Combustion using Low-Octane Gasoline with Fully Premixed and Partially Stratified Charges,* SAE Paper 2012-01-1120.

[101] S. L. Kokjohn, R. M. Hanson, D. A. Splitter and R. D. Reitz, *Experiments and Modeling of Dual-Fuel HCCI and PCCI Combustion using in-Cylinder Fuel Blending,* SAE Paper 2009-01-2647.

[102] R. M. Hanson, S. L. Kokjohn, D. A. Splitter and R. D. Reitz, *An Experimental Investigation of Fuel Reactivity Controlled PCCI Combustion in a Heavy-Duty Engine,* SAE Paper 2010-01-0864.

[103] C. S. Lee, K. H. Lee and D. S. Kim, "Experimental and numerical study on the combustion characteristics of partially premixed charge compression ignition engine with dual fuel< sup>☆</sup>," *Fuel,* vol. 82, pp. 553-560, 2003.

[104] S. Ma, Z. Zheng, H. Liu, Q. Zhang and M. Yao, "Experimental investigation of the effects of diesel injection strategy on gasoline/diesel dual-fuel combustion," *Appl. Energy,* vol. 109, pp. 202-212, 2013.

[105] J. Benajes, A. Garc ía, V. Domenech and R. Durrett, "An investigation of partially premixed compression ignition combustion using gasoline and spark assistance," *Appl. Therm. Eng.,* vol. 52, pp. 468-477, 2013.

[106] J. Benajes, S. Molina, A. Garc ía, J. Monsalve-Serrano and R. Durrett, "Conceptual model description of the double injection strategy applied to the gasoline partially premixed compression ignition combustion concept with spark assistance," *Appl. Energy,* vol. 129, pp. 1-9, 2014.

[107] R. Hanson, D. Splitter and R. Reitz, *Operating a Heavy-Duty Direct-Injection Compression-Ignition Engine with Gasoline for Low Emissions,* SAE Paper 2009-01-1442.

[108] H. Solaka, U. Aronsson, M. Tuner and B. Johansson, *Investigation of Partially Premixed Combustion Characteristics in Low Load Range with Regards to Fuel Octane Number in a Light-Duty Diesel Engine,* SAE Paper 2012-01-0684.

[109] G. Kalghatgi, R. Kumara Gurubaran, A. Davenport, A. Harrison, Y. Hardalupas and A. Taylor, "Some advantages and challenges of running a Euro IV, V6 diesel engine on a gasoline fuel," *Fuel,* vol. 108, pp. 197-207, 2013.

[110] V. Manente, B. Johansson and P. Tunestal, "Characterization of partially premixed combustion with ethanol: EGR sweeps, low and maximum loads," *Journal of Engineering for Gas Turbines and Power,* vol. 132, pp. 082802, 2010.

[111] V. Manente, B. Johansson, P. Tunestal and W. J. Cannella, *Influence of Inlet Pressure, EGR, Combustion Phasing, Speed and Pilot Ratio on High Load Gasoline Partially Premixed Combustion,* SAE Paper2010-01-1471.

[112] V. Manente, C. Zander, B. Johansson, P. Tunestal and W. Cannella, *An Advanced Internal Combustion Engine Concept for Low Emissions and High Efficiency from Idle to Max Load using Gasoline Partially Premixed Combustion,* SAE Paper 2010-01-2198.

[113] A. Trueba, B. Barbeau, O. Pajot and K. Mokaddem, *Pilot Injection Timing Effect on the Main Injection Development and Combustion in a DI Diesel Engine,* SAE Paper 2002-01-0501.

[114] G. Pitcher, J. Turner and R. Pearson, *GEM Ternary Blends of Gasoline, Ethanol and Methanol: An Initial Investigation into Fuel Spray and Combustion Characteristics in a Direct-Injected Spark-Ignition Optical Engine using Mie Imaging,* SAE Paper 2012-01-1740.

[115] A. Montanaro, M. Migliaccio, L. Allocca, V. Fraioli, S. Lee, A. Zhang and J. Naber, *Schlieren and Mie Scattering Visualization for Single-Hole Diesel Injector Under Vaporizing Conditions with Numerical Validation,* SAE Paper 2014-01-1406.

[116] A. Adam, P. Leick, G. Bittlinger and C. Schulz, "Visualization of the evaporation of a diesel spray using combined Mie and Rayleigh scattering techniques," *Exp. Fluids,* vol. 47, pp. 439-449, 2009.

[117] A. C. Eckbreth, *Laser Diagnostics for Combustion Temperature and Species.* CRC Press, 1996.

[118] B. Williams, P. Ewart, R. Stone, H. Ma, H. Walmsley, R. Cracknell, R. Stevens, D. Richardson, J. Qiao and S. Wallace, *Multi-Component Quantitative PLIF: Robust Engineering Measurements of Cyclic Variation in a Firing Spray-Guided Gasoline Direct Injection Engine,* SAE Paper 2008-01-1073.

[119] C. Schulz, J. Gronki and S. Andersson, *Multi-Species Laser-Based Imaging Measurements in a Diesel Spray,* SAE Paper 2004-01-1917.

[120] R. Zhang, N. Wermuth and V. Sick, *Impact of Fluorescence Tracers on Combustion Performance in Optical Engine Experiments,* SAE Paper 2004-01-2975.

[121] R. P. Fitzgerald, R. R. Steeper and J. A. Snyder, *Effects of LIF Tracers on Combustion in a DI HCCI Engine,* SAE Paper 2008-01-2407.

[122] C. Schulz and V. Sick, "Tracer-LIF diagnostics: quantitative measurement of fuel concentration, temperature and fuel/air ratio in practical combustion systems," *Progress in Energy and Combustion Science,* vol. 31, pp. 75-121, 2005.

[123] T. Baritaud and T. Heinze, *Gasoline Distribution Measurements with PLIF in a SI Engine,* SAE Paper 922355.

[124] G. Bruneaux, *A Study of Mixture Formation in Direct Injection Diesel Like Conditions using Quantitative Fuel Concentration Visualizations in a Gaseous Fuel Jet,* SAE Paper 2002-01-1632.

[125] N. Wermuth and V. Sick, *Absorption and Fluorescence Data of Acetone, 3-Pentanone, Biacetyl, and Toluene at Engine-Specific Combinations of Temperature and Pressure,* SAE Paper 2005-01-2090.

[126] K. Carabell and P. Farrell, *A/F Ratio Visualization in a Diesel Spray,* SAE Paper 940680.

[127] G. Särner, M. Richter, M. Aldén, L. Hildingsson, A. Hultqvist and B. Johansson, *Simultaneous PLIF Measurements for Visualization of Formaldehyde-and Fuel-Distributions in a DI HCCI Engine,* SAE Paper 2005-01-3869.

[128] L. Hildingsson, B. Johansson, A. Hultqvist, S. Gustaf, M. Richter and M. Ald, *Simultaneous Formaldehyde and Fuel-Tracer Lif Imaging in a High-Speed Diesel Engine with Optically Accessible Realistic Combustion Chamber,* SAE Paper 2005-24-008.

[129] M. H. Davy, P. A. Williams and R. W. Anderson, *Effects of Fuel Composition on Mixture Formation in a Firing Direct-Injection Spark-Ignition (DISI) Engine: An Experimental Study using Mie-Scattering and Planar Laser-Induced Fluorescence (PLIF) Techniques,* SAE Paper 2000-01-1904.

[130] S. Busch, C. Disch, H. Kubach and U. Spicher, *Optical Investigations of the Vaporization Behaviors of Isooctane and an Optical, Non-Fluorescing Multicomponent Fuel in a Spark Ignition Direct Injection Engine,* SAE Paper 2010-01-2271.

[131] V. Sick, M. C. Drake and T. D. Fansler, "High-speed imaging for direct-injection gasoline engine research and development," *Exp. Fluids,* vol. 49, pp. 937-947, 2010.

[132] E. Berrocal, E. Kristensson, P. Hottenbach, M. Aldén and G. Grünefeld, "Quantitative imaging of a non-combusting diesel spray using structured laser illumination planar imaging," *Applied Physics B,* vol. 109, pp. 683-694, 2012.

[133] B. Stojkovic and V. Sick, "Evolution and impingement of an automotive fuel spray investigated with simultaneous Mie/LIF techniques," *Applied Physics B,* vol. 73, pp. 75-83, 2001.

[134] M. Uhl, R. Schießl, U. Maas and A. Dreizler, *Time Resolved Spray Characterisation in a Common Rail Direct-Injection Production Type Diesel Engine using Combined Mie/LIF Laser Diagnostics,* SAE Paper 2003-01-1040.

[135] B. Maunoury, T. Duverger, K. Mokaddem and F. Lacas, *Phenomenological Analysis of Injection, Auto-Ignition and Combustion in a Small DI Diesel Engine,* SAE Paper 2002-01-1161.

[136] W. Zeng, M. Xu, M. Zhang, Y. Zhang and D. Cleary, *Characterization of Methanol and Ethanol Sprays from Different DI Injectors by using Mie-Scattering and Laser Induced Fluorescence at Potential Engine Cold-Start Conditions,* SAE Paper 2010-01-0602.

[137] M. Andersson, W. Jonas, S. Hemdal, P. Dahlander and I. Denbratt, *Evaporation of Gasoline-Like and Ethanol-Based Fuels in Hollow-Cone Sprays Investigated by Planar Laser-Induced Fluorescence and Mie Scattering,* SAE Paper 2011-01-1889.

[138] J. E. Dec and W. Hwang, *Characterizing the Development of Thermal Stratification in an HCCI Engine using Planar-Imaging Thermometry,* SAE Paper 2009-01-0650.

[139] J. Lee and K. Nishida, "Development of an LIF image processing technique for measuring drop sizes in a pre-swirl spray," *International Journal of Automotive Technology,* vol. 9, pp. 381-390, 2008.

[140] L. A. Melton, "Spectrally separated fluorescence emissions for diesel fuel droplets and vapor," *Appl. Opt.,* vol. 22, pp. 2224-2226, 1983.

[141] M. R. Herfatmanesh, P. Lu, M. A. Attar and H. Zhao, "Experimental investigation into the effects of two-stage injection on fuel injection quantity, combustion and emissions in a high-speed optical common rail diesel engine," *Fuel,* vol. 109, pp. 137-147, 2013.

[142] C. Arcoumanis, A. Hadjiapostolou and J. Whitelaw, *Flow and Combustion in a Hydra Direct-Injection Diesel Engine,* SAE Paper 910177.

[143] M. Lai, N. A. Henein, X. Xie, T. Chue, Y. Itoh and W. Bryzik, *Diesel Cold-Starting Study using Optically Accessible Engines,* SAE Paper 952366.

[144] N. Shimazaki, H. Hatanaka, K. Yokota and T. Nakahira, *A Study of Diesel Combustion Process Under the Condition of EGR and High-Pressure Fuel Injection with Gas Sampling Method,* SAE Paper 960030.

[145] I. Yamaguchi, T. Nakahira, M. Komori and S. Kobayashi, *An Image Analysis of High Speed Combustion Photographs for DI Diesel Engine with High Pressure Fuel Injection,* SAE Paper 901577.

[146] M. R. Herfatmanesh, "*Investigation of single and split injection strategies in an optical diesel engine,*" PhD Thesis, 2010.

[147] R. Joel, *Basic Engineering Thermodynamics.* Pearson Education India, 1987.

[148] H. Zhang, "Experimental investigation of gasoline–Dimethyl Ether dual fuel CAI combustion with internal EGR," PhD Thesis, 2011.

[149] G. M. Rassweiler and L. Withrow, *Motion Pictures of Engine Flames Correlated with Pressure Cards,* SAE Paper 380139.

[150] H. Zhao and N. Ladommatos, "Engine combustion instrumentation and diagnostics," *Warrendale, PA: Society of Automotive Engineers, 2001.842,* 2001.

[151] S. Ishikawa, Y. Ohmori, S. Fukushima, T. Suzuki, A. Takamura and T. Kamimoto, *Measurement of Rate of Multiple-Injection in CDI Diesel Engines,* SAE Paper 2000-01-1257.

[152] A. Takamura, T. Ohta, S. Fukushima and T. Kamimoto, *A Study on Precise Measurement of Diesel Fuel Injection Rate,* SAE Paper 920630.

[153] T. Ikeda, Y. Ohmori, A. Takamura, Y. Sato, L. Jun and T. Kamimoto, *Measurement of the Rate of Multiple Fuel Injection with Diesel Fuel and DME,* SAE Paper 2001-01-0527.

[154] X. Seykens, L. Somers and R. Baert, "Modeling of common rail fuel injection system and influence of fluid properties on injection process," *Proceedings of VAFSEP,* pp. 6-9, 2004.

[155] A. Vacca and B. Manhartsgruber, "A Novel Approach for the Prediction of Dynamic Features of Air Release and Absorption in Hydraulic Oils," *Journal of Fluids Engineering,* vol. 135, 2013.

[156] B. D. Nikolić, B. Kegl, S. D. Marković and M. S. Mitrović, "Determining the speed of sound, density and bulk modulus of rapeseed oil, biodiesel and diesel fuel," *Thermal Science,* vol. 16, pp. 505-514, 2012.

[157] J. Dernotte, C. Hespel, F. Foucher, S. Houille and C. Mounaïm-Rousselle, "Influence of physical fuel properties on the injection rate in a Diesel injector," *Fuel,* vol. 96, pp. 153-160, 2012.

[158] E. Torres-Jimenez, M. Kegl, R. Dorado and B. Kegl, "Numerical injection characteristics analysis of various renewable fuel blends," *Fuel,* vol. 97, pp. 832-842, 2012.

[159] K. Huhtala and M. Vilenius, *Study of a Common Rail Fuel Injection System,* SAE Paper 2001-01-3184.

[160] R. Payri, F. Salvador, J. Gimeno and G. Bracho, "The effect of temperature and pressure on thermodynamic properties of diesel and biodiesel fuels," *Fuel,* vol. 90, pp. 1172-1180, 2011.

[161] A. L. Boehman, D. Morris, J. Szybist and E. Esen, "The impact of the bulk modulus of diesel fuels on fuel injection timing," *Energy Fuels*, vol. 18, pp. 1877-1882, 2004.

[162] M. Chorążewski, F. Dergal, T. Sawaya, I. Mokbel, J. E. Grolier and J. Jose, "Thermophysical properties of Normafluid (ISO 4113) over wide pressure and temperature ranges," *Fuel,* vol. 105, pp. 440-450, 2013.

[163] B. A. D'Alleva, *Procedure and Charts for Estimating Exhaust Gas Quantities and Compositions.* Research Laboratories, General Motors Corporation, 1960.

[164] L. Eltinge, *Fuel-Air Ratio and Distribution from Exhaust Gas Composition,* SAE Paper 680114.

[165] R. S. Spindt, *Air-Fuel Ratios from Exhaust Gas Analysis,* SAE Paper 650507.

[166] J. Brettschneider, "Berechnung des luftverhältnisses lambda von luft-kraftstoff-gemischen und des einflusses von messfehlern auf lambda," *BOSCH TECH BER,* vol. 6, 1979.

[167] W. Simons, "Berechnungen zur Bestimmung der Luftzahl bei Ottomotoren," *MTZ Motortechnische Zeitschrift,* vol. 46, pp. 257-259, 1985.

[168] T. Fukui, Y. Tamura, S. Omorl and S. Saitoh, *Accuracy of A/F Calculation from Exhaust Gas Composition of SI Engines,* SAE Paper 891971.